Durham University

Durham E-Theses

Exploring the star formation histories of galaxies

Eric Findlay Bell

How to cite:

Bell, Eric Findlay (1999) Exploring the star formation histories of galaxies. Doctoral thesis, Durham University.

Use policy

The full-text may be used and/or reproduced, and given to third parties in any format or medium, without prior permission or charge, for personal research or study, educational, or not-for-profit purposes provided that:

- a full bibliographic reference is made to the original source
- a https://etheses.durham.ac.uk/id/eprint/4796/ is made to the metadata record in Durham E-Theses
- the full-text is not changed in any way

The full-text must not be sold in any format or medium without the formal permission of the copyright holders.

Please consult the full Durham E-Theses policy for further details.

Academic Support Office, The Palatine Centre, Durham University, Stockton Road, Durham, DH1 3LE
e-mail: e-theses.admin@durham.ac.uk Tel: +44 0191 334 6107
https://etheses.durham.ac.uk

Exploring the Star Formation Histories of Galaxies

Eric Findlay Bell

A thesis submitted to the University of Durham
in accordance with the regulations for
admittance to the Degree of Doctor of Philosophy.

The copyright of this thesis rests with the author. No quotation from it should be published without his prior written consent and information derived from it should be acknowledged.

Department of Physics
University of Durham
August 1999

The copyright of this thesis rests with the author. No quotation from it should be published without the written consent of the author an information derived from it should be acknowledged.

17 JAN 2000

O SON OF MAN!

Wert thou to speed through the immensity of space

and traverse the expanse of heaven,

yet thou would find no rest save in submission to Our command

and humbleness before Our Face.

Bahá'u'lláh

Exploring the Star Formation Histories of Galaxies

Eric Findlay Bell

Abstract

In this thesis, I explore the star formation histories of both spiral and elliptical galaxies.

In Part 1, I present an in-depth study of the star formation histories of spiral galaxies with a wide range of properties. Optical and near-infrared colours are used in conjunction with up-to-date stellar population synthesis models to constrain the ages and metallicities of my sample galaxies.

I find that age and metallicity gradients are common in spiral galaxies of all types. The age of a spiral galaxy correlates mainly with its surface brightness, and its metallicity correlates strongly with both its surface brightness and absolute magnitude. Using simple models, I demonstrate that the correlations observed in this thesis show that the star formation history of a region within a galaxy depends primarily on its surface density, and possibly on the dynamical time. Metal-enriched outflow from low mass galaxies seems to be required to reproduce a reasonably strong metallicity-magnitude correlation. These variations in star formation history are a continuous function of the physical parameters: in particular, I find no evidence for a bimodal spiral galaxy surface brightness distribution.

In Part 2, I present a short study on the formation epoch of early-type galaxies. I developed a photometric redshift estimator optimised for redshifts $z \sim 1$. The redshift estimator provides redshifts accurate to $\sim$ 10 per cent. This redshift estimator is then applied to a sample of morphologically-selected early-type galaxies in the northern Hubble Deep Field. Comparison of their colour-magnitude relation with a passively evolved Coma cluster colour-magnitude relation indicates that over half of the sample must form at redshifts greater than two.

Contents

Chapter 1 Introduction 1

1.1 Galaxy types 1

1.2 Observational properties of early and late-type galaxies 2

1.2.1 Colours 3

1.2.2 Spectra: absorption and emission lines 4

1.2.3 The dynamics of bulges and discs 5

1.3 Stellar populations in early and late types: techniques 6

1.3.1 Resolved stellar populations 7

1.3.2 Integrated light from stellar populations: the models 7

1.4 Stellar populations in early and late types: results 11

1.4.1 The star formation histories of early-type galaxies 11

1.4.2 The star formation histories of late-type galaxies 12

1.5 Modelling the formation of early and late-type galaxies 13

1.5.1 The nature hypothesis 14

1.5.2 The nurture hypothesis 14

1.5.3 Testing the two hypotheses 15

1.6 The questions addressed by this thesis 16

1.6.1 Star formation and feedback 16

1.6.2 Early-type galaxies at high redshift 17

Part 1 The star formation histories of spiral galaxies 19

Chapter 2 Low surface brightness galaxies 21

2.1 Introduction 21

2.2 Observations and data reduction 23

2.2.1 Sample selection 23

2.2.2 Near-infrared data 24

2.2.2.1 Apache Point Observatory data 26

2.2.2.2 South Pole data 30
2.2.3 Optical data 33

2.3 Photometry results **35**
2.3.1 Surface and aperture photometry 35
2.3.2 Bulge/disc decompositions 38
2.3.3 Comparison with existing data 39
2.3.4 LSBG morphology 41

2.4 Star formation histories **42**
2.4.1 Results 45
2.4.1.1 Colour gradients 45
2.4.1.2 Colour differences between galaxies 46
2.4.2 Are the stellar population differences real? 48
2.4.2.1 Are IMF uncertainties important? 48
2.4.2.2 Dust reddening 48

2.5 Discussion **49**
2.5.1 Quantifying the colour-colour plane 49
2.5.2 The correlations 51
2.5.2.1 Limitations of our dataset 53
2.5.2.2 Ages and metallicities 53
2.5.2.3 Trends in LSBG age 53
2.5.2.4 Trends in LSBG metallicity 54
2.5.3 SFH as a function of total mass and density 54
2.5.4 A unifying view 58

2.6 Conclusions **58**

Chapter 3 The stellar populations of spiral galaxies **61**

3.1 Introduction **61**

3.2 The data, stellar population and dust models **63**
3.2.1 The data 63
3.2.2 The stellar population models 66
3.2.3 The dust models 67

3.3 Maximum-likelihood fitting **68**

3.3.1 Estimating age and metallicity gradients 70

3.4 Results **72**

3.4.1 Colour-colour plots 72

3.4.2 Local ages and metallicities 76

3.4.3 Global relations 78

3.4.3.1 Global ages 78

3.4.3.2 Global metallicities 84

3.4.3.3 Age gradients 85

3.4.3.4 Metallicity gradients 87

3.5 Discussion **87**

3.5.1 Surface brightness vs. magnitude 87

3.5.2 Star formation histories in terms of masses and densities . 91

3.5.3 Does the choice of IMF and SPS model affect our conclusions? 93

3.5.4 How important is dust extinction? 94

3.5.5 Comparison with HII region metallicities 95

3.5.6 A possible physical interpretation 97

3.6 Conclusions **101**

Chapter 4 Spiral galaxy evolution **103**

4.1 Introduction **103**

4.2 The Model **104**

4.2.1 Basic assumptions and equations 104

4.2.2 Determining ages and metallicities 105

4.3 Galaxy evolution **107**

4.3.1 Closed box model 107

4.3.2 Infall model 113

4.3.3 Outflow model 116

4.3.4 Summary 118

4.4 Star formation laws **119**

4.4.1 Density threshold 119

4.4.2 Dynamical time dependence 122

4.5 Conclusions and prospects **124**

Chapter 5 The bimodal surface brightness distribution **126**

5.1 Introduction **126**

5.2 Constructing a null hypothesis **128**

5.3 Results **129**

5.4 Discussion **132**

5.5 Conclusions **135**

Part 2 The formation epoch of early type galaxies **137**

Chapter 6 A Bayesian photometric redshift classifier **138**

6.1 Introduction **138**

6.2 Colour tracks as a function of star formation history **141**

6.2.1 Model 141

6.2.1.1 Equations and parameters 141

6.2.1.2 Elliptical galaxies and bulges 142

6.2.1.3 Discs 143

6.2.2 Colour tracks 146

6.3 Bayesian classification **153**

6.3.1 Basic scheme 153

6.3.2 Prior distribution 154

6.3.2.1 The local luminosity function 154

6.3.2.2 Volume element 155

6.3.2.3 Comparison with observation 156

6.3.2.4 The effect of the prior 157

6.3.3 The models included in the classifier 157

6.3.4 Error estimates 158

6.4 Testing **160**

6.4.1 Abell 370 161

6.4.2 Hubble Deep Field 164

6.5 Application to high redshift clusters **166**

6.5.1 Biases in the recovered galaxy properties 167

6.5.2 Optimal passbands for cluster identification 172

6.6 Conclusions **172**

Chapter 7 The colour-magnitude relation: HDF **174**

7.1 Introduction **174**

7.2 The field colour-magnitude relation at $z = 0.9$ **175**

7.2.1 Early-type galaxies in the Hubble Deep Field 175

7.2.2 Rest-frame colours and magnitudes 176

7.2.3 The colour-magnitude relation 178

7.3 Constraints on star formation history **180**

7.4 Discussion **184**

7.5 Conclusions **186**

Chapter 8 Conclusions and prospects **187**

8.1 Part 1: The star formation histories of spiral galaxies **187**

8.1.1 Conclusions 187

8.1.2 Future work 188

8.2 Part 2: The formation epoch of early-type galaxies **190**

8.2.1 Conclusions 190

8.2.2 Future work 191

8.3 What have we learned from this thesis? **191**

Appendix A Low surface brightness galaxies: photometry **193**

A.1Photometry results 193

Bibliography 209

List of Figures

1.1 Hubble Diagram 1
1.2 Breaking the age-metallicity degeneracy 9
2.1 Comparison with literature 40
2.2 Low surface brightness galaxy colours 43
2.3 SFH with surface brightness and magnitude 52
2.4 SFH with density and mass 55
3.1 The ages and metallicities of UGC 3080 71
3.2 Colour-colour plot: type 73
3.3 Colour-colour plot: magnitude 74
3.4 Colour-colour plot: central surface brightness 75
3.5 Colour-colour plot: scale length 76
3.6 Colour-colour plot: gas fraction 77
3.7 Local ages and metallicities 78
3.8 Global correlations: age 79
3.9 Global correlations: metallicity 80
3.10 Global correlations: age gradient 81
3.11 Global correlations: metallicity gradient 82
3.12 Global correlations: physical parameters 83
3.13 Age gradient with galaxy type 86
3.14 Residuals 89
3.15 Correlations with mass and density 91
3.16 Comparison of metallicities 96
3.17 Local density dependent star formation law 98
4.1 Global correlations: selection limits 108
4.2 Local correlations: fiducial model 110
4.3 Age at the half light radius: fiducial model 111
4.4 Metallicity at the half light radius: fiducial model 112
4.5 Population gradients: fiducial model 113
4.6 Local correlations: infall model I2 114
4.7 Age at the half light radius: infall model I2 115
4.8 Local correlations: outflow model 116
4.9 Metallicity at the half light radius: outflow model 117

4.10 Local correlations: critical density model 121
4.11 Local correlations: critical density model with infall 122
4.12 Local correlations: dynamical time model 123
4.13 Population gradients: dynamical time model 123
5.1 Bimodal surface brightness distribution 130
5.2 Uncertainties in the inclination corrections 133
6.1 Gas mass to light ratio vs. colours 145
6.2 Colour-colour plots in the observer's frame 147
6.3 Example spectra 148
6.4 Comparison with observed $n(z)$ 156
6.5 Effects of photometry errors 159
6.6 Field galaxies: Abell 370 161
6.7 Cluster members: Abell 370 162
6.8 The colour-magnitude diagram for Abell 370 163
6.9 The colour histogram for Abell 370 164
6.10 Hubble Deep Field 165
6.11 Field galaxies: simulated cluster field 168
6.12 Cluster members: simulated cluster field 168
6.13 The colour-magnitude diagram of the simulated cluster 169
6.14 The colour histogram of the simulated cluster 170
7.1 The colour-magnitude relation of HDF early-types 179
7.2 Residuals from the Coma CMR 182
A.1 Surface photometry 202
A.1 Surface photometry: continued 203
A.1 Surface photometry: continued 204
A.1 Surface photometry: continued 205
A.1 Surface photometry: continued 206
A.1 Surface photometry: continued 207
A.1 Surface photometry: continued 208

List of Tables

2.1 Sample parameters 25
2.2 Near-infrared observing log 27
2.3 Photometric calibration 29
2.4 Photometric calibration 32
2.5 Optical observing log 34
2.6 Photometric calibration 35
2.7 Ellipticities and position angles 36
3.1 Fits to the correlations 88
3.2 IMF and model uncertainties 93
4.1 Model descriptions 119
5.1 Significance of the bimodality 132
6.1 Integrated colours of spiral galaxies 144
6.2 Colour degeneracies 151
6.3 Adopted luminosity function parameters 155
6.4 Passband choice for random galaxy simulations 160
6.5 Simulated galaxies in a $z = 1$ cluster field. 166
6.6 Colour-magnitude relations 169
6.7 Effects of passband coverage 171
7.1 Peculiar galaxies 183
A.1 Bulge/disc decompositions 194
A.1 Bulge/disc decompositions: continued 195
A.1 Bulge/disc decompositions: continued 196
A.1 Bulge/disc decompositions: continued 197
A.1 Bulge/disc decompositions: continued 198
A.1 Bulge/disc decompositions: continued 199
A.1 Bulge/disc decompositions: continued 200
A.1 Bulge/disc decompositions: continued 201

Preface

The work described in this thesis was undertaken between 1996 and 1999 whilst I was a research student under the supervision of Dr Richard Bower and Dr Bernard Rauscher in the Department of Physics at the University of Durham. This work has not been submitted for any other degree at the University of Durham or at any other University.

The work presented in this thesis is my own, unless stated explicitly otherwise. I played a leading rôle in the work presented in Chapters 2 to 6. Chapter 7 was carried out in collaboration with Tadayuki Kodama and Richard Bower and is included in this thesis as an example application of the photometric redshift estimator I developed in Chapter 6.

A number of the results presented here have appeared in the following papers:

- Bell E. F., Bower R. G., de Jong R. S., Hereld M., Rauscher B. J., 1999, MNRAS, 302, 55L
- Bell E. F., Bower R. G., de Jong R. S., Rauscher B. J., Barnaby D., Harper D. A., Hereld M., Loewenstein R. F., 1999, in *IAU 171 Conference Proceedings* — "The Low Surface Brightness Universe", eds. J. I. Davies, C. Impey and S. Phillipps
- Bell E. F., Barnaby D., Bower R. G., de Jong R. S., Harper D. A., Hereld M., Loewenstein R. F., Rauscher B. J., 1999, MNRAS, submitted
- Bell E. F., de Jong R. S., 1999, MNRAS, submitted
- Bell E. F., de Blok W. J. G., 1999, MNRAS, accepted
- Kodama T., Bell E. F., Bower R. G., 1999, MNRAS, 302, 152
- Kodama T., Bower R. G., Bell E. F., 1999, MNRAS, 306, 561
- Kodama T., Bell E. F., Bower R. G., 1999, in "Photometric Redshifts and High Redshift Galaxies" eds. R. Weymann, L. Storrie-Lombardi, M. Sawicki, R. Brunner, ASP Conference Series, in press

Acknowledgments

I'd like to thank my supervisors, Richard Bower and Bernard Rauscher, for their constant, unfailing support and encouragement over my three years in Durham. Working under them has been a fantastic experience that I'll always carry with me: special thanks to Richard for teaching me about ice cream's relevance to astronomy. I'd also like to thank the helpful souls who I've tricked into working with me: Roelof de Jong, Erwin de Blok, Tadayuki Kodama, and David Barnaby. I've enjoyed working with you all immensely, and have profited greatly from your help and wisdom. Many thanks to those who have allowed me to steal their data: Stacy McGaugh, Karen O'Neil, David Sprayberry and Marc Verheijen.

Working in the astronomy department in Durham has been a wonderful experience: the research environment is a lively one, filled with debate and discussion. I've profited greatly from the numerous discussions and debates I've engaged in here! Special thanks (and commiserations) are due for the unfortunate few who were forced to share an office with me: Harald, Claire, Katherine, Doug (for the briefest of times), James, Fiona, David and Kevin. Hopefully their lives will improve after I submit this thesis! Many thanks also to Harald, Taddy, Claire, Fiona and Andrew for ripping my introduction to shreds — if you think it's bad now, you should have seen it then! Special thanks to Alan Lotts for keeping the computers in working order — without your constant hard work, none of us would ever get anything done.

It is a great pleasure to thank many of my friends who are fortunate enough not to be astronomers: without all of you, my life in Durham would have been dull and lifeless. The entire north-eastern Bahá'í community deserves many thanks for teaching me so much about how to live a good life: special thanks to those who fed me (you know who you are — your fridges are a lot less full)! Special thanks to David and Margaret for making life fun!

Of course, I couldn't have gotten here if it weren't for the constant support and love from my family, who have encouraged my interest in astronomy unfailingly over the years, and have helped to fund much of my student life! The in-laws deserve special mention, for just making life grand. Special thanks are reserved for my mentor in astronomy, Jim Moravec, who nurtured my interest in astronomy at a crucial time: without you, I would have never gotten this far.

I dedicate this work to my wife, Maureen: you have given me the opportunity to discover just how wonderful this amazing universe can be.

Chapter 1

Introduction

That there are many different types of galaxy has long been recognised. In contrast, the differences in formation history and evolution leading to these different galaxy types have been the subject of vigorous debate for decades. Understanding the star formation histories of galaxies is a vital piece of this puzzle: the star formation history of a galaxy is an important observational relic of its formation and evolution. In this thesis, we explore the star formation histories of a wide range of different galaxy types in an attempt to learn something of how they formed and evolved.

1.1 Galaxy types

Hubble (1936) sums up the observational census in his tuning fork diagram, which describes the morphological differences between galaxies along the so-called Hubble sequence (Fig. 1.1; taken from Kormendy and Bender 1996).

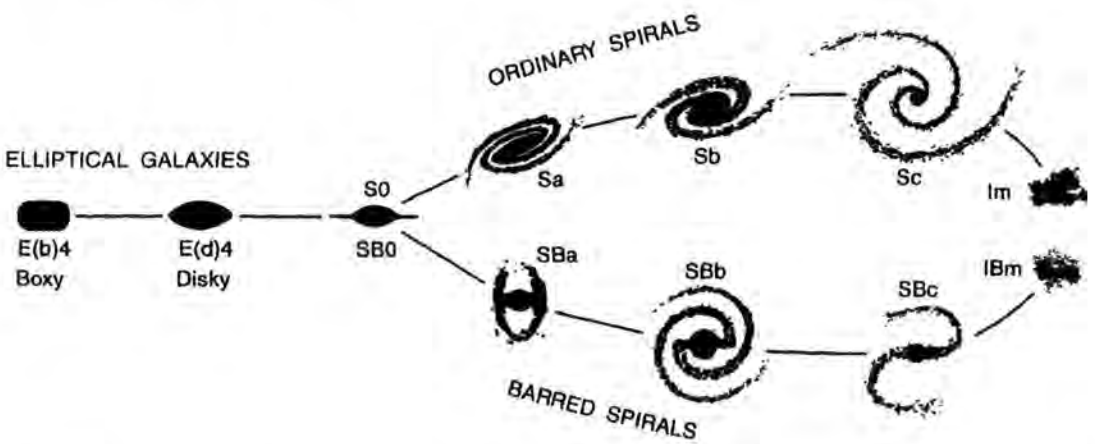

Figure 1.1: The 'revised' Hubble Tuning fork diagram, taken from Kormendy & Bender (1996). For further discussion, see the text.

The mainly elliptical early-type galaxies have a smooth optical appearance and are dominated by an elliptical, centrally condensed core. Only a small fraction of the total light of early-type galaxies, if any, comes from a flatter disc with a similarly smooth optical appearance. As one travels from left to right along the Hubble sequence, the bulge becomes an increasingly less important component of the light distribution of galaxies. The disc, at the same time, becomes more prominent, also becoming more richly structured, with tight, well-organised spiral structure giving way to more loose, haphazard spiral arms in the very latest type galaxies.

Hubble envisaged an evolutionary connection between these different types of galaxy. He postulated that galaxies formed as featureless balls of stars (elliptical galaxies), and as they collapsed they started to rotate, gradually flattening and appearing more disc-like (lenticular galaxies). This collapse continued, and these increasingly disc-like galaxies developed spiral arms (spiral galaxies). This evolutionary connection proposed by Hubble has given rise to the terms early-type for elliptical and lenticular galaxies (as these galaxies were early in their evolutionary history) and late-type for spiral and irregular galaxies (as these galaxies were towards the end of their evolutionary history). The bewildering variety of galaxy morphologies that we see today is then the direct result of i) the spread in galaxy formation times and ii) the evolution between the relatively featureless early-type galaxies and the richly structured late-type galaxies.

Today, our understanding of the differences and evolutionary connections between early and late-type galaxies is much advanced. In the first part of this introduction, we look at some of the observational developments in the understanding of early and late type galaxies. We then interpret these observations using stellar population and chemical evolution models. Then we consider differences in their formation and evolution histories that may have led to these stellar population differences. Finally, an overview of the main questions addressed by this thesis is given. Note that a detailed thesis plan is not given in the introduction: a detailed plan is given in the preambles to Parts 1 and 2 of this thesis.

1.2 Observational properties of early and late-type galaxies

Over the years, it has become clear that there are many phenomenological differences between early and late-type galaxies. The main morphological differences between early and late-types have been discussed above, and was the original distinguishing property between these different types of galaxy. Below, we discuss the colours, spectra and dynamics of early and late-type galaxies, linking these observations with their morphology.

1.2.1 Colours

Early-type galaxies are typically red in the optical and in the near-infrared, whereas late-type galaxies are much bluer, especially towards their outer regions, and in their spiral arms (e.g. Peletier, Valentijn & Jameson 1990; Bower, Lucey & Ellis 1992a; de Jong 1996c, dJIV hereafter; Chapters 2 & 3). Roughly speaking, the colours of a stellar population[1] are directly related, via Wien's law, to the main-sequence turn-off temperature on the Hertzsprung-Russell diagram. In turn, the temperatures of stars and their masses (and therefore, via the main sequence lifetime-mass relation, their ages) are linked, implying that early-type galaxies are older, on average, than late-type galaxies. In practice, this simplistic interpretation of galaxy colours fails as both the age and metallicity (defined here as the mass fraction of elements heavier than helium) of a stellar population affects its colours. [2] In addition, the shorter-lived but very bright later stages of stellar evolution complicate the above simple-minded interpretation of the colours of these composite stellar populations (e.g. Bruzual & Charlot 1993; Worthey 1994; Charlot, Worthey & Bressan 1996; Kodama & Arimoto 1997, KA97 hereafter; Trager 1999). The factors affecting the colours and spectra of galaxies, and the uncertainties in understanding and modelling these effects are further discussed in section 1.3.

However, the situation is even more complicated: the colours of a galaxy are not only affected by its stellar population (through their e.g. age or metallicity), but are also affected by interstellar dust reddening. Distributed throughout galaxies, dust profoundly affects our understanding of their stellar populations. As particles of dust are similar in size to the wavelength of visible light, they effectively absorb and scatter ultraviolet and visible light, re-radiating the energy in the mid- and far-infrared. The efficiency of absorption and scattering changes as a function of wavelength: the total attenuation of light (due to the effects of both absorption and scattering) as a function of wavelength is given by the extinction curve. The amount of extinction increases sharply as a function of decreasing wavelength, with the extinction curve being reasonably approximated by λ^{-1}. Due to this wavelength dependence in the efficiency of extinction, light is reddened, as well as dimmed by dust. This provides a method of detecting dust: deep multi-colour imaging of both early and late-type galaxies has conclusively illustrated the increasing importance of dust from early to late-type galaxies, with significant amounts of dust detected in $\gtrsim 1/2$ of early-type

[1] Here we define a stellar population as an evolving single burst with a unique single age and metallicity and a mass spectrum given by the stellar initial mass function (see also section 1.3).

[2] Metallicity affects the colours of stellar populations for two main reasons: because the radius of metal poor stars tends to be smaller than those of metal rich stars, and because stars with a lower metallicity have fewer spectral lines at (primarily bluer) wavelengths (Tinsley 1980; Pagel 1998).

galaxies, and in nearly all late-type galaxies. (e.g. Block et al. 1994; Goudfrooij & de Jong 1995; van Dokkum & Franx 1995; de Jong et al. 1998; Kuchinski et al. 1998; Tully et al. 1998).

1.2.2 Spectra: absorption and emission lines

Broad band colours only probe the broad shape of the spectral energy distribution (SED) of early and late-type galaxies. By dispersing the light using e.g. diffraction gratings, it is possible (using longer integration times on larger telescopes) to extract much more information from the more detailed spectra of galaxies.

One of the main differences between the spectra of early and late-type galaxies reflects the colour differences between these types of galaxies that we discussed above: early-type galaxies have SEDs which peak in the optical, between 5000Å and 7000Å, with a sharp cut-off below 4000Å (the so-called 4000Å break: see Fig. 6.3 of Chapter 6 for an example early-type galaxy SED). In stark contrast, the SEDs of late-type galaxies increase almost monotonically with decreasing wavelength, reflecting their bluer colours.

Early-type galaxies typically have a dense forest of strong stellar absorption lines, caused by the absorption of light from hot stellar interiors by the gas in their cooler atmospheres in narrow wavelength ranges. In contrast, the very latest type galaxies have a barely detectable stellar continuum (with rather fewer absorption lines, due to the differences in early and late-type stellar populations) but a much larger contribution from intense emission lines from HII regions (relatively dense pockets of hydrogen, helium and heavy elements, ionised by short wavelength light from recently formed O and B stars). Correspondingly, the metallicities of early-type galaxies are typically measured using absorption lines, which reflect a luminosity-weighted mean metallicity of the entire stellar population. In contrast, the metallicities of late-type galaxies are measured using emission lines, which provide a 'snapshot' of the gas metallicity at the present day. Therefore, comparison of the metal abundances in early and late-type galaxies is not straightforward, due to the differences in measurement technique.

Two main trends are observed in both early and late-type galaxies. Firstly, the metallicity of galaxies typically increases with their mass (e.g. Skillman, Kennicutt & Hodge 1989; Vila-Costas & Edmunds 1992; Zaritsky, Kennicutt & Huchra 1994; Kuntschner 1998; Colless et al. 1999; Jørgensen 1999). The colour-magnitude relation in early-type galaxies is qualitatively consistent with this metallicity-mass relation (e.g. Visvanathan & Sandage 1972; Larson, Tinsley & Caldwell 1980; Bower, Lucey & Ellis 1992, BLE hereafter; Kodama et al. 1998; Stanford et al. 1998; Chapter 7), as is the dust-free colour-magnitude relation in spiral galaxies (Peletier & de Grijs

1998). Secondly, most galaxies have abundance gradients, where the outer regions of galaxies are less chemically enriched than the inner regions of galaxies (with the notable exception of barred spiral galaxies; bars are thought to induce radial gas flows which 'erase' pre-existing abundance gradients; e.g. Martin & Roy 1994). There have been suggestions that there is little *intrinsic* scatter in the abundance gradients exhibited by both early and late-type galaxies (e.g. Kuntschner 1998; Henry & Worthey 1999); however, this has been questioned by e.g. Vila-Costas & Edmunds (1992) for late types and Kobayashi & Arimoto (1999) for elliptical galaxies. Due to the differences between the methods used to probe the metallicities in early and late-type galaxies, it is not clear whether all galaxies have the same metallicity-mass relation, or how comparable the abundance gradients in early and late-type galaxies are. For an excellent review of the abundance properties of early and late-type galaxies see e.g. Henry & Worthey (1999).

1.2.3 The dynamics of bulges and discs

The star formation histories of early and late-type galaxies are a powerful diagnostic of their formation and evolution. However, much can be learned about galaxy formation and evolution by understanding the *dynamics* of the gaseous and stellar content of bulges and discs. Three main techniques are used to study the dynamics of early and late-type galaxies.

1. Absorption line studies allow investigation of the dynamics of the stellar populations of early-type galaxies. More luminous elliptical galaxies are typically supported by velocity dispersion, with little or no rotational support (Kormendy & Bender 1996); many lower luminosity elliptical galaxies are rotationally supported (e.g. Davies et al. 1983; Halliday 1998). Many early-type galaxies show evidence of kinematic irregularities in their central regions, where in addition to the larger bulge component, a kinematically distinct bulge or disc component is present (e.g. Halliday 1998; Hau, Carter & Balcells 1999). These relatively common kinematically distinct substructures suggest some kind of either major or minor merger event, indicating that mergers occur during the formation history of at least a large fraction of elliptical galaxies (Hau & Thomson 1994; Balcells & González 1998; Hau, Carter & Balcells 1999).

2. The dynamics of the ionised gas in galaxies can be probed using optical emission lines. There are typically only small amounts of ionised gas in early-types (Goudfrooij et al. 1994): sometimes it comes from a small ionised gas disc similar to a small stellar disc seen in absorption, suggesting a common origin (Hau, Carter & Balcells 1999). In late-type galaxies, because of the typically larger gas content and more widespread star formation, the ionised gas distribution

extends to much larger radii, often extending even to the edge of the optical disc or beyond (Ferguson et al. 1998). This more extended optical line emission originates in both the dense and diffuse gas components of spiral galaxies, in roughly equal proportions (e.g. Ferguson et al. 1996; Wang, Heckman & Lehnert 1999). Because of the larger radial extent of the gas, it is possible to study the dynamics of almost the entire optical disc, revealing solid body rotation in the central regions of the galaxy, asymptotically flattening off at larger galactocentric radii (e.g. Vogt et al. 1996; Courteau 1997; Rubin, Waterman & Kenney 1999). These observations invariably indicate, through the failure of the rotation curve to decline at large radii, the presence of large quantities of unseen matter in the outer regions of spiral galaxies.

3. Investigation of the 21 cm radio spectral line of neutral hydrogen presents us with the opportunity to investigate the dynamics of the (sometimes much more extended) neutral hydrogen content of galaxies (e.g. de Blok et al. 1996; Verheijen 1997; Bosma 1998). These studies, in probing to larger galactocentric radii, probe the distribution of matter to much greater distances than the optical line studies described above. In almost all cases, the rotation curve of the neutral hydrogen remains flat out to huge radii: in the well studied case of the dwarf galaxy DDO 154, the rotation curve arguably does not decrease out to a distance of 15 disc scale lengths, implying that at least 90 per cent of its mass is in an unseen form (Carignan & Freeman 1988). Since its widespread acceptance in the late 1970s as an explanation for the 'flat' rotation curves of spiral galaxies, overwhelming evidence in favour of huge quantities of dark matter has been uncovered: for example, the velocity dispersions of rich clusters of galaxies (e.g. Carlberg et al. 1996), relative velocities of galaxy pairs (Zaritsky & White 1994) and gravitational lensing (Fort & Mellier 1994; Brainerd, Blandford & Smail 1996).

1.3 Stellar populations in early and late types: techniques

The observational differences outlined above suggest significant differences between the formation histories of early and late-type galaxies. Star formation histories are one of the the main observational probes of the formation histories of galaxies; therefore, a better understanding of the star formation histories of early and late-type galaxies is a vitally important step in building up an understanding of the physics involved in galaxy formation and evolution.

1.3.1 Resolved stellar populations

Disentangling star formation histories from even resolved stellar populations is difficult: most studies of the stellar populations of nearby galaxies do not reach the bottom of the red giant branch (Tolstoy et al. 1998; Hurley-Keller, Mateo & Nemec 1998; Minniti, Zijlstra & Alonso 1999), although e.g. Gallart et al. (1999) and Holtzman et al. (1999) use HST to reach further down the main sequence for the nearby dwarf spheroidal Leo I and the Large Magellanic Cloud respectively. This can cause considerable problems in determining the star formation histories for old ($\gtrsim$ 5 Gyr) stellar populations: the latest stages of stellar evolution are subject to considerable modelling uncertainties (Charlot, Worthey & Bressan 1996; Maraston 1998; Traat 1999), and the differences in colour and magnitude for large differences in age or metallicity can be quite small (e.g. Bertelli et al. 1994). Despite these difficulties, significant progress has been made in understanding the star formation histories of nearby galaxies (Grebel 1998; Tolstoy 1999a, 1999b). A picture has emerged where we see that the star formation histories of even outwardly quite similar galaxies are very diverse and richly varied (Tolstoy 1999a). Colour-magnitude diagrams of local galaxies show features indicating that these galaxies did not form stars continuously during their history; rather that they form their stars in bursts, indicating a complex evolutionary history, depending on many, not necessarily internal, parameters (Grebel 1998). In addition, evidence is seen for an underlying old stellar population in almost all nearby galaxies (Grebel 1998; Tolstoy 1999b).

1.3.2 Integrated light from stellar populations: the models

Determining star formation histories from the integrated light of more distant stellar populations is even more challenging. The light from different evolutionary stages of stars in a given stellar population, and from different stellar populations, is mixed up in a galaxy's integrated spectrum. Therefore, the interpretation of the spectrum from an integrated stellar population is subject to many degeneracies and uncertainties. The best example of this problem is the age-metallicity degeneracy: the spectra of composite stellar populations are virtually identical if the percentage change in age or metallicity (Z) follows $\Delta\mathrm{age}/\Delta Z \sim 3/2$ (Worthey 1994). The age-metallicity degeneracy is broken only for certain special combinations of spectral line indices, or for limited combinations of broad band colours (Worthey 1994; dJIV; Trager 1999; Vazdekis & Arimoto 1999): these special line indices or colours are more sensitive to age or metallicity effects, and can be used, in conjunction with stellar population synthesis models to place constraints on the age and metallicity of a stellar population.

The use of optical–near-infrared broad band colours to break the age-metallicity degeneracy deserves special mention here, as it is the method we use in Chapters 2 and 3 to constrain the star formation histories of spiral galaxies. The basic principle is illustrated in Fig. 1.2 (kindly provided by S. Trager; from Trager 1999).

In Fig. 1.2 we can see the basic principle underlying any technique that breaks the age-metallicity degeneracy: we must compare a quantity that is sensitive to the position of the main sequence turn-off (MTSO; e.g. Hβ or optical colours, due to the high temperature of the MTSO) with a quantity that is more sensitive to the position of the red giant branch (RGB; e.g. metal lines or near-infrared colours, due to the low temperatures of the RGB).

However, even using these special colours or indices, significant systematic errors in the star formation histories remain, because of uncertainties in both the stellar population synthesis models, and because of (necessary) simplifying assumptions that must be made in the analysis of the integrated light from composite stellar populations.

- Significant inaccuracies are introduced by the star formation histories that we assume for the composite stellar population. Because of the degeneracies introduced by our use of an integrated spectrum, it is very difficult to determine a unique star formation history. For this reason, a certain *type* of star formation history is typically assumed, and parameters describing that type of star formation history are determined when investigating the spectra of galaxies. For early-type galaxies, a single, short burst of star formation is typically assumed; the age and metallicity of that burst are then the parameters of interest (González 1993; Kuntschner & Davies 1998; Trager 1999). For late-type galaxies, because of the obvious importance of recent star formation, an exponentially declining star formation rate and single stellar metallicity are assumed; the exponential timescale and metallicity are the parameters of interest (dJIV; McCracken 1999; Chapters 2 and 3). However, we know from the studies of resolved stellar populations in local galaxies that galaxies tend to form their stars in multiple bursts (Grebel 1998; Tolstoy 1999a); therefore, our assumption of a single burst *or* a smoothly varying exponential star formation rate will almost certainly be inaccurate. In this case, what we will measure using our parameters is some kind of *luminosity-weighted* average of the stellar population's properties (de Jong & Davies 1997; Kuntschner & Davies 1998; Trager 1999). The luminosity-weighted ages and metallicities are still useful; they allow us to probe systematic differences in star formation history with e.g. type, luminosity, etc.; however, *they do not reflect the true ages or metallicities of the composite stellar populations.*

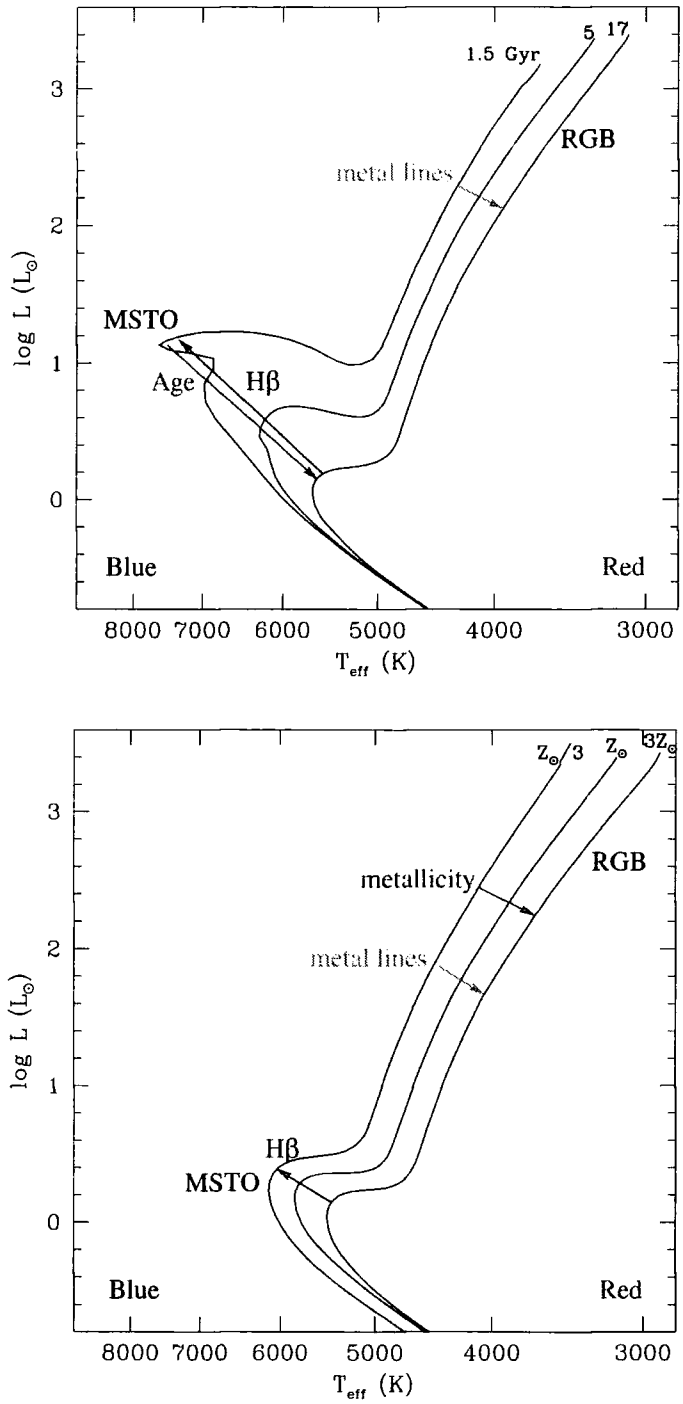

Figure 1.2: Breaking the age-metallicity degeneracy. The upper panel shows age effects on the Hertzsprung-Russell diagram, and the lower panel shows metallicity effects on the same scale. One can immediately see that age and metallicity effects on the red giant branch (RGB) are very similar; however, their effects on the main sequence turn-off (MTSO) are quite different, allowing discrimination between age and metallicity effects. Figure courtesy of S. Trager (from Trager 1999).

- Another source of uncertainty in determining star formation histories is inaccuracy in the stellar evolution tracks used in the stellar population synthesis models. Of particular concern are the lifetimes and luminosities of the short-lived but bright latest stages of stellar evolution: the complex structure and evolution of these cool stars and uncertainties regarding the importance of mass loss all contribute to large inaccuracies in the colours and luminosities of composite stellar populations, especially in the near-infrared (Charlot, Worthey & Bressan 1996; Maraston 1998; Origlia et al. 1999; Maraston, Greggio & Thomas 1999).

- In addition, there are considerable uncertainties in translating the stellar evolution tracks into observables, such as broad band colours or line strengths. One of the main challenges lies in modelling the spectra of types of stars which are rare in the solar neighbourhood, such as young, low metallicity stars: for this type of star, we must extrapolate from relatively well-constrained regions of parameter space into unexplored territory using stellar atmosphere models (e.g. Kurucz 1979). Other uncertainties include modelling the complex spectra of cool stars and calibration of the colour-temperature relation (Charlot, Worthey & Bressan 1996; Sekiguchi & Fukugita 1999).

- The stellar initial mass function (IMF), the mass spectrum of newly-formed stars, is quite uncertain, especially at the low and high mass ends (see e.g. Scalo 1998; Elmegreen 1999). Uncertainties at the low mass end of the IMF are fairly insignificant (in terms of star formation or chemical evolution histories, but not for dynamics): because low mass stars are so faint, they only significantly change the stellar mass to light ratio of the stellar population. Uncertainties at the high mass end of the IMF are more significant: while the influence of high mass stars is short-lived, they are nevertheless very luminous, and produce a large fraction (around half) of the metals produced by a given mass of stellar population. For this reason, the high mass end of the IMF is important: a different ratio of low to high mass stars produces substantially different mixes of heavy elements in a galaxy's stellar populations (Chiosi et al. 1998; Pagel 1998).

There are a number of other significant uncertainties in the stellar population models (e.g. non-solar abundance ratios); however one of the largest, which is rarely addressed, is the influence of binary stars. More than half of all local stars are in multiple star-systems; however, the differences between the evolution of single and binary stars are still essentially unknown.

1.4 Stellar populations in early and late types: results

Despite these major sources of uncertainty, significant progress has been made in understanding the star formation histories of early and late-type galaxies.

1.4.1 The star formation histories of early-type galaxies

Comparison of the observational data with stellar population synthesis models have yielded considerable insight into the star formation histories of early-type galaxies. Because early-type galaxies lack the ongoing star formation so characteristic of later type galaxies, their spectra are better suited to detailed comparison with the models. There are two main results, with a number of exceptions and caveats.

Gradients: *Early-type galaxies have well-established abundance gradients, and little, if any age gradient.* The main evidence supporting this scenario comes from detailed study of line strength gradients in elliptical and lenticular galaxies. All absorption lines are sensitive to both age and metallicity effects, but in different amounts. By using a primarily age-sensitive absorption line such as one of the Balmer-series lines like Hβ or Hγ in conjunction with an age and metallicity sensitive line such as Mg_2 or Mgb (Worthey 1994; Trager 1999, see Fig. 1.2), it is possible to probe *both* age and metallicity gradients. This issue was explored by e.g. Kuntschner (1998), Halliday (1998) and Kobayashi & Arimoto (1999) (but for only a small subsample of their overall sample). They found that the line strength gradients in early-type galaxies are mostly consistent with metallicity gradients: a few, faint elliptical or lenticular galaxies have young, metal rich core;, however, the majority of early-types lack significant age gradients (Kuntschner 1998; Halliday 1998). This conclusion is supported by an innovative study of colour gradients in Hubble Deep Field early-types at high redshift: Tamura et al. (1999) find that the measured colour gradients in the Hubble Deep Field early-types are consistent with the hypothesis that *local* early-type galaxy line strength and colour gradients are due to metallicity gradients but are inconsistent with the hypothesis that they are due to age gradients.

Global relations: *The metallicity and mass of an early-type galaxy are related: trends in the global ages of ellipticals are proving difficult to come to any sort of consensus on.* Studies of the Balmer series and e.g. magnesium or iron line strengths have come to differing conclusions. Kuntschner and Davies (1998) and Jørgensen (1999) show that the central parts of most early-types in the clusters differ only in terms of their metallicity: their ages are relatively similar. This is consistent with the scatter (BLE; Bower, Kodama & Terlevich 1998) and evolution with redshift (Kodama et al. 1998) of the colour-magnitude relation: analysis of the colour-magnitude relation

using stellar population synthesis models shows that the colour-magnitude relation is primarily a metallicity sequence, and the scatter in the relation reflects age differences. In stark contrast, studies of less homogeneous samples of field and cluster ellipticals, such as that of González (1993), have indicated that the metallicities of early-types are quite similar, and that they have a range of luminosity-weighted ages. Other studies suggest possible age differences between cluster and field selected samples of early types: Guzman et al. (1992) and Bernardi et al. (1998) report small offsets in the $Mg_2 - \sigma$ relation between lower density and higher density environments.

Systematic differences in the star formation histories of early-type galaxies are suggested by the so-called *magnesium overabundance*. The abundance of magnesium (and other light elements) in early-type galaxies tends to be enhanced relative to iron, when compared with the solar neighbourhood. Furthermore, the overabundance seems to depend on galaxy mass: higher mass galaxies tend to have larger overabundances than lower mass galaxies, which have nearly solar abundance ratios (Kuntschner 1998; Henry & Worthey 1999; although see Kobayashi & Arimoto 1999 for a differing view). Stellar population synthesis and chemical evolution modelling of elliptical galaxies indicate two main possibilities for creating such an overabundance: both hinge on the relative importance of Type II supernovae (which create primarily light elements, and stem from relatively high-mass progenitors) and Type Ia supernovae (which produce primarily iron-peak elements, and have fairly low mass white dwarf binary progenitors). In one scenario, elliptical galaxies form in a short burst of star formation, with lower mass galaxies forming more gradually than higher mass ellipticals (Arimoto & Yoshii 1987; KA97). An alternative view postulates similar formation timescales for the formation of low and high mass early-types, but explains the magnesium overabundance in terms of IMF differences, where high mass galaxies have a shallower IMF (therefore more high mass stars) than lower mass galaxies (Chiosi et al. 1998). Either way, there are systematic trends in the star formation properties of early-type galaxies as a function of mass.

1.4.2 The star formation histories of late-type galaxies

There is a much larger amount of ongoing star formation (and dust) in late-type galaxies, making the interpretation of their broad band colours difficult using stellar population synthesis models. Additionally, most late-type galaxies have relatively few absorption features, lower surface brightnesses and a significant number of strong emission features in their spectra (Kennicutt 1992): this means that analysis of their spectra in terms of the stellar population models are difficult, and give us only very loose constraints on their star formation histories. Despite these tremendous

difficulties, some progress in understanding the star formation histories of late-type galaxies has been made.

Gradients: *Spiral galaxies have both age and metallicity gradients, in the sense that their outer regions are younger and more metal poor than their inner regions.* Studies of radial trends in HII region gas abundances with radius have shown that metallicity gradients are common in ordinary spiral galaxies (Vila-Costas & Edmunds 1992; Zaritsky, Kennicutt & Huchra 1994; Garnett et al. 1997), but are much weaker in barred spiral galaxies, possibly due to the effects of bar-induced gas flows (Vila-Costas & Edmunds 1992; Martin & Roy 1994). The evidence for age gradients in spirals is more limited: dJIV finds that optical–near-IR colour gradients are common in his diameter-limited sample of spiral galaxies. Comparison with stellar population synthesis models showed that these colour gradients are primarily consistent with the presence of a gradient in mean stellar age, where the outer regions of spiral galaxies are younger than their inner regions. Note that dust is unlikely to produce these colour gradients (dJIV; Kuchinski et al. 1998).

Global relations: *Bright spiral galaxies are both older and more metal rich than fainter spiral galaxies.* The main evidence for this trend in star formation history and metallicity with luminosity is from the dust-free colour-magnitude relation from Peletier & de Grijs (1998): comparison of the spiral galaxy colour-magnitude relation with stellar population synthesis models indicated that the spiral galaxy colour-magnitude relation, unlike the early-type galaxy colour-magnitude relation, is likely to be driven by *both* age and metallicity effects. This conclusion is supported by dJIV, who finds that later type spirals are younger and more metal poor than earlier type spirals: as later types are typically fainter than earlier types (de Jong 1996b; dJIII hereafter), his observations are qualitatively consistent with Peletier & de Grijs' dust-free colour-magnitude relation. Trends in metallicity with magnitude are well-documented: see e.g. section 1.2.2 or Vila-Costas & Edmunds (1992), Zaritsky, Kennicutt & Huchra (1994) or Garnett et al. (1997) for more details.

1.5 Modelling the formation of early and late-type galaxies

Taken together, the above observational differences, in conjunction with the evolutionary differences implied by the stellar population synthesis models, are only of use if they are used to try to further our understanding of the physical processes behind galaxy formation and evolution. In this section, I describe two extreme scenarios. The 'nature' hypothesis, as embodied in a monolithic collapse model (e.g. Larson 1975; Larson 1976; Dalcanton, Spergel & Summers 1997), proposes that the differences in the star formation histories and observational properties of early and late-type galaxies are the direct result of the initial conditions of galaxy formation.

The 'nurture' hypothesis, as embodied in the so-called hierarchical models of galaxy formation [3], asserts that galaxies all started off reasonably similarly, and that the effects of interactions with their neighbours has shaped how we see the galaxies today (e.g. Kauffmann & Charlot 1998a; Somerville & Primack 1998; Cole et al. 1999). The truth almost certainly incorporates aspects of both types of model: the physics involved in galaxy formation is so complex that no present-day model can attempt to accurately describe all of the processes. Each approach has its limitations, and its observational successes and failures.

1.5.1 The nature hypothesis

All galaxies start out as slightly overdense concentrations of gas and dark matter at early times. Gradually, the protogalaxy's expansion slows, and it starts to collapse under the influence of its own self-gravity. During this expansion, turn-around and collapse, the protogalaxy is subject to tidal forces from other protogalaxies: these interactions impart angular momentum to the halo, which starts to slowly rotate. Towards the latter stages of collapse, stars may start to form in the collapsing gas: this is a vitally important process to understand in the 'nature' picture of galaxy evolution. Early-type galaxies, which are dominated by an elliptical stellar bulge, form their stars rapidly during the earliest stages of the collapse. Later type galaxies do not form stars as quickly: the gas has the chance to collapse into a thin disc. It is in this disc that the gas subsequently turns into stars. Various bulge-to-disc ratios are understood in the context of this model as resulting from different star formation timescales during the formation of that given galaxy. The main question left unanswered by this model is that of the mechanism determining the balance between the collapse timescale and the star formation timescale (Eggen, Lynden-Bell & Sandage 1962; Larson 1975; Larson 1976; Coles & Lucchin 1995). Note that this mechanism may be linked to the degree of substructure in a collapsing halo. 'Lumpy' haloes will form stars in small galaxies which very quickly merge to form an elliptical galaxy. 'Smoother' haloes may manage to collapse more homogeneously, allowing the bulk of the gas to settle into a disc configuration before forming stars (Arimoto & Yoshii 1987).

1.5.2 The nurture hypothesis

The 'nurture' hypothesis stems from much the same basic picture of protogalaxy formation: the main difference between this picture of galaxy formation and monolithic collapse is that in the

[3] These models are termed hierarchical as the structure forms in a hierarchy, with galaxies forming first: gradually these coalesce into larger and larger superstructures with time.

'nurture' scenario, all galaxies collapse to form a disc system. In this picture, galaxies do not evolve in isolation; instead, galaxies are enmeshed in a complex, hierarchical, web of galaxies and large scale structure. This complex web of galaxies and large scale structure is the distinguishing feature of the nurture hypothesis: structure forms from the 'bottom-up', where galaxies form, and are later incorporated into larger and larger structures. This kind of behaviour is only possible if dark matter is 'cold'; if dark matter were in the form of e.g. neutrinos, structure would form on the largest scales first, percolating down in scale as the universe evolved.

Mergers, which are neglected (or feature only at early times) in the 'nature' hypothesis, are quite common in this scenario. Minor mergers, where a low mass galaxy interacts with and is devoured by a much larger galaxy, leave the morphology of the larger galaxy relatively unaffected. However, major mergers, where the two galaxies are roughly equal masses, have a profound effect on morphology: the merger remnant typically appears roughly spheroidal, with a luminosity profile and kinematic properties reminiscent of an elliptical galaxy (see e.g. Barnes & Hernquist 1992 for a review). These newly-formed elliptical galaxies, depending on gas supply, may re-form a disc: in this way a bulge-disc sequence can be created. Alternative bulge formation mechanisms can also be considered: it may be possible to form a bulge from a dense, dynamically unstable disc, or from the stellar fraction of galaxies accreted in minor mergers (Kauffmann & Charlot 1998a; Somerville & Primack 1998; Cole et al. 1999).

1.5.3 Testing the two hypotheses

'Nurture' models are well-supported by observations: these models enjoy their greatest successes in describing large scale structure, and in describing global observables such as the present day luminosity function, the Tully-Fisher relation or the star formation history of the universe (Somerville & Primack 1998; Cole et al. 1999). The performance of 'nurture' models in explaining the properties of early-type galaxies is more mixed. Because of the importance of mergers in producing the early-type galaxy population, 'nurture' models naturally accommodate the observations of kinematically decoupled cores in many ellipticals. Hierarchical models also predict strong evolution of the early-type galaxy population with redshift: observations of the K band luminosity function and the number densities of faint, extremely red galaxies support the hierarchical picture (e.g. Cowie et al. 1996; Zepf 1997; Barger et al. 1999). On the other hand, the relatively small scatter of the colour-magnitude relation in the field may present a serious problem for hierarchical models (Larson, Tinsley & Caldwell 1980; Bower, Kodama & Terlevich 1998; Chapter 7). This stems from the inability of hierarchical models to reproduce *both* the metallicity-magnitude

relation *and* the luminosity function (Kauffmann & Charlot 1998a; Cole et al. 1999). There are also potential problems in linking elliptical galaxies to spiral-spiral mergers: the central density of stars is unlikely to be high enough in a purely stellar merger, although a central starburst in gas-rich mergers may alleviate this problem (Barnes & Hernquist 1996). For these issues, monolithic collapse models can provide a better match to the observations (Arimoto & Yoshii 1987; KA97; Kodama et al. 1998). Note however that the monolithic collapse models are clearly wrong at some level: there is a huge amount of observational evidence at both low and high redshift indicating that mergers are increasingly important at early times (Barnes 1999).

1.6 The questions addressed by this thesis

From the above discussion, it is clear that both types of model have considerable progress to make if they are to accurately describe galaxy formation and evolution. In this thesis, we concentrate on two main questions raised by these galaxy formation models. For this reason, we split this thesis into two parts. Here, we give an overview of the two main questions we address: we give a much more detailed plan of each part of the thesis at the beginning of each of those parts.

1.6.1 Star formation and feedback

One of the primary uncertainties plaguing galaxy formation modellers is our lack of knowledge regarding the star formation law and the importance of stellar feedback on galactic scales (e.g. Somerville & Primack 1998; Cole et al. 1999). Late-type galaxies offer an ideal test-bed in which to derive and test star formation laws (e.g. Kennicutt 1989; Kennicutt 1998), and in which to study the importance and behaviour of stellar feedback (e.g. MacLow & Ferrera 1999; Martin 1999). This is because mergers are expected not to be an important feature of the recent history of spiral galaxies: discs are dynamically fragile, implying that spiral galaxies have built up their discs relatively quiescently (Toth & Ostriker 1992; Velazquez & White 1999). Therefore, we can study star formation and feedback processes essentially independently of the detailed formation history of spiral galaxies.

A related problem is our lack of understanding regarding the physical processes that drive the star formation histories of late-type galaxies. Earlier, we saw that there is clear evidence for trends in star formation history with galaxy type; however, it is unclear what drives these differences in star formation history. Part of the problem is the lack of a suitable sample with which to study the systematic trends in star formation history as a function of e.g. magnitude or surface brightness:

most samples lack the dynamic range in e.g. magnitude or surface brightness to be able to detect trends in star formation history as a function of these parameters.

In Part 1, we address these two related problems. We present the results of a programme of optical and near-infrared imaging of low surface brightness spiral galaxies: when combined with existing datasets of a similar quality, the sample covers a large range of surface brightnesses, magnitudes, scale lengths and gas fractions. We then use this optical and near-infrared data to constrain the ages and metallicities of this diverse sample of spiral galaxies. Using these constraints, we can then gain some insight into how the star formation law and feedback *must have operated* to produce the observational correlations between star formation history and galaxy parameters that we see today.

1.6.2 Early-type galaxies at high redshift

A key observational distinction between nature and nurture models is the properties of high redshift early-type galaxies. In the nature picture, early-types are expected to form in a single collapse at early times, and evolve passively thereafter (with perhaps small amounts of residual star formation continuing to the present day fuelled by accretion of gas or satellite galaxies; e.g. Arimoto & Yoshii 1987; KA97). In stark contrast, the nurture model predicts a broad range of early-type galaxy formation times: in particular, field and cluster early-types are expected to have very different mean ages (Kauffmann & Charlot 1998a; Cole et al. 1999). Thus, the properties of high redshift early-types are quite different in the two schemes: nature models predict a substantial contingent of early-type galaxies at high redshift (which formed at similar times, and therefore appear quite similar in their properties), whereas nurture models predict a relatively small number of high redshift early-types (which themselves have a spread in formation times, and look fairly inhomogeneous as a group). However, high redshift early-types are typically very faint in the observed optical wavelength range, making spectroscopic determination of a redshift prohibitively difficult. Thus a scheme must be derived with which we can use broad band colours to estimate (or place limits on) their redshifts. However, the use of a colour-based redshift estimate may be a concern: if the redshift estimator uses the e.g. 4000Å break to estimate the redshifts, it is possible that the galaxy populations recovered using this technique may be biased towards a strong 4000Å break, making unbiased study of high redshift early-types impossible.

In Part 2, we take advantage of this observational test of the competing galaxy formation models by studying the colours of high redshift early-type galaxies. We develop a photometric redshift estimator optimised for detecting high redshift early-types. By testing the estimator with real and

simulated data, we show that the redshift estimator is unbiased, and gives a relatively complete census of the galaxy populations at high redshift. We then use this photometric redshift estimator to compare the colour-magnitude relation of field and cluster early-types at high redshift: this allows us to put strong constraints on the formation epoch of field early-types.

Part 1

The star formation histories of spiral galaxies

In Part 1, we attempt to identify what the most important parameters are in driving the star formation histories of spiral galaxies. As we saw in the introduction, systematic study of the star formation histories of spiral galaxies can give us considerable insight into star formation laws on galactic scales and stellar feedback: both of these processes are poorly understood, and together represent one of the primary uncertainties in many models of galaxy formation and evolution (e.g. Cole et al. 1999).

Differences in the star formation histories of spiral galaxies as a function of Hubble type were studied qualitatively by dJIV, who found that later type spirals were typically fainter, lower surface brightness, younger and more metal poor than their earlier type spiral counterparts. Peletier & de Grijs (1998) studied this more quantitatively by investigating the dust-free colour-magnitude relation for edge-on disc galaxies. They found a tight correlation between colour (an indicator of star formation history) and magnitude (an indicator of stellar mass). It is also possible to explore the star formation histories of spiral galaxies using their HII region metallicities as indicators of their evolutionary status: the HII region heavy element abundances in spiral discs correlate with both their surface brightnesses and magnitudes (Edmunds & Pagel 1984; Skillman, Kennicutt & Hodge 1989; Vila-Costas & Edmunds 1992; Zaritsky, Kennicutt & Huchra 1994). Taken together, these studies suggest that both the mass and density of a spiral galaxy may correlate with its star formation history.

In Part 1, we explore the star formation histories of spiral galaxies using their broad band optical and near-infrared colours. In conjunction with stellar population synthesis models such as those of Bruzual & Charlot (in preparation) or KA97, it is possible to constrain the ratio of young to old

stars (which is in essence an average age) and the galaxy metallicity. However, a limiting factor in this type of analysis is the availability of near-infrared data, especially for faint and/or low surface brightness galaxies. Yet it is precisely these faint or low surface brightness galaxies that give us the dynamic range to discern trends in star formation history with magnitude or surface brightness.

In Chapter 2, we present deep optical and near-infrared imaging for a diverse sample of low surface brightness galaxies. We use their colours to constrain their star formation histories: we find that low surface brightness galaxies cover a wide range of star formation histories, from older, near-solar metallicity stellar populations to young, ultra-low metallicity stellar populations. In Chapter 3, we extend our analysis by including two larger samples of spiral galaxies (dJIV; Tully et al. 1996). This larger galaxy sample has a much larger dynamic range than the low surface brightness galaxy sample of Chapter 2, and therefore allows a much more robust investigation of the processes shaping spiral galaxies in general. We find that surface density is the most important parameter in shaping the star formation history of a galaxy. Mass plays a secondary, but non-negligible rôle: in particular, the metallicity of a galaxy depends equally on both its surface density and mass. In Chapter 4, we study these results more intensively: with the aid of simple chemical evolution models, we find that a density dependence in the star formation law (coupled, perhaps, with a dependence on the dynamical timescale) reproduces the above correlation between age and K band surface brightness. However, the metallicity-magnitude correlation is difficult to accommodate using this mechanism alone: we argue that the ejection of heavy elements by supernovae explosions is an important process in shaping the chemical evolution of galaxies.

In Chapters 2–4, we implicitly assume that the properties of spiral galaxies and physical processes that dictate their star formation histories smoothly vary, so that galaxies come in a continuous range of e.g. masses and surface densities. However, the basis of this argument is clearly flawed if spiral galaxies come in e.g. two distinct families, each with their own distinct evolutionary histories. Tully & Verheijen (1997) claimed that the near-infrared spiral galaxy surface brightness distribution is bimodal, suggesting that there are fundamental differences between high surface brightness and low surface brightness galaxies, placing many of the basic assumptions in Chapters 2–4 in doubt. In Chapter 5, we attempt to assess the statistical significance of this bimodality in the surface brightness distribution, and investigate the uncertainties inherent in the determination of this surface brightness distribution, concluding that there is little concrete evidence for a bimodal surface brightness distribution in their dataset.

Chapter 2

The star formation histories of low surface brightness galaxies

The physical parameters that drive the star formation histories (SFHs) of spiral galaxies have remained elusive for many decades. The problem was twofold. i) Only recently have near-infrared (near-IR) detectors and multi-metallicity stellar population synthesis models become available with which to attack the problem. ii) The samples of galaxies with the required type and quality of data were somewhat limited in terms of the range of galaxy properties covered.

In this chapter, we focus on the second problem: low surface brightness disc galaxies (LSBGs; galaxies with B band central surface brightnesses fainter than 22.5 mag arcsec^{-2}) suffer from a number of severe observational biases against their inclusion in studies of spiral galaxies. We attempt to redress the balance by undertaking a programme of deep optical and near-IR imaging of LSBGs in order to constrain their SFHs.

2.1 Introduction

There has been much recent debate on the SFHs of LSBGs. The best studied LSBGs are blue in the optical and the near-IR (McGaugh & Bothun 1994; de Blok, van der Hulst & Bothun 1995; Bergvall et al. 1999), indicating a young mean stellar age and/or low metallicity. Their measured HII region metallicities are low, at around or below $1/3$ solar abundance (McGaugh 1994; Rönnback & Bergvall 1995; de Blok & van der Hulst 1998a). Morphologically, the best studied LSBGs have discs, but little spiral structure (McGaugh, Schombert & Bothun 1995). The

current massive star formation rates (SFRs) in LSBGs are an order of magnitude lower than those of high surface brightness (HSB) galaxies (van der Hulst et al. 1993; van Zee, Haynes & Salzer 1997). HI observations show that LSBGs have high gas mass fractions, sometimes even approaching unity (de Blok, McGaugh & van der Hulst 1996; McGaugh & de Blok 1997). As yet, there have been no CO detections of LSBGs, only upper limits on the CO abundances which indicate that LSBGs have CO/HI ratios significantly lower than those of HSB galaxies (Schombert et al. 1990; de Blok & van der Hulst 1998b). All of these observations are consistent with a scenario in which LSBGs are relatively unevolved, low mass surface density, low metallicity systems, with roughly constant or even increasing SFRs (de Blok, McGaugh & van der Hulst 1996; Gerritsen & de Blok 1999).

However, this scenario has difficulty accommodating giant LSBGs: with scale lengths typically in excess of 5–10 h_{65}^{-1} kpc, these galaxies are similar to, but less extreme than, Malin 1. Quillen & Pickering (1997), in an as yet unpublished work, obtained near-IR H band imaging of two giant LSBGs. They concluded that the optical–near-IR colours of both the central and outer regions of their galaxies were compatible with those seen in old stellar populations (such as E/S0 galaxies).

Another difficulty for this scenario is posed by the recent discovery of a substantial population of red LSBGs (O'Neil et al. 1997a, 1997b). The optical colours of these galaxies are similar to those of old stellar populations, but the red colours could be caused by age or metallicity effects. Either way, the existence of old or metal-rich LSBGs is difficult to understand if all LSBGs are unevolved and gas-rich. This same age-metallicity degeneracy plagues the analysis of the colours of blue LSBGs. Padoan, Jimenez & Antonuccio-Delogu (1997) question the apparent youth of blue LSBG stellar populations: they find that LSBG optical colours are consistent with those of old, very low metallicity stellar populations.

This uncertainty caused by the age/metallicity degeneracy is partially avoidable; for stellar populations with ongoing star formation, it is possible to learn something of their SFH using a combination of optical and near-IR colours. Essentially, it is possible to compare the SFHs of galaxies in a relative sense, using a kind of 'birthrate parameter' relating the amount of recent star formation to the cumulative amount of previous star formation (in this work, we parameterise the SFHs using an exponential SFH with a timescale τ and an average age $\langle A \rangle$). As a guide to interpreting these optical and near-IR colours, we use the latest multi-metallicity stellar population synthesis models of e.g. Bruzual & Charlot (in preparation) and Kodama & Arimoto (1997, KA97). The limiting factor in applying this technique is typically the availability of near-

IR imaging; especially so for LSBGs, where the near-IR central surface brightness can be up to a factor of 500 fainter than the sky surface brightness at these wavelengths.

In this chapter, we present optical and near-IR imaging for a diverse sample of 26 LSBGs in order to explore their SFHs. In our study we include examples of i) the well-studied blue-selected LSBGs taken from de Blok et al. (1995, 1996), de Jong & van der Kruit (1994; dJI hereafter) and the ESO-LV catalogue, ii) the more poorly studied, intriguing red-selected LSBGs from O'Neil et al. (1997a, 1997b), and iii) the LSBG giants, taken from Sprayberry et al. (1995). Earlier results of this programme were presented in Bell et al. (1999), where the stellar populations in a subset of five red and blue LSBGs were explored; red LSBGs were found to be much older and metal-rich than blue LSBGs, indicating that the two classes of galaxy do not share a common origin. Here, we explore the differences in SFH between red, blue and giant LSBGs. We also attempt to understand which, if any, galaxy parameters (e.g. mass, or density) affect the SFHs of LSBGs, driving the differences between e.g. red and blue LSBGs.

The plan of this Chapter is as follows. The observations and data reduction are described in section 2.2. In section 2.3 we present the photometry for our sample, compare with existing published photometry, and discuss the morphologies of LSBGs in the optical and the near-IR. In section 2.4 we present the optical–near-IR colours for our sample of galaxies, discussing them in terms of differences in SFH. In section 2.5, we elaborate on this colour-based analysis and explore trends in SFH with physical parameters. Finally, we present our conclusions in section 2.6.

2.2 Observations and data reduction

2.2.1 Sample selection

Our sample of 26 LSBGs was selected with a number of criteria in mind. They must be detectable using reasonable exposure times on 4-m class telescopes in the near-IR, and must span a wide range of observed LSBG properties, such as physical size, surface brightness and colour. In addition, we selected galaxies with as much existing optical and HI data as possible. Our sample is by no means complete, but is designed instead to span as wide a range as possible of observed LSBG parameters.

Our northern sample was selected from a number of sources (de Blok et al. 1995, 1996; O'Neil et al. 1997a, 1997b; Sprayberry et al. 1995; dJI) to have moderately low published B band inclination corrected central surface brightness $22.5 \lesssim \mu_{B,0} \lesssim 23.5$ mag arcsec^{-2}. Furthermore, this sample

was selected to have major axis radii to the 25 B mag arcsec^{-2} isophote larger than $\sim$ 16 arcsec. Galaxies with only moderately low surface brightness were chosen, as the near-IR sky background at temperate sites is very high due to the large thermal flux from the telescope and sky.

In order to explore the properties of galaxies with even lower surface brightnesses, we imaged a small sample of galaxies using the South Pole 0.6-m telescope. The K band sky background at the South Pole is suppressed by a factor of $\sim$ 20 compared to temperate sites, allowing unprecedented sensitivity for faint extended K band surface photometry (see e.g. Nguyen et al. 1996; Rauscher et al. 1998). Our southern hemisphere sample is selected from the ESO-Uppsula Catalogue (Lauberts & Valentijn 1989) to have larger sizes and lower surface brightnesses compared to the northern sample: $\mu_{B,0} \geq 23.0$ mag arcsec^{-2}, 65 arcsec $\leq \mathrm{R}_{eff} \leq$ 150 arcsec, inclination less than 67° and galactic latitude $|b| \geq 20°$ to avoid excessive foreground galactic extinction (where R_{eff} denotes the galaxy half light radius).

Our sample is described in further detail in Table 2.1. Galaxy types and heliocentric velocities were typically taken from the NASA/IPAC Extragalactic Database (NED). Galaxy distances D were determined from velocities centred on the Local Group (Richter, Tammann & Huchtmeier 1987) assuming a a Hubble constant H_0 of 65 kms^{-1}Mpc^{-1}. For galaxies within $\sim$ 150 Mpc, we further take into account the local bulk peculiar motions (Branchini et al. 1999). Typical distance uncertainties, corresponding to the uncertainties in the peculiar motions, are typically $\sim$ 7 Mpc. HI gas masses were calculated using $M_{\mathrm{HI}} = 2.36 \times 10^5 D^2(\mathrm{Mpc}) \int \mathrm{S(Jy)dv(kms^{-1})}$ (de Blok et al. 1996), where S is the HI line flux in Janskys and dv is the line width in km s^{-1}. HI fluxes were taken from NED, except for the HI fluxes from de Blok et al. (1996), Sprayberry et al. (1995) and O'Neil, Bothun & Schombert (1999) . Note that in Table 2.1 all the galaxies without HI masses have not yet been observed in HI *except* C1-4 and C3-2, which were not detected with Arecibo in 5 $\times$ 5 minutes and 12 $\times$ 5 minutes respectively yielding 3σ upper limits on their HI gas fractions of $\sim$ 15 per cent. In Table 2.1 we have also presented the foreground galactic extinction in B band, as estimated by Schlegel, Finkbeiner and Davis (1998). We have checked the Infra Red Astronomical Satellite (IRAS) point source and small scale structure catalogues (Moshir et al. 1990) for our sample: only the Seyfert 1 LSBG giant 2327-0244 was detected (at both 60μm and 100μm).

2.2.2 *Near-infrared data*

In this section, we describe the near-IR observations and data reduction. As pointed out in the previous section, we used both the APO 3.5-m telescope and the South Pole 0.6-m telescope

Table 2.1. Sample parameters

Object	RA(2000)	Dec(2000)	Type	D(Mpc)	$\log_{10} M_{HI}/M_{\odot}$	A_B	Source
UGC 128	00 13 51.3	35 59 41	Sdm	69	10.12±0.06[d]	0.28	A
ESO-LV 280140[a]	00 19 58.5	-77 05 27	SB(s)d	35	9.82±0.15[e]	0.23	F
UGC 334	00 33 54.9	31 27 04	SAB(s)cd	90	10.01±0.08[f]	0.24	E
0052-0119	00 55 08.9	-1 02 47	Sd	213	—	0.15	D
UGC 628	01 00 52.0	19 28 37	Sm:	85	9.85±0.13[f]	0.19	A
0221+0001	02 24 01.3	00 15 07	Sc	575	—	0.19	D
0237-0159	02 40 11.0	-1 46 27	Sc	197	—	0.13	D
ESO-LV 2490360[a]	03 59 15.2	-45 52 15	IB(s)m	24	9.56±0.21[e]	0.04	F
F561-1	08 09 41.3	22 33 33	Sm	82	9.39±0.05[g]	0.20	B
C1-4	08 19 24.4	21 00 12	S0[b]	56	—	0.21	C
C3-2	08 22 35.9	20 59 47	SB0a[b]	—	—	0.16	C
F563-V2	08 53 03.5	18 26 05	Irr	74	9.52±0.06[g]	0.07	B
F568-3	10 27 20.5	22 14 22	Sd	99	9.66±0.04[g]	0.09	B
1034+0220[a]	10 37 27.6	02 05 21	Sc	326	—	0.14	D
N10-2	11 58 42.4	20 34 41	Sb[b]	—	—	0.10	C
1226+0105	12 29 12.8	00 49 03	Sc	362	10.63±0.01[h]	0.10	D
F574-1	12 38 07.3	22 18 45	Sd	112	9.67±0.04[g]	0.10	B
F579-V1	14 32 50.0	22 45 46	Sd	103	9.47±0.04[g]	0.12	B
I1-2	15 40 06.8	28 16 26	Sd[b]	147[i]	9.73±0.05[i]	0.11	C
F583-1	15 57 27.6	20 40 07	Sm/Irr	41	9.45±0.11[g]	0.20	B
ESO-LV 1040220	18 55 41.3	-64 48 39	IB(s)m	23	9.54±0.21[e]	0.36	F
ESO-LV 1040440	19 11 23.6	-64 13 21	SABm	23	9.56±0.22[e]	0.16	F
ESO-LV 1870510	21 07 32.7	-54 57 12	SB(s)m	29	—	0.15	F
ESO-LV 1450250	21 54 05.7	-57 36 49	SAB(s)dm	34	10.08±0.16[e]	0.13	F
P1-7	23 20 16.2	08 00 20	Sm:	43	9.32±0.11[i]	0.45	C
2327-0244[c]	23 30 32.3	-2 27 45	SB(r)b pec	157	10.18±0.07[j]	0.22	D

We use $H_0 = 65$ km s^{-1} Mpc^{-1} to compute the distances and HI mass: distance uncertainties are ~ 7 Mpc.
List of source papers: A — de Blok et al. (1995); B — de Blok et al. (1996);
C — O'Neil et al. (1997); D — Sprayberry et al. (1995); E — dJI; F — ESO-LV
[a] Has a confirmed companion at a similar redshift [b] Our own classification
[c] Has been detected at 60 and 100 microns using IRAS [d] HI Flux from Wegner, Haynes & Giovanelli (1993)
[e] HI Flux from Huchtmeier & Richter (1989) [f] HI Flux from Schneider et al. (1992)
[g] HI Flux from de Blok et al. (1996) [h] HI Flux from Sprayberry et al. (1995)
[i] HI Flux from O'Neil, Bothun & Schombert (1999) [j] HI Flux from Theureau et al. (1998)

for these observations. Due to the widely different characteristics of these two telescopes, the observation strategy and data reduction differed considerably between these two sets of data.

Before we discuss the observations and reduction of each data set separately, it is useful to provide an overview of the observation techniques and reduction steps common to our two sets of near-IR imaging data. The near-IR sky background is much higher than the optical sky background. Therefore, in order to be able to accurately compensate for temporal and positional variation in the high sky background, offset sky frames were taken in addition to the target frames.

Our data were dark subtracted and were then flat fielded using a clipped median combination of all of a given night's offset sky frames. After this dark subtraction and flat fielding, large-scale structure in the images (on scales of $\gtrsim$ 1/8 of the chip size) was readily visible at levels comparable to the galaxy emission. This structure was minimised by subtracting an edited, averaged combination of nearby offset sky frames from each target frame. This step is the most involved one, and is the greatest difference between the reduction of the two datasets: detailed discussion of our editing of the sky frames is presented in sections 2.2.2.1 and 2.2.2.2. The data were then aligned by centroiding bright stars in the individual frames, or if there are no bright stars to align on, using the telescope offsets. These aligned images were then median combined together (with suitable scalings applied for non-photometric data). Finally, the data were photometrically calibrated using standard stars. Readers not interested in the details of the near-IR data reduction can skip to section 2.2.3.

2.2.2.1 Apache Point Observatory data

Observations and preliminary reductions: Our northern sample of 20 galaxies was imaged in the near-IR K' passband (1.94–2.29 μm) using the GRIM II instrument (with a 256 $\times$ 256 NICMOS 3 detector and 0.473 arcsec pixel^{-1}) on the Apache Point Observatory (APO) 3.5-m telescope. K' band was used in preference to the more commonly used K band to cut down the contribution to the sky background from thermal emission. The near-IR observing log is presented in Table 2.2.

The data were taken in blocks of six 9.8 second exposures (or if the sky brightness was high, twelve 4.8 second exposures), yielding $\sim$ 1 minute of exposure time per pointing. For these observations, we took two pointings on the object (offset from each other by $\gtrsim$ 20 arcsec, to allow better flat fielding accuracy and to facilitate cosmic ray and bad pixel removal), bracketed on either side by pointings on offset sky fields (offset by $\gtrsim$ 2 arcmin).

Table 2.2. Near-infrared observing log

Galaxy	Date	Telescope[a]	Exposure
UGC 128	05/09/98	APO 3.5-m	360×4.8s
ESO-LV 280140	25/08/97	SP 0.6-m	11×600s
	27/08/97	SP 0.6-m	12×600s
UGC 334	06/09/98	APO 3.5-m	288×4.8s
0052-0119	05/09/98	APO 3.5-m	312×4.8s
UGC 628	09/11/98	APO 3.5-m	138×9.8s
0221+0001	09/11/98	APO 3.5-m	144×9.8s
0237-0159	05/09/98	APO 3.5-m	264×4.8s
ESO-LV 2490360	28/08/97	SP 0.6-m	11×600s
	29/08/97	SP 0.6-m	10×600s
F561-1	21/03/97	APO 3.5-m	66×9.8s
	08/03/98	APO 3.5-m	60×9.8s
C1-4	21/03/97	APO 3.5-m	96×9.8s
C3-2	22/03/97	APO 3.5-m	143×9.8s
F563-V2	21/03/97	APO 3.5-m	96×9.8s
F568-3	21/03/97	APO 3.5-m	96×9.8s
1034+0220	08/03/98	APO 3.5-m	110×9.8s
N10-2	21/03/97	APO 3.5-m	88×9.8s
1226+0105	08/03/98	APO 3.5-m	114×9.8s
F574-1	22/03/97	APO 3.5-m	130×9.8s
	08/03/98	APO 3.5-m	84×9.8s
F579-V1	22/03/97	APO 3.5-m	126×9.8s
	05/05/98	APO 3.5-m	90×9.8s
I1-2	06/09/98	APO 3.5-m	240×4.8s
F583-1	22/03/97	APO 3.5-m	204×9.8s
ESO-LV 1040220	12/08/97	SP 0.6-m	18×600s
	13/08/97	SP 0.6-m	6×600s
	14/08/97	SP 0.6-m	18×600s
ESO-LV 1040440	28/08/97	SP 0.6-m	600s
	29/08/97	SP 0.6-m	2×600s
	30/08/97	SP 0.6-m	14×600s
ESO-LV 1870510	23/08/97	SP 0.6-m	17×600s
	24/08/97	SP 0.6-m	6×600s
ESO-LV 1450250	17/08/97	SP 0.6-m	6×600s
	19/08/97	SP 0.6-m	8×600s
	20/08/97	SP 0.6-m	14×600s
	24/08/97	SP 0.6-m	9×600s
P1-7	05/09/98	APO 3.5-m	252×4.8s
2327-0244	09/11/98	APO 3.5-m	168×9.8s

[a] A K' filter was used at the APO 3.5-m telescope, and a K_{dark} filter was used with the South Pole 0.6-m telescope.

The six or twelve separate exposures at each pointing were co-added to give reasonable signal in each image. A 3σ clipped average dark frame (formed from at least 20 dark frames taken before and after the data frames) was subtracted from these co-added images. The accuracy of this dark subtraction is ~ 0.01 per cent of the sky level. These dark subtracted data were then flat fielded with a scaled 2.5σ clipped median combination of the night's offset sky frames. We determined that the flat fielding is accurate to better than ~ 0.5 per cent.

Sky subtraction: Sky subtraction was then carried out on all of the target galaxy frames using an automatically edited weighted average of the two nearest offset sky frames. Stars were automatically edited out of this averaged sky frame by comparing each pixel in a single sky frame with the same pixel in a 10×10 median filtered version of that frame; pixels with ratios deviating by more than $+0.5$ per cent from unity were disregarded in formation of the weighted average.

After this sky subtraction large scale gradients in the sky level across the image, and on some occasions, residual large-scale variations in the dark frame, were visible in our sky subtracted images. In order to take off these structures we used a preliminary, mosaicked galaxy image to subtract off the galaxy emission in our sky subtracted frame, leaving only an image of the structure in the sky level. We then fit a gradient to this image using the IRAF package IMSURFIT. The residual variations in the dark frame took the form of coherent drifts in two well-defined strips and/or quadrants of the detector. For both types of variation in the dark frame, images were constructed to mimic these basic structures. These images were added or subtracted (with a number of different trial amplitudes) from each image of the sky structure, and the overall image variance was determined. The amplitude of the dark level pattern that minimised each image's variance was then chosen as best representation of the structure. The best-fit gradient and dark level structure was then subtracted from the object image, yielding a much improved galaxy image. The addition or subtraction of a gradient will not affect the photometry in a given individual object frame. The subtraction of the structure in the dark frame could, in principle, change the galaxy photometry in a given galaxy frame; however, it is justified, given the amplitude of the dark frame variation and the linear geometry of the structure in the image. It is impossible to introduce artifacts from either the gradient or dark subtraction that will mimic a centrally-concentrated galaxy light profile. This suggests, and tests carried out using corrected and uncorrected galaxy images show, that these corrections do not significantly affect the galaxy photometry, but reduce the size of the errors in the important outer regions of the galaxy profile.

Mosaicking and calibration: After sky subtraction, it is necessary to register and mosaic the individual dithered object exposures together. In most cases, the centroids of bright stars were used

Table 2.3. Photometric calibration for the Apache Point Observatory K' data

Date	$Z_{0,K'}$	RMS	Sky Level
21/03/97	22.53 ± 0.04	0.04	13.0±0.1
22/03/97[a]	—	—	~13.1
05/03/98[a]	—	—	~13.5
08/03/98	22.52 ± 0.05	0.05	13.6±0.2
05/05/98[a]	—	—	~12.8
05/09/98	22.39 ± 0.04	0.04	12.6±0.2
06/09/98	22.39 ± 0.04	0.05	12.51±0.08
08/11/98	22.39 ± 0.04	0.04	13.00±0.04

The K' magnitude of a source giving 1 count sec^{-1} is $m_{K'} = Z_{0,K'} - 0.09 \sec z$

Note that an airmass term of -0.09 mag airmass^{-1} was assumed for these fits.

[a] Calibrated using United Kingdom Infrared Telescope service observations on 6th Dec. 1997 and 19th Feb. 1998.

to align the images, which was typically accurate to $\sim$ 0.25 arcsec. In a few cases, there were no stars in the frame bright enough to centroid with: in these cases the telescope offsets were used to align the images. This procedure was typically accurate to $\sim$ 0.5 arcsec. These images were then median combined with a 2.5σ clipping algorithm applied.

Calibration was achieved using standard stars from Hunt et al. (1998). Their standard star list is an extension of the UKIRT faint standard list of Casali & Hawarden (1992), and consistent results were obtained using both sets of standard star magnitudes. An airmass term of -0.09 mag airmass^{-1} was assumed for the calibration (representing the typical airmass term for most sites in K band, and the average airmass term determined from our two full nights with a sufficient number of calibration stars); because our observing time was often in half nights, the small number of standard stars frequently did not allow accurate determination of both a zero point and airmass term. For those nights without photometric calibration, the data were calibrated using United Kingdom Infrared Telescope (UKIRT) data (reduced in a similar way to the galaxy data) in H and K to determine the K' magnitude of bright stars in the field of our targets. This calibration was typically accurate to $\sim$ 0.05 mag. This calibration was cross-checked with galaxies with known zero-points; the UKIRT and Apache Point Observatory calibration agree to within their combined photometric uncertainties. K' calibration for the Apache Point Observatory data is given in Table 2.3. Note that our K' magnitudes can readily be translated into the more standard K band using

Wainscoat & Cowie's (1992) relation $K' - K = (0.22 \pm 0.03)(H - K)$, assuming a typical $H - K$ colour of ~ 0.3 from dJIV.

2.2.2.2 South Pole data

Observations and preliminary reductions: The six galaxies in our southern sample were imaged in the K_{dark} passband (2.27–2.45 μm) using the GRIM I instrument on the South Pole 0.6-m telescope. GRIM I uses a NICMOS 1 128 $\times$ 128 array with a pixel scale of 4.2 arcsec pixel^{-1}. The K_{dark} filter was used in preference to the more common K filter to reduce the background: the K_{dark} filter selects a portion of K band that is relatively free from the intense and highly variable forest of OH lines that dominate the sky background between $\sim$ 1.9μm and 2.27μm. From 2.27–2.45μm, there are few OH lines, and the background is almost entirely due to thermal emission from the telescope and atmosphere. By observing at the South Pole, where mean winter temperatures are ~ -65°C, this thermal emission is greatly reduced, yielding a net background nearly 3 mag lower than at a mid-latitude site, and over 1 mag lower than those achievable at the South Pole using a standard K filter (Nguyen et al. 1996). The observation dates and on-source exposure times are presented in Table 2.2.

The data were taken using a 10 minute exposure time, with every object frame bracketed by two offset sky frames (with offsets $\sim$ 10 arcmin). Each object and sky pointing was offset by $\sim$ 1 arcmin to ensure accurate cosmic ray, bad pixel and flat fielding artifact removal. Dark subtraction was performed each night using 3σ clip average dark frames. Due to the long exposure times (10 minutes), the bias level varied significantly during the exposure, leading to dark frame variations with amplitudes $\lesssim$ 5 per cent. The data were flat fielded using a 2.5σ clipped median combination of a given night's offset sky frames. The uncertainty in the flat field was determined from the night-to-night variation in the flat field: over the central region of the chip used for galaxy photometry, the night-to-night RMS variations in the flat frame are $\sim$ 3 per cent. Both the dark and flat field variations are much larger than those typical of more modern near-IR chips at temperate sites (where the exposure time is much shorter). However, these variations in the dark frame and in the flat field are largely compensated for during the sky subtraction step and so will not greatly affect the final accuracy of our galaxy photometry and sky level determination. The flat field uncertainty will, however, affect the galaxy photometry slightly, potentially introducing spurious structure over reasonably large spatial scales at the $\sim$ 0.03 mag level.

Sky subtraction: Because of the large field of view of the device, and the large pixel scale (4.2 arcsec pixel^{-1}), the offset sky frames were heavily contaminated with stars. For this reason, the

techniques used for sky subtraction for the APO data are not suitable, as weighted averaging of the nearest two star-subtracted sky frames gives a poor result, with many stellar artifacts visible across the frame. We have used a modified version of the sky subtraction method of Rauscher et al. (1998) as follows.

1. Stars were automatically edited out from each sky frame. For each sky frame, we fit a 5th order polynomial in x and y (with cross terms enabled) to the sky frame, rejecting pixels (and their neighbours within a 2 pixel radius) with larger than 2.5σ deviations from the local (5×5 pixel) median. These surface fits to the frame were used to replace the above rejected pixel regions. These edited frames were then median filtered using a 8×8 box, to further reject any residual structure in the wings of any bright star. This process was carried out for each sky frame in turn.

2. For each pixel, its value in each of these edited frames is determined, and a cubic spline is fit to the variation of this pixel value as a function of time (note that cubic spline fits are simply an alternative way of interpolating between two data points that also takes into account longer scale trends in the values).

3. The time of each object frame is then used to 'read off' the pixel values given by the 128^2 cubic spline fits. This manufactured cubic spline fit image is used as the sky image.

By using this method for background estimation, it is possible to use long timescale trends in the data to better estimate the sky structure at the time that the object frame was observed. In this way, it is possible to reduce the limiting 1σ noise over large scales in the final mosaic by $\sim$ 0.3 mag (to between 23.4 and 24.1 mag arcsec^{-1}, depending on exposure time), compared to simple linear interpolation of the sky frames. Further description of the background subtraction method can be found in Rauscher et al. (1998, 1999).

Mosaicking and calibration: These dark subtracted, flat fielded and sky subtracted images are then mapped onto a more finely-sampled grid, with 16 pixels mapping onto every input pixel. Object image alignment is performed using centroiding on several bright stars in the field near the galaxy; typical uncertainties in alignment are $\lesssim$ 0.5 arcsec. Conditions during August 1997 were only rarely photometric at the South Pole, thus images were scaled to have common intensities before combination. This was achieved using the IRAF task *linmatch*, using several high contrast areas of the image to define the scaling of the images. In this way, images were scaled to an accuracy of $\sim$ 2 per cent before combination into a final mosaic. These images are then median-combined with a 2.5σ clip applied to form the final object image.

Table 2.4. Photometric calibration for the South Pole K_{dark} data

Date	Z_0	A	$Z_0(\sec z = 1.2)$	RMS
12/08/97	15.60	0.07	15.52	0.08
13/08/97	15.56	0.07	15.48	0.10
14/08/97	15.80	0.18	15.58	0.06
17/08/97[a]	16.10	0.32	15.72	0.07
19/08/97[b]	16.26	0.86	15.23	0.07
20/08/97	16.29	0.68	15.47	0.10
23/08/97	16.67	0.69	15.84	0.07
24/08/97	16.23	0.35	15.81	0.06
25/08/97	15.88	0.15	15.70	0.08
27/08/97	15.97	0.26	15.65	0.17
28/08/97	—	—	—	—
29/08/97	15.77	0.04	15.72	0.12
30/08/97	16.25	0.32	15.87	0.10

The K magnitude for an object giving 1 count $\sec^{-1}$ is $m_K = Z_0 - A \sec z$

Most nights were non-photometric. Despite the large variations seen in zero point calibration, repetition of objects on different nights indicated that the calibrations are repeatable to better than 0.1 mag.

[a] First part only

[b] Thick ice fog

Photometric calibration was achieved using stars taken from the NICMOS standard star list of Persson et al. (1998) and Elias et al. (1982). and is presented in Table 2.4. Due to the frequently non-photometric conditions during our run at the South Pole and the the $\sim$ 3 per cent flat fielding uncertainty, the photometry is expected to be relatively inaccurate. However, each galaxy was observed on multiple nights, yielding different estimates of the zero point, allowing us to estimate the accuracy of the calibration of the final galaxy image. Calibration typically repeated to better then 0.1 mag in absolute terms (see the zero point at $\sec z = 1.2$ in Table 2.4): the variations in the zero point calibration are quite small when considered over the range of airmasses of these observations ($1.1 \lesssim \sec z \lesssim 1.5$). The final zero points are accurate to better than 0.1 mag, except for the zero point for ESO-LV 2490360, which is uncertain to $\sim$ 0.2 mag, as it was observed on

only one relatively clear night. For further details of the calibration of 1997 observing season South Pole data, see Barnaby et al. (in preparation).

2.2.3 Optical data

Around 70 per cent of the optical photometry presented in this Chapter is derived from optical images kindly provided by Erwin de Blok, Stacy McGaugh, Karen O'Neil and David Sprayberry. The remainder of the optical data were obtained with the Cerro Tololo Interamerican Observatory (CTIO) 0.9-m (with a 2048×2048 Tectronix CCD and pixel scale of 0.40 arcsec pixel^{-1}), the Jacobus Kapteyn 1.0-m (JKT; with a 1024×1024 Tektronix CCD and pixel scale of 0.33 arcsec pixel^{-1}), or the Issac Newton 2.5-m telescope (INT; as part of its service observing programme; with a 2048×2048 Loral CCD and pixel scale of 0.37 arcsec pixel^{-1}). A summary of the new optical data presented in this Chapter is given in Table 2.5.

The optical data were overscan corrected, trimmed, and corrected for any structure in the bias frame by subtracting a 2.5σ clipped combination of between 5 and 20 individual bias frames. This bias subtraction is typically accurate to $\lesssim$ 0.1 per cent of the sky level. The data were then flat fielded using 2.5σ clipped combinations of twilight flat frames. From comparison of twilight flats taken at different times, and from inspection of the sky level in our galaxy images, we find that the flat fielding is typically accurate to $\lesssim$ 0.4 per cent. In addition, the R band frames taken with the INT show low-level fringing; this fringing has been taken out using a scaled fringe frame constructed from all the affected science frames. The application of this fringe correction reduces the level of the fringing by a factor of around four, and allows better determination of the sky level in the outermost regions of the image. Because we average over large areas, the application of this fringing correction does not affect the surface brightness profile or integrated magnitude to within the uncertainty in the sky level.

If more than one image of the galaxy was taken, the images were aligned by shifting the images in x and y so that the centroids of bright stars on the image coincided. The accuracy of this procedure is typically $\sim$ 0.1 arcsec for all of our optical data. These aligned images were then averaged (for two or three frames) or median combined (for more than three frames) using a 2.5σ clipping algorithm.

The data were calibrated using at least ten standard star fields from Landolt (1992), with the exception of the INT service data, for which only one standard field was taken on 25 November 1997 and two standard fields were taken on 19 December 1997 at similar airmasses to the science data. Mean extinction coefficients for La Palma were used for those calibrations, and were checked

Table 2.5. Optical observing log

Galaxy	Date	Telescope/Filter	Expos.
ESO-LV 280140	4-5/10/97	CTIO 0.9-m / B	6×600s
	4-5/10/97	CTIO 0.9-m / R	6×300s
ESO-LV 2490360	4-5/10/97	CTIO 0.9-m / B	6×600s
	4-5/10/97	CTIO 0.9-m / R	6×300s
C1-4	25/11/97	INT 2.5-m / R	480s
C3-2	25/11/97	INT 2.5-m / R	480s
F563-V2	25/11/97	INT 2.5-m / V	480s
	25/11/97	INT 2.5-m / R	480s
N10-2	13/07/98	JKT 1.0-m / B	600s
	13/07/98	JKT 1.0-m / V	300s
	25/11/97	INT 2.5-m / R	2×480s
F574-1	19/12/97	INT 2.5-m / B	600s
	19/12/97	INT 2.5-m / V	480s
F579-V1	13/07/98	JKT 1.0-m / B	2×900s
	13/07/98	JKT 1.0-m / V	900s
I1-2	13/07/98	JKT 1.0-m / B	900s
	13/07/98	JKT 1.0-m / R	600s
F583-1	13/07/98	JKT 1.0-m / B	2×900s
	13/07/98	JKT 1.0-m / V	900s
ESO-LV 1040220	4-5/10/97	CTIO 0.9-m / B	6×600s
	4-5/10/97	CTIO 0.9-m / R	6×300s
ESO-LV 1040440	4-5/10/97	CTIO 0.9-m / B	6×600s
	4-5/10/97	CTIO 0.9-m / R	6×300s
ESO-LV 1870510	4-5/10/97	CTIO 0.9-m / B	6×600s
	4-5/10/97	CTIO 0.9-m / R	6×300s
ESO-LV 1450250	4-5/10/97	CTIO 0.9-m / B	6×600s
	4-5/10/97	CTIO 0.9-m / R	6×300s

Table 2.6. Photometric calibration for the optical data

Tel.	Date	Pass	Z_0	A	C	RMS
INT	25/11/97	V	25.54	0.12		0.05
		R	25.48	0.07		0.05
INT	19/12/97	B	25.47	0.24	+0.025$(B-V)$	0.02
		V	25.32	0.12		0.01
CTIO	04/10/97	B	22.72	0.29	-0.06$(B-R)$	0.03
		R	22.85	0.09		0.025
CTIO	05/10/97	B	22.68	0.21	-0.06$(B-R)$	0.015
		R	22.85	0.07		0.015
JKT	13/07/98	B	22.82	0.21	+0.048$(B-V)$	0.018
		V	22.80	0.12	+0.015$(B-V)$	0.015
		R	22.96	0.08		0.016

The magnitude of an object giving 1 count sec^{-1} is $m_{\rm Pass} = Z_0 - A \sec z + C$

in V band by comparison with the results from the Carlsberg Meridian Telescope for those nights, whose extinction coefficients were found to be identical to within 0.01 mag to La Palma's average values. The adopted calibrations, along with their RMS scatter, are presented in Table 2.6.

2.3 Photometry results

The calibrated images for a given galaxy were aligned using the IRAF tasks GEOMAP and GREGISTER. A minimum of five stars were used to transform all of the images of a given galaxy to match the R band image. The typical alignment accuracy was $\sim$ 0.2 arcsec. Foreground stars and background objects were interactively edited out using the IRAF task IMEDIT. For the aperture photometry, these undefined areas were smoothly interpolated over using a linear interpolation. For the surface photometry, these areas were defined as bad pixels, and disregarded during the fitting process.

2.3.1 Surface and aperture photometry

These edited, aligned images were analysed using the STSDAS task ELLIPSE and IRAF task PHOT. The central position and ellipse parameters used to fit the galaxy were defined in R band. R band was chosen as it was a good compromise between signal-to-noise (which is good for the optical V

Table 2.7. Estimated sample ellipticities, position angles and largest radius at which they can be measured

Galaxy	e	PA (deg)	r_{max} (arcsec)
UGC 128	0.43 ± 0.07	62 ± 5	54
ESO-LV 280140	0.28 ± 0.08	125 ± 10	160
UGC 334	0.4 ± 0.1	45 ± 10	—
0052-0119	0.25 ± 0.04	75 ± 5	60
UGC 628	0.45 ± 0.05	135 ± 5	66
0221+0001	0.18 ± 0.05	160^a	29
0237-0159	0.10 ± 0.05	115 ± 10	—
ESO-LV 2490360	0.31 ± 0.08	138 ± 7	90
F561-1	0.10 ± 0.05	60 ± 10	—
C1-4	0.55 ± 0.05	52 ± 2	41
C3-2	0.32 ± 0.03	29 ± 3	30
F563-V2	0.28 ± 0.08	150 ± 10	37
F568-3	0.22 ± 0.05	165 ± 5	32
1034+0220	0.25 ± 0.04	45 ± 5	23
N10-2	0.45 ± 0.05	2 ± 3	30
1226+0105	0.20 ± 0.05	75 ± 25	20
F574-1	0.58 ± 0.03	85 ± 4	46
F579-V1	0.11 ± 0.03	123 ± 9	33
I1-2	0.18 ± 0.08	70 ± 15	26
F583-1	0.55 ± 0.06	176 ± 4	49
ESO-LV 1040220	0.43 ± 0.06	99 ± 6	70
ESO-LV 1040440	0.14 ± 0.07	137 ± 12	160
ESO-LV 1870510	0.50 ± 0.08	12 ± 5	120
ESO-LV 1450250	0.4 ± 0.1	150 ± 8	120
P1-7	0.31 ± 0.07	8 ± 4	21
2327-0244[b]	0.5 ± 0.1	115 ± 3	66

[a] Relatively unconstrained

[b] These parameters may be affected by the strong bar

and R images) and the dust and star formation insensitivity of the redder (and especially near-IR) passbands. The centre of the galaxy was defined as the centroid of the brightest portion of the galaxy. The ellipse parameters were determined by fixing the central position of the galaxy, and letting the position angle and ellipticity vary with radius. Because of low signal-to-noise in the outer parts of the galaxy, the fitting of the ellipse parameters was disabled at a suitable radius, determined iteratively by visually examining the quality of the ellipse parameters as a function of radius. In exceptional cases (usually because the galaxy had a flocculent disc, with only a few overwhelmingly bright regions, or because the galaxy was very irregular and/or lopsided), the ellipse parameters were fixed at all radii as they were unstable over almost all of the galaxy disc. In these cases the galaxy ellipticity and position angle were determined visually. Galaxies for which the ellipticity and position angle were fixed are indicated in Table A.1 in Appendix A. We also present our 'best estimates' of ellipticity and position angle, and the radius at which the fitting of the ellipticity and position angle was disabled in Table 2.7.

The sky level (and its error estimate) was estimated using both the outermost regions of the surface brightness profiles and the mean sky level measured in small areas of the image which were free of galaxy emission or stray starlight. Owing to the low surface brightness of our sample in all passbands, the error in the sky level dominates the uncertainty in the photometry. This was also demonstrated using Monte Carlo simulations, which included the effects of seeing uncertainty, sky level errors and shot noise. This sky level, averaged over large areas, is typically accurate to a few parts in 10^5 of the sky level for the K' images, and better than ~ 0.5 per cent of the sky level for the optical and K_{dark} images.

The raw surface photometry profiles in all passbands are presented in Fig. A.1 in Appendix A. The lower two panels show the ellipticity and position angle of the galaxies as a function of radius as determined from the R band images. Also shown are the adopted ellipticities and position angles (dashed lines) and the largest radius at which they can be measured (arrow). The upper panel shows the raw surface brightness profiles in these ellipses in all the available passbands for the sample galaxies. These curves have not been corrected for the effects of seeing, galaxy inclination, K-corrections, $(1+z)^4$ surface brightness dimming or for the effects of foreground galactic extinction. The symbols illustrate the run of surface brightness with radius in different passbands, and the dotted lines indicate the effects of adding or subtracting the estimated sky error from the surface brightness profile. The surface brightness profile is plotted out to the radius where the sky subtraction error amounts to ± 0.2 mag or more in that passband. The solid line is the best fit bulge/disc profile fit to the surface photometry, as described in the next section.

'Total' aperture magnitudes are derived for the galaxies by extrapolating the high signal-to-noise regions of the aperture photometry to large radii using the bulge/disc decompositions described in the next section. The aperture magnitude is determined using the IRAF task PHOT in an annulus large enough to include as much light as possible, while being small enough to have errors due to sky level uncertainties smaller than 0.1 mag. This aperture magnitude was then extrapolated to infinity using the best fit bulge/disc fit to the surface brightness profile. The quoted uncertainty in the Table A.1 in Appendix A primarily reflects the uncertainty in the adopted aperture magnitude: extrapolation errors are difficult to accurately define. The median extrapolation is ~0.02 mag, and 90 per cent of the extrapolations are smaller than ~0.5 mag. Cases where the extrapolation has exceeded 0.15 mag have been flagged in Table A.1 in Appendix A.

2.3.2 Bulge/disc decompositions

The surface brightness profile $\Sigma(r)$ (in linear flux units) was fitted using one of four possible profiles: an exponential disc profile only, an exponential bulge plus disc profile, a de Vaucouleurs $r^{1/4}$ law bulge plus exponential disc profile, and a de Vaucouleurs $r^{1/4}$ law bulge only. The exponential profile is given by:

$$\Sigma(r) = \Sigma_0 e^{-r/h}, \tag{2.1}$$

where r is the semi-major axis radius of the ellipse, Σ_0 is the central surface brightness of the disc in linear units, and h is the major axis exponential disc scale length. The de Vaucouleurs profile is given by:

$$\Sigma(r) = \Sigma_e e^{-7.67[(r/r_e)^{1/4}-1]}, \tag{2.2}$$

where Σ_e is the surface brightness in linear units at the half light major axis radius r_e. These exponential or $r^{1/4}$ law model profiles were convolved with a Gaussian with a full width half-maximum equal to the seeing quality before fitting. The sky level was not permitted to vary when performing these fits.

Independent fitting for each passband was carried out using the method of Levenberg and Marquardt (Press et al. 1986). The reduced χ^2 statistic was used to determine the quality of the fit (using the measured RMS in each ellipse as the error in the flux in that ellipse); χ^2 was minimised for each of the four types of fit, and the best values of χ^2 for each fitting function compared. One fitting function was chosen in preference to another if its χ^2 was on average better, over most of the passbands. Most cases were clear cut, with reductions in χ^2 by a factor of two or more compared

to the other three fitting functions. However, there were two main types of marginal case where the difference between minimum χ^2 for two models was small (i.e. less than $\sim$ 10 per cent), and the best model varied between passbands. One case is where there is no evidence for a bulge component in the bluer passbands, but tentative evidence for an exponential bulge component in the red passbands. In this case, a disc only fit is chosen for simplicity. The other marginal case arises when a galaxy with a strong bulge is fit by an exponential or de Vaucouleurs bulge equally well: in this case, the choice of bulge profile is fairly arbitrary, and the choice is made to minimise systematic deviations of the fit from the data. These two types of case are both flagged in Table A.1 in Appendix A.

In a number of cases, the disc parameters are relatively ill-constrained, as there is significant structure in the surface brightness profile in some of the bluer passbands, or in the K' profile. This structure is typically due to the low signal-to-noise of the data (especially in U or K' bands), by real structure in the surface brightness profile caused by e.g. recent star formation (affecting the U and B band profiles particularly) or by asymmetries in the most irregular LSBGs in our sample. In these cases, we have chosen to fix some of the fit parameters to achieve a better convergence. We usually choose to fix the disc scale length, as it is possible to use the disc scale lengths in other passbands, along with the mean variation in scale length with passband (dJIV), to estimate the scale length in this colour. While clearly not optimal, this method allows us to use the same functional form for fitting the surface brightness profile for all the different passbands. Cases where the fit has been constrained have been flagged in Table A.1 in Appendix A.

2.3.3 Comparison with existing data

We show a comparison between our measurements of total galaxy magnitude, disc central surface brightness and disc scale length and the corresponding literature measurements in all available passbands in Fig. 2.1. Note that there is a mean offset in magnitude of -0.28 mag between our magnitudes and those of Sprayberry et al. (1995) (stars in Fig. 2.1). This offset does not significantly affect the colours of the galaxies as it is constant over all passbands. The source of this offset is unknown; however, if it is corrected for their magnitudes agree with ours with a RMS of $\sim$ 0.1 mag. Therefore, in Fig. 2.1 and the subsequent comparison, we correct Sprayberry et al.'s magnitudes for this offset. For the complete sample, 68 per cent of the magnitude differences are smaller than 0.17 mag (68 per cent interval), and 50 per cent of the magnitude differences are smaller than 0.09 mag. For the central surface brightnesses and scale lengths, the 68 per cent intervals are 0.33 mag arcsec^{-2} and 18 per cent, respectively. The distributions of all of these

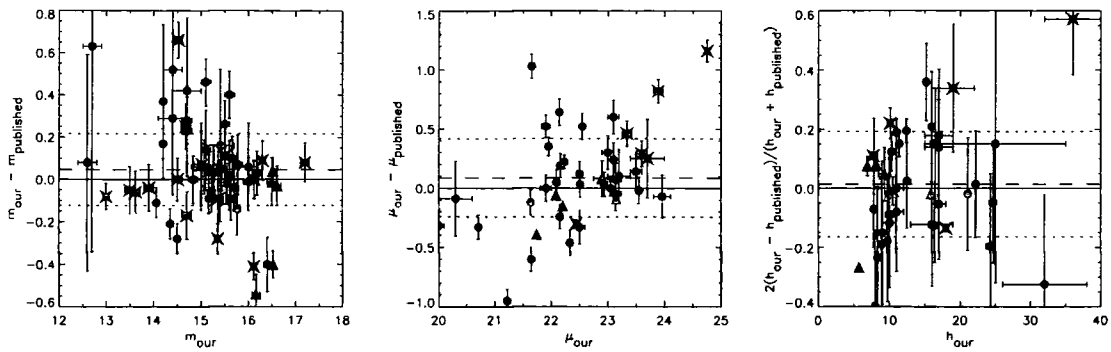

Figure 2.1: Comparison between our measurements of magnitude, central surface brightness and scale length and those in the literature. Solid lines denote the line of equality, dashed lines denote the mean residual, and dotted lines the 68 per cent interval. Circles denote the blue selected subsample of LSBGs, triangles the red selected subsample, and stars the giant LSBGs from Sprayberry et al. (1995).

residuals are strongly non-Gaussian, with a relatively narrow 'core' of accurate comparisons with a more extended envelope of less accurate comparisons, with a few pathological cases.

It is important to understand the origin of the larger magnitude errors. Many of the less accurate magnitude comparisons are from very extended galaxies, which have a large portion of their flux outside the boundaries of the detector. Hence their magnitudes are less accurate due to the more uncertain sky levels and larger total magnitude extrapolations. These less accurate comparisons may be a concern however: do our quoted uncertainties reflect the true uncertainties? To check this, we compared the ratio of the magnitude difference and the combined measurement errors: the median value of this ratio is ~ 0.8. Therefore, we feel that our formal magnitude error bars are likely to represent the true uncertainties.

The central surface brightnesses and scale lengths compare less favourably, with many of the central surface brightnesses in particular disagreeing by more than their combined formal error bars. However, the formal error bars only give the estimated errors for a given fitting method. In this case, we have compared our measurements derived using an automated bulge/disc decomposition with measurements derived using a variety of fitting methods, including 'marking the disc' fits (Sprayberry et al. 1995; de Blok et al. 1995, 1996), disc only fits to the whole surface brightness profile (O'Neil et al. 1997a), bulge/disc decompositions similar to those presented here (McGaugh & Bothun 1994), and sophisticated two-dimensional modelling of the luminosity distribution (de Jong 1996a; dJII hereafter). Therefore, the formal errors derived using each method are unlikely to reflect the true uncertainties introduced by the use of different fitting methods (see e.g. dJII for a more detailed discussion of the differences between fitting techniques). An additional source of

scatter is the presence of a bulge component: when included, a bulge component can take some of the light from the disc component, and increase the uncertainty in the disc parameters accordingly. We conclude that the formal errors for the central surface brightness and scale length are unlikely to represent the true range of uncertainties introduced by using different fitting methods: more representative uncertainties are given by the 68 per cent intervals of the differences between our measurements and those in the literature and are $\sim$ 0.3 mag and $\sim$ 20 per cent respectively: these uncertainties are comparable to those found by e.g. dJII, de Blok et al. (1995) and Chapter 5.

We have also compared our adopted ellipticities and position angles with those in our sample's source papers. Our ellipticities compare well with those in the literature: most galaxies have ellipticity differences of $\sim$ 0.05 or smaller. A few galaxies have ellipticity differences greater than 0.1; these differences are typically due to the influence of bars, or due to low signal-to-noise in both sets of images. Comparison of our adopted position angles with those in the literature shows agreement to $\sim 7°$.

2.3.4 LSBG morphology

It is interesting to compare and comment on the morphologies and surface brightness profiles of LSBGs in the optical and the near-IR. Bergvall et al. (1999) found a tendency towards similar morphologies in the optical and near-IR for their sample of LSBGs. We confirm this trend (despite our typically poorer signal-to-noise in the near-IR): this suggests that LSBGs lack the dust content and significant amounts of recent star formation that make morphological classification so passband-dependent for galaxies with higher surface brightness (Block et al. 1994; Block & Ivânio 1999).

Our sample, because of its explicit selection to cover as wide a range of LSBG parameters as possible, has a wide range of morphologies, and as is discussed in the next section, SFHs. The red selected LSBG subsample contains a lenticular galaxy (C1-4), two early type spirals, and two later type spirals. O'Neil et al. (1997a), because of their typically lower spatial resolution, did not find strong evidence for bulges in most of the red LSBGs. However, with our higher resolution data (usually the INT 2.5-m R band images), we find that four out of the five red selected LSBGs show evidence for an exponential bulge component. The LSBG giants all have very strong bulges, with bulge to disc ratios of the order of unity in most passbands. Two LSBG giants are better fit with an exponential bulge component, and the rest are better fit (in the χ^2 sense) by a $r^{1/4}$ law bulge profile. The discs of LSBG giants usually have pronounced spiral structure (see, e.g. Sprayberry et al. 1995 for images).

The blue selected LSBGs come with a variety of morphologies, from relatively well-defined spiral morphologies with weak bulges, to galaxies with nearly exponential disc profiles, to galaxies with central 'troughs' in their luminosity profiles, compared with expectations from an exponential disc fit. Two examples of these 'trough' galaxies are ESO-LV 1040220 and 1040440. These galaxies have galactic extinction and inclination corrected central surface brightnesses in B of 24.1 and 23.4 mag arcsec^{-2} respectively. Thus, in many respects, they are similar to the blue LSBGs studied by Bergvall et al. (1999). They found that at surface brightnesses lower than $\sim$ 23 B mag arcsec^{-2}, centrally-depressed surface brightness profiles are quite common. On the basis of this limited and incomplete sample, it is difficult to properly confirm their finding, but our analysis of the surface brightness profiles certainly tentatively supports their observation.

In Table A.1 in Appendix A, and to a certain extent Fig. A.1 in Appendix A, it is apparent that the disc scale lengths typically decrease and the bulge to disc ratios increase with increasing wavelength. These are clear signatures of colour gradients in our sample of LSBGs. In the next section, we investigate these colour gradients: we will argue that these are primarily due to stellar population gradients.

2.4 Star formation histories

The main motivation for this programme of optical and near-IR imaging was to study the stellar populations of a diverse sample of LSBGs. In this section, we construct accurate colours as a function of radius for our sample and compare these colours with model stellar populations.

We first degrade all of the edited images of a given galaxy to the same angular resolution, and carry out surface photometry in three radial bins: $0 < r/h_K < 0.5$, $0.5 < r/h_K < 1.5$ and $1.5 < r/h_K < 2.5$, where h_K is the K band disc scale length. Galactic extinction corrections were taken from Schlegel et al. (1998; see Table 2.1). K-corrections for the LSBG giants (as they are at non-negligible redshifts) were computed using non-evolving Sbc spectra from King & Ellis (1985), and are typically 0.2 mag in B, negligible in R and -0.2 mag in K. If required, K' magnitudes were converted to K magnitudes using the relation in Wainscoat & Cowie (1992), assuming a typical $H - K$ colour of $\sim$ 0.3 mag (dJIV). The error in this correction is unlikely to exceed 0.05 mag.

We show Galactic extinction and K-corrected $B - R$ and $R - K$ colours for our sample of LSBGs in Fig. 2.2. Measurements in the three radial bins per galaxy are connected by solid lines, measurements of the central bin are denoted by solid symbols and measurements of the colours at two K band disc scale lengths are denoted by open symbols. Note that we only show colours

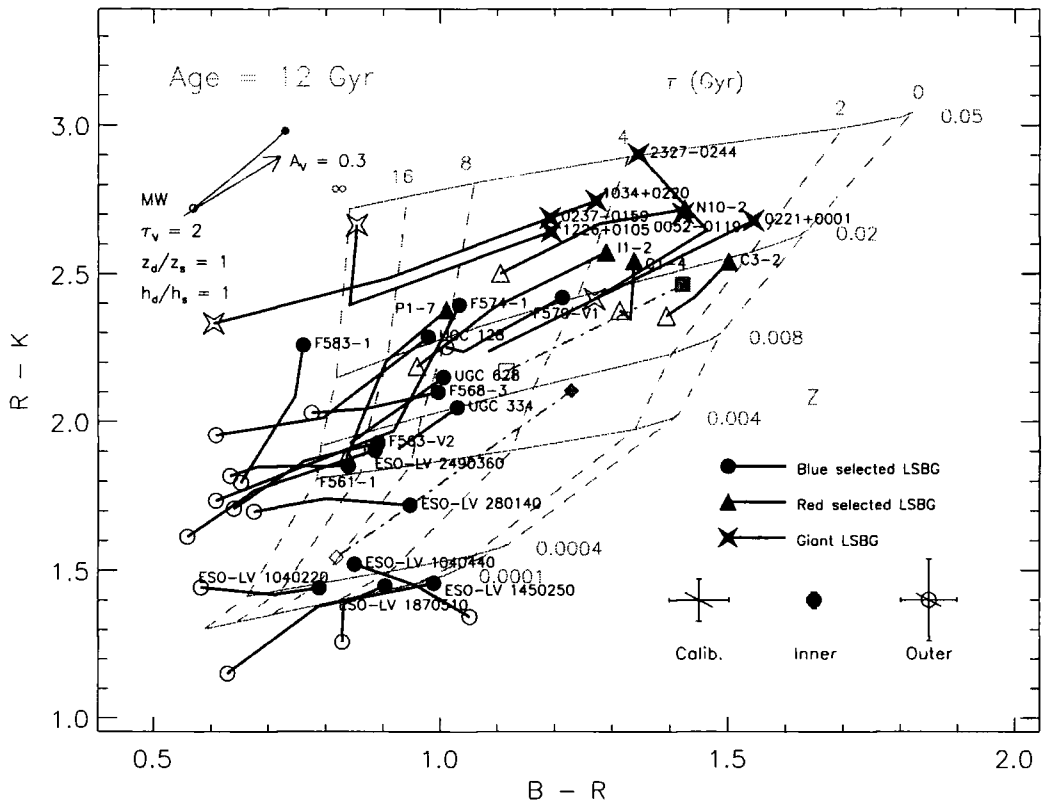

Figure 2.2: Galactic extinction and K-corrected $B-R$ and $R-K$ colours for our LSBG sample in three radial bins per galaxy: $0 < r/h_K < 0.5$ (solid symbols), $0.5 < r/h_K < 1.5$ and $1.5 < r/h_K < 2.5$ (open symbols). Circles denote the blue selected subsample of LSBGs, triangles the red selected subsample, and stars the giant LSBGs. Typical colour uncertainties in the inner and outer bins of the sample due to sky level errors are shown in the lower right hand corner. Calibration uncertainties are also shown. As R band is used to form both colours, the effects of a typical 1σ error in R is also shown (diagonal line). Over-plotted are Bruzual & Charlot's (in preparation) GISSEL98 stellar population models, and a foreground screen and Triplex model (Disney, Davies & Phillipps 1989; Evans 1994) dust reddening vector. Average Sa–Sc (grey squares) and Sd–Sm (grey diamonds) colours from dJIV at the centre (solid symbols) and at 2 disc scale lengths (open symbols) are also shown.

with sky subtraction uncertainties smaller than 0.3 mag. Average zero point uncertainties and uncertainties in the inner and outer points due to sky level errors are also shown. Because R band is used in both colour combinations, errors in R band affect both colours. Accordingly, the average 1σ R band error is also shown (the short diagonal line). A $B-R$ against $R-K$ colour-colour plot was chosen to maximise the number of galaxies on the diagram. Other colour combinations (e.g. $B-V$ against $R-K$, etc.) limit the number of galaxies that can be plotted, but yield consistent positions on the stellar population grids. Note that P1-7 is placed on the plot assuming a $V-R$

colour of 0.40 ± 0.03 (derived from the degenerate $B - V$ against $V - R$ colour-colour diagram using a typical galactic extinction corrected colour for P1-7 of $B - V \sim 0.57$).

Overplotted on the same diagram are stellar population models and model dust reddening vectors. We use the GISSEL98 implementation of the stellar population models of Bruzual & Charlot (in preparation). For Fig. 2.2 we adopt a Salpeter (1955) initial mass fuction (IMF) and an exponentially decreasing star formation rate characterised by an e-folding timescale τ and a single, fixed stellar metallicity Z (where $Z = 0.02$ is the adopted solar metallicity). For these models, the galaxy age (i.e. the time since star formation first started in the galaxy) is fixed at 12 Gyr. Note that the shape of the model grid is almost independent of galaxy age $\gtrsim 5$ Gyr. The solid grey lines represent the colours of stellar populations with a fixed metallicity and a variety of star formation timescales. The dashed grey lines represent the colours of stellar populations with different, fixed stellar metallicities and a given star formation timescale. There is some uncertainty in the shape and placement of the model grid: Charlot, Worthey and Bressan (1996) discussed the sources of error in stellar population synthesis models, and concluded that the uncertainty in model calibration for older stellar populations is ~ 0.1 mag in $B - R$ and ~ 0.2 mag in $R - K$, which is roughly comparable to the calibration error bars in Fig. 2.2. The colour uncertainties are larger for some stellar populations than for others: e.g. the optical–near-IR colours for older, near-solar metallicity stellar populations are relatively secure, whilst the colours for younger, extreme metallicity stellar populations are much more uncertain. Other sources of systematic error include dust reddening and SFH uncertainties (as our assumption of a smoothly varying SFR is almost certainly unrealistic; see also section 1.3 in Chapter 1). For these reasons the positions of galaxies and colour trends between galaxies should be viewed relatively, e.g. that one class of galaxies is more metal-rich than another class of galaxies.

We also include vectors describing the effect of dust reddening using either a screen model (arrow) or the more realistic geometry of a Triplex dust model (Disney, Davies & Phillipps 1989; Evans 1994; curved line). For the Triplex model a closed circle denotes the central reddening, and an open circle the reddening at 2.5 disc scale lengths. For both reddening vectors we use the Milky Way extinction law (and for the Triplex model, the albedo) from Gordon, Calzetti & Witt (1997). Our Triplex model assumes equal scale length vertically and radially exponential dust and stellar distributions, and a central optical depth (for viewing a background object) in V band of 2. These parameters are designed to be a reasonable upper limit to the effects of reddening in most reasonably bright spiral galaxies: Kuchinski et al. (1998) find from their study of 15 highly-inclined spiral galaxies that they are well-described by the above type of model, with central V

band optical depths of between 0.5 and 2. For the purposes of calculating the Triplex reddening vector, we use the optical depth due to absorption only for two reasons. Firstly, one might naïvely expect that for face-on galaxies at least as many photons will scatter into the line of sight as out of it. Secondly, dJIV finds that an absorption-only Triplex model is a reasonably accurate description of the results of his realistic Monte-Carlo simulation (including the effects of both scattering and absorption) of a face-on Triplex geometry spiral galaxy.

2.4.1 Results

In the following interpretation of Fig. 2.2, for the most part, we *explicitly neglect the possible effects of dust reddening*. There are a number of arguments that suggest that the effects of dust reddening, while present, are less important than stellar population differences both within and between galaxies. We consider these effects more carefully in section 2.4.2.2.

2.4.1.1 Colour gradients

The majority of the LSBGs in our sample with colours in at least two radial bins have significant optical–near-IR colour gradients. For the most part , *these colour gradients are consistent with the presence of a mean stellar age gradient*, where the outer regions of galaxies are typically younger, on average, than the inner regions of galaxies. This is consistent with the findings of dJIV who concludes that age gradients are common in spiral galaxies of all types. Note that this is inconsistent with the conclusions of Bergvall et al. (1999), who find little evidence for optical–near-IR colour gradients in their sample of blue LSBGs. However, their sample was explicitly selected to lack significant $B - R$ colour gradients, so that we disagree with their conclusion is not surprising. The fact that Bergvall et al. managed to find galaxies without significant colour gradients is interesting in itself; while colour gradients are common amongst disc galaxies, *they are by no means universally present.* This is an important point, as, by studying the systematic differences in physical properties between galaxies with and without colour gradients, it may be possible to identify the physical mechanism by which an age gradient is generated in disc galaxies.

There are galaxies which have colour gradients which appear inconsistent with the presence of an age gradient alone. The two early-type LSBGs C1-4 and C3-2 have small colour gradients which are more consistent with small metallicity gradients than with age gradients. In addition, a few of the bluer late-type LSBGs have colour gradients that are rather steeper than expected on the basis of age gradients alone, most notably F583-1 and P1-7, both of which appear to have colour gradients more consistent with a metallicity gradient. There are also conspicuous 'kinks'

in the colour profiles of F574-1 and 2327-0244, and a possible kink in the colour profile of UGC 128. In the case of F574-1, it is likely that the central colours of the galaxy are heavily affected by dust reddening. F574-1 is quite highly inclined ($67° \pm 3°$, assuming an intrinsic disc axial ratio q_0 of 0.15; Holmberg 1958) and shows morphological indications of substantial amounts of dust extinction in the INT 2.5-m B and V band images. This may also be the case for UGC 128, although the inclination is smaller in this case and there are no clear-cut morphological indications of substantial dust reddening. The LSBG giant 2327-0244 has a red nucleus in the near-IR but a relatively blue nucleus in the optical. However, 2327-0244 is a Seyfert 1 and has a central starburst (Terlevich et al. 1991), making our interpretation of the central colours in terms of exponentially decreasing SFR models invalid.

2.4.1.2 Colour differences between galaxies

In considering colour trends between LSBGs, we will first consider the star formation histories of different classes of LSBG, and then look at the star formation histories in a more global context.

Blue Selected LSBGs: The majority of blue selected LSBGs, e.g. F561-1, UGC 334 and ESO-LV 2490360, are also blue in the near-IR. Their colours indicate that most blue selected LSBGs are younger than HSB late-types, with rather similar metallicities (compare the positions of the main body of blue selected LSBGs to the average Sd–Sm galaxy from de Jong's sample). This relative youth, compared to the typically higher surface brightness sample of dJIV suggests that the age of a galaxy may be more closely related to its surface brightness than the metallicity is. We will come back to this point later in section 2.5.2.

Four out of the fifteen blue selected LSBGs fail to fit this trend: ESO-LV 1040220, ESO-LV 1040440, ESO-LV 1450250 and ESO-LV 1870510 all fall substantially ($\sim$ 0.3 mag) bluewards of the main body of blue LSBGs in $R - K$ colour, indicating a lower average metallicity. While it should be noted that the South Pole subsample all have larger zero point uncertainties than the northern hemisphere sample, we feel that it is unlikely that the zero point could be underestimated so substantially in such a large number of cases. While the models are tremendously uncertain at such young ages and low metallicities, these optical–near-IR colours suggest metallicities $\lesssim 1/10$ solar. This raises an interesting point: most low metallicity galaxies in the literature are relatively high density blue compact dwarf galaxies (Thuan, Izotov & Foltz 1999; Izotov et al. 1997; Hunter & Thronson 1995). Thus, these galaxies and e.g. the blue LSBGs from Bergvall et al. (1999) offer a rare opportunity to study galaxy evolution at both low metallicities *and* densities, perhaps giving us quite a different view of how star formation and galaxy evolution work at low metallicity.

Red selected LSBGs: In Bell et al. (1999), we found that two red selected LSBGs (C1-4 and C3-2) were old and metal rich, indicating that they are more evolved than blue selected LSBGs. In this larger sample of five red selected LSBGs, we find that this is not always the case. The galaxies N10-2, C3-2, and C1-4 (with B band central surface brightnesses ~ 22.5 mag arcsec^{-2}) *are* comparitively old and metal rich, with central colours similar to old, near-solar metallicity stellar populations. However, I1-2 and P1-7 (with lower B band central surface brightnesses ~ 23.1 mag arcsec^{-2}) both have reasonably blue galactic extinction corrected optical–near-IR colours. I1-2 has a stellar population similar to de Blok et al.'s (1996) F579-V1, which is part of our blue selected subsample: these galaxies lie in the overlap between the two samples. P1-7 is relatively similar to other, brighter blue LSBGs such as UGC 128 and F574-1: it was included in the red selected subsample only by virtue of its relatively high foreground extinction $A_B = 0.45$ mag.

Gerritsen & de Blok (1999) predict that around 20 per cent of LSBGs should have $B - V \sim 1$ and relatively low surface brightnesses $\mu_{B,0} \gtrsim 24.0$ mag arcsec^{-2}. In this context it is interesting to note that our sample does not include any red, truly LSB galaxies (i.e. with $B - V > 0.8$ and $\mu_{B,0} \gtrsim 23.5$ mag arcsec^{-2}). While this is partially by design (we did not include very low surface brightness galaxies as detecting them in the near-IR would be difficult), it is intriguing to note that the red selected LSBGs with lower surface brightnesses all have bluer colours, possibly implying a defecit of red, very LSB galaxies. However, this type of galaxy is difficult to observe and catalogue: O'Neil et al.'s (1997a, 1997b) catalogue includes only a few reliable face-on candidate red, very LSB galaxies. Proper characterisation of these galaxies may prove quite crucial in testing LSBG formation and evolution models.

Giant LSBGs: LSBG giants have galactic extinction and K-corrected optical–near-IR colours which are similar to the redder LSBGs from O'Neil et al. (1997a, 1997b), indicating central stellar populations that are reasonably old with roughly solar metallicity. However these central colours are not consistent with an old, single burst stellar population, although this conclusion is somewhat dependent on the choice of K-correction and model uncertainties (K-correction uncertainties are typically $\lesssim 0.05$ mag in each axis at 20000 km s^{-1} for a change in galaxy type from Sbc to Sab, or Sbc to Scd). The outer regions of LSBG giants are much younger, on average, whilst still retaining near-solar metallicities. Comparing the $B - V$ and $R - K$ colours for the LSBG giants with some of the bluer HSB Sa–Sc galaxies from dJIV shows that both sets of galaxies have similar stellar populations. Thus, LSBG giants do not have unique SFHs (implying that there need be no difference in e.g. star formation mechanisms between the HSB Sa–Sc galaxies and the

LSBG giants); however, it is interesting that LSBG giants can have both a substantial young stellar population and a high metallicity, whilst possessing such low stellar surface densities (assuming reasonable stellar mass to light ratios).

Summary: Overall, there is a clear age and metallicity sequence, with red LSBGs and LSBG giants in the high stellar metallicity and older average age corner of the plot, progressing to the lower stellar metallicity and younger average age region of the plot for the blue LSBGs. *This suggests that LSBGs, just like HSBGs, come in a variety of morphological types and SFHs; moreover, their morphologies and SFHs are linked.*

2.4.2 Are the stellar population differences real?

2.4.2.1 Are IMF uncertainties important?

We have constructed Fig. 2.2 using a Salpeter (1955) IMF. However, the IMF is still reasonably uncertain, especially at the very low mass and high mass ends (see e.g. Elmegreen 1999, Scalo 1998). Variation of the low mass end of the IMF only significantly changes the (relatively ill-constrained) stellar mass to light ratio. Variation of the high mass end of the IMF, as illustrated by using e.g. the Scalo (1986) or Miller & Scalo (1979) IMF, only significantly changes the high metallicity, young stellar populations corner of the colour-colour plane: the colours in these regions are subject to considerable modelling uncertainties at any rate. We conclude that our results are robust to reasonable IMF uncertainties (see also section 3.5.3 in Chapter 3).

2.4.2.2 Dust reddening

We have interpreted Fig. 2.2 in terms of stellar population differences; however, we have so far neglected the effects of dust reddening on the colours of our stellar populations. In Fig. 2.2 we show both a screen $A_V = 0.3$ and absorption-only Triplex model $\tau_V = 2$ dust reddening vector, both assuming Milky Way extinction and albedo curves. SMC extinction and albedo curves make little difference to the direction of the reddening vectors, but increase the length of the Triplex model reddening vector slightly because of the lower albedo at all wavelengths, compared to the Milky Way dust properties. The screen model vector is shown for illustrative purposes only, as the dust will be distributed roughly similarly to the starlight in realistic spiral galaxies, as assumed in the Triplex model.

The colour gradients in our sample of LSBGs are unlikely to be due to the effects of dust reddening for four reasons.

1. The optical depth that we choose for the Triplex model is on the high end of the plausible dust optical depths derived by Kuchinski et al. (1998).

2. The Triplex model assumes that all of the dust is distributed smoothly throughout the galaxy. In real galaxies typically 1/3 of the dust is gathered into optically thick clumps, which, when viewed face-on, simply tend to 'drill holes' in the light distribution but not produce any significant colour changes (dJIV; Kuchinski et al. 1998). This dust would be more easily found in more edge-on galaxies, as in the edge-on orientation the probability of a clump along the line of sight is much larger than in a face-on disc. Therefore, Kuchinski et al.'s dust optical depths are likely to account for both the clumped and unclumped dust.

3. Most LSBGs have lower metallicity than their higher surface brightness counterparts. This implies that the dust to gas ratio should be lower in LSBGs than in HSBGs.

4. Only one galaxy in our sample, the starbursting Seyfert 1 2327-0244, has been detected by IRAS. This is in stark contrast to the diameter limited sample of dJI, for which 78 per cent of the sample was detected by IRAS. This suggests that dust is much less important in LSBGs than in their higher surface brightness counterparts: indeed, many of the non-detections in dJI's sample were LSBGs.

The above arguments suggest that the Triplex dust reddening vector in Fig. 2.2 is an upper limit to the real effects of dust reddening. Comparison of this upper limit on the dust reddening effects with the colour gradients in our sample suggests that most galaxies must have stellar population gradients to produce such pronounced colour gradients. This conclusion is supported by the direct modelling of Kuchinski et al. (1998), who use their own best-fit galaxy models to estimate the colour gradients in face-on spiral galaxies: they conclude that colour gradients as large as the ones we observe in LSBGs, or observed by dJIV, are too large to arise solely from reddening by realistic amounts of dust. The same argument applies to relating different populations of LSBG: the amount of reddening required to make an intrinsically blue LSBG appear red is too large to be compatible with the observational evidence cited above (see also section 3.5.4 in Chapter 3).

2.5 Discussion

2.5.1 Quantifying the colour-colour plane

In section 2.4.1, we saw a pronounced age/metallicity sequence. LSBGs can have a diverse range of stellar populations: red selected LSBGs can be quite old and metal rich, whilst most blue

selected LSBGs are much younger, and more metal poor. However, from Fig. 2.2 alone, it is difficult to see *why* the star formation histories of low surface brightness galaxies are as diverse as they are. For this reason, we have chosen to quantify the positions of galaxies on the colour-colour plane by assigning average ages and metallicities from the GISSEL98 stellar population models of Bruzual & Charlot (in preparation).

A finely interpolated grid of stellar population models was generated, covering a range of star formation timescales and metallicities. The metallicity ranges from $\langle Z \rangle = \log_{10}(Z/Z_{\odot}) = -2.0$ (1/100 solar) to $\langle Z \rangle = 0.4$ (2.5 times solar). In Fig. 2.2, we can see that some galaxies have optical–near-IR colours too blue to be described adequately by a constant star formation rate: for this reason, we must include exponentially *increasing* SFHs in our model grid. We include star formation timescales τ ranging from 0 (an average age of 12 Gyr) to ∞ (constant star formation with an average age of 6 Gyr) to -1 Gyr (an average age of 1 Gyr). We can see from the range of models included above that τ is an inappropriate parameter for describing the SFHs: we parameterise the SFH using the average age of the stellar population (see Eqn. 3.3 of Chapter 3)

For each galaxy, the galactic extinction and K-corrected $B - R$ and $R - K$ colours between $0.5 < r/h_K < 1.5$ (when available; the LSBG giants 0052-0119 and 0237-0159 have only central colours and are omitted from further consideration) are compared with the colours of the finely interpolated stellar populations grid. The quantity $\chi^2 = \sum_{i=(B-V),(R-K)}(M_i - O_i)^2/\sigma_i^2$ is minimised, where M_i is the model colour, O_i is the observed colour and σ_i is the error in the observed colour. Error bars are obtained for the average ages and metallicities by fitting the colours plus or minus their 1σ sky level and zero point errors added in quadrature.

This procedure has a number of limitations. Firstly, we neglect the effects of dust reddening. We considered the possible effects of dust earlier in section 2.4.2.2, and concluded that the effects of dust are fairly minimal for this sample. Our use of the colours between $0.5 < r/h_K < 1.5$ should act to further lessen the importance of dust reddening on our results. Secondly, because we use simple SFHs assuming a single metallicity, and because of stellar population model uncertainties, the ages and metallicities we determine are unlikely to be accurate in absolute terms. However, the idea of this simple analysis is to identify relative trends in SFH and metallicity, and their possible causes. The ages and metallicities we derive here will serve this purpose well: the optical–near-IR colours provide a robust way to order galaxies in terms of the relative importance of $\gtrsim 5$ Gyr old stars compared to younger $\lesssim 2$ Gyr old stars, which we parameterise using the average age of the stellar population. To better understand the relative uncertainties, we have also carried out the

analysis using the stellar population models of KA97: the results obtained with KA97's models are indistinguishable (in a relative sense) to the results presented in Figs. 2.3 and 2.4. An extended version of this analysis using all the available colour combinations for a much larger sample of galaxies will be presented in Chapter 3.

2.5.2 The correlations

In order to understand what physical mechanisms might be driving the SFHs of LSBGs, we plot the best-fit average ages and metallicities against physical parameters, such as K central surface brightnesses, K absolute magnitudes, K disc scale lengths and gas fractions. These correlations are presented in Fig. 2.3. Note that we do not attempt to provide a best fit or attach any kind of statistical significance to these relationships. We feel that this is over-interpreting this relatively limited dataset at this stage.

Galactic extinction and K-corrected K absolute magnitudes are calculated using distances from Table 2.1. These absolute magnitudes are combined with the HI masses (multiplied by 1.33 to account for the helium mass fraction) from Table 2.1 to derive the gas fractions, using a K band M/L of 0.6 $M_{\odot}/L_{\odot}$ (c.f. Verheijen 1998; Chapter 6) and assuming a solar K band absolute magnitude of 3.41 (Allen 1973). Note that these gas fractions do not account for any molecular or hot gas component. The same distances are used to derive the K band disc scale lengths in kpc. The K band surface brightnesses have been corrected for galactic extinction, K corrections, $(1+z)^4$ surface brightness dimming and inclination. Inclination corrections C^i have been determined using an intrinsic edge-on disc axial ratio $q_0 = 0.15$ assuming that the disc is transparent; these corrections are given by:

$$C^i = -2.5\log_{10}\left(\frac{(1-e)^2 - q_0^2}{1-q_0^2}\right)^{1/2}, \tag{2.3}$$

where e is the adopted disc ellipticity from Table 2.7 (Holmberg 1958).

Before discussing Fig. 2.3, it is useful to note that the average ages of ESO-LV 1040220, 1040440, 1450250 and 1870510 are all potentially quite uncertain. This is due to their low metallicities: they have optical–near-IR colours suggesting metallicities less than 1/100 solar metallicity (which falls off the model grid). At these metallicities, the model predictions (especially for young ages) are all rather uncertain. Therefore, we feel that their ages are less constrained (even in a relative sense) than their error bars otherwise suggest. These points are denoted by naked sets of error bars in Figs. 2.3 and 2.4. In the discussion that follows, we typically ignore the average ages for these four data points.

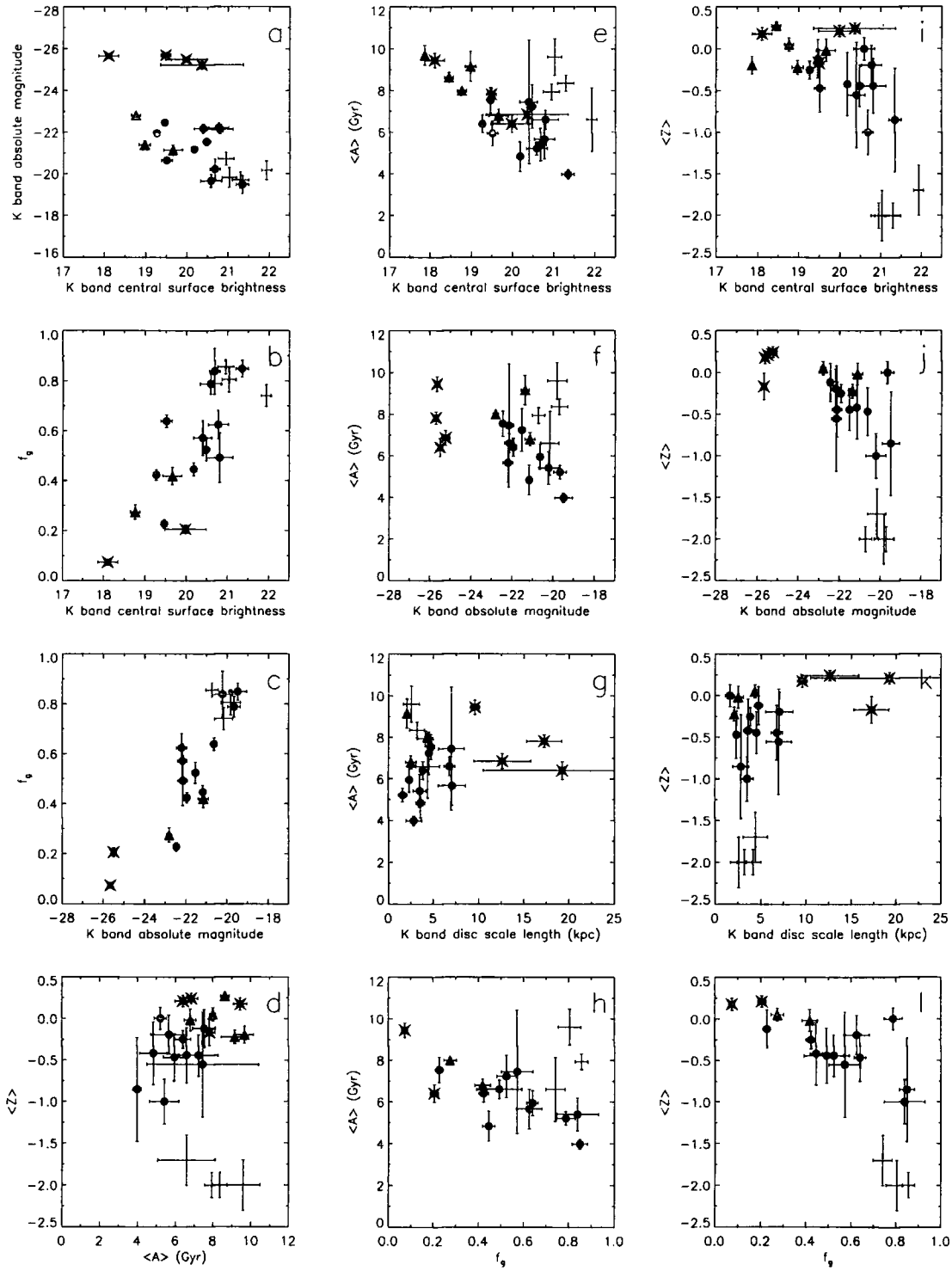

Figure 2.3: Correlations between best-fit average ages, metallicities, K central surface brightnesses, K absolute magnitudes, K disc scale lengths and gas fractions. Circles denote the blue selected subsample of LSBGs, triangles the red selected subsample, and stars the giant LSBGs. Note that the ages for the four ESO-LV galaxies near the low metallicity edge of the grid are highly uncertain: these points are denoted by naked error bars in all plots.

2.5.2.1 Limitations of our dataset

In Fig. 2.3, panel a, we show the relationship between K band central surface brightness and K band absolute magnitude in our dataset. In panels b and c, we show the relationship between gas fraction and K band surface brightness and magnitude respectively. The main purpose of these panels is to simply show that in our sample of LSBGs, surface brightness, magnitude and gas fraction are quite strongly inter-related, and it is expected that correlations of any given quantity with surface brightness will be reflected by correlations of that same quantity with magnitude and gas fraction. Thus, on the basis of this dataset alone, it will be difficult to unambiguously differentiate between trends in the stellar populations of LSBGs driven by magnitude, trends driven by surface brightness, or trends driven by the gas fraction. Note that because of selection effects (primarily that we select only galaxies with low B band surface brightness), panels a, b and c are unlikely to be representative of any universal correlation between surface brightness, magnitude and gas fraction.

2.5.2.2 Ages and metallicities

Fig. 2.3, panel d shows the correlation between the best-fit average age and metallicity. Ignoring the uncertain ages of the ultra-low metallicity LSBGs, there is a correlation, albeit a noisy one, between age and metallicity, in the sense that older galaxies tend to be more metal rich. This correlation quantifies the global trend between age and metallicity observed earlier in Fig. 2.2. This correlation is expected: galaxies appear old through a lack of recent star formation, implying a lack of gas (see also panel h, the age–gas fraction correlation). Most of our sample LSBGs are reasonably massive, meaning that their gas is unlikely to have been ejected by e.g. supernova driven winds. Therefore, their low gas fraction is likely to be due to consumption by star formation: this results in reasonably high stellar metallicities (see e.g. Pagel 1998). Note that some low surface brightness dwarf spheroidals may run counter to this argument, having low metallicities and reasonably old average ages (e.g. Mateo 1998): to explain this one would have to invoke removal of the gas from these low mass galaxies by e.g. supernova-driven winds (Dekel & Silk 1986) or, for cluster dwarf spheroidals, ram-pressure stripping (Abadi, Moore & Bower 1999).

2.5.2.3 Trends in LSBG age

In panels e, f, g and h, we show the trends in age with K central surface brightness, K absolute magnitude, K disc scale length and gas fraction respectively. Age does not appear to correlate with disc scale length. Neglecting the uncertain ages of the four low metallicity ESO-LV galaxies, there appear to be trends in age with surface brightness, magnitude and gas fraction, in the sense

that lower K band surface brightness, lower K luminosity and higher gas fraction LSBGs all have younger average ages. Furthermore, the scatter between age and surface brightness appears smaller than the scatter in the age–magnitude and age–gas fraction correlations. This suggests, tentatively, that the age–surface brightness correlation is the main correlation in this dataset, and the other correlations are the result of the magnitude–surface brightness and gas fraction–surface brightness correlations. We return to this issue later in section 2.5.3.

2.5.2.4 Trends in LSBG metallicity

In panels i, j, k and l of Fig. 2.3, we show the trends in LSBG metallicity with K band surface brightness, magnitude, disc scale length and gas fraction. Note that the metallicities of the four low metallicity ESO-LV galaxies are reasonably well-constrained (i.e. the metallicities are likely to be below $\sim 1/10 Z_{\odot}$;, therefore, it is fair to include them in the discussion of these trends. Metallicity, unlike age, seems to be correlated with K band disc scale length. This seems primarily because of the LSBG giants: they are bright and have large scale lengths, so their high metallicities will produce correlations between metallicity and magnitude and metallicity and scale length. It is likely that a metallicity–magnitude relation is more fundamental; however, it is impossible to rule out scale length dependence in the metallicity on the basis of this dataset.

Metallicity, like age, seems to correlate well with K band surface brightness, magnitude and gas fraction in the sense that LSBGs with lower metallicities have lower surface brightnesses, lower luminosities and higher gas fractions than LSBGs with higher metallicities. Both age and metallicity are also linked (panel d), so the similarity in trends with physical parameters between age and metallicity is not surprising. Again, as was the case for the age, it is more or less impossible to tell, on the basis of this dataset alone, which of the magnitude–metallicity or surface brightness–metallicity correlations are more fundamental.

2.5.3 SFH as a function of total mass and density

In order to investigate how the *baryonic* mass and surface density affect the SFHs of LSBGs, we have modified the K surface brightnesses and absolute magnitudes by turning the neutral gas fraction of the galaxy into stars using the correction to the magnitude $+2.5 \log_{10}(1 - f_g)$. This correction assumes that the gas will turn into stars with the same K band mass to light ratio as was assumed for the stellar population, which in this case is 0.6 $M_{\odot}/L_{\odot}$. This correction makes a number of assumptions.

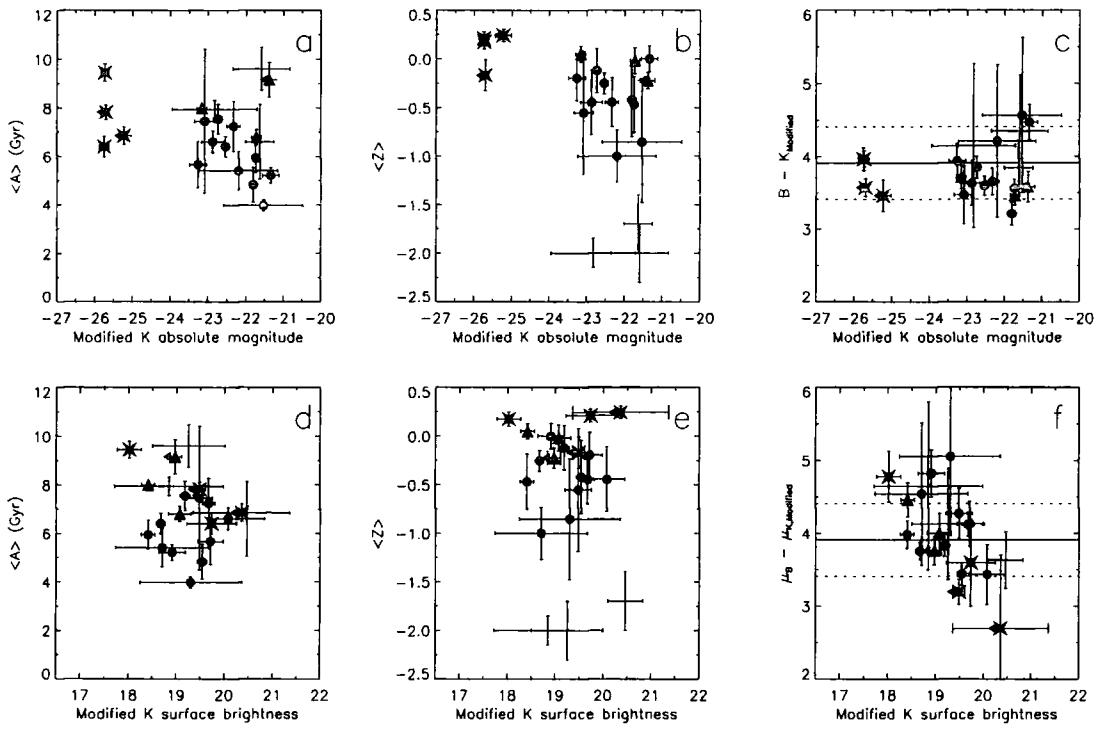

Figure 2.4: Correlations between best-fit average ages and metallicities and K band surface brightnesses and magnitudes, modified by turning all of the available gas mass into stars with a K band mass to light ratio of 0.6 $M_{\odot}/L_{\odot}$. Circles denote the blue selected subsample of LSBGs, triangles the red selected subsample, and stars the giant LSBGs: naked error bars denote the four low metallicity galaxies with potentially large age errors. Red selected or giant LSBGs at known distances for which there are no gas masses are shown as lower limits by error bars, with a solid triangle pointing towards the direction in which the galaxies move with increasing gas fraction: the vertex of the solid triangle denotes the modified surface brightness or magnitude assuming a gas fraction of 0.2. Panels c and f show the difference between the B band absolute magnitude and the modified K absolute magnitude and the difference between the B band central surface brightness and modified K band central surface brightness, respectively. Solid lines denote an average 'colour' $B - K_{\mathrm{Modified}} = 3.9$, and the dashed line a scatter of 0.5 mag around this average.

1. The K band mass-to-light ratio is expected to be relatively robust to the presence of young stellar populations; however, our assumption of a constant K band mass to light ratio is still a crude assumption. Note, however, that the relative trends in Fig. 2.4 are quite robust to changes in stellar mass-to-light ratio: as the stellar mass-to-light ratio increases, the modified magnitudes creep closer to their unmodified values asymptotically.

2. The presence of molecular gas is not accounted for in this correction. Assuming a typical galactic CO to H_2 conversion ratio, the non-detections of LSBGs by Schombert et al. (1990) and de Blok & van der Hulst (1998b) imply H_2 to HI ratios smaller than 0.25, and exceptionally as low as 0.04. Therefore, the contribution of molecular hydrogen to the gas mass of LSBGs

is expected to be relatively minor, but because of the expected metallicity dependence in the CO to H_2 conversion ratio, the importance of molecular hydrogen in LSBGs remains fairly unconstrained (Mihos, Spaans & McGaugh 1999).

3. The correction to the surface brightness implicitly assumes that the gas will turn into stars with the same spatial distribution as the present-day stellar component. This is a poor assumption as the gas distribution is usually much more extended than the stellar distribution; most LSBG gas distributions are centrally peaked, however, and so the correction is unlikely to be completely wrong.

All of the above arguments suggest that the modified magnitudes and surface brightnesses are unlikely to give an accurate measure of the true masses and densities of LSBGs. These quantities do, however, better reflect the total mass and density of the galaxy than the K band magnitudes and surface brightnesses alone, and so are useful as an indication of the kind of trends we would see if we could work out the baryonic masses and densities of LSBGs. The median correction is -0.9 mag, and 68 per cent of the corrections lie within 0.7 mag of this value.

The trends in age and metallicity with modified K band central surface brightness and absolute magnitude are shown in Fig. 2.4. Three red and giant LSBGs with known redshifts but unknown (or unmeasurable) HI fluxes have been placed on Fig. 2.4 also: error bars denote their (unmodified) magnitudes or surface brightnesses, and solid triangles denote the direction that these galaxies move in with increasing gas fraction, with the vertex of the triangle indicating the offset that is produced by converting a gas fraction of 0.2 into stars. For reference, in panels c and f, we also show the relationship between B band magnitude and surface brightness and the modified K band magnitude and surface brightness. Surprisingly, we find that B band magnitude and surface brightness are reasonable reflections of the modified magnitudes and surface brightnesses of LSBGs (remembering the uncertain assumptions that went into constructing the modified magnitudes and surface brightnesses). Both the B band magnitudes and surface brightnesses have a mean offset from the modified K band values consistent with a +3.9 mag offset, with an RMS of around 0.5 mag (solid and dotted lines in panels c and f). This relationship may be caused by the sensitivity of the optical mass to light ratios to recent star formation: B band mass to light ratios decrease for younger populations in a such a way as to make the increase in brightness for younger populations offset almost exactly (to within a factor of 60 per cent or so, from the 0.5 mag scatter) by their larger gas fractions, making the B band a reasonable total mass indicator in LSBGs (assuming that the K band stellar mass to light ratio is fairly constant).

In panels a and b of Fig. 2.4, we see that the LSBG ages and metallicities correlate with their modified K band magnitudes (baryonic masses). In stark contrast, in panels d and e, we see that the ages and metallicities correlate poorly with the modified K band surface brightnesses (baryonic surface densities). This result is puzzling, especially in the light of the tight correlation between average age and surface brightness in panel e of Fig. 2.3. There are two possible interpretations of this huge scatter in the age–modified surface brightness plane.

Is it possible that there is little or no correlation between the SFH and surface density of a galaxy, as panels d and e suggest? In this case, we must explain the strong correlations between age and K band surface brightness and metallicity and K band surface brightness in panels e and i of Fig. 2.3. This may be possible to explain via selection effects: because we selected our galaxies to have a relatively narrow range of B band surface brightness, and older, more metal rich galaxies are redder, we would naturally expect to see an artificial correlation between K band surface brightness (which would be higher because of the redder colours) and age (which correlates with these red colours). Note, however, that this interpretation has real difficulty in explaining the tightness and dynamic range of the age–K band surface brightness correlation.

Conversely, is it possible that there is a correlation between baryonic surface density and age, and that for some reason it is masked in this dataset? There is quite a narrow range (only $\sim$ 2 mag arcsec^{-2}) of modified surface brightness: the close correspondence between B band and modified K band surface brightnesses (panel f of Fig. 2.4) means that because we selected our galaxies to have a relatively narrow range of B band surface brightness, we have implicitly selected for a narrow range in baryonic central surface density. Also, our modifications to the surface brightnesses were large for gas-rich galaxies with low K band surface brightnesses and much smaller for gas-poor galaxies with higher K band surface brightnesses, steepening the relationship between SFH and modified surface brightness considerably. Thus, we may simply lack an adequate surface density range to be able to distinguish a steep trend in age with surface density, especially in the presence of significant uncertainties in the ages and surface densities. Note that this is the interpretation that we prefer: the correlation between age and K band surface brightness is quite tight, which is quite suggestive of some kind of correlation between density and SFH. Note that the age–mass relation would survive in this case relatively unscathed: the dynamic range for the age–mass relation is in excess of 5 magnitudes, which makes it quite robust to changes $\sim$ 1 mag in the relative positioning of the data points along the trend.

2.5.4 A unifying view

All the above correlations are consistent with the proposition that *the age of a LSBG stellar population is primarily correlated with its surface density and that its metallicity is correlated with both surface density and mass*, albeit with considerable scatter. Panels e, f, i and j of Fig. 2.3 all strongly support this scheme: in particular, LSBG giants have a range of K band surface brightnesses (and ages; panel f) but have bright K band absolute magnitudes (and high metallicities; panel j). The main obstacle for such a scenario is the lack of correlation between modified K band surface brightnesses and age and metallicity, which *may* be due to our explicit selection of galaxies with only a relatively narrow range of B band central surface brightness (c.f. Chapter 3).

An important question to ask is if this scenario is physically plausible. A relationship between surface brightness/density and average age would be easy to understand: a density dependent (e.g. Schmidt 1959) star formation law would result in such a correlation (note that a magnitude–age correlation might suggest a mass-dependent infall timescale, or a mass-dependent star formation law; c.f. Chapter 4). Such a scenario would also very naturally account for the existence of age gradients in LSBGs: the outer regions of LSBGs are less dense, and would form stars less quickly than their inner regions, resulting in an age gradient.

Such a scheme is qualitatively consistent with those proposed by e.g. de Blok et al. (1996), Jimenez et al. (1998) or Gerritsen & de Blok (1999). In these schemes, it is primarily the low surface density that slows down the evolution of LSBGs (either explicitly through a density-dependent star formation law or implicitly, through an inability to build up a high gas metallicity). Metallicity's mass dependence is likely to stem from the relative importance of feedback: the efficiency with which a galaxy ejects its metals in a supernova-driven wind, the strength of which sensitively depends on galaxy mass (e.g. MacLow & Ferrera 1999).

While the above scenario is consistent with the data, it is unlikely to be unique: because of the correlation between surface brightness and magnitude, a purely mass-dependent age and metallicity may be plausible. Note, however, that a mass-dependent age has some disadvantages: the ages of LSBG giants support a surface brightness dependent age, and age gradients would have to be explained using a different mechanism.

2.6 Conclusions

We have performed deep imaging of a sample of 26 LSBGs in the optical and near-IR in order to study their stellar populations. By comparing their optical–near-IR colours with the latest stellar

population models, it is possible to constrain the young to old star ratio (parameterised by the average age of the galaxy) and the galaxy metallicity. We have found the following.

- Optical–near-IR colour gradients are common in LSBGs. Most colour gradients are consistent with a mean stellar age gradient, with the outer regions of galaxies appearing younger than the inner region of galaxies. We argue against the effects of dust reddening as the only cause of LSBG colour gradients. As common as colour gradients are, they are not present in all LSBGs (Bergvall et al. 1999); this is important, because it may provide a chance to directly observe what drives the age gradient in LSBGs.

- We find that LSBGs have a wide range in morphologies and stellar populations, ranging from old, near solar metallicity populations for the very reddest LSBGs, to younger, high metallicity populations in the LSBG giants, to young and metal poor populations in the blue gas-rich LSBGs.

- By comparing the observed optical–near-IR colours between 0.5 and 1.5 disc scale lengths with stellar population models, we have determined best-fit average ages and metallicities that are robust in a relative sense, so that trends in age and metallicity will be quite secure.

- When the highly uncertain ages of the lowest metallicity galaxies are excluded, there are strong trends between both age and metallicity and K band surface brightness, absolute magnitude and gas fraction. LSBGs with low K band surface brightnesses, low K luminosities and high gas fractions are all fairly unevolved, young, low metallicity systems. In contrast, LSBGs with higher K band surface brightnesses, higher K band luminosities and smaller gas fractions appear much more evolved, with older average ages and higher (near solar) metallicities.

- We have constructed crude estimates of the total mass and total densities of the atomic hydrogen, helium and stars in LSBGs by turning the gas into stars with a constant K band mass to light ratio of 0.6 $M_{\odot}/L_{\odot}$. Surprisingly, we find that the B band absolute magnitudes and surface brightnesses are reasonable predictors of the mass and density estimators, to within a factor of $\sim$ 60 per cent or so. We find that the ages and metallicities of LSBGs correlate well with our mass estimator, but correlate poorly with our surface density estimator. We argue that the poor correlation between our surface density estimator and SFH is the result of the narrow dynamic range in surface density probed by our sample, compounded by errors in SFH and density determination.

- Our results are consistent with a scenario in which the age of a LSBG is correlated primarily with its surface density, and the metallicity of a LSBG is correlated with both its surface density and mass (albeit with much scatter). This kind of correlation would be observed if the star formation law depended on gas surface density, and if the efficiency with which a galaxy retained its newly-synthesised metal content was a function of its mass (see Chapter 4).

Chapter 3

The stellar populations of spiral galaxies

In Chapter 2, we studied the star formation histories (SFHs) of low surface brightness galaxies (LSBGs): in particular, we found that our results were consistent with a scenario in which the age of a LSBG depended primarily on its surface density and its metallicity primarily on its mass. In this Chapter, we extend our SFH analysis to a larger dataset to probe SFH trends in spiral galaxies with a wider range of properties.

3.1 Introduction

It has long been known that there are systematic trends in the SFHs of spiral galaxies; however, it has been notoriously difficult to quantify these trends and directly relate them to observable physical parameters. This difficulty stems from the age-metallicity degeneracy: the spectra of composite stellar populations are virtually identical if the percentage change in age or metallicity (Z) follows $\Delta\text{age}/\Delta Z \sim 3/2$ (Worthey 1994). This age-metallicity degeneracy is split only for certain special combinations of spectral line indices or for limited combinations of broad band colours (Worthey 1994; dJIV). In this Chapter, we use a combination of optical and near-infrared (near-IR) broad band colours to partially break the age-metallicity degeneracy and relate these changes in SFH with a galaxy's observable physical parameters.

The use of broad band colours is now a well established technique for probing the SFH of galaxy populations. In elliptical and S0 galaxies there is a strong relationship between galaxy colour and absolute magnitude (Visvanathan & Sandage 1972; Larson, Tinsley & Caldwell 1980; BLE; Terlevich et al. 1999): this is the so-called colour-magnitude relation (CMR). This correlation, which is also present at high redshift in both the cluster and the field (Ellis et al. 1997; Stanford,

Eisenhardt & Dickinson 1998; Chapter 7), seems to be driven by a metallicity-mass relationship in a predominantly old stellar population (BLE; Kodama et al. 1998; Bower, Kodama & Terlevich 1998). The same relationship can be explored for spiral galaxies: Peletier and de Grijs (1998) determine a dust-free CMR for edge-on spirals. They find a tight CMR, with a steeper slope than for elliptical and S0 galaxies. Using stellar population synthesis models, they conclude that this is most naturally interpreted as indicating trends in both age and metallicity with magnitude, with faint spiral galaxies having both a younger age and a lower metallicity than brighter spirals.

In the same vein, radially-resolved colour information can be used to investigate radial trends in SFH. In dJIV, radial colour gradients in spiral galaxies were found to be common and were found to be consistent predominantly with the effects of a stellar age gradient. This conclusion is supported by Abraham et al. (1998), who find that dust and metallicity gradients are ruled out as major contributors to the radial colour trends observed in high redshift spiral galaxies. Also in dJIV, late-type galaxies were found to be on average younger and more metal poor than early-type spirals. As late-type spirals are typically fainter than early-type galaxies (in terms of total luminosity and surface brightness; dJIII), these results are qualitatively consistent with those of Peletier & de Grijs (1998). However, due to the lack of suitable stellar population synthesis models at that time, the trends in global age and metallicity in the sample were difficult to meaningfully quantify and investigate.

In this Chapter, we extend the analysis presented in dJIV by using the new stellar population synthesis models of Bruzual & Charlot (in preparation) and Kodama & Arimoto (1997, KA97), and by augmenting his sample with low-inclination galaxies from the Ursa Major cluster from Tully et al. (1996; TVPHW hereafter) and low surface brightness galaxies from Chapter 2. A maximum-likelihood method is used to match all the available photometry of the sample galaxies to the colours predicted by these stellar population synthesis models, allowing investigation of trends in galaxy age and metallicity as a function of local and global observables.

The plan of this Chapter is as follows. In section 3.2, we review the sample data, the stellar population synthesis models and the dust models used in this analysis. In section 3.3, we present the maximum-likelihood fitting method and review the construction of the error estimates. In section 3.4, we present the results and investigate correlations between our derived ages and metallicities and the galaxy observables. In section 3.5 we discuss some of the more important correlations and the limitations of the method, compare with literature data and discuss plausible physical mechanisms for generating some of the correlations in section 3.4. Finally, we review our

main conclusions in section 3.6. Note that we homogenise the distances of Chapter 2, dJIV and TVPHW to a value of $H_0 = 65$ kms^{-1}.

3.2 The data, stellar population and dust models

3.2.1 The data

In order to investigate SFH trends in spiral galaxies, it is important to explore as wide a range of galaxy types, magnitudes, sizes and surface brightnesses as possible. Furthermore, high-quality surface photometry in a number of optical and at least one near-IR passband is required. Accordingly, we include the samples of de Jong & van der Kruit (1994; dJI), TVPHW and Chapter 2 in this study to cover a wide range of galaxy luminosities, surface brightnesses and sizes. The details of the observations and data reduction can be found in the above references; below, we briefly outline the sample properties and analysis techniques.

The sample of undisturbed spiral galaxies described in dJI was selected from the UGC (Nilson 1973) to have red diameters of at least 2 arcmin and axial ratios greater than 0.625. The sample presented in Chapter 2 was taken from a number of sources (de Blok et al. 1995, 1996; O'Neil et al. 1997a, 1997b; Sprayberry et al. 1995; Lauberts & Valentijn 1989; dJI) to have low estimated blue central surface brightnesses $\mu_{B,0} \gtrsim 22.5$ mag arcsec^{-2} and diameters at the 25 B mag arcsec^{-2} isophote larger than 16 arcsec. TVPHW selected their galaxies from the Ursa Major Cluster (with a velocity dispersion of only 148 km s^{-1}, it is the least massive and most spiral-rich nearby cluster): the sample is complete down to at least a B band magnitude of $\sim$ 14.5 mag, although their sample includes many galaxies fainter than that cutoff. We take galaxies from the three samples with photometric observations (generously defined, with maximum allowed calibration errors of 0.15) in at least 2 optical and one near-IR passband, axial ratios greater than 0.4, and accurate colours (with errors in a single passband due to sky subtraction less than 0.3 mag) available out to at least 1.5 K-band disc scale lengths. For the Ursa Major sample, we applied an additional selection criterion that the K' band disc scale length must exceed 5 arcsec, to allow the construction of reasonably robust central colours (to avoid the worst of the effects of mismatches in seeing between the different passbands). This selection leaves a sample of 64 galaxies from dJI (omitting UGC 334, as we use the superior data from Chapter 2 for this galaxy: note that we show the two sets of colours for UGC 334 connected with a dotted line in Figs. 3.3–3.5 to allow comparison), 23 galaxies from Chapter 2 and 34 galaxies from TVPHW (omitting NGC 3718 because of its highly peculiar morphology, NGC 3998 because of poor R band calibration, and NGC 3896 due to its

poor K' band data). In this way, we have accumulated a sample of 121 low-inclination spiral galaxies with radially-resolved, high-quality optical and near-IR data.

Radially-resolved colours from Chapter 2 and dJIV were used in this study, and surface photometry from TVPHW was used to construct radially-resolved colours. Structural parameters and morphological types were taken from the sample's source papers and dJII. In the next two paragraphs we briefly outline the methods used to derive structural parameters and determine radially-resolved galaxy colours in the three source papers.

Galaxy structural parameters were determined using different methods in each of the three source papers. For the sample taken from dJI, a two-dimensional exponential bulge-bar-disc decomposition was used (dJII). Chapter 2 uses a one-dimensional bulge-disc decomposition (with either an exponential or a $r^{1/4}$ law bulge). TVPHW use a 'marking the disc' fit, where the contribution of the bulge to the disc parameters is minimised by visually assessing where the contribution from the bulge component is negligible. Note that dJII shows that these methods all give comparable results to typically better than 20 per cent in terms of surface brightness and 10 per cent in terms of scale lengths, with little significant bias. Note also that we show in Chapter 5 that TVPHW's 'marking the disc' fits are free from personal bias; we reproduce their results using a similar method with a RMS ~ 0.25 mag arcsec^{-2}. Magnitudes for all galaxies were determined from extrapolation of the radial profiles with an exponential disc. The dominant source of error in the determination of the galaxy parameters is due to the uncertainty in sky level (Chapter 2; dJII).

In order to examine radial trends in the stellar populations and galaxy dust content, colours were determined in large independent radial bins to minimise the random errors in the surface photometry and small scale stellar population and dust fluctuations. Up to 7 radial bins (depending on the signal-to-noise in the galaxy images) were used: $0 \leq r/h_K < 0.5, 0.5 \leq r/h_K < 1.5, 1.5 \leq r/h_K < 2.5$ and so on, where r is the major-axis radius, and h_K is the major-axis K band exponential disc scale length. The ellipticities and position angles of the annuli used to perform the surface photometry were typically determined from the outermost isophotes, and the centroid of the brightest portion of each galaxy was adopted as the ellipse centre. Modulo calibration errors, the dominant source of uncertainty in the surface photometry is due to the uncertainty in the adopted sky level (Chapter 2; dJIV).

The galaxy photometry and colours were corrected for Galactic foreground extinction using the dust models of Schlegel, Finkbeiner and Davis (1998). Ninety per cent of the galactic extinction corrections in B band are smaller than 0.36 mag, and the largest extinction correction is 1.4 mag. We correct the K band central surface brightness to the face-on orientation assuming that

the galaxy is optically thin: $\mu_0^i = \mu_0^{obs} + 2.5\log_{10}(\cos i)$, where μ_0^i is the inclination corrected surface brightness and μ_0^{obs} is the observed surface brightness. The inclination i is derived from the ellipticity of the galaxy e assuming an intrinsic axial ratio q_0 of 0.15 (Holmberg 1958): $\cos^2 i = \{(1-e)^2 - q_0^2\}/(1-q_0^2)$. Assuming that the galaxies are optically thin in K should be a reasonable assumption as the extinction in K is around ten times lower than the extinction in B band. Note that we do not correct the observed galaxy colours for the effects of dust: the uncertainties that arise from this lack of correction are addressed in section 3.5.4.

The gas fraction of our sample is estimated as follows. The K band absolute magnitude is converted into a stellar mass using a constant stellar K band mass to light ratio of 0.6 $M_\odot/L_\odot$ (c.f. Verheijen 1998; Chapter 6) and a solar K band absolute magnitude of 3.41 (Allen 1973). The HI mass is estimated using HI fluxes from the NASA/IPAC Extragalactic Database and the homogenised distances, increasing these masses by a factor of 1.33 to account for the unobserved helium fraction (de Blok et al. 1996). We estimate molecular gas masses (also corrected for helium) using the ratio of molecular to atomic gas masses as a function of morphological type taken from Young & Knezek (1989). The total gas mass is then divided by the sum of the gas and stellar masses to form the gas fraction. There are two main sources of systematic uncertainty in the gas fractions not reflected in their error bars. Firstly, stellar mass to light ratios carry some uncertainty: they depend sensitively on the SFH and on the effects of dust extinction. Our use of K band to estimate the stellar masses to some extent alleviates these uncertainties; however, it must be borne in mind that the stellar masses may be quite uncertain. Secondly, the molecular gas mass is highly uncertain: uncertainty in the CO to H_2 ratio, considerable scatter in the molecular to atomic gas mass ratio within a given morphological type and the use of a type-dependent correction (instead of e.g. a more physically motivated surface brightness or magnitude dependent correction) all make the molecular gas mass a large uncertainty in constructing the gas fraction. This uncertainty could be better addressed by using only galaxies with known CO fluxes; however, this requirement would severely limit our sample size. As our main aim is to search for trends in age and metallicity (each of which is in itself quite uncertain) as a function of galaxy parameters, a large sample size is more important than a slightly more accurate gas fraction. Note that this gas fraction is only an estimate of the cold gas content of the galaxy: we do not consider any gas in an extended, hot halo in this Chapter.

3.2.2 The stellar population models

In order to place constraints on the stellar populations in spiral galaxies, the galaxy colours must be compared with the colours of stellar population synthesis (SPS) models. In this section, we outline the SPS models that we use, and discuss the assumptions that we make in this analysis and the uncertainties involved in the use of these assumptions and this colour-based technique.

In order to get some quantitative idea of the inaccuracies introduced in our analysis by uncertainties in SPS models, we used two different SPS models in our analysis: the GISSEL98 implementation of Bruzual & Charlot (in preparation; hereafter BC98) and Kodama & Arimoto (1997; KA97). We use the multi-metallicity colour tracks of an evolving single burst stellar population, with a Salpeter (1955) stellar initial mass function (IMF) for both models, where the lower mass limit of the IMF was 0.1 $M_\odot$ for both the BC98 and KA97 models, and the upper mass limit was 125 $M_\odot$ and 60 $M_\odot$ for BC98 and KA97 respectively. We assume that the IMF does not vary as a function of time. We use simplified SFHs and fixed metallicities to explore the feasible parameter space in matching the model colours with the galaxy colours. Even though fixing the metallicities ignores chemical evolution, the parameter space that we have used allows the determination of relative galaxy ages and metallicities with a minimal set of assumptions.

In this simple case, the integrated spectrum $F_\lambda(t)$ for a stellar population with an arbitrary star formation rate (SFR) $\Psi(t)$ is easily obtained from the time-evolving spectrum of a single-burst stellar population with a given metallicity $f_\lambda(t)$ using the convolution integral (Bruzual & Charlot 1993):

$$F_\lambda(t) = \int_0^t \Psi(t-t') f_\lambda(t') dt'. \tag{3.1}$$

We use exponential SFHs, parameterised by the star formation timescale τ. In this scenario, the SFR $\Psi(t)$ is given by:

$$\Psi(t) = Be^{-t/\tau}, \tag{3.2}$$

where B is an arbitrary constant determining the total mass of the stellar population. In order to cover the entire range of colours in our sample, both exponentially decreasing and increasing SFHs must be considered. Therefore, τ is an inappropriate choice of parameterisation for the SFR, as in going from old to young stellar populations smoothly, τ progresses from 0 to ∞ for a constant SFR, then from $-\infty$ to small negative values. We parameterise the SFH by the average age of the stellar population $\langle A \rangle$, given by:

$$\langle A \rangle = \frac{\int_A^0 t\Psi(t)dt}{\int_A^0 \Psi(t)dt} = A - \tau \frac{1 - e^{-A/\tau}(1 + A/\tau)}{1 - e^{-A/\tau}} \tag{3.3}$$

for an exponential SFH, as given in Equation 3.2, where A is the age of the oldest stars in the stellar population (signifying when star formation started). In our case, we take $A = 12$ Gyr as the age of all galaxies, and parameterise the difference between stellar populations purely in terms of $\langle A \rangle$.

Clearly, the above assumptions that we use to construct a grid of model colours are rather simplistic. In particular, our assumption of a galaxy age of 12 Gyr and an exponential SFH, while allowing almost complete coverage of the colours observed in our sample, is unlikely to accurately reflect the broad range of SFHs in our diverse sample of galaxies. Some galaxies may be older or younger than 12 Gyr, and star formation is very likely to proceed in bursts, instead of varying smoothly as we assume above (Grebel 1998; Tolstoy 1999a). Additional uncertainties stem from the use of a constant stellar metallicity and from the uncertainties inherent to the SPS models themselves, which will be at least ~ 0.05 mag for the optical passbands, increasing to $\gtrsim 0.1$ mag for the near-IR passbands (Charlot, Worthey & Bressan 1996; see section 1.3 in Chapter 1 for further discussion of SPS model uncertainties).

However, the important point here is that the above method gives robust *relative* ages and metallicities. Essentially, this colour-based method gives some kind of constraint on the luminosity-weighted ratio of $\lesssim 2$ Gyr old stellar populations to $\gtrsim 5$ Gyr old stellar populations, which we parameterise using the average age $\langle A \rangle$. Therefore, the details of how we construct the older and younger stellar populations are reasonably unimportant. It is perfectly possible to assume an exponential SFH with an age of only 5 Gyr: if this is done, galaxies become younger (of course), but the relative ordering of galaxies by e.g. age is unaffected. Note that because the colours are luminosity weighted, small bursts of star formation may affect the relative ages and metallicities of galaxies (relative to their underlying ages and metallicities before the burst); however, it is unlikely that a large fraction of galaxies will be strongly affected by large amounts of recent star formation. The basic message is that absolute galaxy ages and metallicities are reasonably uncertain, but the relative trends are robust. Note that all of the results presented in this Chapter were obtained using the BC98 models, unless otherwise stated.

3.2.3 The dust models

To quantify the effects of dust reddening, we adopt the Milky Way (MW) and Small Magellanic Cloud (SMC) extinction curves and albedos from Gordon, Calzetti & Witt (1997). In the top two panels in Figs. 3.2–3.6, we show a MW foreground screen model with a total V band extinction $A_V = 0.3$ mag (primarily to facilitate comparison with other studies). In the lower two panels,

we show the reddening vector from a more realistic face-on Triplex dust model (Disney, Davies & Phillipps 1989, DDP hereafter; Evans 1994). In this model, the dust and stars are distributed smoothly in a vertically and horizontally exponential profile, with equal vertical and horizontal distributions. The two models shown have a reasonable central V band optical depth in extinction, from pole to pole, of two. This value for the central optical depth in V band is supported by a number of recent statistical studies into the global properties of dust in galaxies (Peletier & Willner 1992; Huizinga 1994; Tully & Verheijen 1997; Tully et al. 1998; Kuchinski et al. 1998). However, the Triplex model does not take account of scattering. Monte Carlo simulations of Triplex-style galaxy models taking into account the effects of scattering indicate that because our sample is predominantly face-on, at least as many photons will be scattered into the line of sight as are scattered out of the line of sight (dJIV). Therefore, we use the dust *absorption* curve to approximate the effects of more realistic distributions of dust on the colours of a galaxy. The use of the absorption curve is the main reason for the large difference in the MW and SMC Triplex model vectors: Gordon et al.'s (1997) MW dust albedo is much higher than their SMC dust albedo, leading to less absorption per unit pole to pole extinction. Note also that the Triplex dust reddening vector produces much more optical reddening than e.g. those in dJIV: this is due to our use of more recent near-IR dust albedos, which are much larger than e.g. those of Bruzual, Magris & Calvet (1988). These dust models are *not* used in the SFH fitting: these models are used in Figs. 3.2–3.6 and section 3.5.4 to allow us to quantify the effects that dust reddening may have on our results.

3.3 Maximum-likelihood fitting

Before we describe the maximum-likelihood fitting method in detail, it is important to understand the nature of the error budget in an individual galaxy colour profile. There are three main contributions to the galaxy photometric errors *in each passband* (note that because of the use of large radial bins, shot noise errors are negligible compared to these three sources of error).

1. Zero-point calibration errors $\delta\mu_{cal}$ affect the whole galaxy colour profile systematically by applying a constant offset to the colour profiles.

2. In the optical passbands, flat fielding errors $\delta\mu_{ff}$ affect the galaxy colour profile randomly as a function of radius. Because of the use of large radial bins in the construction of the colours, the dominant contribution to the flat fielding uncertainty is the flat field structure over the largest scales. Because the flat fielding structure is primarily large scale, it is fair to reduce the flat fielding error by a factor of $\sim$ 10 as one radial bin will only cover typically one tenth or less

of the whole frame. We assume normally-distributed flat fielding errors with a σ of 0.5/10 per cent of the galaxy and sky level in the optical (0.5 per cent was chosen as a representative, if not slightly generous, flat field error over large scales). In the near-IR, sky subtraction to a large extent cancels out any flat fielding uncertainties: we, therefore, do not include the effect of flat fielding uncertainties in the error budget for near-IR passbands.

3. Sky level estimation errors $\delta\mu_{sky}$ affect the shape of the colour profile in a systematic way. If the assumed sky level is too high, the galaxy profile 'cuts off' too early, making the galaxy appear smaller and fainter than it is, whereas if the sky level is too low the galaxy profile 'flattens off' and the galaxy appears larger and brighter than it actually is. As long as the final estimated errors in a given annulus due to sky variations are reasonably small ($\lesssim$ 0.3 mag) this error $\delta\mu_{sky}$ is related to the sky level error $\delta\mu_s$ (in magnitudes) by:

$$\delta\mu_{sky} \simeq \delta\mu_s 10^{0.4(\mu-\mu_s)}, \tag{3.4}$$

where μ is the average surface brightness of the galaxy in that annulus and μ_s is the sky surface brightness.

These photometric errors have different contributions to the total error budget at different radii, and have different effects on the ages, metallicities, and their gradients. If a single annulus is treated on its own, the total error estimate for each passband $\delta\mu_{tot}$ is given by:

$$\delta\mu_{tot} = (\delta\mu_{cal}^2 + \delta\mu_{ff}^2 + \delta\mu_{sky}^2)^{1/2}. \tag{3.5}$$

We use magnitude errors instead of flux errors in constructing these error estimates: this simplifies the analysis greatly, and is more than accurate enough for our purposes.

We fit the SPS models to each set of radially-resolved galaxy colours using a maximum-likelihood approach. Note that we do *not* include the effects of dust in the maximum-likelihood fit.

- We generate a finely-spaced model grid by calculating the SPS models for a fine grid of τ values. These finely spaced τ grids are then interpolated along the metallicity using a cubic spline between the model metallicities. These models then provide a set of arbitrary normalisation model magnitudes $\mu_{\mathrm{model},i}(\langle A\rangle, Z)$ for each passband i for a range of SFHs and metallicities.

- We read in the multi-colour galaxy surface brightnesses as a function of radius, *treating each annulus independently* (each annulus has surface brightness $\mu_{\mathrm{obs},i}$). The total error estimate $\delta\mu_{tot,i}$ for each annulus is determined for each passband i.

- For each $\langle A \rangle$ and metallicity Z, it is then possible to determine the best normalisation between the model and annulus colours μ_c using:

$$\mu_c = \frac{\sum_{i=1}^{n} \{\mu_{\mathrm{obs},i} - \mu_{\mathrm{model},i}(\langle A \rangle, Z)\}/\delta\mu_{tot,i}^2}{\sum_{i=1}^{n} 1/\delta\mu_{tot,i}^2}, \tag{3.6}$$

where n is the number of passbands and its corresponding χ^2 is given by:

$$\chi^2 = \frac{1}{n-1} \sum_{i=1}^{n} \frac{(\mu_{\mathrm{obs},i} - \mu_{\mathrm{model},i}(\langle A \rangle, Z) - \mu_c)^2}{\delta\mu_{tot,i}^2}. \tag{3.7}$$

The best model $(\langle A \rangle, Z)$ match is the one with the minimum χ^2 value. This procedure is then carried out for all of the galaxy annuli. Note that minimising χ^2, strictly speaking, requires the errors to be Gaussian; however, using magnitude errors $\lesssim 0.3$ mag does not lead to significant errors in χ^2.

3.3.1 Estimating age and metallicity gradients

In order to gain insight into age and metallicity trends as a function of radius, we perform a *weighted* linear fit to the ages and metallicities of each galaxy. This fit is parameterised by a gradient per disc scale length and an intercept at the disc half light radius.

Each point entering the fit is weighted by the total age or metallicity error in each annulus, determined using $\Delta\chi^2 = 1$ intervals for the age and metallicity parameters individually (i.e. the age or metallicity range for which the reduced χ^2 is smaller than $\chi^2_{\mathrm{best\,fit}} + 1$). The first two, three or four bins of the radially-resolved ages and metallicities are used in the fit. Galaxies with only central colours are omitted from the sample, and galaxies with more than four bins are fit only out to the fourth bin. Including the fifth, sixth and seventh bins in the gradient fits does not significantly affect our results, but can increase the noise in the gradient determinations.

As two out of the three sources of photometric error are correlated over the galaxy, it is impossible to use the $\Delta\chi^2 = 1$ contours for each annulus to estimate e.g. the errors in age and metallicity gradients. This is because to a large extent calibration uncertainties will not affect the age or metallicity gradient; however, the errors for the age or metallicity intercept will depend sensitively on the size of calibration error. We, therefore, produce error estimates using a Monte Carlo approach.

For each galaxy, we repeat the above SFH derivation and analysis 100 times, applying a normally distributed random calibration, flat fielding and sky level errors. This approach has the virtue that the different types of photometric error act on the galaxy profile as they should, allowing valid

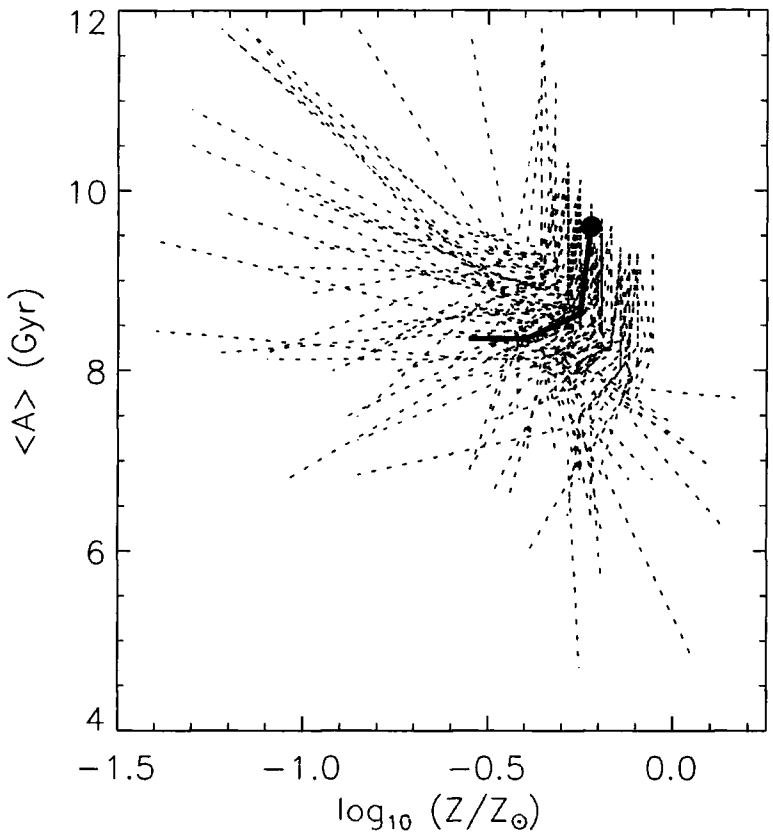

Figure 3.1: An example of the derived ages and metallicities, with their associated Monte Carlo error estimates, for UGC 3080. The solid line denotes the best fit age and metallicities of UGC 3080 as a function of radius, in bins of $0 \leq r/h_K < 0.5$ (filled circle), $0.5 \leq r/h_K < 1.5, 1.5 \leq r/h_K < 2.5$ and $2.5 \leq r/h_K < 3.5$. The dotted lines denote the 100 Monte Carlo simulations, with realistic photometric errors applied. The galaxy centre seems both reasonably old and metal rich, and becomes younger and more metal poor as you go further out into the spiral disc. Note that the Monte Carlo simulation indicates that these trends are reasonably significant for this galaxy.

assessment of the accuracy of any trends in age or metallicity with radius. An example of the ages and metallicities derived with this approach for the galaxy UGC 3080 is presented in Fig. 3.1. The solid line indicates the best-fit model for the galaxy colours as a function of radius, and the dotted lines the Monte Carlo simulations with realistic (or perhaps slightly conservative) photometric errors. Note that the errors in age and metallicity increase substantially with radius. This is primarily due to the sky subtraction errors, as their effect increases as the surface brightness becomes fainter with radius. Note that because we use a weighted fit, the age and metallicity gradients are robust to the largest of the sky subtraction errors in the outer parts.

The error in any one parameter, e.g. metallicity, in any one annulus is given by the half of the interval containing 68 per cent of the e.g. metallicities in that annulus (the one sigma confidence interval). Errors in the age or metallicity gradients and intercepts are determined by fitting the 100 Monte Carlo simulated datasets in the same way as the real data. As above, the errors in each of these fit parameters are determined by working out the one sigma confidence interval of the simulations for each fit parameter alone.

3.4 Results

3.4.1 Colour-colour plots

In order to better appreciate the characteristics of the data, the model uncertainties and the potential effects of dust reddening on the results, it is useful to consider some colour-colour plots in some detail. In Figs. 3.2 through 3.6 we show $B - R$ against $R - K$ colours as a function of radius for our sample galaxies. Central colours are denoted by solid circles (for the sample from dJIV), open circles (for Chapter 2) or stars (for the sample from TVPHW). Overplotted is the SPS model of KA97 in the upper right panel; in the remaining panels we plot BC98's model. Note that the lower right panel is labelled with the average age of the stellar population $\langle A \rangle$; the remaining panels are labelled with the star formation timescale τ. In the upper panels we show a dust reddening vector assuming that dust is distributed in a foreground screen, and in the lower panels we show two absorption reddening vectors from the analytical treatment of DDP and Evans (1994).

These figures clearly reiterate the conclusions of Chapter 2 and dJIV, where it was found that colour gradients were common in all types of spiral discs. Furthermore, these colour gradients are, for the most part, consistent with gradients in mean stellar age. The effects of dust reddening may also play a rôle; however, dust is unlikely to produce such a large colour gradient: see section 3.5.4 and e.g. Kuchinski et al. (1998) for a more detailed justification.

A notable exception to this trend are the relatively faint S0 galaxies from the sample of TVPHW (see Fig. 3.2). These galaxies show a strong metallicity gradient, and an inverse age gradient, in that *the outer regions of the galaxy appear older and more metal poor* than the younger and more metal rich central regions of the galaxy. This conclusion is consistent with the results from studies of line strength gradients: Kuntschner (1998) finds that many of the fainter S0s in his sample have a relatively young and metal rich nucleus, with older and more metal poor outer regions.

Also, in Fig. 3.2, we find that there is a type dependence in the galaxy age and metallicity, in the sense that later type galaxies are both younger and more metal poor than their earlier

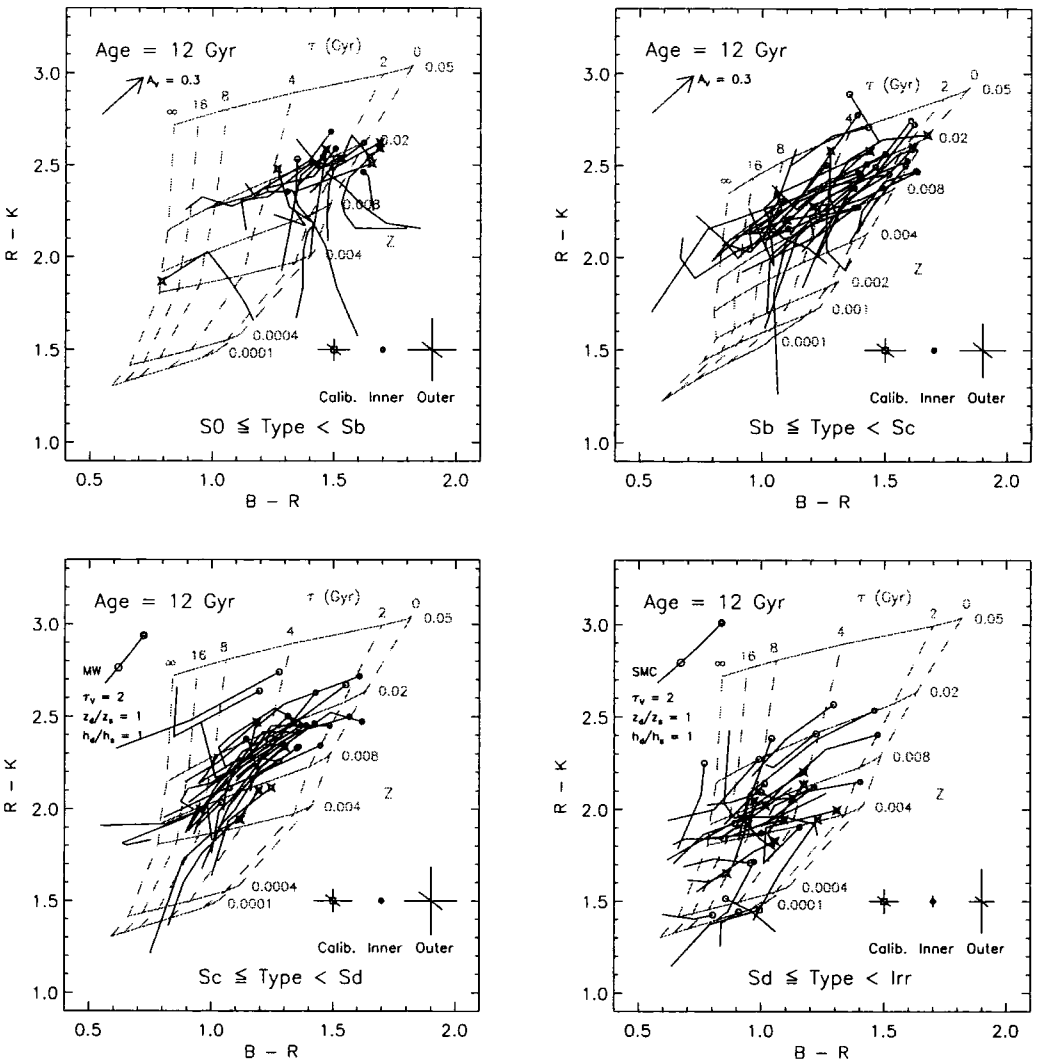

Figure 3.2: Trends in optical–near-IR colour with morphological type. We plot $B-R$ against $R-K$ colours for those galaxies with photometry in B, R and K (92 per cent of the sample; solid lines). Central colours are denoted by solid circles (for the sample from dJIV), open circles (for the sample from Chapter 2) or stars (for the sample from TVPHW). Overplotted are the KA97 (upper right panel) and BC98 (remaining panels) stellar population models. Note that the lower right panel is labelled with the average age of the stellar population $\langle A \rangle$; the remaining panels are labelled with the star formation timescale τ. We also show the calibration uncertainties and the sky subtraction uncertainties in the inner and outer annuli: the diagonal lines in these error bars represent the effect of a 1σ shift in the R band photometry. Overplotted also are the foreground screen (upper panels) and Triplex model (lower panels) dust models. In the Triplex model, the solid circle denotes the central reddening, and the open circle the reddening at the half light radius. Further discussion of the data and model grids is undertaken in the text.

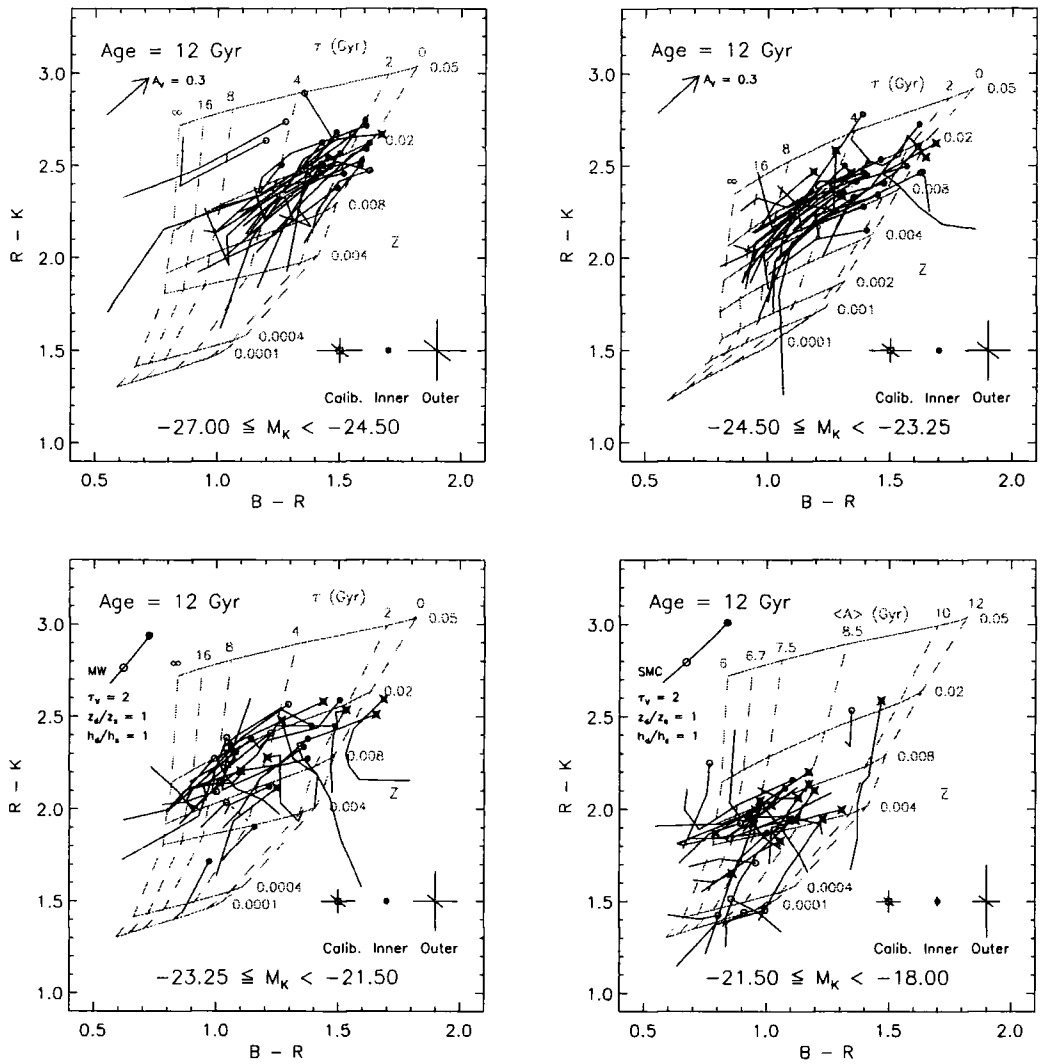

Figure 3.3: Trends in optical–near-IR colour with K band magnitude. The symbols are as in Fig. 3.2. The two sets of colours for UGC 334 from dJIV and Chapter 2 are also shown, connected by a dotted line.

type counterparts. This is partially consistent with dJIV, who finds that later type spirals have predominantly lower stellar metallicity (but he finds no significant trends in mean age with galaxy type).

In Figs. 3.3 to 3.6 we explore the differences in SFH as a function of the physical parameters of our sample galaxies. Figure 3.5 suggests there is little correlation between galaxy scale length and SFH: there may be a weak correlation in the sense that there are very few young and metal poor large scale length galaxies. In contrast, when taken together, Figs. 3.3, 3.4 and 3.6 suggest that there are real correlations between the SFHs of spiral galaxies (as probed by the ages and

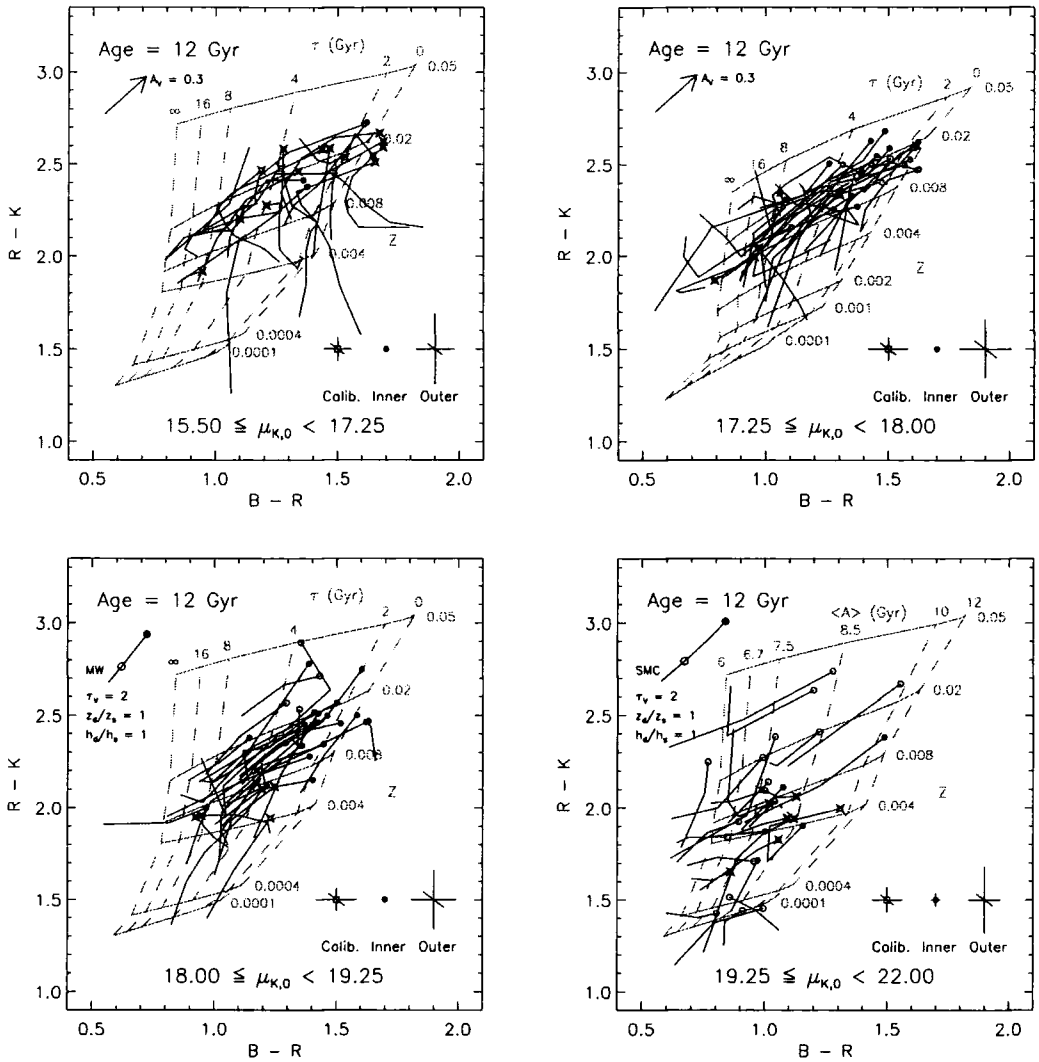

Figure 3.4: Trends in optical–near-IR colour with K band central surface brightness. The symbols are as in Fig. 3.2. The two sets of colours for UGC 334 from dJIV and Chapter 2 are also shown, connected by a dotted line.

metallicities) and the magnitudes, central surface brightnesses and gas fractions of galaxies in the sense that brighter, higher surface brightness galaxies with lower gas fractions tend to be older and more metal rich than fainter, lower surface brightness galaxies with larger gas fractions. Later, we will see these trends more clearly in terms of average ages and metallicities, but it is useful to bear in mind these colour-colour plots when considering the trends presented in the remainder of this section.

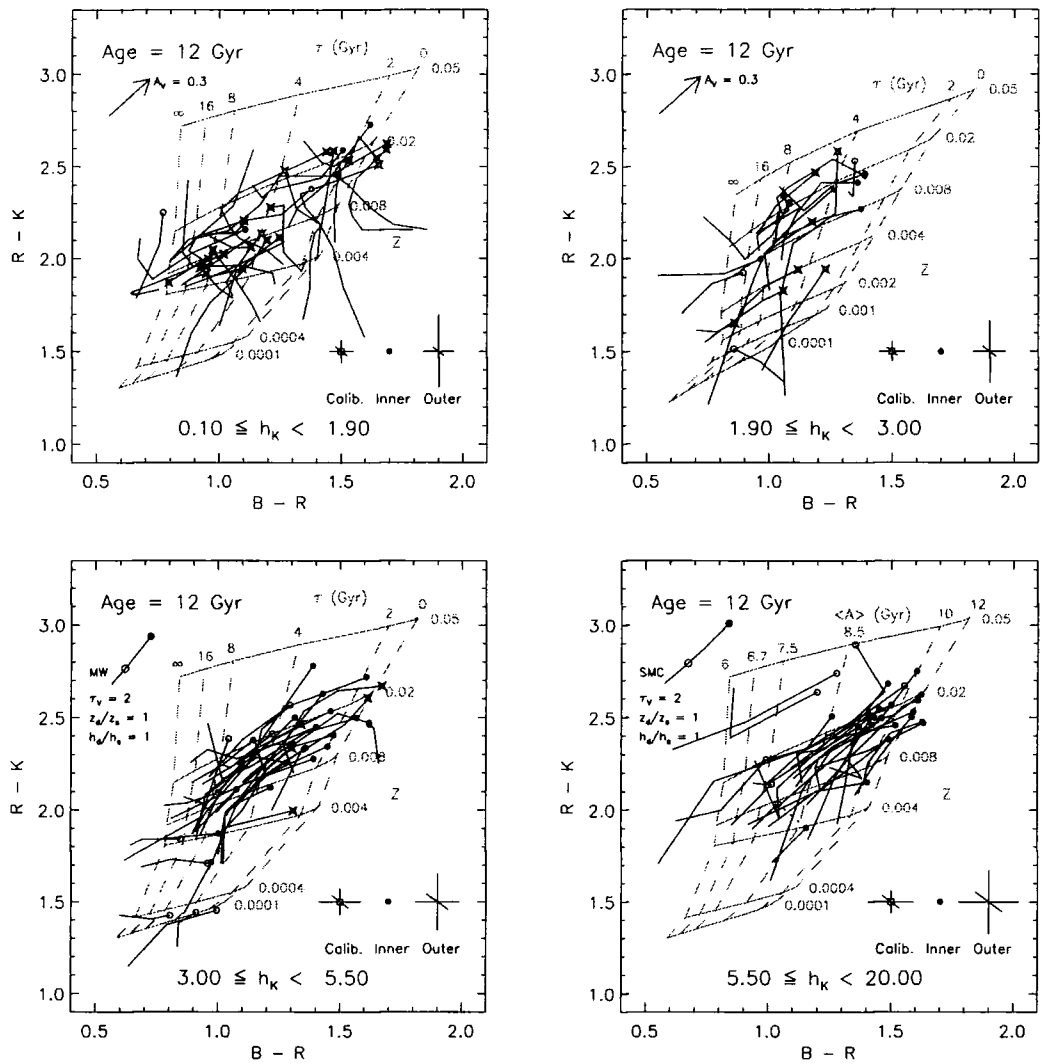

Figure 3.5: Trends in optical–near-IR colour with K band disc scale length in kpc. The symbols are as in Fig. 3.2. The two sets of colours for UGC 334 from dJIV and Chapter 2 are also shown, connected by a dotted line.

3.4.2 Local ages and metallicities

We investigate the relation between the average ages and metallicities inferred from the colours of each galaxy annulus and the average K band surface brightness in that annulus in Fig. 3.7. Representative error bars from the Monte Carlo simulations are shown in the lower left hand corner of the plots. Strong, statistically significant correlations between local age and the K band surface brightness, and between local metallicity and the K band surface brightness are found. While the scatter is considerable, the existence of such a strong relationship between local K band

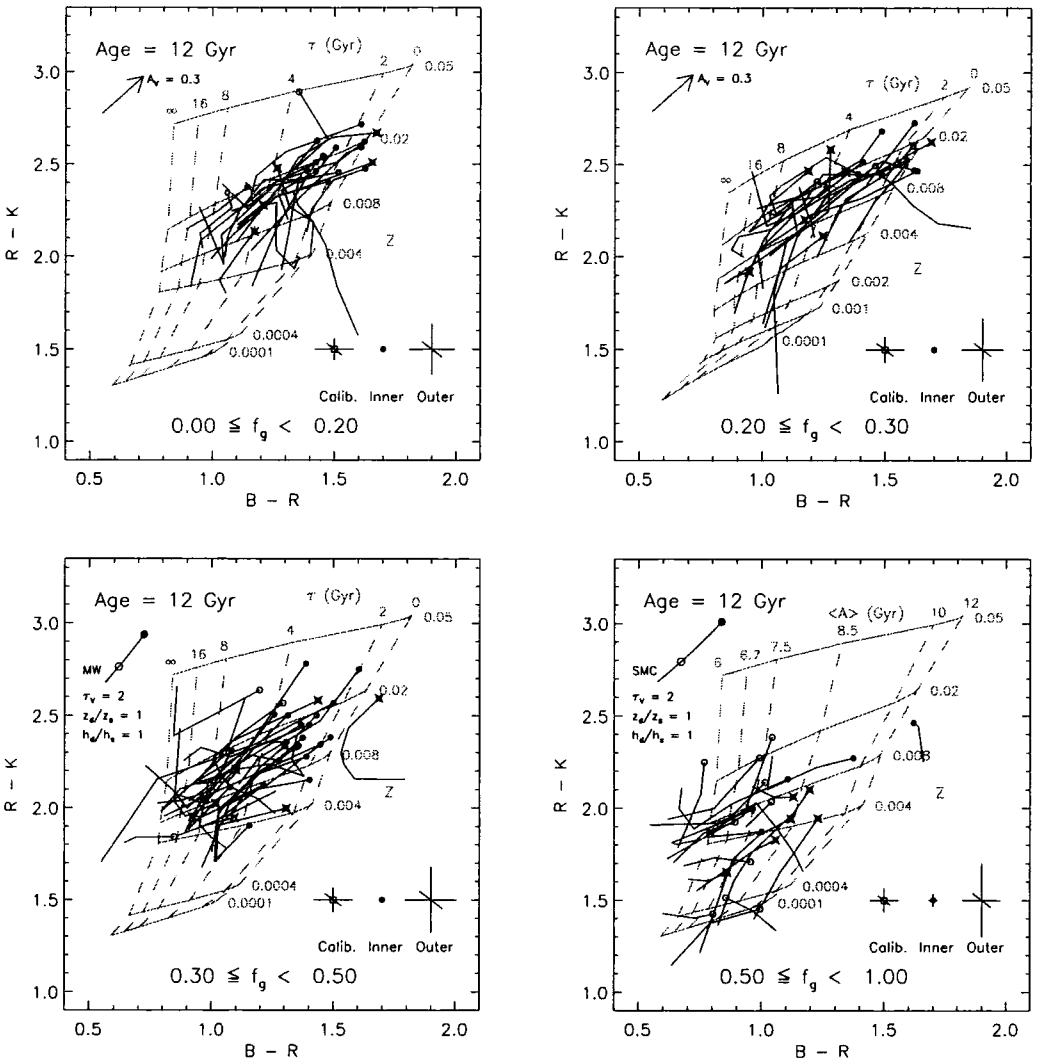

Figure 3.6: Trends in optical–near-IR colour with gas fraction. The symbols are as in Fig. 3.2.

surface brightness and the age and metallicity in that region is remarkable. In order to probe the dependence of the SFH on the structural parameters of our sample, we have carried out *unweighted* least-squares fits of these and subsequent correlations: the results of these fits are outlined in Table 3.1. In Table 3.1 we give the coefficients of the unweighted least-squares fits to the correlations significant at the 99 per cent level (where the significances are determined from a Spearman rank order test), along with errors derived from bootstrap resampling of the data (Press et al. 1986). We will address these correlations further in the next section and in the discussion (section 3.5), where we attempt to relate these strong local correlations with global correlations.

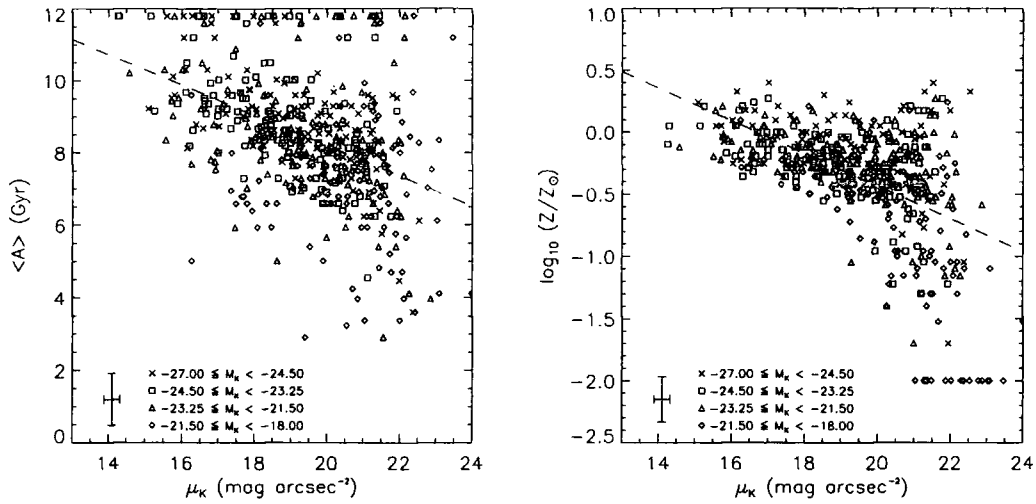

Figure 3.7: Local average age (left) and metallicity (right) against K band surface brightness. The average age $\langle A \rangle$ and metallicity $\log_{10}(Z/Z_\odot)$ of each galaxy annulus is shown against the local average K band surface brightness μ_K. The galaxies are binned by K band absolute magnitude: note that this binning clearly shows the magnitude dependence in the local metallicity–surface brightness correlation. The dashed lines are unweighted least-squares fits to the data: the fits are given in Table 3.1. A significant number of data points have average ages of 11.9 Gyr or metallicities of $\log_{10}(Z/Z_\odot) = -2$: these data points fall outside the model grids.

3.4.3 Global relations

In addition to the individual annulus age and metallicity estimates, we calculated age and metallicity best-fit gradients and intercepts (as described in section 3.3.1). These fit parameters are useful, in that they allow us to probe the *global* relationships between e.g. magnitude and SFH.

These fits to an individual galaxy are parameterised by their gradient (in terms of the inverse K band scale lengths) and their intercept (expressed as the intercept at the disc half light radius R_{eff}). We explore correlations between the structural parameters and the radial age and metallicity fit parameters in Figs. 3.8–3.11.

3.4.3.1 Global ages

In Fig. 3.8, we see how the age intercept at the half light radius relates to the K band surface brightness, K band absolute magnitude, K band disc scale length and gas fraction.

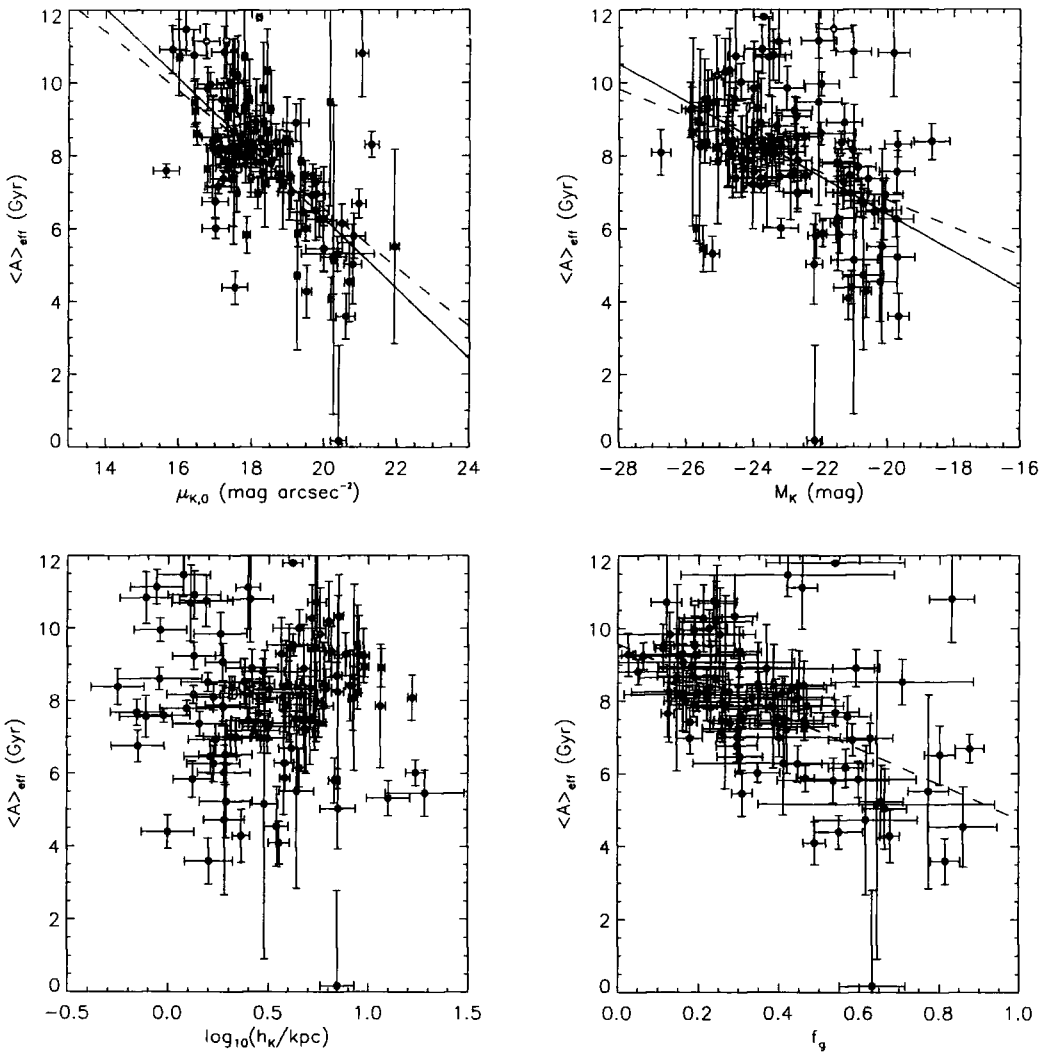

Figure 3.8: Correlations between the average age $\langle A \rangle_{eff}$ at the disc half light radius and the K band central surface brightness $\mu_{K,0}$, K band absolute magnitude M_K, K band disc scale length h_K and gas fraction f_g (see text for the details of the derivation of the gas fractions). In this and subsequent figures error bars denote the estimated 68 per cent confidence intervals, and dashed lines are unweighted least-squares fits to trends significant at greater than the 99 per cent level (see Table 3.1). The solid lines in the top two panels denote the unweighted least-squares fit to the age–magnitude–surface brightness correlation, projected onto the age–surface brightness and age–magnitude planes.

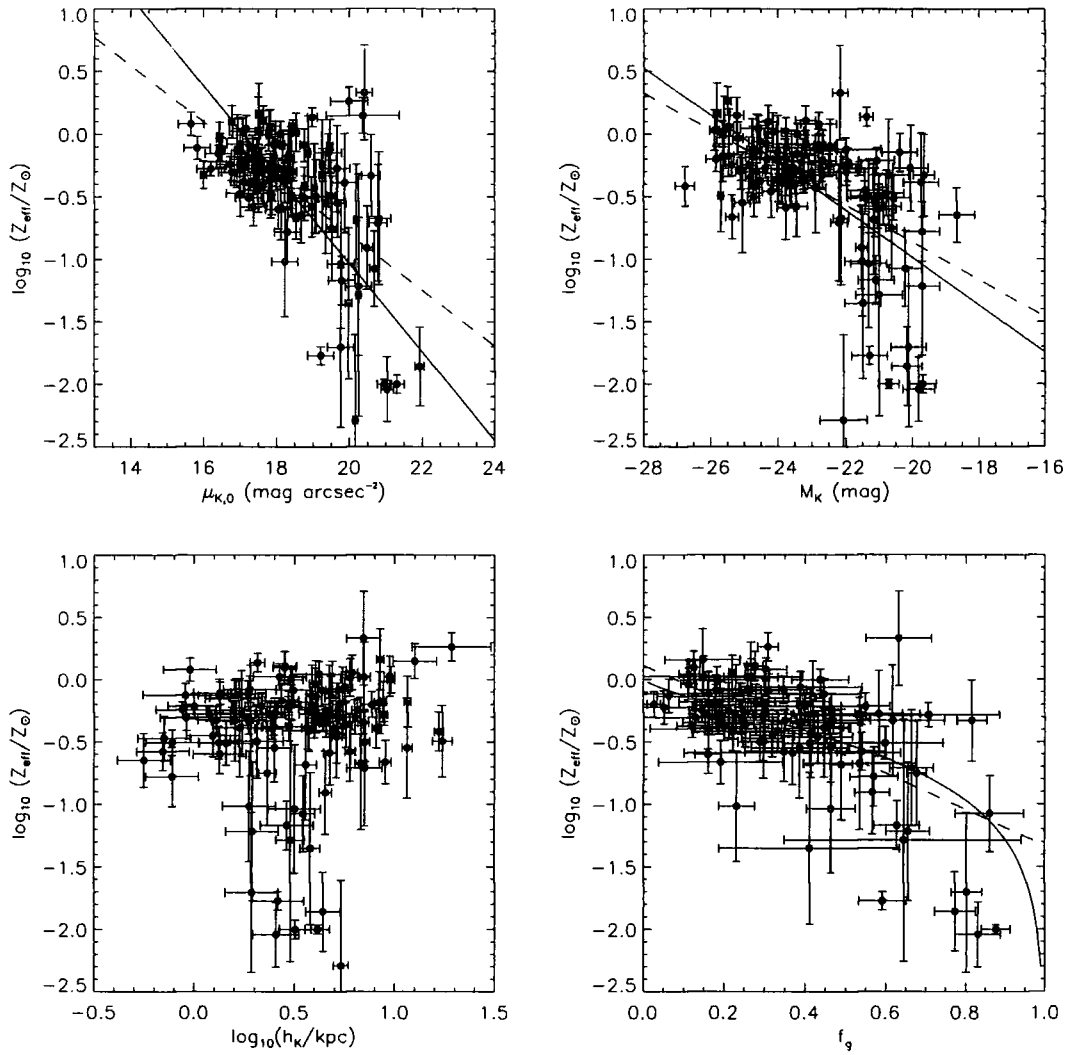

Figure 3.9: Correlations between the average metallicity $\log_{10}(Z_{eff}/Z_{\odot})$ at the disc half light radius and K band central surface brightness, K band absolute magnitude, K band disc scale length and gas fraction. Dashed lines are unweighted least-squares fits to trends significant at greater than the 99 per cent level (see Table 3.1). The solid lines in the top two panels denote the unweighted least-squares fit to the metallicity–magnitude–surface brightness correlation, projected onto the metallicity–surface brightness and metallicity–magnitude planes. The solid line in the lower right panel shows the expectation for the mean stellar metallicity with gas fraction for a closed-box model with a solar metallicity yield.

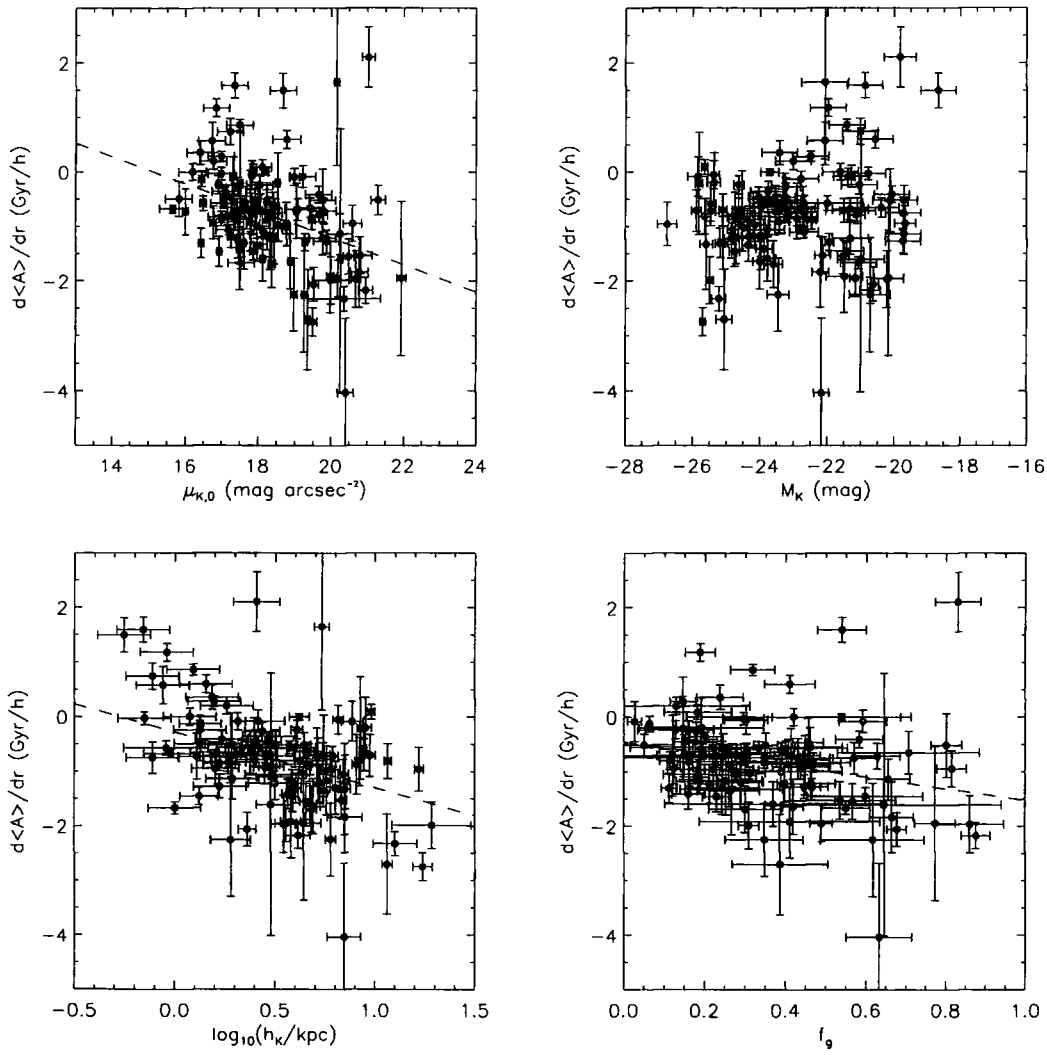

Figure 3.10: Correlations between the average age gradient per K band disc scale length ($d\langle A\rangle/dr$) and the K band central surface brightness, K band absolute magnitude, K band disc scale length and the gas fraction. Dashed lines are unweighted least-squares fits to trends significant at greater than the 99 per cent level (see Table 3.1).

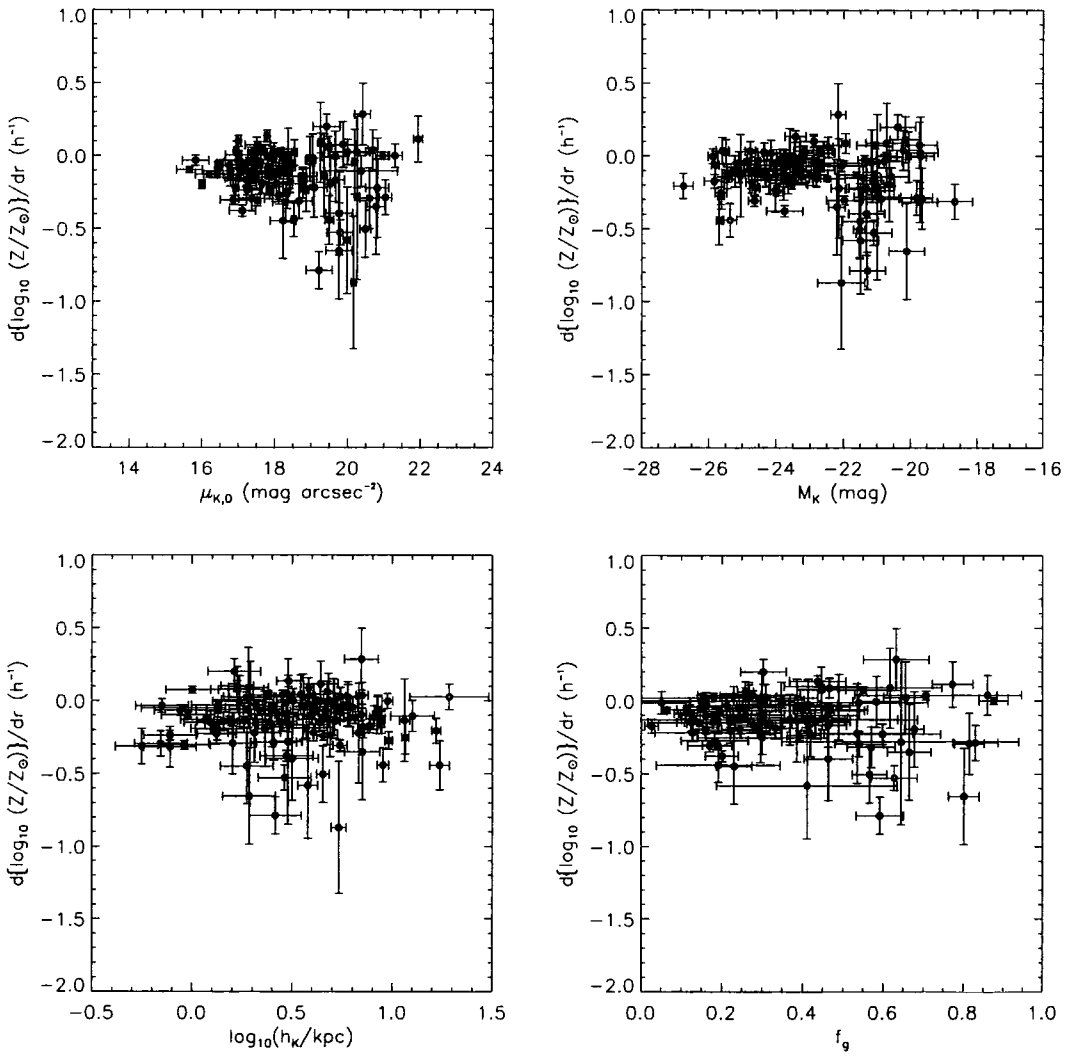

Figure 3.11: Correlations between the average metallicity gradient $d\log_{10}(Z_{eff}/Z_{\odot})/dr$ in terms of the K band disc scale length h_K and the K band central surface brightness, K band absolute magnitude, K band disc scale length and gas fraction.

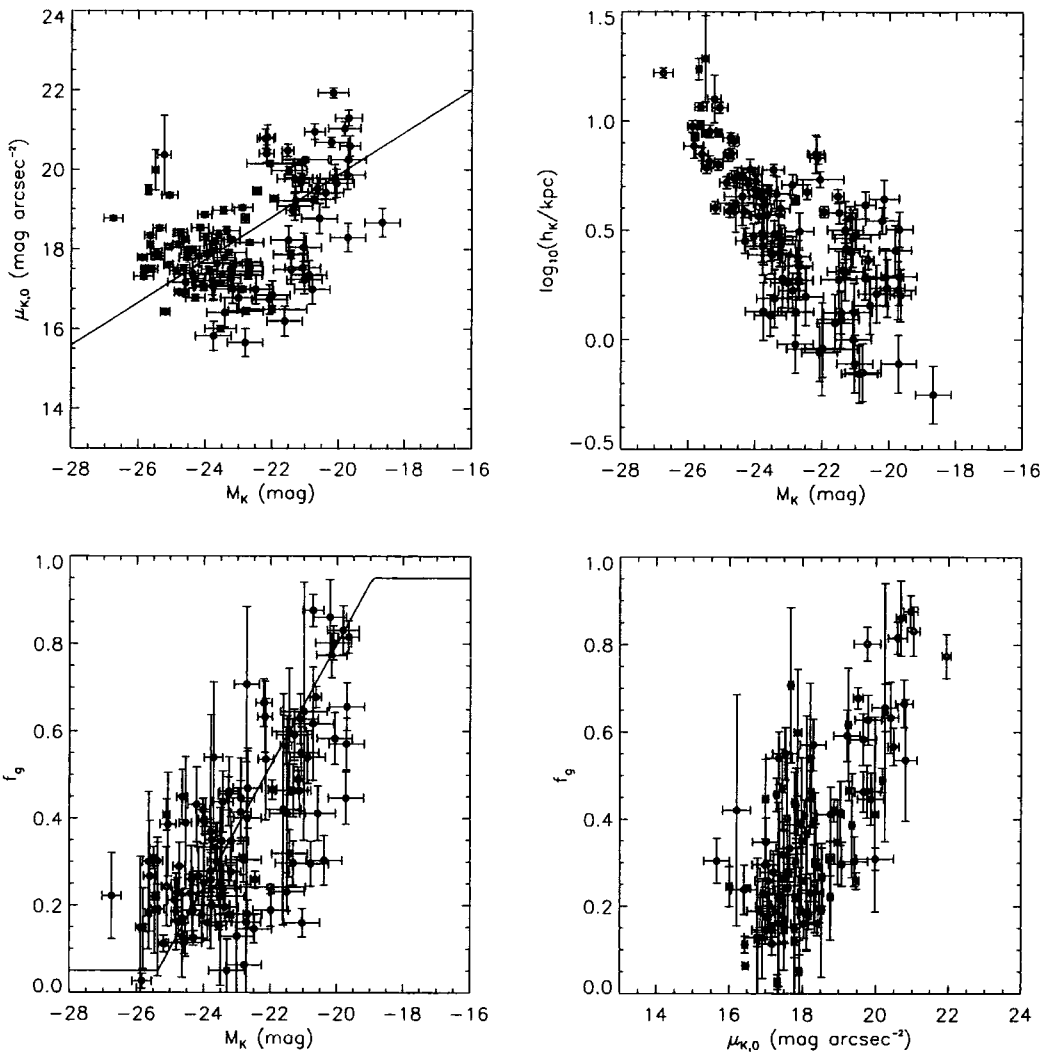

Figure 3.12: Correlation between K magnitudes, K band central surface brightnesses, K band disc scale lengths and gas fractions. Correlations between the physical parameters are important to bear in mind when interpreting the correlations in Figs. 3.8–3.11. The solid line in the upper left panel is the unweighted least-squares bisector fit to the magnitude–central surface brightness correlation. The solid line in the lower left panel is the estimated fit to the gas fraction–magnitude relation (see section 3.5.5).

As expected from the strong correlation between the local surface brightness and age, there is a highly significant correlation between the K band central surface brightness and age. We see also that there are also highly significant correlations between the K band absolute magnitude and age, and the gas fraction and age. There is no significant correlation between age and K band disc scale length.

An important question to ask at this stage is: are these correlations related to each other in some way? We investigate this in Fig. 3.12, where we plot some of the physical parameters against each other. We see that the K band absolute magnitude of this sample is correlated (with large scatter) with the K band central surface brightness. We also see in Fig. 3.12 that the brightest galaxies all have the largest scale lengths. In addition, both magnitude and surface brightness correlate strongly with the gas fraction. From these correlations, we can see that all of the three correlations between age and central surface brightness, magnitude and gas fraction may have a common origin: the correlation between these three physical parameters means that it is difficult, using Fig. 3.8 alone, to determine which parameters age is sensitive to. We do feel, however, that the correlations between age and surface brightness and age and magnitude do not stem from the correlation between age and gas fraction for two reasons. Firstly, the scatter in the age–gas fraction relationship is comparable to or even larger than the age–surface brightness and age–magnitude correlations. Secondly, the gas fraction is an indication of the total amount of star formation over the history of a galaxy (assuming that there is little late gas infall), implying that the gas fraction is quite dependent on the SFH. Therefore, correlations between SFH and gas fraction are likely to be driven by this effect, rather than indicating that gas fraction drives SFH.

To summarise Figs. 3.8 and 3.12, the age of a galaxy is correlated strongly with the K band surface brightness, K band absolute magnitude and the gas fraction. We discuss these important correlations further in section 3.5.1.

3.4.3.2 Global metallicities

In Fig. 3.9, we see how the metallicity intercept at the disc half light radius relates to the K band surface brightness, K band absolute magnitude, K band disc scale length and gas fraction.

The trends shown in Fig. 3.9 are similar to those seen in Fig. 3.8: this demonstrates the close correlation between the age and metallicity of a galaxy, in the sense that older galaxies are typically much more metal rich than their younger brethren. However, there are some important differences between the two sets of correlations.

Firstly, although the correlation is not statistically significant, there is a conspicuous lack of galaxies with large scale lengths and low metallicities. This lack of large, metal poor galaxies can be understood from the relationship between magnitude and scale length in Fig. 3.12: large galaxies, because of their size, are bright by default (even if they have low surface brightnesses; Chapter 2) and have near-solar metallicities.

Secondly, there seems to be a kind of 'saturation' in the stellar metallicities that was not apparent for the mean ages. It is particularly apparent in the correlation between the metallicity and K band absolute magnitude: the metallicity of galaxies with an absolute K band magnitude of -22 is very similar to the metallicity of galaxies that are nearly 40 times brighter, with an absolute K band magnitude of -26. The metallicity of galaxies fainter than an absolute K band magnitude of -22 can be much lower, to the point where the metallicities are too low to be included reliably on the stellar population model grid. This 'saturation' is easily understood in terms of the gas fractions: the near-solar metallicity galaxies tend to have gas fractions $\lesssim 0.5$. In this case, assuming a closed box model of chemical evolution (i.e. no gas flows into or out of the galaxy, and the metals in the galaxy are well-mixed) , the stellar metallicity will be within 0.5 dex of the yield (see Pagel 1998 and references therein), which in this case would indicate a yield around, or just above, solar metallicity. This case is shown in the lower right panel of Fig. 3.9 (also Fig. 3.16), where we show the stellar metallicity of a solar metallicity yield closed box model against the gas fraction. Note that the gas metallicity in the closed box model continues to rise to very low gas fractions: this will become important later when we compare the stellar metallicity–luminosity relation from this work with the gas metallicity–luminosity relation (section 3.5.5).

3.4.3.3 Age gradients

In Fig. 3.10, we see how the age gradient (per K band disc scale length) relates to the K band surface brightness, K band absolute magnitude, K band disc scale length and gas fraction.

An important first result is that, on average, we have a strong detection of an overall age gradient: the average age gradient per K band disc scale length is -0.79 ± 0.08 Gyr h^{-1} (10σ; where the quoted error is the error in the mean gradient).

We see that the age gradient does not correlate with the K band absolute magnitude. However, there are statistically significant correlations between the age gradient and K band central surface brightness, K band disc scale length and gas fraction. Smaller galaxies, higher surface brightness galaxies and low gas fraction galaxies all tend to have relatively flat age gradients (with much scatter, that almost exceeds the amplitude of the trend).

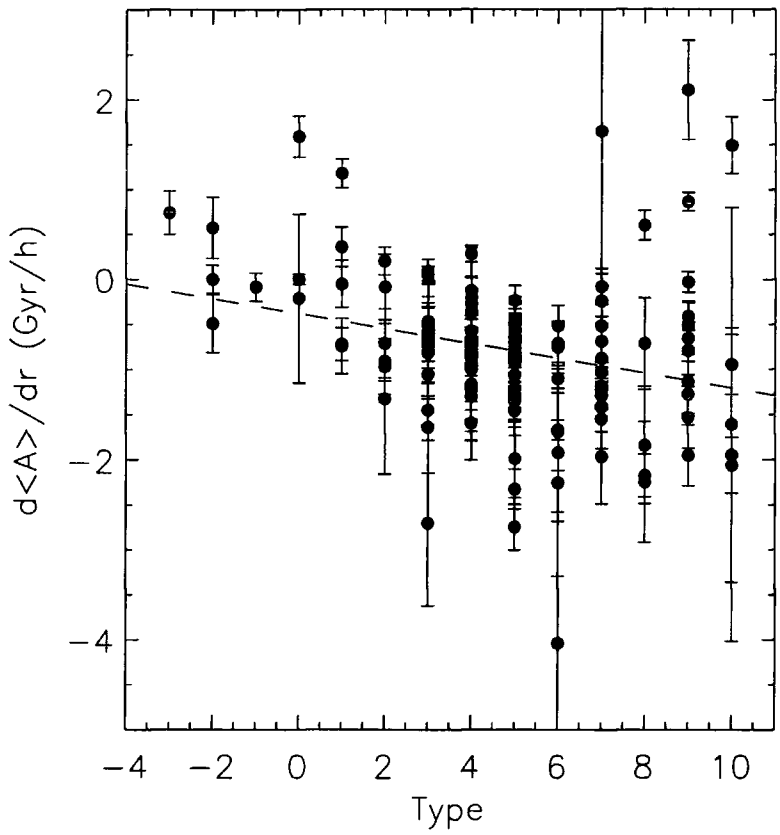

Figure 3.13: Correlations between galaxy type and age gradient. The x-axis is the T-type, where types between −3 and 0 correspond to S0s, and types 1 through 10 correspond to a smooth sequence from Sa to Im. The dashed line is the unweighted least-squares fit to the data.

One possibility is that the S0s with 'inverse' age gradients (in the sense that their central regions were younger than their outer regions) are producing these trends, as the S0s in this sample are relatively faint (therefore not producing much of a trend in age gradient with magnitude) but have high surface brightness, small sizes and low gas fractions (therefore producing trends in all of the other physical parameters).

We investigate this possibility in Fig. 3.13. Here we see that the trend is not simply due to 'contamination' from a small population of S0s: S0s contribute to a more general trend of decreasing age gradients for earlier galaxy types. Therefore, this decrease in age gradient is a real effect. We address a possible cause for this phenomenon later in section 3.5.6.

3.4.3.4 Metallicity gradients

In Fig. 3.11, we see how the metallicity gradient (per K band disc scale length) relates to the K band surface brightness, K band absolute magnitude, K band disc scale length and gas fraction. The metallicity gradient is fairly poorly determined because of its typically smaller amplitude, and sensitivity to the rather noisier near-IR colours. Also, because of its smaller amplitude, metallicity gradients are more susceptible to the effects of dust reddening than were the rather larger age gradients. On average (assuming that the effects of dust are negligible), we have detected an overall metallicity gradient (although with much scatter): the average metallicity gradient per K band disc scale length is -0.14 ± 0.02 dex h^{-1} (7σ; where again the quoted error is the error in the mean gradient). Due to the large observational scatter, however, we have failed to detect any trends in metallicity gradient with galaxy properties.

3.5 Discussion

3.5.1 Surface brightness vs. magnitude

In the previous section, we presented a wide range of correlations between diagnostics of the SFH and the physical parameters that describe a spiral galaxy. Our main finding was that the SFH of a galaxy correlates well with both the K band absolute magnitude and K band surface brightness. However, this leaves us in an uncomfortable position: because of the surface brightness–magnitude correlation in our dataset (Fig. 3.12), it is impossible to tell from Figs. 3.8, 3.9 and 3.12 alone what parameter is more important in determining the SFH of a galaxy.

One straightforward way to investigate which parameter is more important is by checking if the offset of a galaxy from e.g. the age–magnitude correlation of Fig. 3.8 correlates with surface brightness.

In the upper panels of Fig. 3.14, we show the residuals from the age–surface brightness correlation and the metallicity–surface brightness correlation against magnitude. Age residual does not significantly correlate with magnitude (the correlation is significant at only the 97 per cent level and is not shown). Metallicity residuals are significantly correlated with the magnitude, where brighter galaxies tend to be more metal rich than expected from their surface brightness alone.

In the lower panels of Fig. 3.14, we show the residuals from the age–magnitude correlation and the metallicity–magnitude correlation. In contrast to the upper panels of this figure, there are highly significant correlations between the age residual and surface brightness, and the metallicity residual and surface brightness.

Table 3.1. Unweighted least-squares fits for the statistically significant correlations (with significance > 99 per cent) between SFH and galaxy structural parameters presented in Figs. 3.7–3.11 and 3.13–3.15.

X	Y	Slope	Intercept
μ_K	$\langle A \rangle$ (Gyr)	−0.42±0.04	8.20±0.07
μ_K	$\log_{10}(Z/Z_\odot)$	−0.132±0.011	−0.43±0.03
$\mu_{K,0}$	$\langle A \rangle_{eff}$ (Gyr)	−0.81±0.14	6.6±0.3
M_K	$\langle A \rangle_{eff}$ (Gyr)	−0.38±0.09	6.8±0.3
f_g	$\langle A \rangle_{eff}$ (Gyr)	−4.8±1.0	9.6±0.3
$\mu_{K,0}$	$\log_{10}(Z_{eff}/Z_\odot)$	−0.22±0.04	−0.80±0.09
M_K	$\log_{10}(Z_{eff}/Z_\odot)$	−0.15±0.02	−0.86±0.09
f_g	$\log_{10}(Z_{eff}/Z_\odot)$	−1.4±0.3	0.12±0.08
$\mu_{K,0}$	$d\langle A \rangle/dr$ (Gyr/h)	−0.25±0.07	−1.2±0.2
$\log_{10}(h_K)$	$d\langle A \rangle/dr$ (Gyr/h)	−1.0±0.3	−0.30±0.15
f_g	$d\langle A \rangle/dr$ (Gyr/h)	−1.1±0.5	−0.5±0.2
Type	$d\langle A \rangle/dr$ (Gyr/h)	−0.08±0.03	−0.38±0.16
M_K	$\log_{10}(Z_{eff}/Z_\odot) - \log_{10}(Z_\mu/Z_\odot)$	-0.08±0.02	-0.22±0.07
$\mu_{K,0}$	$\langle A \rangle_{eff} - \langle A \rangle_M$ (Gyr)	-0.60±0.15	-0.9±0.3
$\mu_{K,0}$	$\log_{10}(Z_{eff}/Z_\odot) - \log_{10}(Z_M/Z_\odot)$	-0.13±0.03	-0.22±0.08
Modified $\mu_{K,0}$	$\langle A \rangle_{eff}$ (Gyr)	-0.9±0.2	5.7±0.5
Modified M_K	$\langle A \rangle_{eff}$ (Gyr)	-0.52±0.09	6.0±0.4
Modified $\mu_{K,0}$	$\log_{10}(Z_{eff}/Z_\odot)$	-0.21±0.05	-0.9±0.1
Modified M_K	$\log_{10}(Z_{eff}/Z_\odot)$	-0.14±0.03	-0.9±0.1

Surface brightness intercepts are quoted at a K band surface brightness of 20 mag arcsec^{-2}.

Absolute magnitude intercepts are quoted at a K band absolute magnitude of −20.

Another way to consider the above is to investigate the distribution of galaxies in the three dimensional age–magnitude–surface brightness and metallicity–magnitude–surface brightness spaces. Unweighted least-squares fits of the age and metallicity as a function of surface brightness and magnitude yield the surfaces:

$$\langle A \rangle_{eff} = 6.24(\pm 0.14) - 0.71(\pm 0.06)(\mu_{K,0} - 20) - 0.15(\pm 0.03)(M_K + 20), \tag{3.8}$$

and

$$\log_{10}(Z_{eff}/Z_\odot) = -0.99(\pm 0.05) - 0.17(\pm 0.01)(\mu_{K,0} - 20) - 0.10(\pm 0.01)(M_K + 20) \tag{3.9}$$

where the quoted errors (in brackets) are derived using bootstrap resampling of the data and the intercept is defined at $\mu_{K,0} = 20$ mag arcsec^{-2} and $M_K = -20$. A best fit line to the dataset is

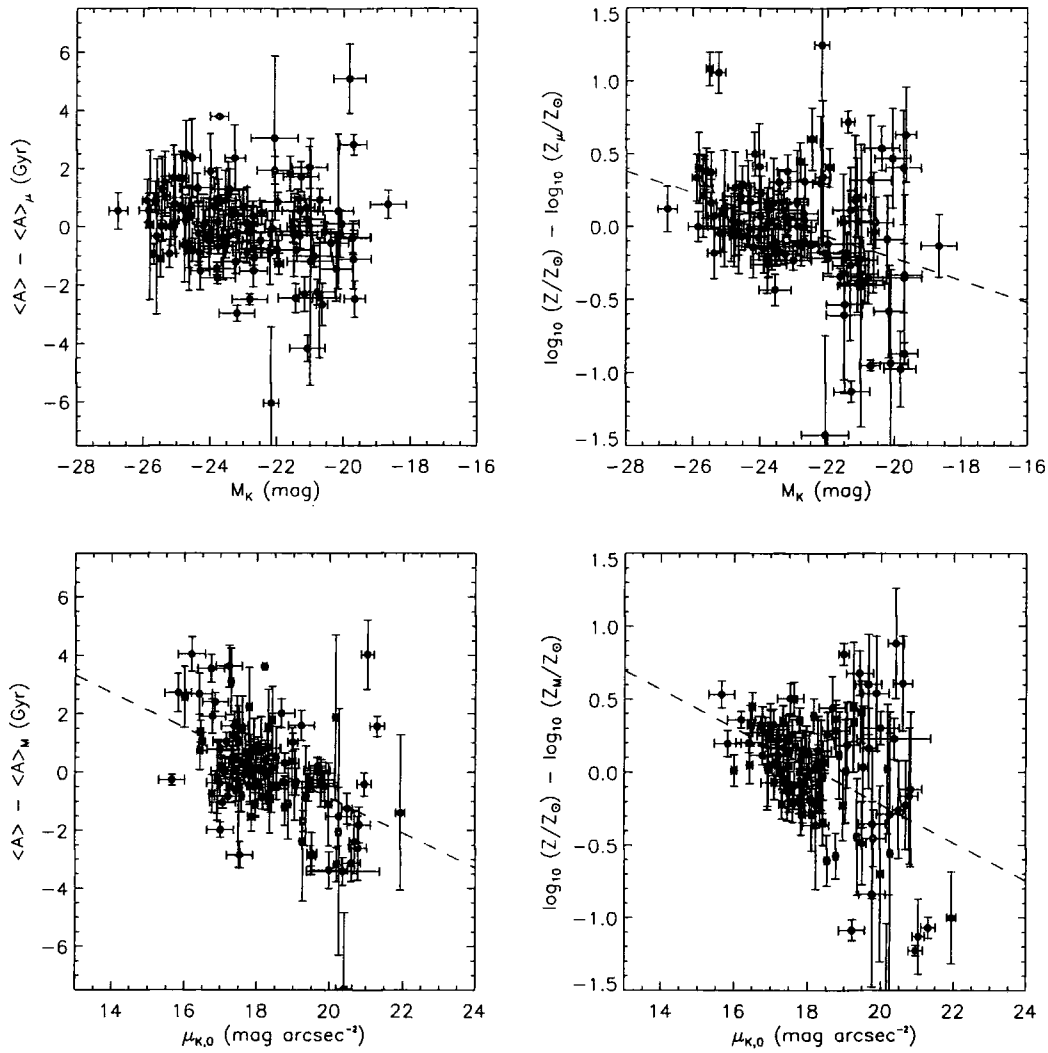

Figure 3.14: The top two panels show the residuals from the age–surface brightness correlation of Fig. 3.8 and the metallicity–surface brightness correlation of Fig. 3.9 against K band absolute magnitude. The lower two panels show the residuals from the age–magnitude correlation of Fig. 3.8 and the metallicity–magnitude correlation of Fig. 3.9 against K band central surface brightness. Dashed lines are unweighted least-squares fits to trends significant at greater than the 99 per cent level (see Table 3.1).

shown in Figs. 3.8 and 3.9. This best fit line is defined by the intersection of the best-fit plane with the least-squares bisector fit (where each variable is treated equally in the fit; Isobe et al. 1990) of the magnitude–surface brightness correlation (Fig. 3.12): $M_K = -19.75 + 1.88(\mu_{K,0} - 20)$. No plots of the distribution of galaxies in these three-dimensional spaces are shown: the two-dimensional projections of this space in Figs. 3.8, 3.9 and 3.12 are among the best projections of this three-dimensional space.

From the above fits, we can see quite clearly that age is primarily sensitive to central surface brightness: the change in average age per magnitude change in central surface brightness is much larger than change in age per magnitude change in luminosity. The stellar metallicity of a galaxy is sensitive to both surface brightness and magnitude: this is clear from the fairly comparable change in metallicity per magnitude change in surface brightness or luminosity.

We have also analysed the residuals from the age–local K band surface brightness and metallicity–local K band surface brightness correlations as a function of central K band surface brightness and K band absolute magnitude (Fig. 3.7). *The age of an annulus in a galaxy primarily correlates with its local K band surface brightness* and correlates to a lesser extent with the galaxy's K band central surface brightness and magnitude. *The metallicity of a galaxy annulus correlates equally well with both the local K band surface brightness and total galaxy magnitude* and only very weakly with the central K band surface brightness. Thus, the results from the analysis of local ages and metallicities are consistent with the analysis of the global correlations: much (but not all) of the variation that was attributed to the *central* surface brightness in the global analysis is driven by the *local* surface brightness in the local analysis. Note that it is impossible to tell whether it is the global correlations that drive the local correlations, or vice versa. The local K band surface brightnesses (obviously) correlate with the central K band surface brightnesses, meaning that it is practically impossible to disentangle the effects of local and global surface brightnesses.

However, there must be other factors at play in determining the SFH of spiral galaxies: the local and global age and metallicity residuals (once all the above trends have been removed) show a scatter around 1.4 times larger than the (typically quite generous) observational errors, indicating cosmic scatter equivalent to $\sim$ 1 Gyr in age and $\sim$ 0.2 dex in metallicity. This scatter is intrinsic to the galaxies themselves and *must* be explained in any model that hopes to accurately describe the driving forces behind the SFHs of spiral galaxies. However, note that some or all of this scatter may be due to the influence of small bursts of star formation on the colours of galaxies.

To summarise, *K band surface brightness (in either its local or global form) is the most important 'predictor' of the the SFH of a galaxy*: the effects of K band absolute magnitude modulate the overall trend defined by surface brightness. Furthermore, it is apparent that the metallicity of a galaxy depends more sensitively on its K band magnitude than does the age: this point is discussed later in section 3.5.6. On top of these overall trends, there is an intrinsic scatter, indicating that the surface brightness and magnitude cannot be the only parameters describing the SFH of a galaxy.

3.5.2 Star formation histories in terms of masses and densities

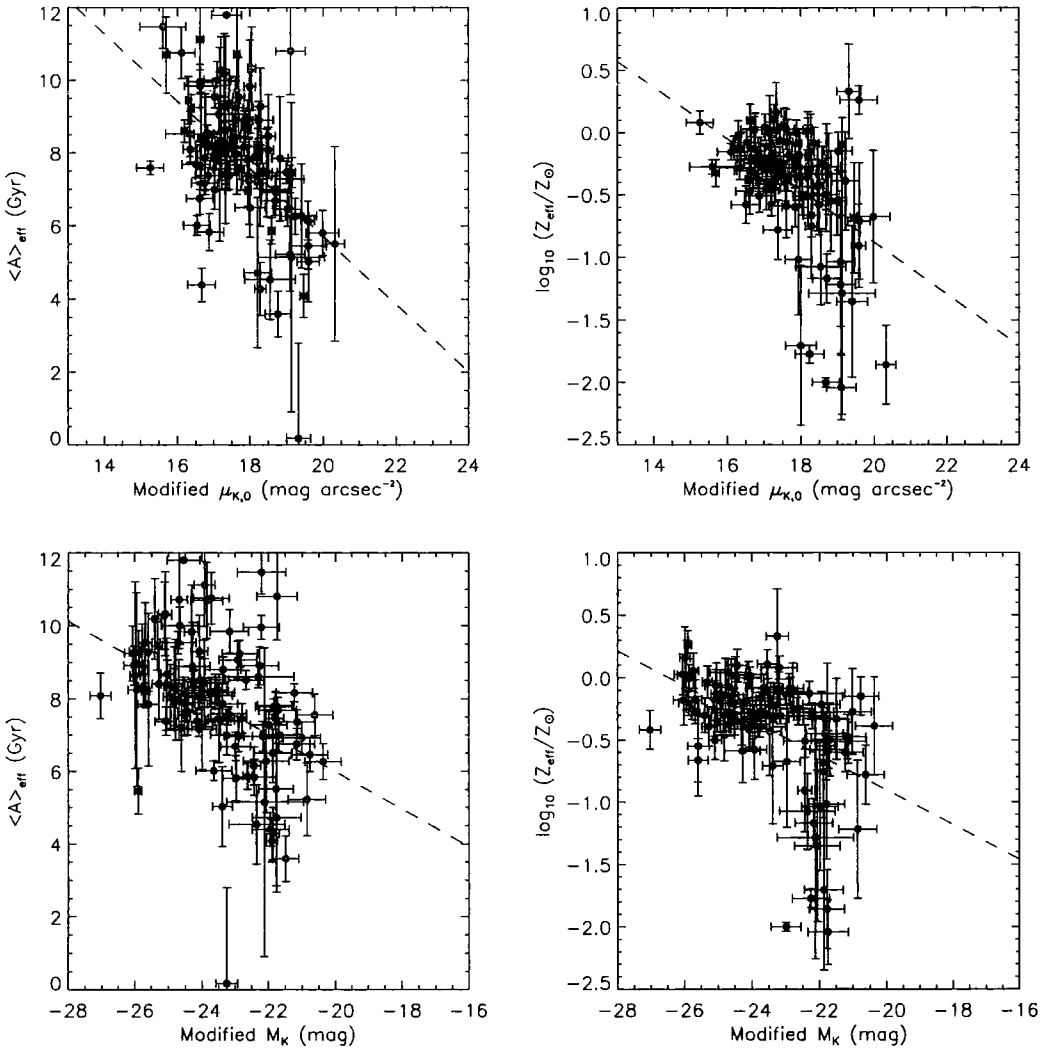

Figure 3.15: Correlations between the average age and metallicity at the disc half light radius and the modified K band central surface brightness and absolute magnitudes. The surface brightnesses and absolute magnitude are modified to approximate *total* baryonic densities and masses, by turning the gas fraction of the galaxies into stars with a K band mass to light ratio of 0.6 $M_{\odot}/L_{\odot}$. Dashed lines are unweighted least-squares fits to trends significant at greater than the 99 per cent level (see Table 3.1).

In the above, we have seen how age and metallicity vary as a function of K band surface brightness and K band absolute magnitude. K band stellar mass to light ratios are expected to be relatively insensitive to differences in stellar populations (compared to optical passbands; e.g.

dJIV). Therefore, the variation of SFH with K band surface brightness and absolute magnitude is likely to approximately represent variations in SFH with stellar surface density and stellar mass (especially over the dynamic range in surface brightness and magnitude considered in this Chapter).

However, these trends with K band surface brightness and K band absolute magnitude may not accurately represent the variation of SFH with *total* (baryonic) surface density or mass (c.f. Chapter 2): in order to take that into account, we must somehow account for the gas fraction of the galaxy. Accordingly, we have constructed 'modified' K band surface brightnesses and magnitudes by adding $2.5\log_{10}(1 - f_g)$ (c.f. Chapter 2). This correction, in essence, converts all of the gas fraction (both the measured atomic gas fraction, and the much more uncertain molecular gas fraction) into stars with a constant stellar mass to light ratio in K band of 0.6 $M_\odot/L_\odot$.

In this correction, we make two main assumptions. Firstly, we assume a constant K band stellar mass to light ratio of 0.6 $M_\odot/L_\odot$. This might not be such an inaccurate assumption: the K band mass to light ratio is expected to be relatively robust to the presence of young stellar populations; however, our assumption of a constant K band mass to light ratio is still a crude assumption and should be treated with caution. Note, however, that the relative trends in Fig. 3.15 are quite robust to changes in stellar mass to light ratio: as the stellar mass to light ratio increases, the modified magnitudes and surface brightnesses creep closer to their unmodified values asymptotically.

Secondly, the correction to the surface brightness implicitly assumes that the gas will turn into stars with the same spatial distribution as the present-day stellar component. This is quite a poor assumption as the gas distribution is usually much more extended than the stellar distribution: this would imply that the corrections to the central surface brightnesses are likely to be overestimates. However, our purpose here is not to construct accurate measures of the baryonic masses and densities of disc galaxies; our purpose is merely to try to construct some kind of representative mass and density which will allow us to determine if the trends in SFH with K band magnitude and surface brightness reflect an underlying, more physically meaningful trend in SFH with mass and density.

In Fig. 3.15 we show the trends in age at the disc half light radius (left hand panels) and metallicity at the disc half light radius (right hand panels) with modified K band central surface brightness (upper panels) and modified K band magnitude (lower panels). *It is clear that the trends in SFH with K band surface brightness and absolute magnitude presented in Figs. 3.8 and 3.9 represent an underlying trend in SFH with the total baryonic galaxy densities and masses.* The best fit slopes are typically slightly steeper than those for the unmodified magnitudes and surface brightnesses

(Table 3.1): because low surface brightness and/or faint galaxies are gas-rich, correcting them for the contributions from their gas fractions tends to steepen the correlations somewhat. We have also attempted to disentangle surface density and mass dependencies in the SFH using the method described above in section 3.5.1: again, we find that surface density is the dominant parameter in determining the SFH of a galaxy, and that the mass of a galaxy has a secondary, modulating effect on the SFH.

3.5.3 Does the choice of IMF and SPS model affect our conclusions?

We have derived the above conclusions using a Salpeter (1955) IMF and the BC98 models, but are our conclusions affected by SPS model details such as IMF, or the choice of model? We address this possible source of systematic uncertainty in Table 3.2, where we compare the results for the correlation between the K band central surface brightness $\mu_{K,0}$ and age intercept at the disc half light radius $\langle A \rangle_{eff}$ using the models of BC98 with the IMF adopted by Kennicutt (1983) and the models of KA97 with a Salpeter IMF.

Table 3.2. Unweighted least-squares fits for the correlation between the K band central surface brightness $\mu_{K,0}$ and age intercept at the half light radius $\langle A \rangle_{eff}$ using different SPS models and IMFs.

Model	IMF	Slope	Intercept
BC98	Salpeter	-0.81 ± 0.14	6.6 ± 0.3
BC98	Kennicutt	-0.93 ± 0.14	6.2 ± 0.3
KA97	Salpeter	-0.82 ± 0.12	6.1 ± 0.3

The intercept is quoted at a K band central surface brightness of 20 mag arcsec^{-2}.

From Table 3.2, it is apparent that our results are quite robust to changes in both the stellar IMF and SPS model used to interpret the data. In none of the cases does the significance of the correlation vary by a significant amount, and the slope and intercept of the correlation varies within its estimated bootstrap resampling errors. This correlation is not exceptional; other correlations show similar behaviour, with little variation for plausible changes in IMF and SPS model. In conclusion, while plausible changes in the IMF and SPS model will change the details of the correlations (e.g. the gradients, intercepts, etc.), the existence of the correlations themselves is very robust to changes in the models used to derive the SFHs.

3.5.4 How important is dust extinction?

Our results account for average age and metallicity effects only; however, from Figs. 3.2–3.6 it is clear that dust reddening can cause colour changes similar to those caused by age or metallicity. In this section, we discuss the colour changes caused by dust reddening. We conclude that dust reddening will mainly affect the metallicity (and to a lesser extent age) gradients: however, the magnitude of dust effects is likely to be too small to significantly affect our conclusions.

In Figs. 3.2–3.6, we show the reddening vectors for two different dust models (Milky Way and Small Magellanic Cloud dust models) and for two different reddening geometries (a simple foreground screen model and exponential star and dust disc model). We can see that the reddening effects of the foreground screen (for a total V band extinction of 0.3 mag) are qualitatively similar (despite its unphysical dust geometry) to the central V band absorption of a $\tau_V = 2$ Triplex dust model. For the Triplex model, the length of the vector shows the colour difference between the central (filled circle) and outer colours, and the open circle denotes the colour effects at the disc half light radius.

How realistic are these Triplex vectors? dJIV compares absorption-only face-on Triplex dust reddening vectors with the results of Monte Carlo simulations, including the effects of scattering, concluding that the Triplex model vectors are quite accurate for high optical depths but that they considerably *overestimate* the reddening for lower optical depths (i.e. $\tau_V \lesssim 2$). However, both these models include only the effects of smoothly distributed dust. If a fraction of the dust is distributed in small, dense clumps, the reddening produced by a given overall dust mass decreases even more: the dense clumps of dust tend to simply 'drill holes' in the face-on galaxy light distribution, producing very little reddening per unit dust mass (Huizinga 1994; dJIV; Kuchinski et al. 1998). The bottom line is that in such a situation, the galaxy colours are dominated by the least obscured stars, with the dense dust clouds having little effect on the overall colour. Therefore, the Triplex model vectors in Figs. 3.2–3.6 are arguably overestimates of the likely effects of dust reddening on our data.

From Figs. 3.2–3.6, we can see that the main effect of dust reddening would be the production of a colour gradient which would mimic small artificial age and metallicity gradients. Note, however, that the amplitudes of the majority of the observed colour gradients are larger than the Triplex model vectors. In addition, we have checked for trends in age and metallicity gradient with galaxy ellipticity: no significant trend was found, suggesting that age and metallicity trends are unlikely to be solely produced by dust. Coupled with the above arguments, this strongly suggests that most of the colour gradient of a given galaxy is likely to be due to stellar population differences.

This is consistent with the findings of Kuchinski et al. (1998), who found, using more realistic dust models tuned to reproduce accurately the colour trends in high-inclination galaxies, that the colour gradients in face-on galaxies were likely to be due primarily to changes in the underlying stellar populations with radius. Therefore, our measurements of the age and metallicity gradients are likely to be qualitatively correct, but trends in dust extinction with e.g. magnitude or surface brightness may cause (or hide) weak trends in the gradients.

The age and metallicity intercepts at the half light radius would be relatively unaffected: in particular, differences between the central V band optical depths of 10 or more cannot produce trends in the ages or metallicities with anywhere near the dynamic range observed in the data. *Therefore, the main conclusion of this Chapter, that the SFH of a spiral galaxy is primarily driven by surface density and is modulated by mass, is robust to the effects of dust reddening.*

3.5.5 Comparison with HII *region metallicities*

In Fig. 3.16, we plot our colour-based stellar metallicities at the disc half light radius against measures of the global gas metallicity via HII region spectroscopy. B band magnitudes were transformed into K band magnitudes using an average $B - K$ colour of 3.4 ± 0.4 (dJIV). For bright galaxies, we have plotted metallicity determinations from Vila-Costas & Edmunds (1992; diamonds) and Zaritsky et al. (1994; diagonal crosses) at a fixed radius of 3 kpc. To increase our dynamic range in terms of galaxy magnitude, we have added global gas metallicity measures from the studies of Skillman et al. (1989; triangles) and van Zee et al. (1997; squares). Measurements for the same galaxies in different studies are connected by solid lines.

From Fig. 3.16, it is clear that our colour-based stellar metallicities are in broad agreement with the trends in gas metallicity with magnitude explored by the above HII region studies. However, there are two notable differences between the colour-based stellar metallicities and the HII region metallicities.

Firstly, there is a 'saturation' in stellar metallicity at bright magnitudes not seen in the gas metallicities, which continue to rise to the brightest magnitudes. In section 3.4.3.2, we argued that this 'saturation' was due to the slow variation of stellar metallicity with gas fraction at gas fractions lower than $\sim$ 1/2. In Fig. 3.16 we test this idea. The dashed line is the gas metallicity–magnitude relation expected if galaxies evolve as closed boxes with solar metallicity yield, converting between gas fraction and magnitude using the by-eye fit to the magnitude–gas fraction correlation $f_g = 0.8 + 0.14(M_K - 20)$ (where the gas fraction f_g is not allowed to drop below 0.05 or rise above 0.95; see Fig. 3.12). The solid line is the corresponding relation for the stellar

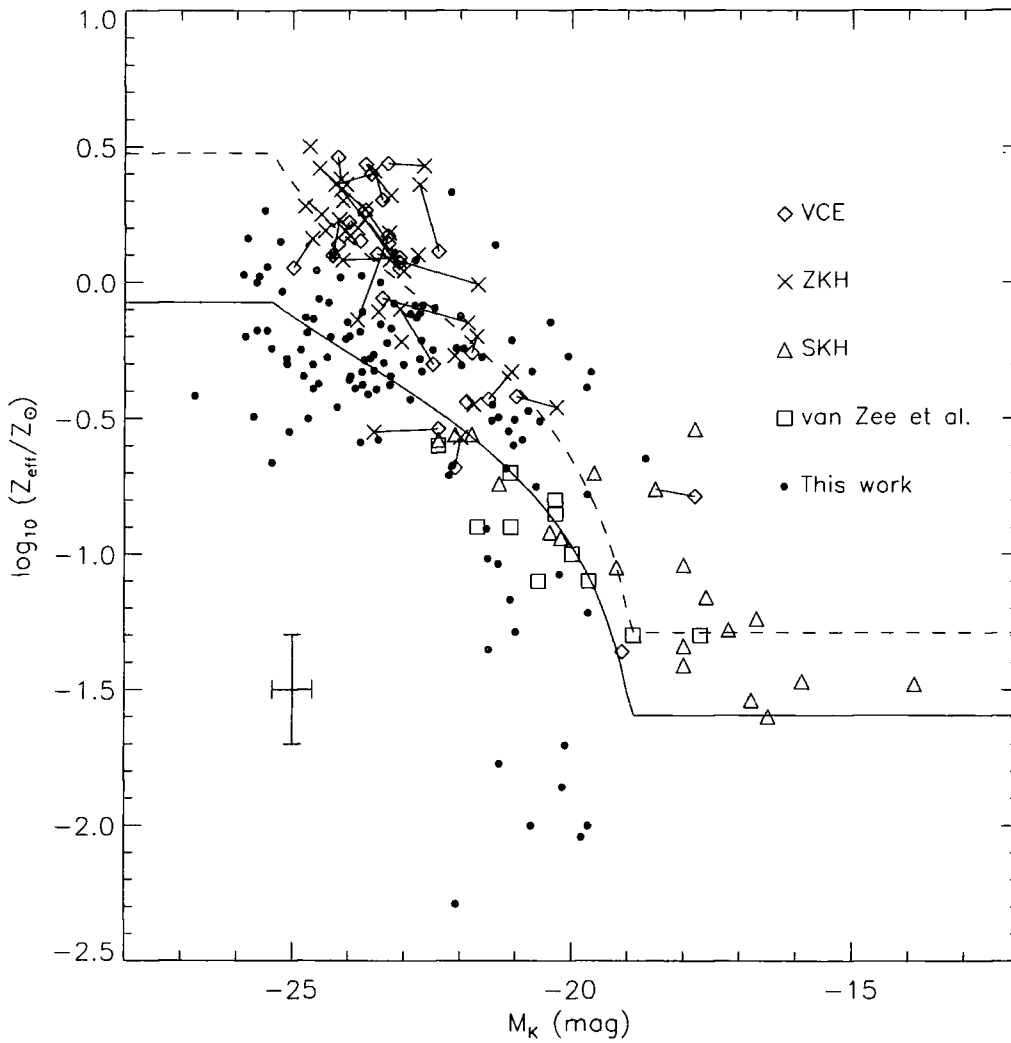

Figure 3.16: Comparison between the trends in gas metallicity and magnitude and stellar metallicity and magnitude. Our data from Fig. 3.9 are overplotted on HII region metallicity determinations at a radius of 3 kpc for the sample of Vila-Costas & Edmunds (1992; VCE) (diamonds) and Zaritsky et al. (1994; ZKH) (diagonal crosses). Global gas metallicity determinations for dwarf galaxies are taken from Skillman et al. (1989; SKH) (triangles) and van Zee et al. (1997) (squares). Multiple metallicity determinations for the same galaxy are connected by solid lines. The dashed and solid lines are the closed box predictions for the gas metallicity–magnitude and stellar metallicity–magnitude relations, respectively (see text for details).

metallicity. Note that at K band absolute magnitudes brighter than -25 or fainter than -19 the model metallicity–magnitude relation is poorly constrained: the gas fractions at the bright and faint end asymptotically approach zero and unity respectively. The closed box model indicates that our interpretation of the offset between gas and stellar metallicities at the brightest magnitudes is essentially correct: the gas metallicity of galaxies is around 0.4 dex higher than the average stellar metallicity. Furthermore, the slope of the gas metallicity–magnitude relation is slightly steeper than the stellar metallicity–magnitude relation. However, the simple closed box model is far from perfect: this model underpredicts the stellar metallicity of spiral galaxies with $K \sim -21$. This may be a genuine shortcoming of the closed box model; however, note that we have crudely translated gas fraction into magnitude: the closed box model agrees with observations quite closely if we plot gas and stellar metallicity against gas fraction (Fig. 3.9).

Secondly, there is a sharp drop in the estimated stellar metallicity at faint magnitudes that is not apparent in the gas metallicities. This drop, which occurs for stellar metallicities lower than $\sim 1/10$ solar, is unlikely to be physical: stellar and gas metallicities should be quite similar at high gas fractions (equivalent to faint magnitudes; Fig. 3.16). However, the SPS models are quite uncertain at such low metallicities, suggesting that the SPS models overpredict the near-IR magnitudes of very metal-poor composite stellar populations.

We have also compared our derived metallicity gradients with the gas metallicity gradients from Vila-Costas & Edmunds (1992) and Zaritsky, Kennicutt & Huchra (1994). Though our measurements have large scatter, we detect an average metallicity gradient of -0.06 ± 0.01 kpc^{-1} for the whole sample. This gradient is quite comparable to the average metallicity gradient from the studies Vila-Costas & Edmunds (1992) and Zaritsky, Kennicutt & Huchra (1994) of -0.065 ± 0.007 kpc^{-1}. Given the simplicity of the assumptions going into the colour-based analysis, and considerable SPS model and dust reddening uncertainties, we take the broad agreement between the gas and stellar metallicities as an important confirmation of the overall validity of the colour-based method.

3.5.6 A possible physical interpretation

In order to demonstrate the utility of the trends presented in section 3.4 in investigating star formation laws and galaxy evolution, we consider a simple model of galaxy evolution. We have found that the surface density of a galaxy is the most important parameter in describing its SFH; therefore, we consider a simple model where the star formation and chemical enrichment history are controlled by the surface density of gas in a given region (Schmidt 1959; Phillpps, Edmunds

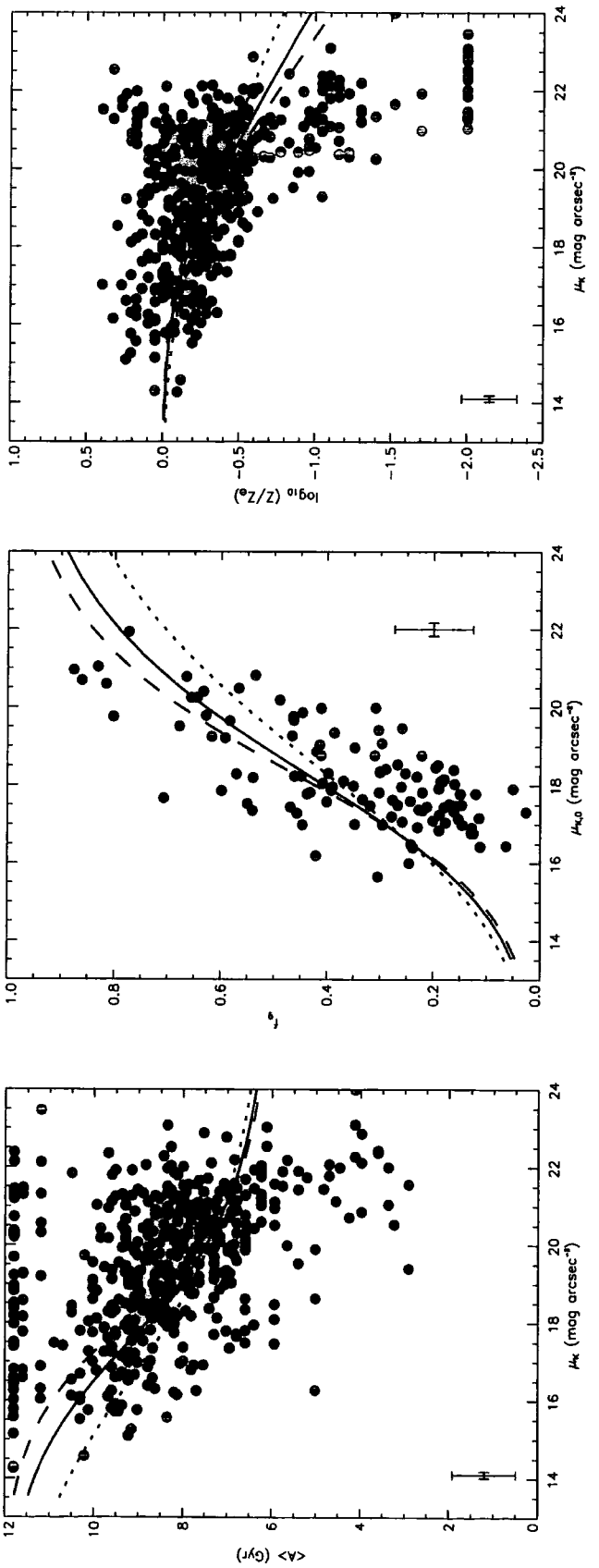

Figure 3.17: Local average age (left), gas fraction (middle) and metallicity (right) against K band surface brightness. The lines are predictions of the local density dependent model presented in the text with $n = 1.4, k = 0.020$ (dotted), $n = 1.6, k = 0.007$ (solid) and $n = 1.8, k = 0.0025$ (dashed).

& Davies 1990; Phillipps & Edmunds 1991; Dopita & Ryder 1994; Elmegreen & Parravano 1994; Prantzos & Silk 1998; Kennicutt 1998). In our model, we assume that the initial state 12 Gyr ago is a thin layer of gas with a given surface density $\Sigma_{\rm gas}$. We allow this layer of gas to form stars according to a Schmidt (1959) star formation law:

$$\psi(t) = -\frac{1}{1-R}\frac{d\Sigma_{\rm gas}(t)}{dt} = k\Sigma_{\rm gas}(t)^n, \tag{3.10}$$

where $\psi(t)$ is the SFR at a time t, $(1-R)$ is the fraction of gas that is locked up in long-lived stars (we assume $(1-R) = 0.7$ hereafter; this value is appropriate for a Salpeter IMF), k is the efficiency of star formation and the exponent n determines how sensitively the star formation rate depends on the gas surface density (Phillipps & Edmunds 1991). Integration of Equation 3.10 gives:

$$\Sigma_{\rm gas}(t)/\Sigma_0 = e^{-(1-R)kt}, \tag{3.11}$$

for $n = 1$ and:

$$\Sigma_{\rm gas}(t)/\Sigma_0 = [(n-1)(1-R)\Sigma_0^{n-1}kt + 1]^{1/1-n}, \tag{3.12}$$

for $n \neq 1$ where Σ_0 is the initial surface density of gas. Note that the star formation (and gas depletion) history of the $n = 1$ case is *independent* of initial surface density. To be consistent with the trends in SFH with surface brightness presented in this Chapter n must be larger than one.

We allow no gas inflow or outflow from this region, i.e. our model is a closed box. In addition, in keeping with our definition of the star formation law above (where we allow a fraction of the gas consumed in star formation to be returned immediately, enriched with heavy elements), we use the instantaneous recycling approximation. While this clearly will introduce some inaccuracy into our model predictions, given the simplicity of this model a more sophisticated approach is not warranted. Using these approximations, it is possible to relate the stellar metallicity Z to the gas fraction f_g (e.g. Pagel & Patchett 1975; Phillips & Edmunds 1991; Pagel 1998):

$$Z(t) = p(1 + \frac{f_g \log f_g}{1-f_g}), \tag{3.13}$$

where p is the yield, in this case fixed at solar metallicity $p = 0.02$. Numerical integration of the SFR from Equations 3.10, 3.11 and 3.12 allows determination of the average age of the stellar population $\langle A \rangle$.

In modelling the SFH in this way, we are attempting to describe the broad strokes of the trends in SFH observed in Fig. 3.7, using the variation in SFH caused by variations in *initial surface density alone*. In order to meaningfully compare the models to the data, however, it is necessary

to translate the initial surface density into a surface brightness. This is achieved using the solar metallicity SPS models of BC98 to translate the model SFR into a K band surface brightness. While the use of the solar metallicity model ignores the effects of metallicity in determining the K band surface brightness, the uncertainties in the K band model mass to light ratio are sufficiently large that tracking the metallicity evolution of the K band surface brightness is unwarranted for our purposes.

Using the above models, we tried to reproduce the trends in Fig. 3.7 by adjusting the values of n and k. We found that reasonably good fits to both trends are easily achieved by balancing off changes in n against compensating changes in k over quite a broad range in n and k. In order to improve this situation, we used the correlation between K band central surface brightness and gas fraction as an additional constraint: in order to predict the relationship between central surface brightness and global gas fraction, we constructed the mass-weighted gas fraction for an exponential disc galaxy with the appropriate K band central surface brightness. We found that models with $n \sim 1.6$ and $k \sim 0.007$ fit the observed trends well, with modest increases in n being made possible by decreasing k, and vice versa. Plots of the fits to the age, metallicity and gas fraction trends with surface brightness are given in Fig. 3.17.

The success of this simple, local density-dependent model in reproducing the broad trends in Fig. 3.17 is quite compelling, re-affirming our assertion that *surface density plays a dominant rôle in driving the SFH and chemical enrichment history of spiral galaxies*. This simple model also explains the origin of age and metallicity gradients in spiral galaxies: the local surface density in spiral galaxies decreases with radius, leading to younger ages and lower metallicities at larger radii. Indeed, the simple model even explains the trend in age gradient with surface brightness: high surface brightness galaxies will have a smaller age gradient per disc scale length because of the flatter slope of the (curved) age–surface brightness relation at high surface brightnesses.

However, our simple model is clearly inadequate: there is no explicit mass dependence in this model, which is required by the data. This may be alleviated by the use of a different star formation law. Kennicutt (1998) studied the correlation between global gas surface density and SFR, finding that a Schmidt law with exponent 1.5 *or* a star formation law which depends on both local gas surface density and the dynamical timescale (which depends primarily on the rotation curve shape, and, therefore, on mostly global parameters) explained the data equally well. There may also be a surface density threshold below which star formation cannot occur (Kennicutt 1989). In addition, the fact that galaxy metallicity depends on magnitude and surface brightness in almost equal amounts (age is much more sensitive to surface brightness) suggests that e.g. galaxy mass-

dependent feedback may be an important process in the chemical evolution of galaxies. Moreover, a closed box chemical evolution model is strongly disfavoured by e.g. studies of the metallicity distribution of stars in the Milky Way, where closed box models hugely overpredict the number of low-metallicity stars in the solar neighbourhood and other, nearby galaxies (Worthey, Dorman & Jones 1996; Pagel 1998). This discrepancy can be solved by allowing gas to flow in and out of a region, and indeed this is expected in galaxy formation and evolution models set in the context of large scale structure formation (Cole et al. 1999; Kauffmann & Charlot 1998a; Valeagas & Schaeffer 1999). In Chapter 4, we address these issues in more detail, where we use simple disc galaxy evolution models to try to describe the trends observed in this Chapter.

3.6 Conclusions

We have used a diverse sample of low-inclination spiral galaxies with radially-resolved optical and near-IR photometry to investigate trends in SFH with radius, as a function of galaxy structural parameters. A maximum-likelihood analysis was performed, comparing SPS model colours with those of our sample galaxies, allowing use of all of the available colour information. Uncertainties in the assumed grid of SFHs, the SPS models and uncertainties due to dust reddening were not taken into account. Because of these uncertainties, the absolute ages and metallicities we derived may be inaccurate; however, our conclusions will be robust in a relative sense. In particular, dust will mainly affect the age and metallicity gradients; however, the majority of a given galaxy's age or metallicity gradient is likely to be due to gradients in its stellar population alone. The global age and metallicity trends are robust to the effects of dust reddening. Our main conclusions are as follows.

- Most spiral galaxies have stellar population gradients, in the sense that their inner regions are older and more metal rich than their outer regions. The amplitude of age gradients increase from high surface brightness to low surface brightness galaxies. An exception to this trend are faint S0s from the Ursa Major Cluster of galaxies: the central stellar populations of these galaxies are younger and more metal rich than the outer regions of these galaxies.

- The stellar metallicity–magnitude relation 'saturates' for the brightest galaxies. This 'saturation' is a real effect: as the gas is depleted in the brightest galaxies, the gas metallicity tends to rise continually, while the stellar metallicity flattens off as the metallicity tends towards the yield. The colour-based metallicities of the faintest spirals fall considerably ($\gtrsim$ 1 dex) below

the gas metallicity–luminosity relation: this may indicate that the SPS models overpredict the K band luminosity of very low metallicity composite stellar populations.

- There is a strong correlation between the SFH of a galaxy (as probed by its age, metallicity and gas fraction) and the K band surface brightness and magnitude of that galaxy. From consideration of the distribution of galaxies in the age–magnitude–surface brightness and metallicity–magnitude–surface brightness spaces, we find that the SFH of a galaxy correlates primarily with either its local or global K band surface brightness: the effects of K band absolute magnitude are of secondary importance.

- When the gas fraction is taken into account, the correlation between SFH and surface density remains, with a small amount of mass dependence. Motivated by the strong correlation between SFH and surface density, and by the correlation between age and local K band surface brightness, we tested the observations against a closed box local density-dependent star formation law. We found that despite its simplicity, many of the correlations could be reproduced by this model, *indicating that the local surface density is the most important parameter in shaping the SFH of a given region in a galaxy.* A particularly significant shortcoming of this model is the lack of a magnitude dependence for the stellar metallicity: this magnitude dependence may indicate that *mass-dependent feedback is an important process in shaping the chemical evolution of a galaxy.* However, there is significant cosmic scatter in these correlations (some of which may be due to small bursts of recent star formation), suggesting that the mass and density of a galaxy may not be the only parameters affecting its SFH.

Chapter 4

Spiral galaxy evolution

In Chapter 3, we saw strong correlations between the star formation history (SFH) and K band surface brightness of a galaxy, and between the metallicity and both K band surface brightness and absolute magnitude. In particular, in section 3.5.6 we argued that these correlations could be the result of a local surface density dependent star formation law (SFL), coupled with mass-dependent chemically-enriched outflows. In this Chapter, we investigate this idea in more detail by using simple 'toy' models to explore the effects of different physical processes or SFLs.

4.1 Introduction

The chemical evolutionary histories of spiral galaxies provide considerable insight into many of the important processes involved in galaxy formation and evolution. For example, we can study star formation laws (e.g. Wyse & Silk 1989; Phillipps & Edmunds 1991), the interactions between newly-formed stars and the interstellar medium (e.g. Dekel & Silk 1986; MacLow & Ferrera 1999), the importance and effects of gas flows (e.g. Lacey & Fall 1985; Edmunds 1990; Edmunds & Greenhow 1995) and the infall that must accompany disc formation (e.g. Tinsley & Larson 1978; Lacey & Fall 1983). The main challenge is obtaining *unambiguous* insight into particular physical processes. The effects of all of the above (combined with e.g. random variations in star formation rate, and possible variations in e.g. stellar initial mass function) are tangled up together, making it difficult to understand one particular process from studying chemical evolution alone. This ambiguity results from the complexity of galaxy formation: many complex, poorly understood physical processes are at play in determining the formation and evolutionary history of a given galaxy.

However, some progress has been made in understanding the driving forces behind galaxy formation and evolution. A local density dependence in the SFL is strongly favoured, although other

factors may affect the star formation rate over galactic scales (e.g. Schmidt 1959; Dopita 1985; Kennicutt 1989; Wyse & Silk 1989; Dopita & Ryder 1994; Prantzos & Aubert 1995; Kennicutt 1998). Additionally, infall may be important in determining the metallicity distribution of stars in the solar neighbourhood (e.g. Tinsley 1980; Prantzos & Aubert 1995; Pagel 1998). Other processes are more controversial: e.g. gas flows may play a part in chemical evolution, but the evidence is ambiguous, as radial variations in the SFL are able to mimic the properties of gas flows equally well (e.g. Edmunds & Greenhow 1995; Lacey & Fall 1985).

Here, we present a preliminary exploration of some of the processes involved in galaxy formation and evolution; namely infall, outflows and SFLs. Similarly to e.g. Wyse & Silk (1989), Phillipps & Edmunds (1991), or Prantzos & Aubert (1995), we use the trends in metallicity with galaxy properties to explore the importance of these processes in determining the chemical evolution of galaxies. However, we also use the SFHs from Chapter 3 as a constraint, allowing us to assess the importance of these processes in a fresh light.

The plan of this Chapter is as follows. In section 4.2, we describe our 'toy' chemical evolution model, the basic assumptions and equations and outline how we translate the model output into observables which we can readily compare with the data. In section 4.3, we describe the properties of the closed box model and explore the effects of infall and outflow on the models. In section 4.4, we investigate the effects of changing the SFL on our results. Finally, in section 4.5, we summarise our results, and outline promising areas for further development and study.

4.2 The Model

4.2.1 Basic assumptions and equations

In order to make the investigation of the age and metallicity trends a tractable problem, we adopt highly simplified prescriptions describing star formation and galaxy evolution. These simple approximations allow us to investigate which effects play an important rôle in e.g. imprinting mass dependence in the SFH.

Our model spiral galaxy starts off, 12 Gyr ago, as an exponential disc of gas with surface density $\Sigma_0(r) = \Sigma_0(r = 0)e^{-r}$, where Σ_0 is the initial surface density of gas in $M_\odot\,pc^{-2}$, and r is the radius in units of the scale length of the gas (denoted by h). For the infall case (see section 4.3.2), $\Sigma_0(r) = 0$ initially, we gradually build up the gas mass in an exponential disc over time, assuming an exponentially declining infall rate $\tau_{\rm infall}$.

The gas forms stars according to a prescribed SFL: in much of this Chapter we adopt a Schmidt (1959) SFL in terms of the gas surface density $\Sigma_{\rm gas}$:

$$\psi = k\Sigma_{\rm gas}^{n}, \tag{4.1}$$

where ψ is the star formation rate in $\mathrm{M_{\odot}\,pc^{-2}\,Gyr^{-1}}$, k is the efficiency of star formation at a surface density of 1 $\mathrm{M_{\odot}\,pc^{-2}}$ and n is the exponent specifying how sensitively the star formation rate depends on gas surface density.

This star formation produces heavy elements; here we assume the instantaneous recycling approximation (IRA; e.g. Tinsley 1980; Pagel 1998). A fraction R of the mass of newly formed stars is instantaneously returned to the gas (we assume $R = 0.3$, which is appropriate for a Salpeter IMF; c.f. Chapters 3 and 6), along with a mass $p\psi(1-R)$ of heavy elements, where p is the true yield, and is defined as the mass of freshly produced heavy elements per unit mass locked up in long-lived stars, and is taken to be 0.02 (solar metallicity) hereafter unless explicitly stated. Note that, for simplicity, we assume a metallicity-independent yield. Note that our use of the IRA should not lead to significant inaccuracies, as the metallicity of spiral galaxies is typically measured via their oxygen content: for oxygen, the IRA is a fairly accurate approximation as it is produced primarily by Type II supernovae (c.f. Pagel 1998).

Once the IRA is adopted, the following three equations specify the evolution of the galaxy completely:

$$\frac{d\Sigma_{\rm gas}}{dt} = F - E - \psi(1-R) \tag{4.2}$$

$$\frac{d\Sigma_{\rm stars}}{dt} = \psi(1-R) \tag{4.3}$$

$$\frac{d(\Sigma_{\rm gas}Z)}{dt} = p\psi(1-R) - Z\psi(1-R) - Z_E E + Z_F F, \tag{4.4}$$

where $\Sigma_{\rm stars}$ is the surface density of the stars in $\mathrm{M_{\odot}\,pc^{-2}}$, F is the surface density infall rate (with an initial metallicity Z_F) in $\mathrm{M_{\odot}\,pc^{-2}\,Gyr^{-1}}$, E is the surface density of gas ejected in outflows (with metallicity Z_E) in $\mathrm{M_{\odot}\,pc^{-2}\,Gyr^{-1}}$ and Z is the gas metallicity (Tinsley 1980; Pagel 1998).

4.2.2 *Determining ages and metallicities*

We follow the evolution of the galaxy using a numerical scheme with a 20 Myr timestep. We split our model galaxies into 20 radial zones between $r = 0$ and $r = 4$ gas disc scale lengths, to allow study of both global and radial trends in age and metallicity. While many of the cases we study here have analytical solutions, our use of a numerical scheme allows us to use more complex SFLs and e.g. infall or outflow histories.

The purpose of this modelling is to explore which different processes may be able to explain the trends in age and metallicity that were derived in Chapter 3. In order to properly compare the models with the data, it is necessary to use similar techniques for determining the model ages and metallicities as were used to determine the ages and metallicities of the sample galaxies.

Accordingly, we use the colour-based maximum-likelihood technique from Chapter 3 to determine the ages and metallicities of our model galaxies. In order to use this technique, we must have a set of optical and near-infrared colours for our model galaxies. Therefore, in each zone at each timestep, we use the *total* mass of newly-formed stars (both short- and long-lived) to compute the contribution of those stars to the total flux at the present day in the broad band passbands U, B, V, R, I, J, H and K using the multi-metallicity GISSEL98 models of Bruzual & Charlot (in preparation; BC98).

We then use these local colours as input to the maximum-likelihood age and metallicity estimator developed for and presented in Chapter 3. In this way, *we obtain model ages and metallicities determined in exactly the same way as the observations we compare with.* This can be quite important: especially so for older stellar populations. The mass-weighted average ages of older stellar populations determined in e.g. section 3.5.6 can differ considerably from the luminosity-weighted ages derived using the colour-based technique because of only relatively modest amounts of recent star formation.

Using these local age and metallicity estimates, we construct estimates of the global age and metallicity gradients and intercepts (at the K band disc half-light radius), using an unweighted least-squares fit (c.f. Chapter 3). K band disc central surface brightnesses and scale lengths are determined by fitting the first 3 (gas) disc scale lengths of the surface brightness profile. Global gas fractions are determined by direct summation of the gas and stellar masses.

The sample galaxies from Chapter 3 cover a broad range of magnitudes and surface brightnesses. Therefore, to provide a fair comparison, the model galaxies must cover a similarly broad range of magnitudes and surface brightnesses. We adopt an empirical approach: we run a grid of 357 models with total (baryonic and dark) masses between 10^9 $M_\odot$ and 10^{14} $M_\odot$ (we assume a baryon fraction of 0.05 hereafter), and central baryonic surface densities between $10^{0.5}$ $M_\odot$ pc^{-2} and 10^4 $M_\odot$ pc^{-2}. The step size is 0.25 dex. This range is sufficient to cover the full observed range of parameter space probed in Chapter 3, assuming that the baryonic content of a galaxy turns entirely into solar-type stars.

However, this situation is complicated by the (broad) correlation between surface brightness and magnitude (c.f. Fig. 3.12 from Chapter 3). Because of this correlation between surface brightness

and magnitude, any correlation between e.g. the ages and surface brightnesses of the sample from Chapter 3 will automatically translate into a correlation between age and magnitude. However, our model grid does not incorporate this correlation. Therefore, to provide a fair comparison with the data, we select galaxies from the model grid that fall within the region inhabited by the sample galaxies in the K band surface brightness–absolute magnitude plane (Fig. 4.1) using the following criteria:

$$\mu_{K,0} > 13 + 0.6(M_K + 26) \tag{4.5}$$

$$\mu_{K,0} < 20 + 0.6(M_K + 26) \tag{4.6}$$

$$\mu_{K,0} > 19 - 1.25(M_K + 28) \tag{4.7}$$

$$\mu_{K,0} < 23 - 1.25(M_K + 21), \tag{4.8}$$

where $\mu_{K,0}$ is the K band disc central surface brightness and M_K is the K band absolute magnitude of the galaxy. In this way, we can empirically select galaxies with a range of physical parameters consistent with those taken from Chapter 3. Note that galaxies with different sets of surface densities and masses may be chosen, depending on the model details (especially on the efficiency with which stars are turned into gas).

Now, we use this model grid to investigate trends in age and metallicity with local and global structural parameters in sections 4.3 and 4.4, where we vary the galaxy evolution and SFL prescriptions respectively.

4.3 Galaxy evolution

4.3.1 Closed box model

Our fiducial model is a closed box model with a Schmidt law local gas surface density-dependent SFL, with efficiency $k = 0.012\,\mathrm{M}_\odot\,\mathrm{pc}^{-2}\,\mathrm{Gyr}^{-1}$ at a surface density of $1\,\mathrm{M}_\odot\,\mathrm{pc}^{-2}$, and $n = 1.6$ (see Table 4.1; note that small increases in n are possible if k decreases, and vice versa). Our choice of the closed box Schmidt SFL model as our fiducial model is motivated by its success in section 3.5.6 of Chapter 3. The primary prediction of the closed box Schmidt SFL model is that *the SFH and metallicity of a given area in any galaxy depend only on the initial local gas surface density*: this accords reasonably well with the local age and metallicity vs. local K band surface brightness correlation presented in Fig. 3.7 of Chapter 3. Note that the star formation and chemical enrichment history of a galaxy are *independent* of the initial density of gas if $n = 1$, i.e. if the star formation rate is directly proportional to the gas density.

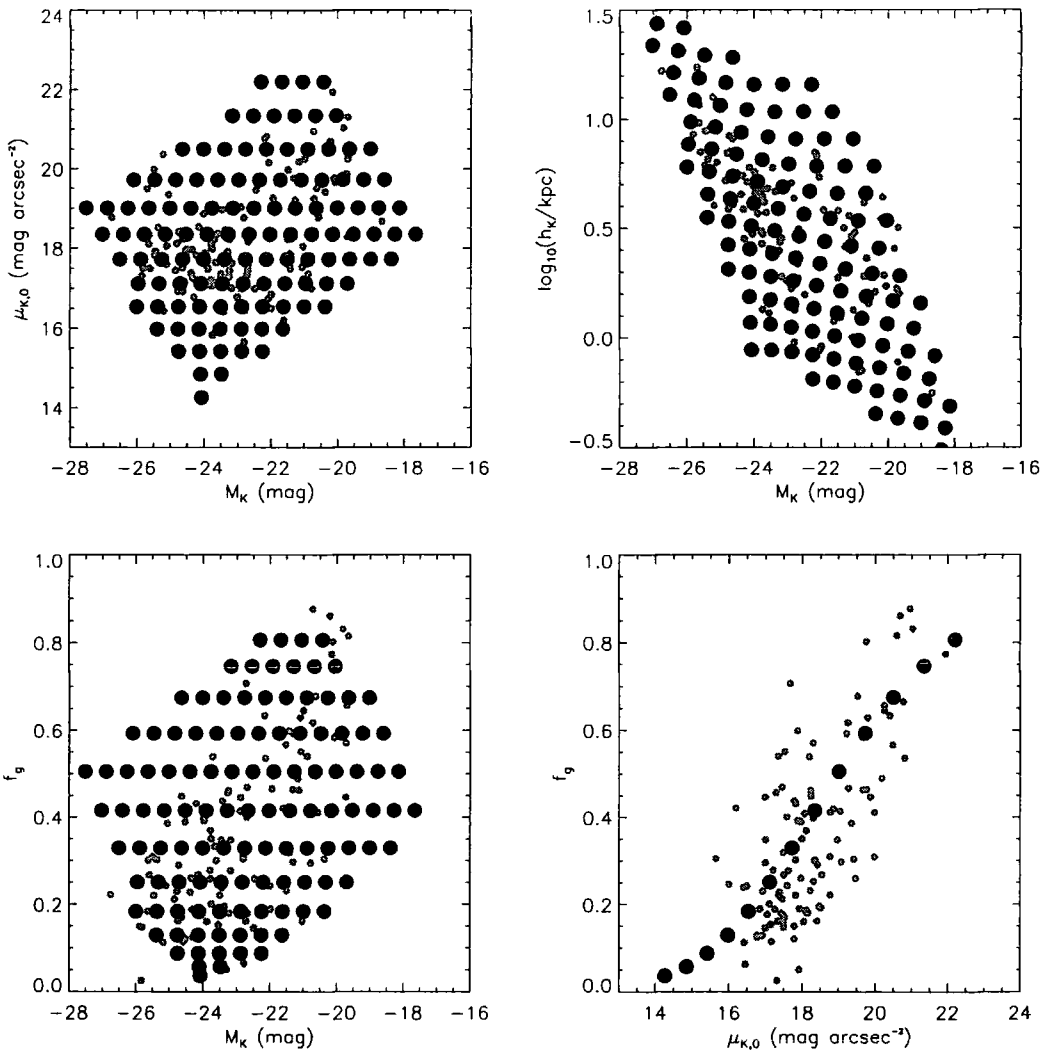

Figure 4.1: Fiducial Model: Correlation between K magnitudes, K band central surface brightnesses, K band disc scale lengths and gas fractions of the data from Chapter 3 (grey circles) and the fiducial model (large black circles). The upper left panel shows our selection criteria based on the observed distribution of galaxies in the M_K vs. $\mu_{K,0}$ plane. The lower right panel shows the surface brightness–gas fraction correlation, which we use as a constraint when searching for adequate model fits to the data.

When we evaluate the effects of different galaxy evolution prescriptions, we will evaluate them with respect to this model. As such, it is worth spending some time on understanding what this model can and cannot reproduce, in terms of the trends observed in Chapter 3.

In Fig. 4.1, some of the main correlations between physical parameters from Chapter 3 are plotted; overplotted are the results from the fiducial model. The upper left hand panel illustrates the selection box. The upper right hand panel is the projection of these selection limits into the magnitude–scale length plane. The lower right hand panel shows the K band central surface brightness–gas fraction correlation: the models are tuned to accurately reproduce this correlation, along with the local K band surface brightness against age and metallicity correlations of Fig. 4.2. The lower left hand panel shows the K band absolute magnitude–gas fraction correlation: for the models, this panel illustrates the surface brightness–gas fraction correlation coupled with the magnitude–surface brightness selection limits.

One important point to note is the mismatch between the observed magnitude–gas fraction correlation and the model magnitude–gas fraction correlation: the model shows a much weaker correlation between magnitude and gas fraction than the data. Part of this problem is due to our adopted selection limits: the regions of the magnitude–surface brightness plane that we select have 'corners' that the data lacks, which gives the model magnitude–gas fraction correlation artificially large scatter. However, we know from Chapter 3 that much of this mismatch between the model and the data is a real problem with our model: the data *require* some magnitude dependence in the SFH (as probed by the gas fraction), which is explicitly not taken into account in the local gas density-dependent SFL.

The local K band surface brightness against age and metallicity correlations are shown in Fig. 4.2. The fiducial model does a good job of reproducing the observed trends in age and metallicity with local K band surface brightness. Note that the lack of scatter in the model age–surface brightness and metallicity–surface brightness correlations is because the ages and metallicities of the fiducial model depend only on initial gas surface density. The departures from a smooth age or metallicity sequence with surface brightness in Fig. 4.2 result from our use of colour-based estimated ages and metallicities. These are primarily due to degeneracies and irregularities in the colour-colour grid for stellar populations with near-constant star formation rates (i.e. average ages $\sim$ 6 Gyr), which cause irregularities in the age–surface brightness and metallicity–surface brightness plots.

In Fig. 4.3 we explore the implications of this model in terms of reproducing the correlations between age at the half light radius and galaxy parameters. We see that the fiducial model repro-

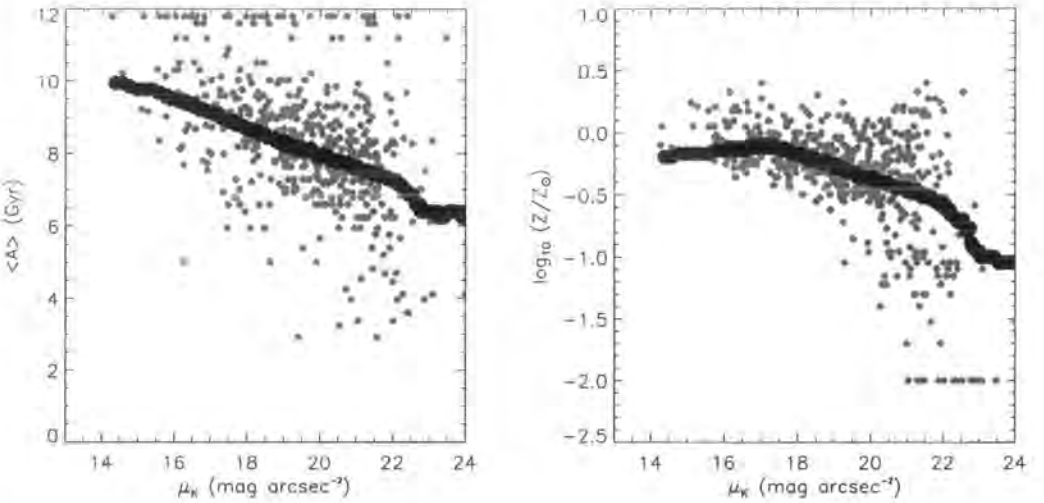

Figure 4.2: Fiducial Model: Correlation between local K surface brightness and the local age and metallicity of the data from Chapter 3 (grey circles) and the fiducial model (large black circles). Note that in this model the star formation and chemical evolution history depends on the initial local gas surface density alone. These two correlations must be roughly reproduced by any successful local density-dependent model. A significant number of data points from Chapter 3 have average ages of 11.9 Gyr or metallicities of $\log_{10}(Z/Z_\odot) = -2$: these data points fall outside the model grids.

duces a correlation between age and K band central surface brightness, and between age and gas fraction. Note however that the slope of the model correlations is too shallow: real galaxies show a steeper correlation between age at the half light radius and K band central surface brightness and gas fraction than the model galaxies. Note also that the selection limits imposed on the model galaxies produce a small residual correlation between age at the half light radius and K band absolute magnitude: this correlation is fictitious (age does not depend on mass in this model) and is the result of the magnitude–surface brightness correlation shown in the upper left hand panel of Fig. 4.1. Note also that this correlation is too shallow: from Chapter 3, we know that this shallow correlation is the result of underpredicting the slope of the age–surface brightness correlation, and is also the result of a real, weak trend between age and K band absolute magnitude.

In Fig. 4.4 we explore correlations between metallicity at the disc half light radius and the galaxy physical parameters, as predicted by the fiducial model. In contrast to the trends in age, the metallicity trends are remarkably well-reproduced by the fiducial (closed box) model. In particular, the metallicity–surface brightness and metallicity–gas fraction correlations are well-described by the fiducual model. Also in Fig. 4.4, we can see that there is a small residual correlation between metallicity and magnitude imposed by the selection limits in Fig. 4.1, but that the slope of the

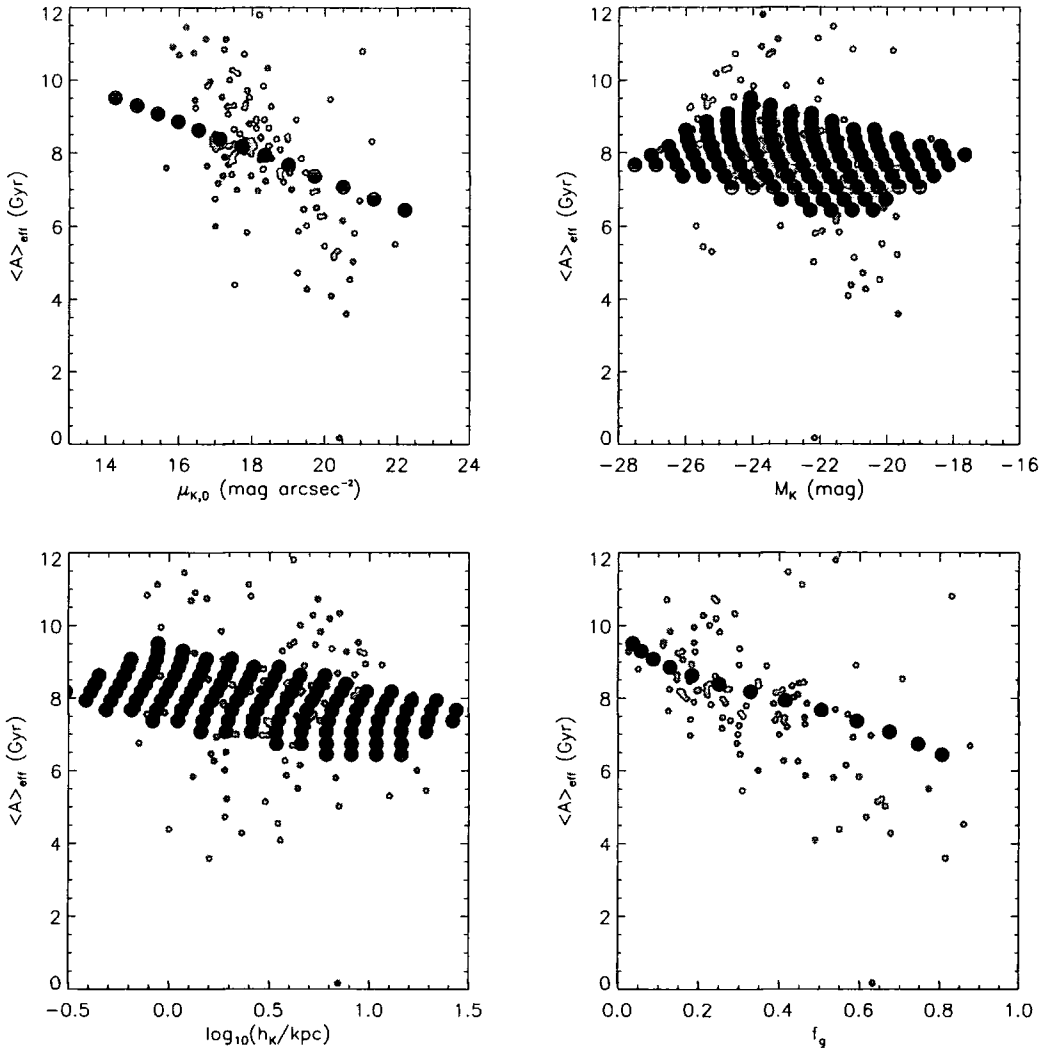

Figure 4.3: Fiducial Model: Correlations between the age at the disc half light radius and the K band disc central surface surface brightness $\mu_{K,0}$, the K band absolute magnitude M_K, the K band disc scale length h_K and gas fraction f_g. Data from Chapter 3 are shown as grey circles; the fiducial model grid is shown as large black circles. Note that some of the older, very low surface brightness galaxies may have significant age errors (Chapter 2).

correlation is too small: this indicates that metallicity has both a surface brightness and magnitude dependence.

In Fig. 4.5, we explore the age (left panel) and metallicity (right panel) gradients per K band disc scale length. For the metallicity (right hand panel), we can clearly see that the fiducial model accurately reproduces the trend in metallicity gradient with K band central surface brightness. In this respect, we disagree with the conclusions of Phillipps & Edmunds (1991), who concluded

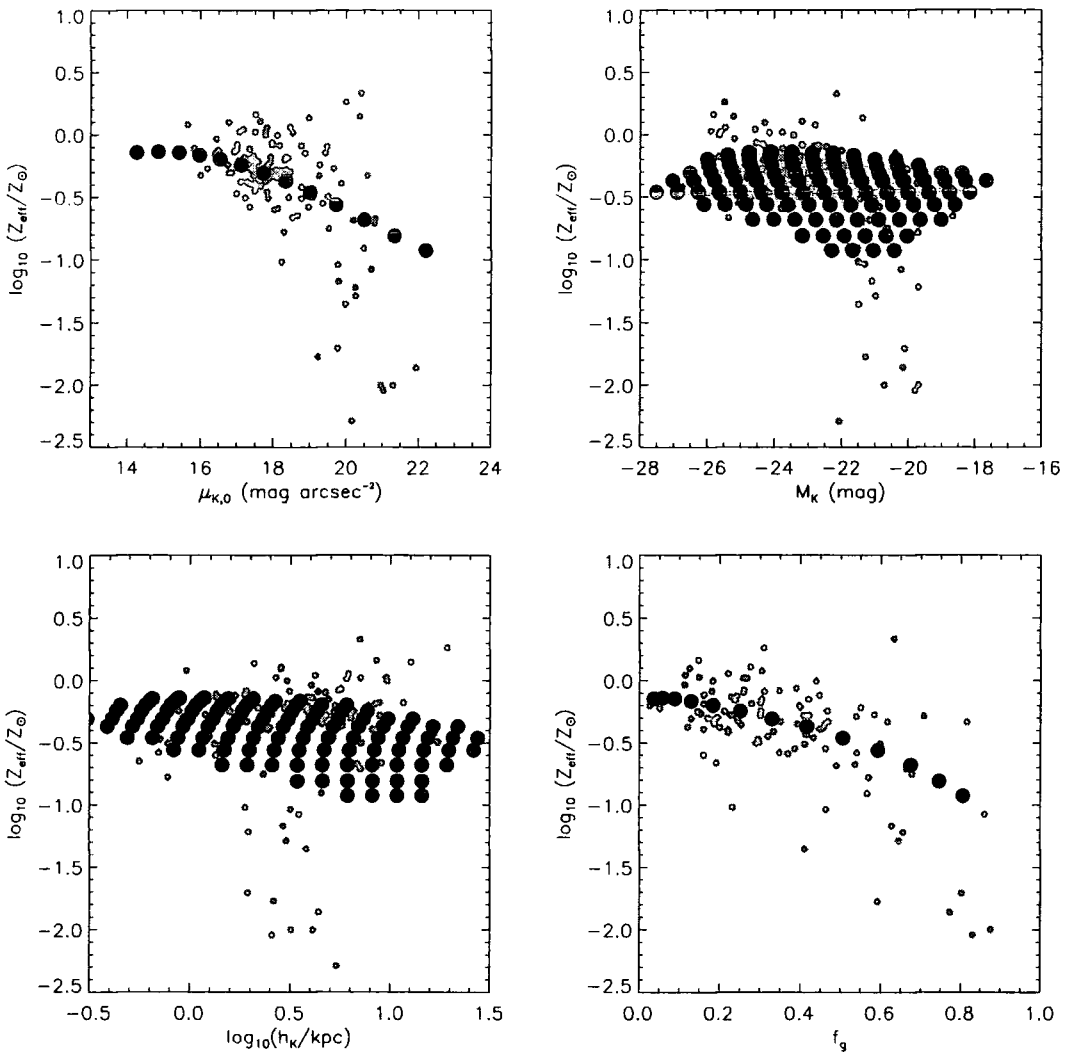

Figure 4.4: Fiducial Model: Correlations between the metallicity at the disc half light radius and the K band disc central surface surface brightness, the K band absolute magnitude, the K band disc scale length and gas fraction. Data from Chapter 3 are shown as grey circles; the fiducial model grid is shown as large black circles. Note that the model grid becomes quite uncertain at very low metallicities: many of the grey data points at metallicities lower than $\log_{10}(Z_{eff}/Z_{\odot}) = -1$ may not have metallicities as low as those plotted on this diagram.

that observed metallicity gradients exceed those achievable with a Schmidt SFL and closed box chemical evolution. Part of this discrepancy may stem from our use of stellar metallicities, and their use of gas metallicities. However, inspection of their Figs. 1 and 2 suggests a good agreement between their simple Schmidt law model and the observations, indicating that they may have overestimated the size of the observational trend between metallicity and surface density when compared to the Schmidt law model.

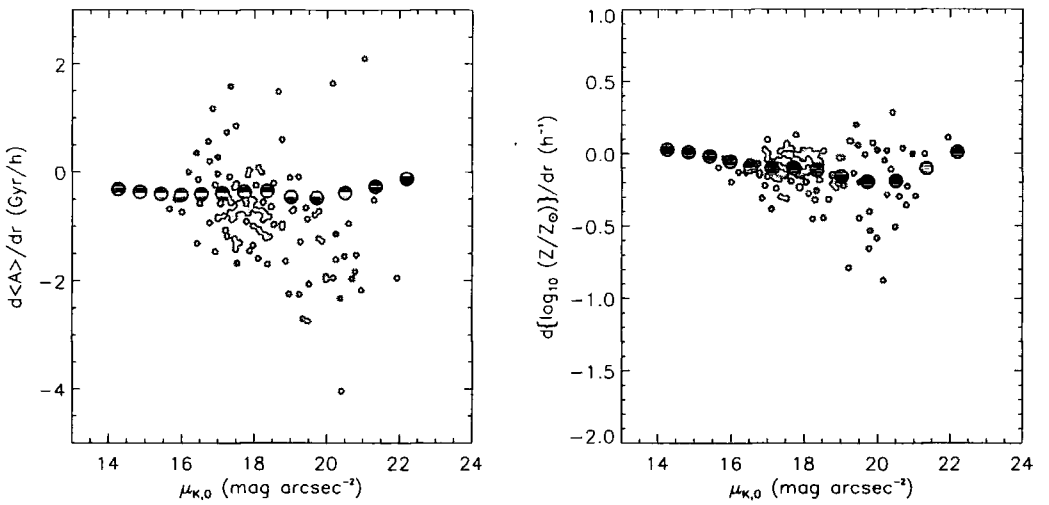

Figure 4.5: Fiducial Model: Correlations between the age and metallicity gradients per K band disc scale length and the K band central surface brightness. Data from Chapter 3 are shown as grey circles; the fiducial model grid is shown as large black circles.

In contrast, the trends in age gradient with K band central surface brightness are poorly reproduced by the fiducial model: there is little if any correlation between age gradient and surface brightness in the model, and the model underpredicts the average age gradient in the data by around a factor of two. This problem is linked with the inability of the model to reproduce the steepness of the global age–K band central surface brightness correlation in Fig. 4.3, as the slope of the model correlation is too shallow, indicating that the rate of change of age with surface brightness (i.e. the age gradient) is underpredicted by the model.

To summarise, the fiducial model does a reasonable job of describing the correlations between the ages and metallicities of galaxies and their physical parameters. The main shortcomings of the fiducial model are a lack of magnitude dependence in both the age and metallicity and the underprediction of the rate of change of age with K band surface brightness. In the next two subsections, we see how modifying the fiducial model by introducing infall or outflow can affect the predicted correlations.

4.3.2 *Infall model*

In order to test the effects of infall in imprinting mass dependence in the SFH of a spiral galaxy, we adopt a simple parameterisation. We assume that the galaxy initially has a surface density of

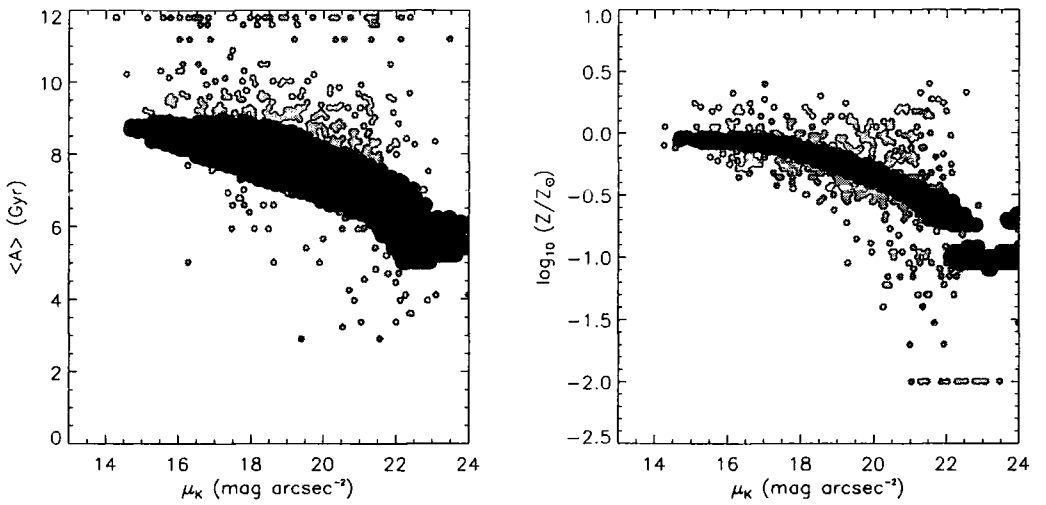

Figure 4.6: Infall Model I2: Correlation between local K surface brightness and the local age and metallicity of the data from Chapter 3 (grey circles) and infall model I2 (large black circles).

zero at all radii: we then build up the exponential disc of the galaxy from a reservoir of metal-free gas with an exponential timescale $\tau_{\rm infall}$. We tested three cases: a mass-independent $\tau_{\rm infall} = 3$ Gyr (model I1), a model in which the timescale is longer for low mass galaxies (where $\tau_{\rm infall}$ ranges from $\tau_{\rm infall} = 7$ Gyr for galaxies with a total mass of 10^{10} M$_\odot$ to $\tau_{\rm infall} = 1$ Gyr for galaxies with a total mass of 10^{14} M$_\odot$; model I2) and a model in which the timescale is longer for high mass galaxies (where $\tau_{\rm infall}$ ranges from $\tau_{\rm infall} = 1$ Gyr for galaxies with a total mass of 10^{10} M$_\odot$ and lower to $\tau_{\rm infall} = 7$ Gyr for galaxies with a total mass of 10^{14} M$_\odot$; model I3). All the model galaxies with infall have a Schmidt SFL with exponent $n = 1.8$ and efficiency $k = 0.012$. A summary of the models is in Table 4.1. For brevity, we only show the relevant results for model I2 (where small galaxies have longer infall timescales), while noting the behaviour of the other infall models.

One general result is that infall reduces the average age of the stellar population, while leaving the average metallicity relatively unaffected (compared to a closed box model). Note that infall 'narrows' the metallicity *distribution* of a stellar population, where there are relatively fewer low or high metallicity stars than the closed box model: this in fact was one of the original motivations for the infall model (e.g. Larson 1972; Tinsley 1980; Prantzos & Aubert 1995; Prantzos & Silk 1998; Pagel 1998).

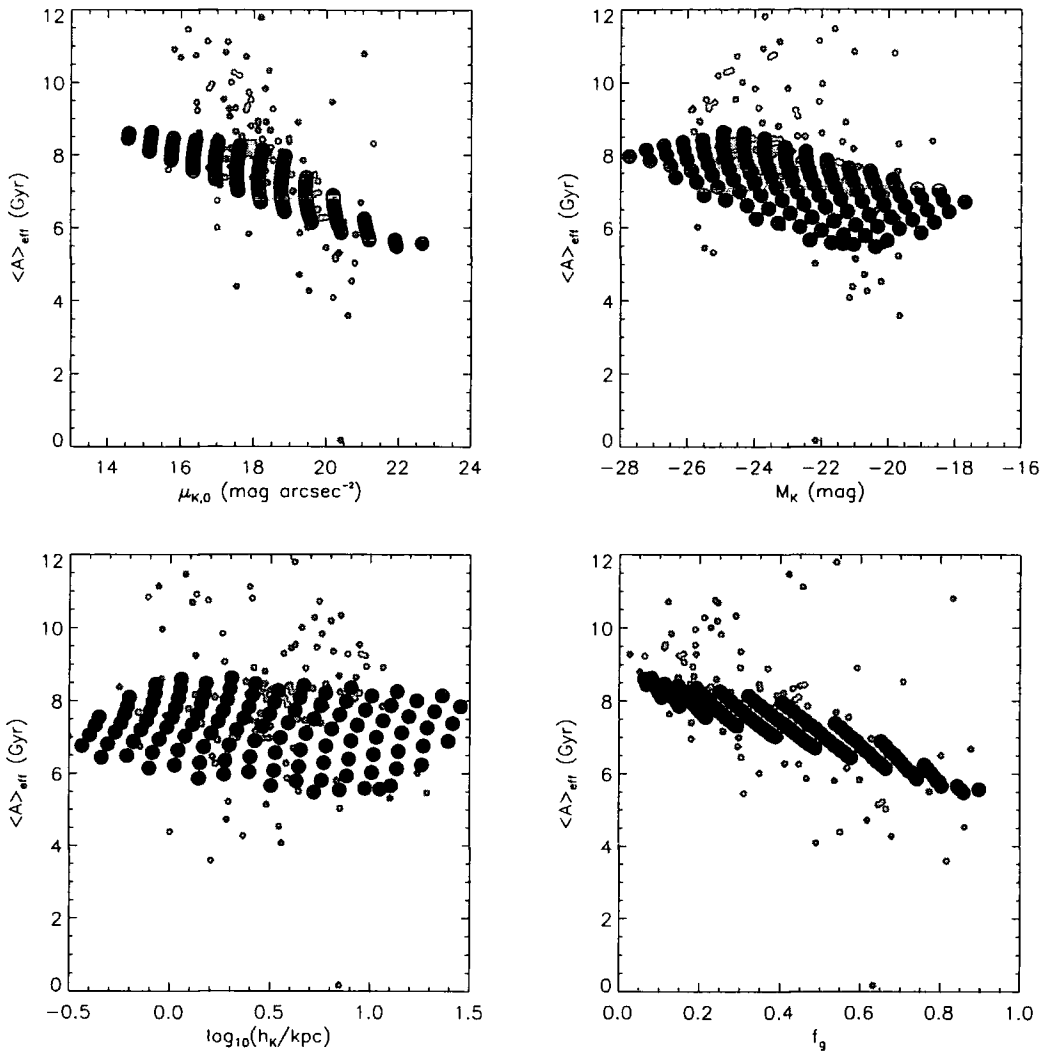

Figure 4.7: Infall Model I2: Correlations between the age at the disc half light radius and the K band disc central surface surface brightness, the K band absolute magnitude, the K band disc scale length and gas fraction. Data from Chapter 3 are shown as grey circles; the infall model I2 grid is shown as large black circles.

The reduction of the average age depends (of course) on infall timescale: one can see from e.g. equation 3.3 of section 3.2.2 that the maximum average age of a stellar population with an exponential infall timescale $\tau_{\rm infall}$ decreases as the infall timescale increases (and is roughly 12 – $\tau_{\rm infall}$ Gyr for $\tau_{\rm infall} \lesssim 4$ Gyr). This gives us a way to 'imprint' mass dependence on the average age of a galaxy, while leaving its metallicity relatively unaffected. In Figs. 4.6 and 4.7 we see an example of this idea, where we see how the local and global ages and local metallicities vary with

local and global observables for the I2 model (where the infall timescale is longer for less massive galaxies).

In Fig. 4.6, we see that the introduction of mass-dependent infall causes some scatter in the local age–surface brightness correlation (but leaves the metallicity–surface brightness correlation relatively unaffected). In Fig. 4.7, we see how the global ages are affected by infall. For cases with mass-dependent infall, we introduce scatter in the age–surface brightness and age–gas fraction correlations. However, importantly, we also introduce mass dependence in the average age: higher mass galaxies in model I2 (I3) have older (younger) ages than were expected in the case of mass-independent infall. Note that the slopes of the age–magnitude correlation appear quite similar in Figs. 4.3 and 4.7. This is because of the maximum age limit imposed by infall: if more massive galaxies had shorter infall timescales than model I2 assumes, they would appear older, and the slope of the age–magnitude correlation would be steeper.

4.3.3 Outflow model

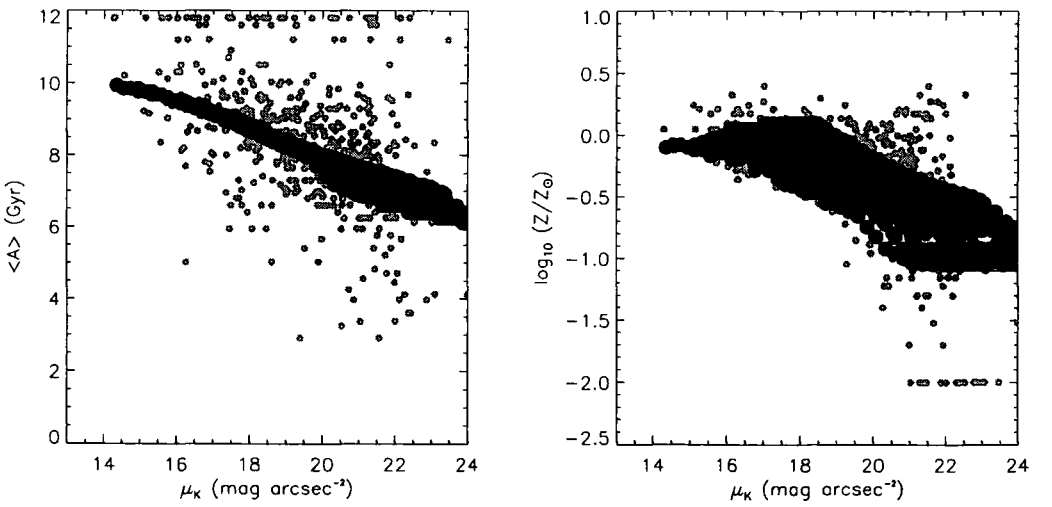

Figure 4.8: Outflow Model O: Correlation between local K surface brightness and the local age and metallicity of the data from Chapter 3 (grey circles) and the outflow model (large black circles).

In order to test the possible importance of outflow, we adopt a simple parameterisation of its effects. Outflow caused by supernovae winds is predicted to be much more effective for low mass galaxies (Dekel & Silk 1986; Arimoto & Yoshii 1987; MacLow & Ferrera 1999; Martin 1999;

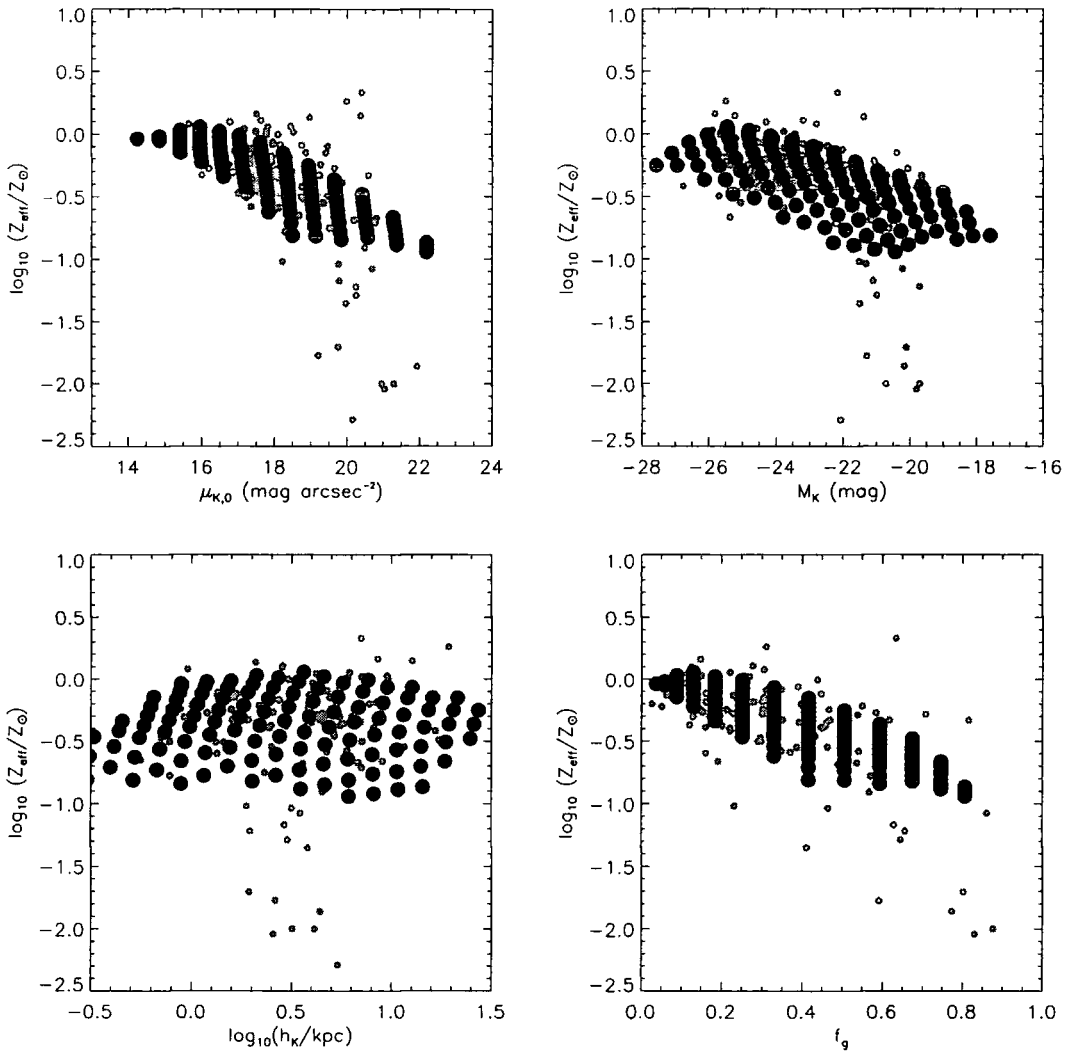

Figure 4.9: Outflow Model O: Correlations between the metallicity at the disc half light radius and the K band disc central surface surface brightness, the K band absolute magnitude, the K band disc scale length and gas fraction. Data from Chapter 3 are shown as grey circles; the outflow model grid is shown as large black circles.

Cole et al. 1999). Furthermore, for galaxies with total masses in excess of 10^9 $M_\odot$, there is very little gas mass loss; however, many of the freshly synthesized metals can be lost reasonably easily (MacLow & Ferrera 1999). Accordingly, we adopt this simple outflow recipe: galaxies with masses greater than 10^{13} $M_\odot$ lose no metals in an outflow; galaxies with masses lower than 10^{13} $M_\odot$ lose increasingly more and more metals with decreasing mass, down to a limit of 10^9 $M_\odot$, where a galaxy loses 90 per cent of its freshly-synthesized metal content. This approximation glosses over

all the physics behind outflow; however, it does allow us to explore the possible effects of outflow in a simple, well-defined way. Note that there is no infall in this model.

Results from the outflow model (model O) are shown in Fig. 4.8. Note that we have increased the true yield p in the outflow case from solar metallicity to 1.5 solar metallicity: as outflow involves the loss of metals from the model galaxies, a larger yield must be used to allow the models to reproduce the mean observed metallicities. In contrast with the infall case, outflow leaves the age of a stellar population relatively unaffected; however, it profoundly affects the metallicity of a galaxy, causing a great deal of scatter in the metallicity–local K band surface brightness diagram. The effects of outflow are more visible in Fig. 4.9, where we plot the metallicity at the disc half light radius against the galaxy parameters. Comparison of Fig. 4.9 for the outflow model with Fig. 4.4 for the fiducial (closed box) model clearly shows that outflow of this type produces a strong mass dependence in the galaxy metallicity; furthermore, a simple model of this type reproduces the metallicity scatter fairly accurately.

4.3.4 Summary

To summarise:

- A local gas surface density-dependent Schmidt SFL describes many of the age and metallicity trends from Chapter 3 surprisingly well. However, the slope of the age–central surface brightness correlation and the age gradients are underpredicted by the fiducial model, which cannot be repaired by invoking infall or outflow.
- If infall is mass-dependent, it can 'imprint' mass-dependency on the galaxy ages without significantly affecting their metallicities.
- If outflow is mass-dependent, it can 'imprint' a metallicity–mass correlation without significantly affecting the ages of the model galaxies.

In this way, the lack of mass dependence in the fiducial model may be alleviated by infall (where less massive galaxies have longer infall timescales) and outflow (where less massive galaxies lose a larger fraction of their newly-synthesized metal content). However, we have not yet considered changes in the SFL: as we found that our results were quite sensitively affected by the SFL in the Schmidt law model, it is worth investigating if some of the shortcomings of the Schmidt law model can be alleviated by the use of an alternative SFL.

Table 4.1. Models used in this Chapter

Model	SFL	n	k	Threshold	Yield	Chemical Evolution
Fiducial	Schmidt	1.6	0.012	N	0.02	closed box
I1	Schmidt	1.8	0.012	N	0.02	mass-independent infall
I2	Schmidt	1.8	0.012	N	0.02	longer infall timescale for small galaxies
I3	Schmidt	1.8	0.012	N	0.02	longer infall timescale for large galaxies
O	Schmidt	1.6	0.012	N	0.03	more outflow from smaller galaxies
TC	Schmidt	1.6	0.012	Y	0.02	closed box
TI	Schmidt	1.6	0.012	Y	0.02	longer infall timescale for small galaxies
D	Ke98	1.0	0.030	N	0.02	closed box

4.4 Star formation laws

4.4.1 Density threshold

One possible modification to the star formation law is the imposition of a cutoff critical density Σ_c below which star formation cannot occur. Kennicutt (1989) found that the radially-averaged star formation rate in a sample of 15 well-studied spiral galaxies was well-described by a critical density model. One physically motivated choice for that critical density is the maximum stable surface density of a thin isothermal gas disc, given by (Toomre 1964; Kennicutt 1989):

$$\Sigma_c = \alpha \frac{\kappa c}{3.36G}, \tag{4.9}$$

where α is a dimensionless constant of order unity, c is the velocity dispersion of the gas (which we take, as Kennicutt did, to be a constant $c = 6\ \mathrm{km\,s^{-1}}$ for all galaxies) and κ is the epicyclic frequency, given by:

$$\kappa = 1.41 \frac{V}{R}(1 + \frac{R}{V}\frac{dV}{dR})^{1/2}, \tag{4.10}$$

where V is the rotational velocity at a radius R (Kennicutt 1989). Kennicutt found that $\alpha \sim 0.67$ was a good fit to his data: stars typically did not form in regions where the density was lower than the critical density, and formed according to a Schmidt law with index $n \sim 1.3 \pm 0.3$ above the critical density threshold.

In order to estimate Σ_c for our model galaxies, we must assume a rotation curve: for simplicity, we adopt the mass-dependent 'universal rotation curve' from Persic & Salucci (1991), given by:

$$V(R) = 200(\frac{M_{\rm baryon}}{M^*_{\rm baryon}})^{1/4}\{1 + (0.12 - 0.24\log_{10}\frac{M_{\rm baryon}}{M^*_{\rm baryon}})(\frac{R}{2.2h} - 1)\}{\rm km\,s^{-1}}, \qquad (4.11)$$

where $M_{\rm baryon}$ is the baryonic mass of the galaxy, $M^*_{\rm baryon}$ is the baryonic mass of a galaxy with an absolute B band magnitude ~ -20.6 (assuming $H_0 = 65$ km s^{-1} Mpc^{-1}; we assume a value $M^*_{\rm baryon} = 1.5 \times 10^{11}\,{\rm M}_\odot$) and h is the scale length of the mass. We use this rotation curve to determine the critical density in our model galaxies: we allow stars to form according to a Schmidt law with $n = 1.6$ and $k = 0.012$ in gas denser than the critical density and do not allow stars to form at densities lower than the critical density. *We do not use a critical density threshold in the central half scale length of the galaxy*: the universal rotation curve is undefined in the inner regions of a galaxy, and the critical density becomes very large in the innermost regions of spiral galaxies due to strong differential rotation. Thus, the behaviour of this star formation law at small radii is ill-constrained in this model: we, therefore, neglect the existence of a critical density at small radii and form stars according to a Schmidt law.

We have run two different density threshold models: one where we assume a closed box and no infall (model TC) and one in which we allow mass-dependent infall for the form assumed for model I2, where lower mass galaxies have longer infall timescales than larger galaxies (model TI).

The closed box density threshold model shows intriguing behaviour: as we use the same Schmidt law parameters (above the critical density) as the fiducial model, we find that the fiducial model and the closed box density threshold model have very similar behaviour (Fig. 4.10). The only significant difference in the threshold model is a sequence of $\sim$ 10 Gyr old regions at all surface brightnesses (these older regions do not significantly affect the global correlations, which are not shown for brevity). This trend can be understood as follows. This galaxy model starts with an initial surface density of gas $\Sigma_{\rm gas}(r)$. For areas with initial surface densities significantly larger than the critical density at that radius $\Sigma_c(r)$, the evolution is unaffected by the critical density, as the gas density never reaches the critical density at that radius. For regions with initial surface densities near the critical density, however, the evolution is profoundly affected: the star formation history is truncated when $\Sigma_{\rm gas}(r) < \Sigma_c(r)$. In these cases, the region lacks the recent star formation that makes the colour-based ages appear younger, thus the colour-based ages are quite old $\sim$ 10 Gyr. Regions with initial gas densities below the critical density simply cannot form stars and are not observed.

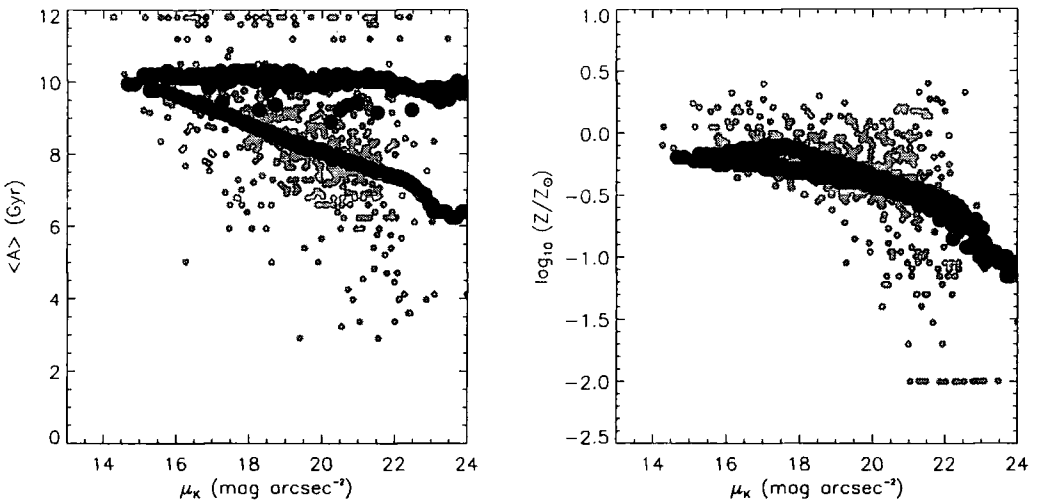

Figure 4.10: Closed Box Critical Density Model TC: Correlation between local K surface brightness and the local age and metallicity of the data from Chapter 3 (grey circles) and the closed box critical density model TC (large black circles).

Indeed, this behaviour was expected when Kennicutt (1989) proposed the existence of a critical density threshold. Many galaxies have gas surface densities close to the critical density, meaning that star formation may use up the remaining gas in a relatively short time. This puts us in the somewhat uncomfortable situation of observing galaxies at a preferred epoch (this is analogous to the gas consumption problem for spiral galaxies e.g. Larson, Tinsley & Caldwell 1980; Kennicutt 1989).

This situation may be alleviated by postulating infall: we test this idea by using the infall histories of model I2 in conjunction with the critical density behaviour of this model in model TI (Fig. 4.11). Because of the infall, regions which have gas densities close to the critical density at the present day only relatively recently reached the critical density and formed a modest amount of stars: this star formation depleted the gas density to the point where the gas density dipped under the critical density again. In this way, the older regions with densities near the critical density that were predicted by the closed box critical density model are avoided, as, instead of forming their stars at early times, they form their stars at later times.

To summarise: the critical density threshold proposed by Kennicutt (1989) does little to affect the global correlations between SFH and physical parameters predicted by models with a Schmidt SFL. This is not to say that the existence of a critical density threshold has no effects at all: it is

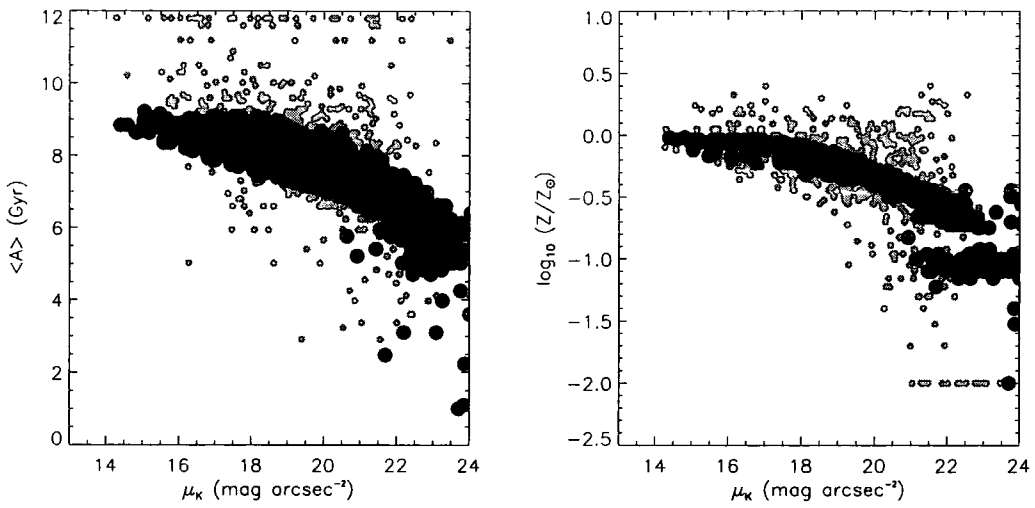

Figure 4.11: Critical Density with Infall Model TI: Correlation between local K surface brightness and the local age and metallicity of the data from Chapter 3 (grey circles) and the critical density with infall model TI (large black circles).

merely to state that the existence of a critical density threshold for star formation mainly affects the spatial distribution of present day star formation and does little to affect the star formation or chemical enrichment histories.

4.4.2 Dynamical time dependence

An alternative SFL was proposed by Kennicutt (1998; Ke98 hereafter) based on his analysis of the global star formation rates of a large sample of spiral and starburst galaxies. The star formation rate in this case scales with the ratio of the gas density to the local dynamical timescale:

$$\psi = k\Sigma_{\rm gas}/\tau_{\rm dyn}, \tag{4.12}$$

where $\tau_{\rm dyn} = 6.16R({\rm kpc})/{\rm V}({\rm km\,s^{-1}})$ Gyr is the dynamical timescale, here defined as the time taken to orbit the galaxy at a distance R. As we did for the critical density model, we use the mass-dependent universal rotation curve of Persic & Salucci (1991) to estimate the dynamical time as a function of radius in our model galaxies. This SFL is similar in many ways to the radially-dependent SFLs proposed by Wyse & Silk (1989) and allows us to explore how explicit radial dependence in the SFL affects how we interpret the trends in SFH with galaxy parameters presented in Chapter 3.

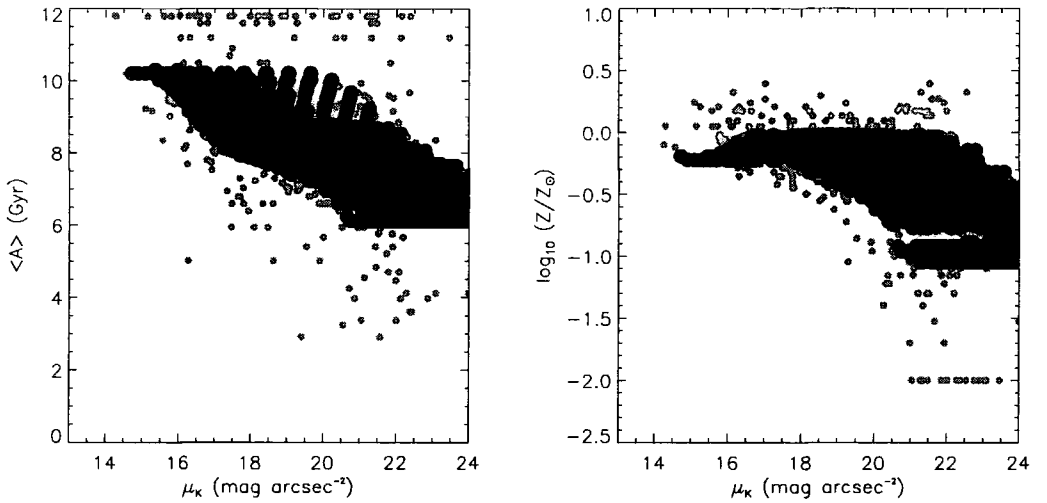

Figure 4.12: Dynamical Time Model D: Correlation between local K surface brightness and the local age and metallicity of the data from Chapter 3 (grey circles) and the dynamical time model D (large black circles).

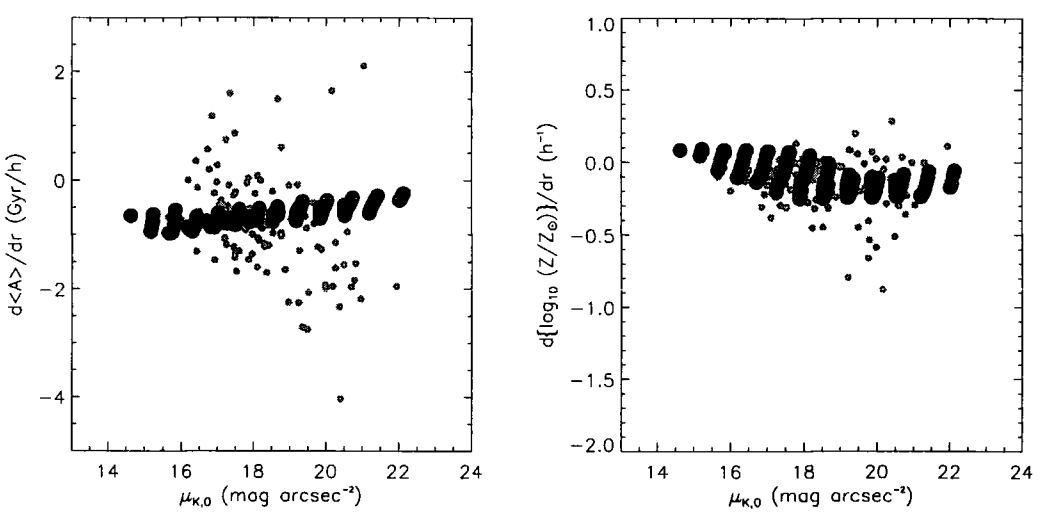

Figure 4.13: Dynamical Time Model D: Correlations between the age and metallicity gradients per K band disc scale length and the K band central surface brightness. Data from Chapter 3 are shown as grey circles; the dynamical time model D grid is shown as large black circles.

In Fig. 4.12 we show the local ages and metallicities given by the dynamical time model (Model D) overplotted on the data for Chapter 3. Kennicutt's (1998) dynamical time dependence describes the trends accurately, while predicting reasonable amounts of scatter. The correlations between global ages and metallicities and the galaxy parameters are similar to those presented in Figs. 4.3 and 4.4 for the fiducial model, but with a reasonably small scatter. One significant difference between the dynamical time model and the fiducial Schmidt SFL model is the predicted age gradients (Fig. 4.13): in contrast to the fiducial model (which substantially underpredicts the average age gradient), the average age gradient expected in the dynamical time model is quite similar to the average observed gradient (c.f. Fig. 4.5). Steeper age gradients are expected from this model: in the limit of a flat rotation curve the Kennicutt (1998) SFL depends linearly on gas density, and the star formation efficiency varies as $1/R$, leading to larger star formation timescales at larger radii. Note, however, that the observed *trend* in age gradient with surface brightness is not reproduced by the dynamical time model. One significant shortcoming of the Kennicutt (1998) dynamical time model is the underprediction of the slope of the age–K band *central* surface brightness correlation: this is a common feature of all the models presented in this Chapter and will require further study to understand the origins of this discrepancy.

4.5 Conclusions and prospects

We have constructed a simple 'toy' model with the aim of gaining some insight into the origins of many of the trends in SFH with galaxy parameters presented in Chapter 3. The model is used to generate colour-based ages and metallicities, which are directly comparable with those derived in Chapter 3. We generated a grid of model galaxies and selected only those which lie in a pre-defined region of the K band absolute magnitude–K band central surface brightness plane.

Using this model, we have found the following:

- A local gas surface density-dependent Schmidt SFL describes many of the age and metallicity trends from Chapter 3 surprisingly well. A model of this type does not explain the mass dependence in SFH required by Chapter 3, however, and significantly underpredicts the age gradient in spiral galaxies and the slope of the age–central surface brightness correlation.
- If infall is mass-dependent, it can 'imprint' mass-dependency on the galaxy ages without significantly affecting their metallicities.
- If outflow is mass-dependent, it can 'imprint' a metallicity-mass correlation without significantly affecting the ages of the model galaxies.

- The existence of a density threshold below which star formation cannot occur does not significantly affect our model predictions, for plausible values of the density threshold.
- Kennicutt's (1998) star formation law which involves both gas density and the dynamical time resolves many of the shortcomings of the Schmidt SFL: scatter in the local age and metallicity vs. surface brightness correlations is naturally accommodated, and the model age gradients are a better (but not perfect) match to the observations.

To summarise, the simplistic modelling presented in this Chapter combined with the observational trends presented in Chapter 3 support the notion that the SFH of a region within a galaxy depends primarily on the *local surface density of gas*. On top of this basic local surface density dependence, *there is some evidence for a dependence on the dynamical timescale*. Large amounts of extended gas infall for more massive galaxies is not favoured: the average ages of such infall models would provide a poor match to the observations presented in Chapter 3. Infall may be important for less massive galaxies, however, and may introduce mass dependence in the average ages of galaxies. One important conclusion is that *metal-enriched outflow from low mass galaxies seems to be required by our data* to provide a mass dependence in the metallicity of spiral galaxies.

More work is clearly required to substantiate these conclusions. In particular, it would be interesting to explore the origin of the steep slope in the age–K band central surface brightness correlation. Many further refinements to this toy model could be made; in particular, better treatment of the rotation curves (especially in the infall cases) and assessment of the effects of a radially-varying infall history would allow much firmer testing of the robustness of our conclusions regarding the accuracy of the Kennicutt (1998) SFL. Another important issue is exploring possible effects that may weaken our conclusions regarding the importance of feedback, as that represents one of the more interesting conclusions of this Chapter. Another area which we have not explored is comparison with other types of data: interesting independent constraints on e.g. the SFL could be gained from comparison of the model predictions and e.g. Kennicutt's (1998) global star formation rate–gas density correlations, Ryder and Dopita's (1994) correlation between Hα and I band surface brightness, or Kennicutt's (1989) radially-averaged star formation rate profiles.

Chapter 5

The bimodal spiral galaxy surface brightness distribution

In Chapters 2–4, we implicitly assumed that the properties of spiral galaxies and physical processes that dictate their star formation histories smoothly vary, so that galaxies possess a continuous range of e.g. masses and surface densities. However, the basis of this argument is clearly flawed if spiral galaxies come in e.g. two distinct families, each with their own distinct evolutionary histories. Tully & Verheijen (1997) claimed that the near-infrared spiral galaxy surface brightness distribution is bimodal, suggesting that there are fundamental differences between high surface brightness and low surface brightness galaxies, placing many of the basic assumptions in Chapters 2–4 in doubt. Here, we assess the statistical significance of this bimodality in the surface brightness distribution and investigate the uncertainties inherent in the determination of this surface brightness distribution.

5.1 Introduction

The distribution of spiral galaxy disc surface brightnesses is of great observational and theoretical importance in extragalactic astronomy. Observationally, knowledge about the present day disc galaxy central surface brightness distribution (SBD) allows us to better understand the importance and implications of surface brightness selection effects, which is important for e.g. understanding the local galaxy luminosity function (e.g. de Jong & Lacey 1998; Dalcanton 1998) or in comparing galaxy populations at low and high redshifts (e.g. Simard et al. 1999). Theories of galaxy formation and evolution link the SBD with the angular momentum, mass and star formation history of galaxies: indeed, the SBD has been used as a constraint on some galaxy evolution models (Dalcanton, Spergel & Summers 1997; Mo, Mao & White 1998; Cole et al. 1999).

Previous studies have generally found a SBD that can be described as flat or slowly declining with surface brightness, modulated by a sharp cut-off at the high surface brightness end, normally associated with the Freeman (1970) value (e.g. de Jong 1996b, dJIII; McGaugh 1996).

Tully and Verheijen (1997; TV hereafter) derived the SBD of a complete sample of 60 spiral discs in the Ursa Major Cluster from an imaging study in the optical and near-infrared (Tully et al. 1996). Their data suggested an inclination-corrected near-infrared *bimodal* SBD (as opposed to the conventional *unimodal* distribution described above) with a peak associated with the Freeman value and a second peak $\sim$ 3 mag arcsec^{-2} fainter, separated by a gap (Fig. 5.1, solid line in panel a). This would have far-reaching implications for our understanding of galaxy formation and evolution. A bimodal SBD would imply that there are two discrete galaxy populations — a high surface density population and one with surface densities a factor of $\sim$ 10 lower (assuming comparable mass to light ratios for the two populations). Correspondingly, the masses, spin distributions and star formation histories of these two families of galaxies would adopt one of two preferred states, and plausible mechanisms for generating these discrete differences in e.g. star formation history, or spin distribution, would have to be found.

Why this bimodal distribution was not found before is an important question. TV address this problem at length: here we will summarise their main arguments. First, the bimodal SBD is based on near-infrared K' data and, in fact, is *only* apparent there. Near-infrared photometry is much less susceptible to the effects of dust extinction than optical photometry. TV demonstrate that in the optical B band the bimodality is washed out by these extinction effects (accordingly, we do not consider TV's optical SBDs here). A bimodal SBD may, therefore, remain undetected in optical studies (e.g. McGaugh 1996, de Jong & Lacey 1998).

Second, the TV SBD has been determined from a complete sample of galaxies at a common distance, making selection effects much easier to understand. This may explain why dJIII, using K band photometry for a sample of field spiral galaxies, did not report any sign of bimodality in his SBD.

In an attempt to investigate whether the bimodal distribution could be caused by environmental differences, TV defined an isolated subsample, consisting of 36 galaxies that have a projected distance $>$ 80 kpc to their nearest neighbour (assuming a distance to the Ursa Major Cluster of 15.5 Mpc, corresponding to $H_0 = 85$ kms^{-1} Mpc^{-1}). They found that the gap is more pronounced in this isolated subsample and attributed intermediate surface brightnesses found in their total sample to interactions (Fig. 5.1, solid line in panel b).

Unfortunately, TV did not attempt to robustly estimate the significance of the apparent bimodality. Their only estimate is based on the isolated subsample where they compare the number of galaxies in the 1.5 mag wide gap (between $\sim$ 17.5 and $\sim$ 19 mag arcsec^{-2}; 3 galaxies) with the number of galaxies that they expected to see in that gap (20 galaxies). This expectation value was derived from a model unimodal distribution normalised to reproduce the peak number of galaxies in the high surface brightness bins, *not* the total number of galaxies. Properly normalising the model distribution lowers the expectation from $\sim$ 20 galaxies to $\sim$ 12 galaxies.

In this Chapter, we investigate the significance of the bimodal near-infrared SBD, focussing on whether this bimodality is simply an artifact of small number statistics. In sections 5.2 and 5.3, we use a Kolmogorov-Smirnov (KS) style of test to address this question, investigating the significance of both the total and isolated samples. In section 5.4, we discuss the results, focussing on the rôle of inclination corrections. We present our main conclusions in section 5.5.

5.2 Constructing a null hypothesis

In order to test the significance of the bimodality in the SBD, it is necessary to choose a null distribution to test the observations against. Ordinarily, it would be best to choose some kind of 'best bet' observationally determined or theoretically motivated null hypothesis: failure of this null hypothesis would indicate that it does not accurately describe the dataset. However, in this case, we wish to quantify the significance of a particular *feature* in the observational distribution, namely the bimodality in the Ursa Major Cluster SBD. For this reason, it is necessary to be careful about choosing a null distribution: if a null distribution was chosen which did not adequately describe the general features of the SBD, then a high significance (i.e. a low probability of obtaining the data from the null) would *not* represent a large degree of bimodality, but rather would indicate that the null hypothesis was a poor match to the general shape of the SBD.

For this reason, we have chosen to *fit* a relatively simple model distribution to the data (taking into account selection effects), allowing us to determine the significance of the bimodality by minimising the mismatches between the general shapes of the two distributions.

For the unimodal model, we use a generalised version of the optical SBD presented in McGaugh (1996):

$$\log_{10}\Phi(\mu_{K',0}) = m(\mu_{K',0} - \mu^*_{K',0})$$

$$\text{where} \quad \begin{cases} m = m_f \text{ if } \mu_{K',0} \geq \mu^*_{K',0} \\ m = 2.6 \text{ if } \mu_{K',0} < \mu^*_{K',0} \end{cases}$$

The critical surface brightness $\mu^*_{K',0}$ and the faint-end slope m_f are adjustable parameters which are fit below. [1] For reasonable values of m_f, the number of galaxies per unit mag arcsec^{-2} only slowly changes with surface brightness and falls quite sharply to zero above a given 'critical' surface brightness $\mu^*_{K',0}$ (see e.g. the dashed line in panel e of Fig. 5.1).

To take into account the selection effects that affect TV's observations, it is also necessary to adopt a scale size distribution: we assume that the scale size distribution is constant (per logarithmic interval) over the interval $\log_{10} h_{K'} = 0.8$ to $\log_{10} h_{K'} = 1.7$ (~6.3 arcsec to 50.1 arcsec or at an adopted distance of 15.5 Mpc, ~0.5 to 3.8 kpc).

Selection criteria are modelled by choosing only galaxies with isophotal magnitudes $m_{K'} < 12$ and isophotal diameters $D_{K'} > 60''$, both measured at the 22.5 K' mag arcsec^{-2} isophote. Though these criteria differ slightly from those used by TV (as their selection was made in B band rather than K' band), they are comparable to better than 0.5 mag, assuming $B - K' \sim 3$ for faint late-type galaxies (de Jong 1996c, dJIV), and accurately follow the surface brightness and size limits on TV's $\mu_{K',0} - \log_{10} h_{K'}$ plane. We emphasize that we do not hope to somehow represent the 'universal' K' band SBD with this function; we simply aim to construct a plausible, simple SBD that provides a sensible single-peaked fit to the observed bimodal Ursa Major SBD.

In panel e in Fig. 5.1, we show a 10^4 galaxy Monte Carlo realisation of a model distribution with $\mu^*_{K',0} = 16.3$ and $m_f = 0.0$ (also in panels a and b and in cumulative form in panels g and h as a dashed line). We also show the same model distribution without the selection effects (with arbitrary normalisation) in panel e as a dashed line.

5.3 Results

In the above section, we described the single-peaked distribution that we will fit to the observed SBD. As we want to take into account selection effects in the null distribution, we cannot make a straightforward fit, but have to use Monte Carlo realisations of the null distribution and associated selection effects. We generate a grid of Monte Carlo unimodal distributions, each containing 10^4 galaxies (later renormalised to contain the same number of galaxies in the observed SBD) and each with different values of $\mu^*_{K',0}$ and m_f (with grid steps of 0.05 in $\mu^*_{K',0}$ and 0.02 in m_f). The best fit unimodal distribution is determined by minimising the Cash statistic $C = -2\sum_{i=1}^{n_{bins}} \log P_i(n, \lambda)$, where $P_i(n, \lambda)$ is the Poissonian probability of observing n galaxies in a bin which the unimodal model predicts should have a mean galaxy number of λ (Cash 1979). The Cash statistic has the

[1] McGaugh's original values were $\mu^*_0 = 21.5$ B_J mag arcsec^{-2} and $m_f = -0.3$, which are roughly consistent with the best fit results described in section 5.3.

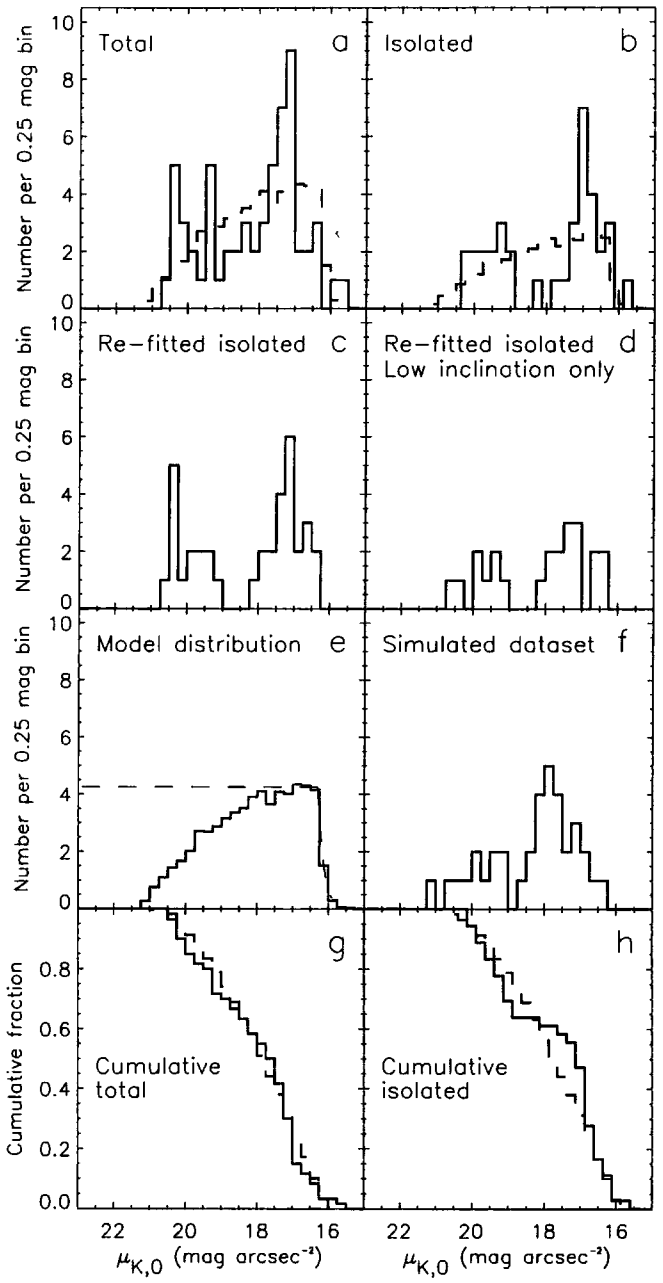

Figure 5.1: The SBD for the total sample of 60 galaxies (solid line in panel a) and for the isolated subsample of 36 galaxies (solid line in panel b). Also shown in panels a and b is a normalised representative null distribution (dashed line). Panel c contains our re-fitted isolated galaxy subsample, and panel d shows the low inclination isolated galaxies only. Panel e contains a representative model distribution taking selection effects into account (solid line), and shows the same distribution without taking into account the selection effects (dashed line, with an arbitrary normalisation). Panel f shows a 36 galaxy realisation of the single-peaked model distribution, chosen to appear reasonably similar to the isolated galaxy subsample. Panels g and h show the cumulative distribution function for the total and isolated subsamples respectively. Solid lines depict the observed cumulative SBDs and dashed lines represent the model distribution.

advantage that the underlying distribution does not have to be Gaussian. As the model grid used to determine the best fit is itself a Monte Carlo realisation of the true underlying model grid, the best fit parameters will depend slightly on the model grid realisation used. This ultimately affects the significances that we will derive later. We have, therefore, run the code 10 times, and thus constructed 10 realisations of the entire model grid, and derived a best fit for each of these realisations. The best fit unimodal distribution typically has parameters around $\mu^*_{K',0} \sim 16.35 \pm 0.05$ mag arcsec^{-2} and a faint end slope $m_f \sim 0.05 \pm 0.08$, where these uncertainties are the RMS variation in the fit parameters.

To estimate the significance of the departures of the observed SBD from the best fit model distribution, we use the KS statistic $d_{\rm max}$, defined as the maximum distance between the cumulative distributions of the model and the data (i.e. the maximum distance between the solid and dashed lines in panels g and h of Fig. 5.1). The $d_{\rm max,obs}$ between this best fit model and observed SBD is then measured.

However, because we have *fitted* a single peaked distribution to the bimodal SBD, it is not possible to convert the measured $d_{\rm max,obs}$ into a probability in the standard way (e.g. Press et al. 1986). [2] Therefore, it is necessary to use Monte Carlo simulations to convert the measured maximum distance into a probability. Accordingly, we generated 100 random simulated datasets from the best fit model and subjected them to the *same fitting and maximum distance measuring procedure as the data.* In this way, we determined what the distribution of maximum distances should be from the simulations. The fraction of simulations with maximum distances larger than the $d_{\rm max,obs}$ then gives us the probability P that the observed dataset was a statistical accident.

Because the model unimodal distributions are Monte Carlo realisations of the true model distributions, this procedure (i.e. generating the 100 datasets and measuring the significance) was repeated for each of the 10 model grid realisations described above, to allow more accurate measurement of the significance. The significance is defined as $1 - P$, with P defined as above. Significances for the total sample of 60 galaxies, and the isolated sample of 36 galaxies are given in Table 5.1. Quoted significances are the mean (along with the error in those means) of the 10 runs. Note that we also carried out this analysis in two different programming languages on two different computers using different sets of random number generators: the results were found to be indistinguishable to within the quoted errors.

[2] Note that the binning of the data in a histogram also, strictly speaking, invalidates the use of a standard KS test, although if the binning is over a much smaller scale than the 'structure' in the SBD (as it is in this case), tests have shown that the effects on the final significances are negligible.

Table 5.1. The significance of the bimodality in the Ursa Major Cluster

Sample	$N_{\rm gal}$	Significance
total	60	58% ± 4%
isolated	36	96.0% ± 0.5%
isolated (re-fit)	36	86% ± 1%
low i isolated	23	42% ± 3%

5.4 Discussion

From Table 5.1, it is clear that the bimodality shown by the total sample is not statistically significant. However, the isolated subsample shows a bimodality significant at the 96 per cent level. To understand if this high significance of the histogram for the isolated subsample reflects a true, astrophysical bimodality in the Ursa Major Cluster, it is necessary to understand the assumptions used to construct the isolated galaxy SBD.

An obvious check is to see whether systematic effects in the data can produce a bimodality, e.g., because of bulge contamination in the fits. We refit the surface brightness profiles presented in Tully et al. (1996), using the 'marking the disc' technique (the same technique that was used by TV), to check that there were no obvious personal biases in the fitting of the surface brightness profiles. Comparing our K' band central surface brightnesses with those of Tully et al. (1996), we found a mean offset of +0.16 mag arcsec^{-2} (in the sense that our re-fit surface brightnesses are fainter) and that 68 per cent of the central surface brightnesses compared to better than ± 0.25 mag arcsec^{-2} (both with and without this mean offset applied; c.f. Chapter 2). When corrected for inclination in exactly the same way as TV (assuming an infinitely thin disc; by subtracting $2.5\log_{10}(b/a)$, where b/a is the minor to major axis ratio), the two versions of the isolated subsample SBD are virtually indistinguishable (see Fig. 5.1, panel c), and the significance of the refitted distribution is hardly different, decreasing slightly to 86 per cent. This suggests that there are no systematic personal biases in the fits TV use that might introduce a spurious bimodality. Note that de Jong (1996a, dJII) shows that the 'marking the disc' technique is unbiased, with ~ 90 per cent of the central surface brightnesses accurate to 0.5 mag, compared to more sophisticated bulge-disc decomposition techniques.

However, because there was no inclination cut applied to the Ursa Major sample, some of the inclination corrections that were applied to the K' band surface brightnesses were rather large: in

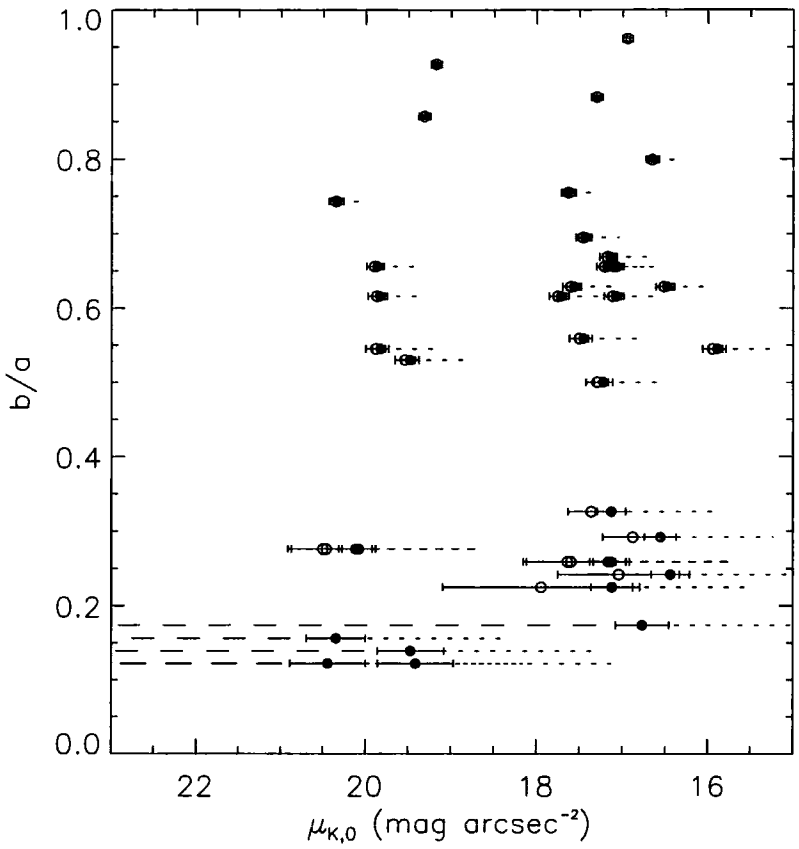

Figure 5.2: Uncertainties in inclination corrected surface brightness against the axial ratio b/a. We show the surface brightness of the galaxy corrected for inclination assuming an infinitely thin disc (solid circles) connected by a dashed line to the inclination corrected surface brightness assuming an intrinsic disc axial ratio q_0 of 0.20 (open circles). Error bars denote the uncertainty in surface brightness due to (a rather generous) error in axial ratio of 0.05. Dotted lines connect the inclination corrected surface brightness to the *uncorrected* surface brightness.

$\sim$ 1/3 of the cases (in either the total or isolated samples) they exceeded 1 mag. However, large inclination corrections are highly uncertain for a number of reasons, even in K' band.

In Fig. 5.2, we show only two of the many uncertainties that affect inclination corrections in K' band. First we computed the corrected surface brightnesses, assuming i) an infinitely thin disc (solid circles) and ii) an intrinsic disc axial ratio $q_0 = 0.2$ (Holmberg 1958; open circles). These two values are connected with a dashed line in Fig. 5.2. The error bars in Fig. 5.2 represent the random uncertainty in the inclination correction due to axial ratio errors of 0.05. Taken together, this shows that the inclination corrections for galaxies with axial ratios b/a below 0.4 have considerable systematic uncertainties stemming from our poor knowledge of the intrinsic axial ratios of galaxies, coupled with the random uncertainty associated with measurement error. Taken

together, consideration of these two uncertainties argues that the inclination corrections applied in this Chapter and by TV are likely to be lower limits.

However, a number of effects conspire to make inclination corrections smaller, suggesting that the inclination corrections might actually be upper limits. Firstly, the effects of dust in nearly edge-on galaxies is non-negligible, even in the K' band, which could lower the inclination correction by roughly 0.3 mag (Tully et al. 1998). Secondly, averaging of the surface brightness profiles over elliptical annuli at high inclinations (as in this case) is likely to produce systematic underestimates of the real central surface brightness (Huizinga 1994). Finally, at large inclinations, the assumption of a thin, uniform slab disc breaks down: vertical and radial structure in the galaxy will affect the inclination correction in non-trivial ways. Accordingly, in Fig. 5.2 we have also connected the inclination corrected surface brightness with the uncorrected surface brightness with a dotted line.

In Fig. 5.2, we can see that uncertainties in these large inclination corrections may go some way towards filling in the gap in the SBD. As an example, we consider the four galaxies with the largest inclination corrections. UGC 6667, UGC 6894, NGC 4010 and NGC 4183 have > 2 mag inclination corrections and uncorrected (reasonably high) K' surface brightnesses between 17 and 18.5 mag arcsec^{-2}. The large corrections move them across the gap from the high surface brightness into the low surface brightness regime. However, if these corrections are at all uncertain, they may in reality lie in the gap of the K' band SBD. Moving even one or two of them into the gap in the isolated galaxy SBD would decrease markedly the significance of the bimodality in the isolated subsample. Certainly a few of the galaxies mentioned above suffer from problems that may seriously affect the value of the inclination correction (not because of the uncertainty in axial ratio, but because of uncertainties in e.g. the vertical and radial structure in the galaxy): NGC 4010 is clearly lopsided, with one half of the galaxy puffed up with respect to the other half, while NGC 4183 has a clear warp.

Because of these serious uncertainties in the larger inclination corrections, and because there are no clear recipes for producing more realistic inclination corrections which take into account dust and the vertical and radial structure of the disc, the only fair thing to do is omit the high-inclination galaxies from the SBD. Accordingly, the high-inclination galaxies were removed from the isolated subsample, leaving 23 galaxies with b/a larger than 0.4, corresponding to an inclination of less than 66° or inclination corrections smaller than 1 mag. The resulting SBD is shown in Fig. 5.1, panel d: the bimodality is insignificant in this SBD, due primarily to small number statistics (Table 5.1). To check how large the sample size needs to be to detect significant bimodality in the low inclination isolated subsample, we simulated intrinsically bimodal datasets and tested them

using the above procedure. Bimodal datasets were generated using two normal distributions with $\sigma = 0.5$ mag and means of 17.15 and 19.85 mag arcsec^{-2}, with the high surface brightness peak containing on average 63 per cent of the galaxies (thus resembling the TV distribution). These simulations showed that in order to detect a bimodality at the 95 (99) per cent level in the low inclination sample at least 4/5 of the time, the sample size needs to be increased to around 50 (100) galaxies.

5.5 Conclusions

We have reanalysed Tully & Verheijen's (1997) bimodal SBD, using a Kolmogorov-Smirnov style of test to estimate the likelihood that a single-peaked distribution would be able to reproduce the bimodality in the Ursa Major Cluster.

- The total sample of 60 galaxies is not bimodal: it is inconsistent with a single-peaked distribution at only the 58 per cent level.
- However, the isolated subsample of 36 galaxies is significantly bimodal: it is inconsistent with the null distribution at the 96 per cent level.
- We refit the K' band surface brightness profiles of the Ursa Major sample, and found that this refit made relatively little difference, with the isolated subsample retaining a reasonable significance of 86 per cent.
- However, we argue that large inclination corrections are uncertain even in the near-infrared, placing the reality of the gap between high and low surface brightness galaxies in some doubt.
- When the galaxies with inclination corrections > 1 mag are removed from the isolated subsample, the significance of the 23 galaxy subsample drops to only 40 per cent.
- Assuming that the low inclination, isolated galaxy SBD is truly bimodal, in order to increase the significance to 95 (99) per cent, it is necessary to increase the low inclination isolated galaxy sample size by around a factor of two (four).

To summarise, if inclination corrections greater than 1 mag can be trusted, then there is reasonable evidence that the Ursa Major Cluster SBD is bimodal. If, however, these large inclination corrections are in some doubt, then the SBD lacks a sufficient number of galaxies to argue convincingly against a unimodal SBD. Either way, to convincingly demonstrate at the 99 per cent level that the near-infrared spiral galaxy SBD is bimodal will require an independent dataset to be used with

around a factor of four more low inclination, isolated galaxies than are included in the Ursa Major Cluster sample.

Part 2

The formation epoch of early type galaxies

In Part 2, we consider constraints that can be placed on the formation epoch of early type galaxies by investigation of their broad band colours. Early type galaxies both in the field and in clusters exhibit a strong correlation between their absolute magnitudes and colours: the colour-magnitude relation (Visvanathan & Sandage 1972; Larson, Tinsley & Caldwell 1980; BLE). The colour-magnitude relation is most naturally interpreted as a metallicity sequence, with much of the scatter in the relation driven by differences in galaxy age (BLE; Kodama et al. 1998; Bower, Kodama & Terlevich 1998). Thus, study of the colour-magnitude relation at high redshifts, where we observe early type galaxies closer to their probable formation epoch, places strong constraints on their star formation history.

In Chapter 6, we describe a Bayesian photometric redshift estimator. The distinguishing features of this particular estimator are that we account for galaxy metallicity explicitly in the estimation procedure and use the magnitude of the galaxy to help distinguish between the inevitable degeneracies in redshift that can arise during photometric redshift estimation. In Chapter 7, we use this redshift estimator to produce a colour-magnitude diagram for morphologically-classified early type galaxies in the northern Hubble Deep Field. We then place constraints on the formation redshifts of these early types, concluding that around half of the stars in early type galaxies at $z \sim 0.9$ formed at redshifts greater than two.

Chapter 6

A Bayesian photometric redshift classifier: identification of high redshift clusters

6.1 Introduction

Constraining the formation epoch of early-type galaxies is a topic of great astrophysical relevance today, both observationally and theoretically. Using large telescopes and a range of increasingly sensitive and innovative instrumentation, it has become possible to use a range of photometric and spectroscopic techniques to place ever tighter constraints on the star formation histories of early-type galaxies. Line strength studies of local galaxies (Kuntschner & Davies 1998; Bernardi et al. 1998; Terlevich et al. 1999) and studies of the colours of early-type galaxies at a range of redshifts from $z = 0$ to $z \gtrsim 1$ (BLE; Stanford et al. 1998; Kodama et al. 1998; Abraham et al. 1999; Menanteau et al. 1999; Chapter 7) all paint a remarkably consistent picture in which the bulk of the stellar populations of early-type galaxies form at redshifts $z \gtrsim 2$ and passively evolve to the present, with only modest amounts of star formation persisting in the faintest early-types to the present day. This picture, in turn, is broadly consistent with the hierarchical growth of galaxies in both clusters and the field, with the stellar populations in the most luminous giant ellipticals forming before the smaller, low-luminosity early-types (Baugh et al. 1998). In addition, an offset is expected between the formation history for ellipticals in the field and in clusters: as clusters form from large overdensities at early times, the formation history is much advanced in clusters compared to early-types in less dense environments, especially for the less luminous early-type galaxies (Baugh et al. 1998, Kauffmann & Charlot 1998a).

However, probing the formation histories of early-type galaxies at even higher redshifts (closer to their probable formation epoch) represents a considerable technical challenge. While images that reach these depths are now relatively commonplace, spectroscopic follow-up of these faint galaxies is extremely time consuming even on 8m-class telescopes. These problems are offset by the multiplex capability of multi-object spectrographs (e.g. LDSS; Allington-Smith et al. 1994) and fibre-optic fed spectrographs (e.g. Taylor 1995) or by surveys targeted at specific redshifts using tuneable narrow band filters (e.g. Jones & Bland-Hawthorn 1997). Nevertheless, even in the best studied deep images, only a small fraction of the galaxies have known spectroscopic redshifts.

Whereas spectroscopic redshifts use sharp absorption and/or emission lines to accurately determine the rest wavelength of the spectrum, it is also possible to exploit the overall characteristic shape of the spectral energy distribution (SED) to estimate the galaxy's redshift. This 'photometric redshift' approach can be applied to broad band images provided they have sufficiently high signal to noise and adequately sample the important features of the SED. In particular, the 4000 Å spectral break and the Balmer and Lyman series limits are important features that arise in almost all galaxy spectra. Although precise redshifts cannot be determined by this method, estimates of (or limits on) z are obtained.

The existing photometric redshift estimators fall into three main classes: empirical redshift estimators, those based on observed SEDs and model-based redshift estimators. Empirical redshift estimators (Connolly et al. 1995) are based on a training set of galaxies for which the redshifts and broad band fluxes are known. These are used to train an estimator, for example a multi-dimensional polynomial fit, that predicts the redshift from the input fluxes with minimum error. The disadvantage of this method is that it requires a relatively large training dataset with high quality colours and known redshifts. This makes it difficult to apply beyond the limits of spectroscopic surveys, although this problem might be alleviated using the colours of distant, gravitationally lensed galaxies. However, this method, when tested against independent but similar data, can give impressive accuracy ($\sigma_z \sim 0.06$; Connolly et al. 1995).

Lanzetta et al. (1996), Mobasher et al. (1996) and Sawicki et al. (1997) use an approach based on local, observationally determined template SEDs of galaxies covering a wide range of spectral types. Redshifts are estimated from broad band data by redshifting each of the templates and determining the best match to the observational colours. They emphasise the importance of using observed templates in order to incorporate the effects of dust. This is particularly important for galaxies in the redshift range $1 < z < 3$ because the optical colours increasingly reflect the rest frame ultraviolet spectrum of the galaxy. One problem with this approach, however, is that the

spectral library does not take into account the evolution of the galaxy stellar populations. However, the method can accommodate evolution in as far as it is equivalent to changing galaxies between different spectral types.

Model-based approaches use stellar population synthesis codes (e.g. Bruzual & Charlot 1993) to produce model SEDs that can then be compared to the observed data. For example, Gwyn & Hartwick (1996) used a spread of galaxy models from single burst stellar populations to models with constant star formation to model present-day galaxies. When generating redshifted model SEDs, the evolution of the stellar population is automatically taken into account. The redshift of the observed galaxy is determined by minimising χ^2 residuals. The main limitation of this approach is model uncertainties: model spectra are less accurate than observational templates and are sensitive to the assumptions that are made about dust, metallicity of the stellar populations and emission from ionised gas in the galaxy (all of which are implicitly included in observed template spectra but not model spectra). For this reason, model-based approaches tend to be somewhat less accurate than approaches based on redshifting observed template SEDs.

In this Chapter, we focus more closely on the interrelation between star formation history and redshift estimation. As we have outlined, photometric redshifts can be susceptible to changes in the galaxy stellar population. For instance, the effects of age, metal abundance and on-going star formation are all reflected in the relative shape of the continuum, particularly when it is convolved with the response of standard broad band filters. It is important that these uncertainties are taken into account when determining the galaxy redshift. We develop a method of photometric redshift determination that explicitly takes into account the degeneracies implied by these variations. Clearly, incorporating additional free parameters to describe the star formation history of the galaxy threatens to make it impossible to extract useful redshift information. However, many of the changes in colour caused by different star formation histories are degenerate: this is the familiar age-metallicity degeneracy that has long plagued the estimation of star formation histories of composite stellar populations. We will show that for red galaxies, the strong 4000 Å break in their spectra means that redshifts can be determined under only weak assumptions about the star formation history. At lower redshifts, due to the lack of strong spectral breaks in the optical, the colours of blue (disc) galaxies become considerably harder to disentangle.

Our approach attempts to deal with this unavoidable degeneracy in colours with variations in redshift and star formation history. We explicitly account for *galaxy metallicities* and *star formation histories*; these effects are in many cases degenerate with uncertainties due to the stellar initial mass function (IMF), recent star formation, dust extinction and cosmology. We retain possible

degeneracies in plausible values of galaxy type and redshift by storing a 'probability map' for each galaxy, which can be used to estimate a range of acceptable redshifts rather than reducing the observed data to a single 'best bet' estimate of galaxy type and redshift. Our motivation is to use this method to study the photometric properties of $z \sim 1$ field and cluster galaxies with as little selection bias as possible.

The structure of this Chapter is as follows. In section 6.2, we discuss the stellar population models used in this redshift estimator. We derive colour tracks for a range of star formation histories and outline the major uncertainties in these tracks. This provides the framework for selecting appropriate filter sets and the required photometric accuracy. Section 6.3 details our Bayesian approach to redshift estimation. We explicitly incorporate a wide variety of plausible star formation histories, and the resulting degeneracies, in our redshift estimates. The rôle of the prior is discussed. In section 6.4, we test our method with galaxies in Abell 370 cluster field and galaxies with known redshifts in the northern Hubble Deep Field (HDF). In section 6.5, we simulate the recovery of a high redshift $z = 1$ cluster, illustrating the strengths and limitations of the use of photometric redshift techniques for the study of high redshift stellar populations (see also Chapter 7). Finally, we present our conclusions in section 6.6.

6.2 Colour tracks as a function of star formation history

6.2.1 Model

The evolutionary population synthesis model of Kodama (1997) was used to predict the photometric properties of evolving stellar populations. This model calculates the spectral evolution of a galaxy with an arbitrary star formation history, taking into account the chemical evolution in a self-consistent way. KA97 applied this model to the elliptical galaxy populations of distant clusters. In this study, disc models with ongoing star formation are considered in addition to the elliptical models. We first describe the basic equations and parameters of this model and then summarise the elliptical galaxy and disc galaxy models.

6.2.1.1 Equations and parameters

We assume that the galactic gas is supplied from a surrounding gas reservoir trapped in the gravitational potential of a galaxy and that the gas is always well-mixed and distributes uniformly in a galaxy (the one-zone approximation). The star formation is described by the following equations. The stellar IMF is given by a single power law:

$$\phi(m) = Am^{-x}, \quad m_l \leq m \leq m_u, \tag{6.1}$$

where m_l and m_u are lower and upper limits of initial stellar mass respectively. The Salpeter (1955) IMF corresponds to $x = 1.35$. The coefficient A is determined by,

$$\int_{m_l}^{m_u} \phi(m)dm = 1. \tag{6.2}$$

The IMF is assumed to be time invariant. The star formation rate (SFR) $\psi(t)$ is assumed to be proportional to the gas mass $M_g(t)$:

$$\psi(t) = \frac{1}{\tau} M_g(t), \tag{6.3}$$

where τ is the star formation time scale in Gyr. Note that this formulation gives an exponentially decaying SFR with an effective time scale τ/α in the case of the simple models, where α is the so-called locked-up mass fraction defined by Tinsley (1980; see also Chapters 3 and 4). The Salpeter mass function ($x = 1.35$) with $m_l = 0.1$, $m_u = 60$ $M_\odot$ gives $\alpha = 0.72$. The gas infall rate $\xi_{in}(t)$ depends on the initial total mass of the gas reservoir M_T and the gas infall time scale τ_{in}:

$$\xi_{in}(t) = \frac{M_T}{\tau_{in}} \exp(-\frac{t}{\tau_{in}}) \tag{6.4}$$

(c.f. Köppen & Arimoto 1990). The gas metallicity $Z_g(t)$ is calculated numerically, using the basic equations of chemical evolution (Tinsley 1980; see also Chapter 4) and stellar nucleosynthesis tables (Nomoto 1993). The metal contribution from SNIa is also considered by fixing their lifetime at 1.5 Gyr. We assume that the metal-enriched gas spreads through the galaxy instantaneously and evenly (the one-zone approximation). As the initial conditions, we assume that there is no gas in a galaxy before the onset of star formation; *i.e.* $M_g(0) = 0$ and $Z_g(0) = 0$. Using the infall history defined as above, our expression for the star formation rate $\psi(t)$ and the metallicity of the stars $Z(t) = Z_g(t)$, the integrated spectrum of a galaxy can be synthesised as a function of time. By specifying the galaxy age, or equivalently its formation redshift, and cosmological parameters, we obtain the spectra and, therefore, colour indices of the galaxy as a function of redshift. The cosmological parameters are set to $H_0 = 50$ km s^{-1} Mpc^{-1}, $\Omega_0 = 1.0$, and $\Lambda_0 = 0.0$, unless otherwise stated.

6.2.1.2 Elliptical galaxies and bulges

For elliptical galaxy models (E models), we use $x = 1.10$, $m_l = 0.1$ $M_\odot$ and $m_u = 60$ $M_\odot$ for the IMF and short time scales of star formation and gas infall: $\tau = \tau_{in} = 0.1$ Gyr. The slope of the IMF differs from the Salpeter value $x = 1.35$ to allow the colours of the reddest giant ellipticals to be reproduced in the context of this model (with a Salpeter IMF, metallicities which are high enough cannot be achieved). In addition, in order to reproduce the observed present-day

dependence of elliptical galaxy colour on luminosity, it is useful to introduce another parameter, the galactic wind epoch t_{gw}. At this time, the energy put into the ISM in the proto-elliptical galaxy by SNe is large enough to overcome the potential of the galaxy, resulting in the ejection of the gas from the galaxy, ending star formation. We constructed a model sequence of elliptical galaxies as a function of total luminosity by simply changing t_{gw} so that they reproduce the colour-magnitude relation (CMR) of Coma ellipticals in $V-K$ and $U-V$ (Bower, Lucey & Ellis 1992a, 1992b) at a galaxy age T_G =12 Gyr. Changing t_{gw} is equivalent to adjusting the mean stellar metallicity of the galaxies; therefore, we call this the *metallicity sequence* of elliptical galaxy models. In this model, the mean stellar metallicity $\langle$[M/H]$\rangle$ changes from 0.06 to −0.52 over a six magnitude range from the brightest E model ($M_V = -23$ mag at $z = 0$). The time until the onset of a galactic wind t_{gw} is always shorter than ~0.5 Gyr, thus the star formation in elliptical galaxies is burst-like. The above model sequence is shown to reproduce the evolution of the CMR of elliptical galaxies in distant clusters in KA97 and Kodama et al. (1998).

To represent the photometric properties of disc galaxy bulges, we borrow the elliptical galaxy models. Observational support for this includes the results of Mg_2 index analysis (Jablonka, Martin, & Arimoto 1996).

6.2.1.3 Discs

For the disc component, the IMF parameters are set to $x = 1.35$, $m_l = 0.1$, $m_u = 60$ $M_\odot$ and longer time scales of star formation and gas infall: $\tau = \tau_{in} = 5$ Gyr. The age of a galactic disc is fixed at 12 Gyr. The disc model time scales are chosen to reproduce the integrated $B-V$ colours and M_g/L_B (gas mass to blue luminosity) ratio of observed discs of various Hubble types as shown in Fig. 6.1 (c.f. Shimasaku & Fukugita 1997).

The $B-V$ colours of discs shown in Fig. 6.1 are estimated from:

- the mean total $B-V$ colours as a function of Hubble type (Buta et al. 1994), and
- subtraction of the bulge light by assuming a bulge colour $B-V = 1.0$ and a bulge to total light ratio (B/T) in B band (Simien & de Vaucouleurs 1986).

The total gas masses normalised by B band disc luminosity (M_g/L_B) as a function of Hubble type are estimated from:

- the mass of neutral atomic gas, calculated from the integrated hydrogen index HI (Buta et al. 1994) and a conversion formula in *Third Reference Catalogue of Bright Galaxies* (RC3) given by de Vaucouleurs et al. (1991),

Table 6.1. Integrated colours of spiral galaxies

		de Jong (1996c)				RC3				Model				
Hubble type	B/T	B−V	V−R	V−I	V−K	U−V	B−V	V−R	V−I	U−V	B−V	V−R	V−I	V−K
Sa	0.41	0.81	0.54	1.02	2.94	0.96	0.74	0.50	1.14	0.85	0.76	0.53	1.17	3.02
Sb	0.24	0.74	0.46	1.04	2.79	0.66	0.61	0.46	0.93	0.63	0.66	0.49	1.07	2.84
Sc	0.09	0.67	0.53	1.08	2.84	0.45	0.53	0.41	0.87	0.45	0.57	0.43	0.95	2.61
Sd	0.02	0.59	0.47	1.02	2.59	0.37	0.50	0.39	0.83	0.36	0.52	0.41	0.89	2.47
Sm	0.00	0.69	0.41	0.75	2.30	0.33	0.50	0.36	0.72	0.33	0.50	0.40	0.87	2.42

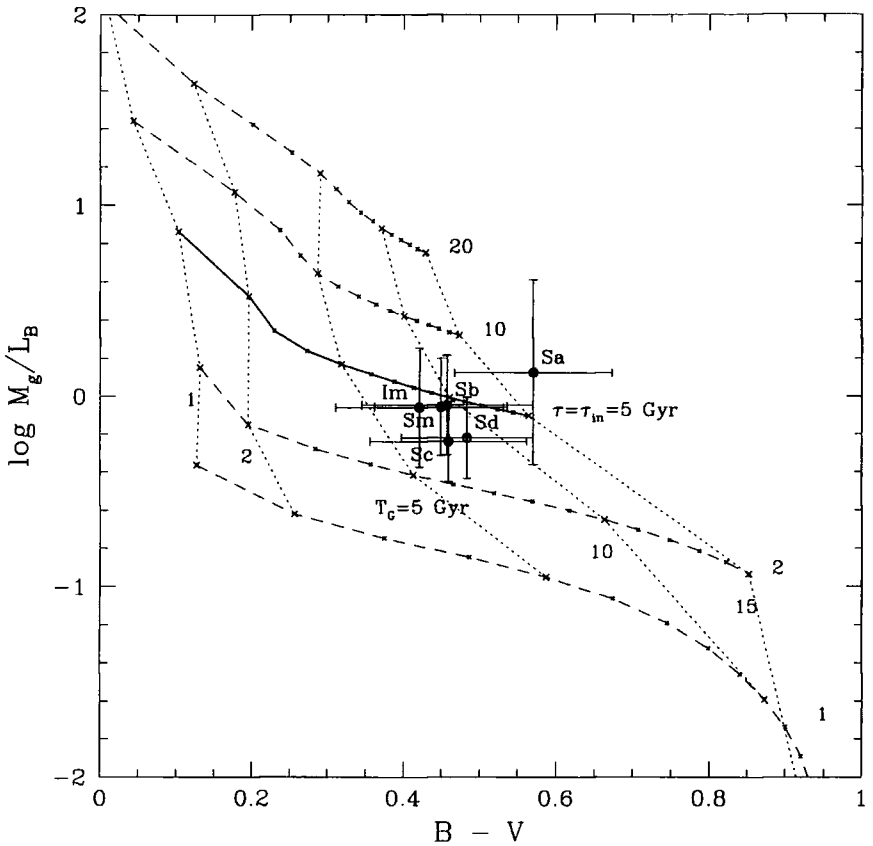

Figure 6.1: Gas mass per unit blue luminosity is plotted against $B - V$ colours. The filled circles show the estimated disc colours of galaxies with types Sa to Im. The solid line and the four dashed line represent the evolutionary models with different τ and τ_{in}. The age T_G is changed from 1 Gyr to 15 Gyr as indicated by crosses and dotted lines.

- the ratio of molecular to atomic gas H_2/HI (Young & Knezek 1989),
- a helium abundance correction of 25%, and
- subtraction of the bulge light contribution to L_B.

Disc properties in Fig. 6.1 are well reproduced by $\tau = \tau_{in} = 5$ Gyr model with an age $T_G = 5 - 15$ Gyr irrespective of the Hubble type. The model also reproduces the age-metallicity relation and the [O/Fe] vs. [Fe/H] diagram of the stars in our own galaxy (Kodama 1997). The constraint on the time scales τ and τ_{in} is weak because of the large observational errors and the permitted range could be from 2 to 8 Gyr (Fig. 6.1). However, as will be shown in section 6.2.2, this uncertainty does not cause problems for the purposes of redshift determination because star forming timescale and B/T variations have degenerate effects.

As an additional check of the validity of our models, the integrated colours of disc galaxies of different Hubble type are compared in Table 6.1. The observational data are mean Hubble type colours taken from de Jong (1996c) and the RC3 (Buta et al. 1994; Buta & Williams 1995). Note that each galaxy type has large intrinsic colour dispersion, typically as much as $0.05 - 0.2$ mag in optical colours and $0.2 - 0.4$ mag in $V - K$. The data are compared to the model with appropriate B band B/T ratio (Simien & de Vaucouleurs 1986). It is clear that the detailed trends of local galaxy colour with B band B/T ratio are well reproduced by our models.

6.2.2 Colour tracks

We now consider the colour evolution of the model galaxies as a function of redshift for a variety of star formation histories.

The two solid curves in Fig. 6.2 show the colour evolution in the observer's frame for a E model with a high metallicity $\langle$[M/H]$\rangle$=0.06 and a model which contains a 50 per cent contribution of disc light in B band at $z = 0$ (see below). The redshift is changed from 0 to 2 in steps of 0.05 as indicated by the dots along the lines. Four different colour-colour plots are shown, to cover a wide range in redshift, demonstrating that the most useful passbands for photometric redshift determination up to redshifts of ~ 1.5 typically bracket the 4000 Å break: $0.25 \leq z \leq 0.4$ for $B - V$ vs. $V - R$, $0.5 \leq z \leq 0.8$ for $V - R$ vs. $R - I$, $0.9 \leq z \leq 1.15$ for $R - I$ vs. $I - K$, and $1.0 \leq z \leq 1.5$ for $R - Z$ vs. $Z - J$. In the above redshift ranges, the middle band in each combination passes through 4000 Å break, the most prominent spectral feature in optical region, which plays an important rôle in redshift estimation. The horizontal colours redden rapidly with redshift while vertical colours stay nearly constant. At around $z = 0.3$, for example, as shown in Fig. 6.3, V band is just on the 4000 Å break and B and V bands lose flux rapidly, while the R band flux is approximately constant as the redshift increases. As a result $V - R$ gets redder while $B - V$ remains almost constant. On the other hand, $B - V$ is more sensitive to changes in stellar population than $V - R$. Therefore, we can see that the effects caused by changes in redshift are almost perpendicular to those caused by changes in star formation history.

In Fig. 6.2, six effects which change the colour evolution of a galaxy with redshift are considered. The six arrows (indicated at three redshift points along the elliptical model colour track) show the change in colour of an old, high metallicity elliptical model ($T_G = 12$ Gyr and $\langle$[M/H]$\rangle$=0.06) caused by the following effects.

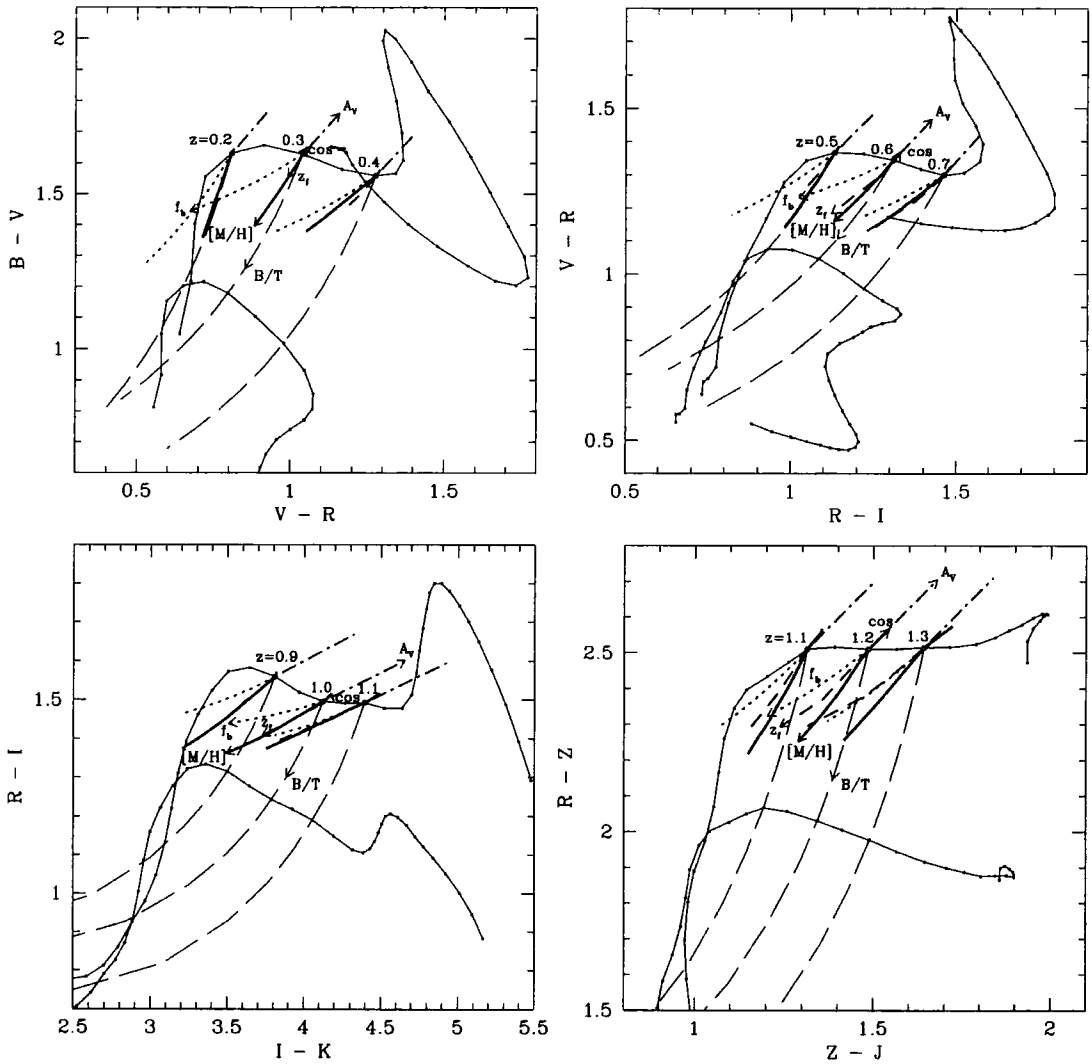

Figure 6.2: Colour-colour plots in the observer's frame. The two solid curves show the colour evolution of an old (T_G = 12 Gyr, or z_f = 4.5), high metallicity (⟨[M/H]⟩=0.06) E model (redder), and the B/T=0.5 model (bluer) which contains half of disc light in B band at z = 0. The redshift range is 0 to 2 in steps of 0.05, indicated by dots along the tracks. The six arrows shown from three redshift points along the track indicate the colour changes due to several different effects. See text for details.

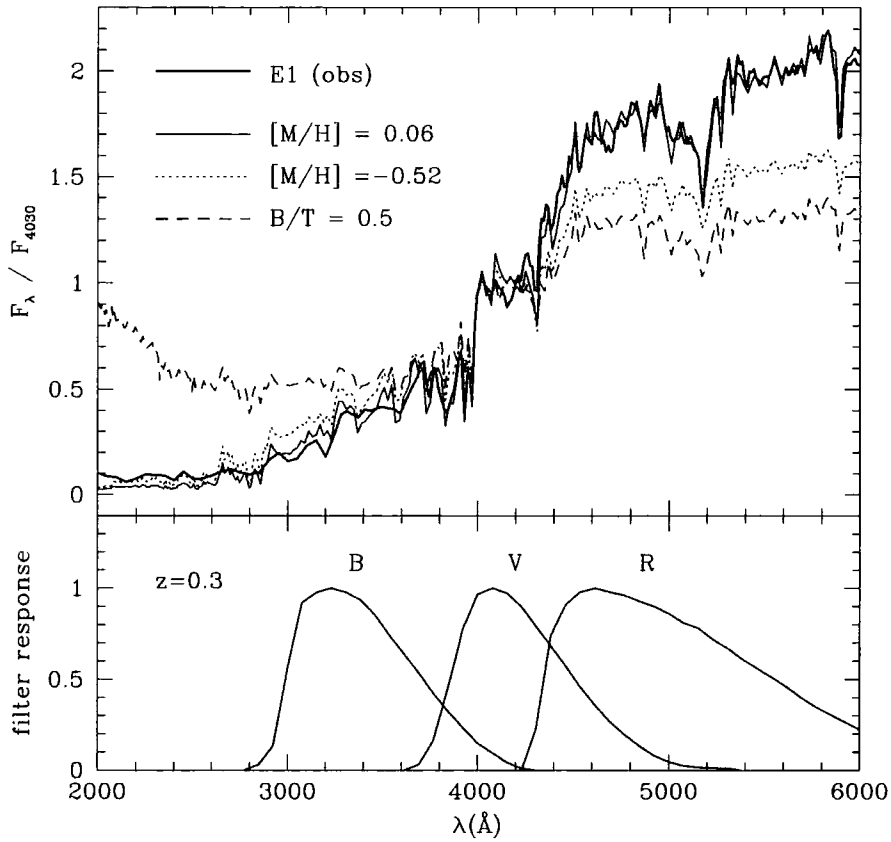

Figure 6.3: Example galaxy spectra at $z = 0$ (upper panel). The flux is normalised at 4030 Å. The thick solid line shows a giant elliptical E1 spectral template (Bica 1988) extended into the UV by the attachment of IUE spectra (Arimoto 1996). Three model spectra are superposed: a high mean metallicity model with $\langle$[M/H]$\rangle = 0.06$ (thin solid line), a lower metallicity model with $\langle$[M/H]$\rangle = -0.52$ (dotted line), and a high metallicity bulge plus disc model with B/T=0.5 (dashed line). The lower panel shows the normalised response functions of standard Johnson-Cousins' B,V and R filters, blueshifted to correspond to those at $z = 0.3$.

1. *metallicity — lower thick solid arrows:* The mean stellar metallicity of the E models is changed from $\langle$[M/H]$\rangle$=0.06 to -0.52. The galaxy age is fixed at 12 Gyr, corresponding to a formation redshift $z_f = 4.5$.

2. *age — dashed arrows:* The formation redshift of the E model is varied from $z_f = 4.5$ to 1.0 (4.5 to 2.0 for the RIK and RZJ diagrams), corresponding to galaxy ages $T_G = 12.0$ to 8.4 Gyr (12.0 to 10.5 Gyr). The metallicity is fixed at $\langle$[M/H]$\rangle$=0.06.

3. *disc component — long dashed arrows:* As outlined earlier, we model disc galaxies by adding a star forming disc component to an E model, which represents the galaxy bulge. The B band B/T ratio at $z = 0$ is changed from 100% to 0%. Note that B/T=0.41, 0.24 and 0.09 correspond to the Hubble types Sa, Sb and Sc, respectively (Simien & de Vaucouleurs 1986). Note also that the *observed* B/T ratio rises with redshift, since the bulge becomes brighter with redshift while the disc brightness remains roughly constant up to $z \sim 1$. For example, the a galaxy with a B band B/T ratio of 0.5 at locally has an observed B/T ratio 0.8 at $z \sim 1$. We checked the effects of disc metallicity on the colours of the galaxy by fixing $[\mathrm{M/H}]_{\mathrm{disc}} = -1.3$ and $[\mathrm{M/H}]_{\mathrm{disc}} = 0$ instead of following the chemical evolution of the disc: $[\mathrm{M/H}]_{\mathrm{disc}}$ is found to have a negligible effect on the colour tracks of the B/T sequence and is not considered hereafter. The time scales τ and τ_{in} were also changed but were found to be similar in effect to changes in B/T ratio at fixed τ and τ_{in}. This is because the colour of the B/T sequence at a given redshift is essentially determined by the ratio of the current star formation rate to the total mass of the galaxy. This parameter can be adjusted *either* by changing the time scales of the disc *or* by changing the B/T ratio. Thus the effects on the colour-colour diagrams of changing the timescales is only to shorten or extend the vectors of the B/T sequence for a given B/T ratio.

4. *recent star burst — dotted arrows:* The possible effects of recent large-scale star formation are considered by the addition of a recent star burst to the E model. The burst population is assumed to be a simple stellar population (SSP) with solar metallicity. The arrow denotes the changes caused by a $T_b = 0.5$ Gyr old burst population corresponding to 10% of the total stellar mass ($f_b = 0.1$) at that redshift. The direction of the vector on the colour-colour diagrams depends on T_b, but unless T_b is around 0.5 (± 0.3) Gyr, the burst sequence follows either the B/T sequence or the age sequence closely. Main-sequence turn-off stars in the burst population with age ~ 0.5 Gyr have an effective temperature of about 10000 K and contribute significantly to the total flux at rest wavelengths of 3000-4000 Å, creating aberrant colour changes in the colour-colour plots.

5. *reddening – dash-dotted arrows:* The extinction effect due to internal dust is estimated by using the extinction curve given by Mathis (1990). The full arrows correspond to $A_V = 0.5$ mag. Note that this reddening vector is along the same direction but larger than those produced by more realistic dust geometries and quantities (see Chapter 3).

6. *cosmology — upper thick solid arrows:* The colour tracks have a weak dependence on the adopted cosmology. Other sets of cosmological parameters are tested; $H_0 = 65, \Omega_0 = 0.1, \Lambda_0 = 0.0$ and $H_0 = 80, \Omega_0 = 0.2, \Lambda_0 = 0.8$. The formation redshift z_f is fixed to 4.5 in all cases. The full arrows show the colour change for the latter cosmology. The colour change from the former cosmology is smaller and along a similar vector.

The age and metallicity sequences (1) and (2) are almost indistinguishable in all the colour-colour plots for ages $\gtrsim$ 1 Gyr. This reflects the age-metallicity degeneracy inherent in old stellar populations (Worthey 1994). However, this degeneracy actually improves the prospects for the determination of photometric redshifts, as the effects of age and metallicity are quite distinct, given the right choice of passbands, to the effects of changing galaxy redshift. In addition, it is clear from Fig. 6.2 that changes in assumed cosmology and interstellar reddening also have colour effects similar to age and metallicity, with an opposite sense. As a result, E-type galaxies at a given redshift should populate in a restricted area on the colour-colour diagram (almost a single line) characteristic of that redshift, irrespective of its stellar population, regardless of interstellar reddening and whichever cosmology is assumed. This means that it is possible to assign redshifts to old stellar populations without prior knowledge of galaxy properties.

However, the colour changes caused by the B/T sequence are not entirely degenerate with those due to age and metallicity on the RIK and RZJ diagrams (Fig. 6.2), due to the presence of on-going star formation. This on-going star formation causes a bluer e.g $R - I$ colour for a given $I - K$ colour than either the effects of age or metallicity for $z \sim 1$ galaxies. Recent large bursts of star formation of age $\sim$ 0.5 Gyr also lead to effects distinct from those of age and metallicity, and those of changing the B/T ratio.

This can lead to considerable uncertainty in the estimation of galaxy redshift, as a given set of colours, on the basis of the colour-colour plots presented in Fig. 6.2, will be consistent with a wide range of redshifts, depending on how the colours are explained by our model; e.g. by changing the B/T ratio, or the metallicity of the galaxy template spectra. However, if a passband with a short rest-frame wavelength is used, it is possible to infer the presence of young stellar populations photometrically, leading to a less ambiguous determination of redshift. This is illustrated in the

upper half of Table 6.2 (see also the lower left panel of Fig. 6.2), where we compare 3 galaxy templates with very similar red colours ($R - I \simeq 1.35$, $I - K \simeq 3.48$) which present very distinct colours in bluer passbands, allowing relatively easy discrimination between these possibilities. Another degeneracy apparent in Fig. 6.2 in redder passbands is that between high redshift, low B/T ratio galaxies and lower redshift early-type galaxies. This, again, is illustrated in the lower half of Table 6.2 where we again see that bluer passbands allow easy splitting of this degeneracy.

Table 6.2. Colour degeneracies

z	B/T	$\langle$[M/H]$\rangle$	$f_b(\%)$	$B-R$	$V-R$	$R-I$	$I-K$
0.9	0.5	0.06	0	1.32	0.86	1.32	3.50
1.0	1.0	−0.52	0	2.57	1.32	1.36	3.49
1.1	1.0	0.06	20	1.64	1.09	1.38	3.46
0.5	1.0	0.06	0	2.98	1.37	1.13	3.10
0.7	0.4	0.06	0	1.48	0.89	1.15	2.98
0.9	0.2	0.06	0	0.80	0.57	1.09	3.00

Another point to note from Fig. 6.2 is that when a particular colour pair is selected to allow the accurate estimation of redshifts within a certain redshift range, this colour pair also provides a means of rejecting galaxies (particularly higher B/T objects) that lie outside this optimal redshift range (although the estimated redshifts will obviously be much less accurate for these objects). Problems will occur for much higher redshift objects and objects with a small B/T ratio, as discussed above.

Despite the demonstrated utility of the bluer passbands in 'breaking' degeneracies between galaxies which look identical in red passbands, we aim to use little of the colour information shortwards of 2500 Å. Primarily, this is because the model spectra are ill-constrained for short UV wavelengths in both elliptical and star forming galaxies because of the effects of the UV-upturn (an anomalous rise in flux towards short UV wavelengths, observed in nearby giant ellipticals; e.g. Burstein et al. 1988) and the uncertain effects of dust extinction (Gordon, Calzetti & Witt 1997, Tully et al. 1998). The source of the UV-upturn is still poorly understood, and the model predictions for its source and effects are still uncertain. If the UV-upturn comes from hot young stars, this population is actually considered in this model by superposing only a small fraction

of on-going star formation onto the passively evolving ellipticals. If, however, the source of the UV-upturn is hot horizontal branch stars, then it is necessary to fine tune the mass loss parameter along the red giant branch to reproduce the UV-upturn (c.f. Yi, Demarque, & Oemler, 1997). Even if this were the case, such hot horizontal branch stars would disappear at high redshift ($z \gtrsim 1$), which is our main region of interest, since the envelope mass of a horizontal branch star gets larger as the mass of a main sequence turn off star gets larger with look back time.

An additional source of uncertainty in our models, especially in the UV, is the neglect of the effects of dust extinction on the colours of the stellar populations incorporating on-going star formation. This would at first appear to be a serious handicap, as disc-dominated galaxies clearly contain significant amounts of dust, especially in the spiral arms, where B band extinction $A_B \sim 1$ mag (White, Keel, & Conselice 1996, Berlind et al. 1997, Gordon, Calzetti & Witt 1997, Tully et al. 1998). However, by inspection of Fig. 6.2, it is clear that the colour changes at rest-frame optical wavelengths are equivalent to increasing B/T ratio, age *or* metallicity, meaning that relatively large uncertainties in dust reddening can be accommodated by changes in other galaxy parameters to compensate for these errors. Note also that the colours of a galaxy are typically determined by the colours of its *least* reddened regions (Kuchinski et al. 1998; Chapter 3), so the effects of dust are likely to be relatively minor for most photometric redshift applications in the optical and near-infrared. This is also demonstrated in Table 6.1, where it is apparent that our models can accurately reproduce the colours of galaxies with ongoing star formation. This situation is unlikely to hold in the UV, however, as prescriptions for the dust extinction law start to diverge at these short wavelengths (Calzetti, Kinney, & Storchi-Bergmann 1994).

Both the UV-upturn and the uncertain effects of dust reddening in the far-UV lead us to place little confidence in our model UV colours. We should, therefore, avoid this spectral region if possible.

In addition, it should be noted that we neglect emission from star forming galaxies, such as the commonly observed [OII], [OIII] and Balmer features at both local(Kennicutt 1992) and high redshifts (Hammer et al. 1997). This should not present a major problem, as the effects of line emission on broad band photometry is not large: a line width with an equivalent width of 20 Å in emission would cause only ~ 0.02 mag of brightening in the broad band magnitude.

Finally, we note that although most of redshift range below 1.5 can be covered by the standard Johnson-Cousins system including Z band, there are some particular redshift ranges where we have larger errors in the estimated redshifts; ie. $z < 0.25$, $0.4 < z < 0.5$, and $0.8 < z < 0.9$. At these redshift ranges, the effect of changing redshift on colours is difficult to distinguish from those

of changes in the stellar population (Fig. 6.2). If we want to handle clusters in these redshift ranges with better precision, we need to use passbands in other photometric systems which properly bracket the 4000 Å break at the cluster redshifts.

6.3 Bayesian classification

6.3.1 Basic scheme

A Bayesian approach allows us to incorporate our existing knowledge of galaxy populations and thus to proportionally weight the areas of parameter space that we search. The Bayesian probability of a particular galaxy having a redshift z and bulge to total luminosity ratio B/T is given by the equation:

$$P_{\rm Gal}(z, {\rm B/T}) = P_1(z, {\rm B/T}|m_B)P_2(z, {\rm B/T}), \tag{6.5}$$

where $P_1(z, {\rm B/T}|m_B)$ is the probability of a given galaxy of apparent magnitude m_B having a redshift z and bulge to total luminosity ratio B/T, and $P_2(z, {\rm B/T})$ is the probability of a given galaxy reproducing the observed galaxy colours. We first deal with the evaluation of $P_2(z, {\rm B/T})$, i.e. the probability of a given model galaxy reproducing the observed galaxy colours.

The basic philosophical approach used for this redshift estimator is the comparison of a galaxy's location on a colour-colour plot and a finely-spaced grid of models superimposed on that plot to estimate the properties of that galaxy (c.f. Chapters 2 and 3). The magnitudes of the observed galaxy are made into colours, and the errors in the colours used to make up a covariance matrix, describing the sizes of the colour errors and their relationships. Then, for all of the model galaxy colours, the difference between them and the observed colours are calculated. Under the assumption that the photometric errors follow a Gaussian distribution, the probability that the model describes the galaxy colours adequately ($P_2(z, {\rm B/T})$) is given by:

$$P_2(z, {\rm B/T}) = 1/[(2\pi)^n|\boldsymbol{C}|]^{1/2} \exp\{-1/2(\boldsymbol{u}^T\boldsymbol{C}^{-1}\boldsymbol{u})\}, \tag{6.6}$$

where n is the number of colours used, $\boldsymbol{u}$ is the vector of differences between the model galaxy colours and the observed colours, $\boldsymbol{C}$ is the covariance matrix of those colours and $|\boldsymbol{C}|$ is the determinant of the covariance matrix. The diagonal elements of $\boldsymbol{C}$ correspond to the variance in the individual colours. The off-diagonal elements correspond to the variance of any passbands in common between two colours, with the appropriate sign (which indicates whether the errors in a given passband affect the colours in the same or an opposite sense). Since we require galaxies to have small ($\lesssim$ 0.1 mag) photometric errors in order to reliably determine their redshift, using a

Gaussian rather than a log-normal is an adequate representation of the error distribution in each band. This assumption considerably shortens the probability computation time. If it is impossible to find a satisfactory match to the galaxy colours, the galaxy is omitted from further consideration.

This procedure gives the probability that an observed galaxy is adequately described by a given model galaxy. This product is evaluated for a large number of plausible model galaxies with a range of B/T ratio and redshift. The other effects, such as age and metallicity of model galaxies are considered later in section 6.3.3. These evaluations makes up a 'probability map' on the plane of B/T ratio and redshift. In order for us to obtain the final probability, $P_{\rm Gal}(z, {\rm B/T})$ of the galaxy having a particular z and B/T, it is necessary to make up a prior distribution, given what is already known about galaxy populations.

6.3.2 Prior distribution

The quantity $P_1(z, {\rm B/T}|m_B)$ is our prior distribution. The effect of the prior is to modulate the redshift estimates provided by the colour analysis by using magnitude information. Note that it makes little difference to the redshift estimate (well within the error bars of the redshift determination) *unless* there is a degeneracy, and the colour of two or more models satisfy the observational constraints equally well at different redshifts. In that case, it is designed to determine which one of these options is more likely to be observed and weights the 'probability map' accordingly.

In forming the prior distribution, we need to know the type dependent luminosity function (LF) $\Phi(m_B, {\rm B/T})$ and the volume element $dV/dzd\Omega$. Using these two elements, the prior is given as follows:

$$P_1(z, {\rm B/T}|m_B) = dV/dzd\Omega\, \Phi(m_B, z, {\rm B/T}). \tag{6.7}$$

These two parts are treated separately below.

6.3.2.1 The local luminosity function

In order to get $\Phi(m_B, {\rm B/T})$ we use the local, type-dependent luminosity function (LF). However, there remains considerable uncertainty in the type-dependent LF, as the splitting into morphological types is carried out in a number of different ways, and the faint end slopes differ considerably between different studies (Marzke et al. 1998, Bromley et al. 1997, Marzke et al. 1994, Bingelli, Sandage & Tammann 1988). We chose to adopt a variant of Marzke et al.'s (1994) determination in the Schechter (1976) form, which is parameterised by Φ^*, α and M_B^*. The parameters for the observed local luminosity function are summarised in Table 6.3 as a function of the Hubble type. To connect between the Hubble types and B/T ratio, we use Simien & de Vaucouleurs

Table 6.3. Adopted luminosity function parameters

Type	B/T	M_B^*	α	Φ^* ($\times 10^{-3}$ Mpc^{-3})
E	1.0	−20.74	−0.85	0.188
S0	0.6	−20.25	−0.94	0.950
Sa–Sb	0.33	−20.23	−0.58	1.088
Sc–Im	0.0	−20.32	−1.07	0.625

(1986). The characteristic magnitude of the LF, $M_B^*(\mathrm{B/T})$, corresponds to the apparent magnitude $m_B^*(z, \mathrm{B/T})$ at a redshift z as:

$$m_B^*(z, \mathrm{B/T}) = M_B^*(\mathrm{B/T}) + DM(z) + \Delta M_B(z, \mathrm{B/T}), \tag{6.8}$$

where DM is the distance modulus at redshift z in the adopted cosmology. ΔM_B is the absolute magnitude change in B band in the observer's frame due to the luminosity evolution and the shift of the wavelength shortwards with redshift and is taken from the model. In this way, we finally obtain the LF in apparent magnitude m_B as a function of redshift and B/T ratio:

$$\Phi(m_B, z, \mathrm{B/T}) = 0.92\Phi^* e^{\{-0.92(\alpha+1)(m_B - m_B^*) - \exp(-0.92(m_B - m_B^*))\}}. \tag{6.9}$$

If the observed galaxy lacks B band data, we use a prior in the band nearest to B. In this case, we make up the local LFs in the alternative band by shifting the B band LFs using model colours of each type.

6.3.2.2 Volume element

The other essential ingredient of the prior is the volume element $dV/dzd\Omega$. The formula for the volume element as a function of redshift was taken from Carroll, Press & Turner (1992), with the addition of some factors of c to satisfy dimensionality considerations, and allows variations in Ω_0, H_0 and the inclusion of the cosmological constant via the term Λ_0:

$$dV/dzd\Omega = \frac{d_M^2}{\{1 + \Omega_k (H_0 d_M/c)^2\}^{1/2}} \frac{d(d_M)}{dz}, \tag{6.10}$$

where, Ω_k is given by $\Omega_k = -\frac{kc^2}{R_0^2 H_0^2}$, R_0 is the scale factor of the universe and k is the curvature of the universe. The quantity d_M is the proper motion distance, and in this case is given by:

$$d_M(z) = \frac{c}{H_0 |\Omega_k|^{1/2}} \operatorname{sinn}\left(|\Omega_k|^{1/2} \mathcal{F}\right), \tag{6.11}$$

where 'sinn' is a function that equals sinh in an open universe, sin in a closed universe, and disappears in a critical universe and $\mathcal{F}$ is given by:

$$\mathcal{F} = \int_0^z [(1+z')^2(1+\Omega_0 z') - z'(2+z')\Lambda_0]^{-1/2} dz', \tag{6.12}$$

which must be integrated numerically for most non-trivial cosmologies.

6.3.2.3 Comparison with observation

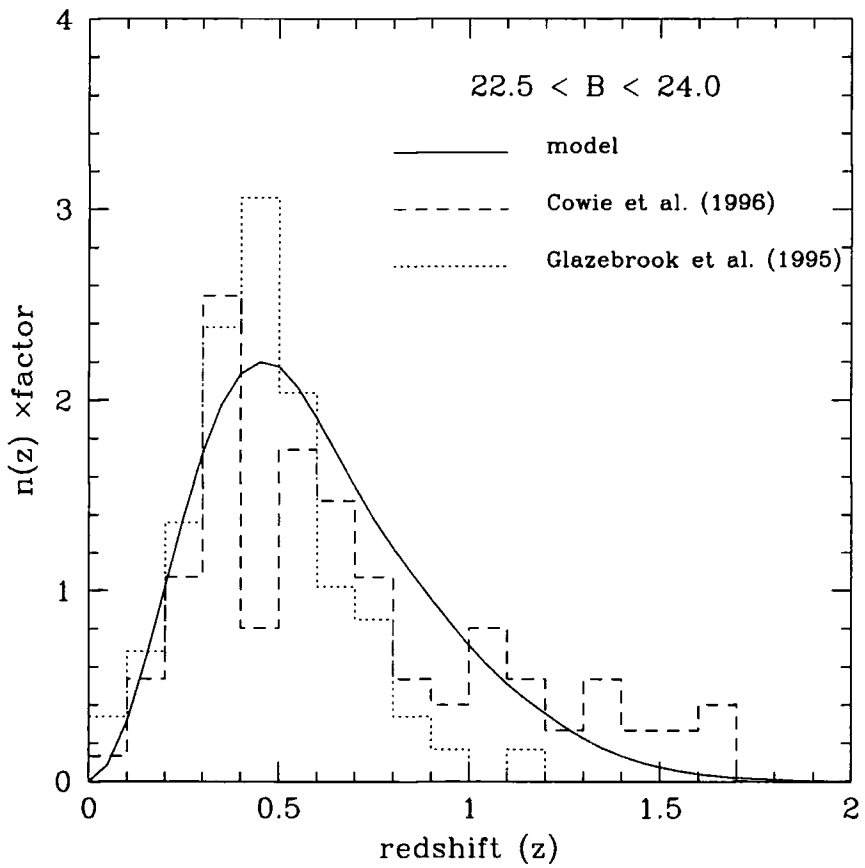

Figure 6.4: The observed $n(z)$ distributions for a sample of galaxies in the magnitude range $22.5 < m_B < 24.0$ from Glazebrook et al. (1995) and Cowie et al. (1996) are plotted against the expectation for the $n(z)$ distribution calculated from our prior distribution. The overall shape is in adequate agreement with the observational data.

The prior was used to calculate the $n(z)$ distribution within a magnitude range $22.5 < m_B < 24.0$. This calculated distribution was then compared to the observed redshift distribution of galaxies within the same magnitude range given by Glazebrook et al. (1995) and Cowie et al. (1996). The comparison is shown in Fig. 6.4. It is clear that the prior reproduces the overall form of the observed $n(z)$ diagram.

6.3.2.4 The effect of the prior

It should be noted that the prior distribution is quite model-dependent, because the type-dependent local LF is ill-constrained and because the detailed type-dependent spectral evolution is poorly understood. Also, here we make two assumptions: that there is no number evolution of galaxies, and that there is no size dependent luminosity evolution, i.e. galaxies with similar B/T ratios have the same colours at all redshifts, regardless of their total luminosity. These assumptions and ingredients may be inadequate to describe the real universe, especially in the context of a hierarchical clustering universe. However, these uncertainties are not so important, because the estimated redshift is essentially determined by the colour term (P_2 in Eq. 6.5), and the prior (P_1) is used supplementarily. The prior becomes important when the solution from the colour term splits into multiple redshift ranges. In such a case, the prior works to avoid unreasonable solutions of redshift for a given apparent magnitude.

We also tested the effect of local LF on the final estimated redshift through the prior by changing the LF parameters listed in Table 6.3. We shifted M_B^* by ± 0.5 magnitude for all types, resulting in a shift of the redshift peak of the n(z) distribution in Fig.6.4 by ∓ 0.1, and we tried fixing the faint end slope α at -1 for all types. In all cases, however, the change in the final estimated redshifts was well within the estimated redshift errors. This experiment shows our method is robust to uncertainties in the prior estimation.

6.3.3 The models included in the classifier

The estimates of redshift and galaxy type will depend quite sensitively on the detailed choice of model galaxy template. In section 6.2.2, we investigated the various effects on the galaxy colours, namely the effects of age, metallicity, B/T ratio, recent star bursts, reddening, and cosmology. However, many of these effects were found to be degenerate. In these models, effects due to age, metallicity, reddening and changes in cosmology are particularly degenerate. Therefore, by including only the metallicity effect explicitly in the classifier, we also cover the other three effects at the same time. To this aim, we considered four B/T sequences with different bulge metallicities. Each sequence gives different probability map on the redshift and B/T plane, and then they are combined into a single 'probability map' by performing a mean of the separate maps. This mean is in essence a weighted mean, as the most plausible metallicity for the model galaxies will have the best match to the colours. In this way, we take into account the metallicity effects explicitly and hence the other degenerate effects.

The remaining significant effect which is not covered is that of a recent burst of star formation. As seen in Fig. 6.2 large amounts of relatively recent star formation can make a galaxy look as if it has a lower redshift than it actually does, if the colours are interpreted as being entirely due to redshift, B/T and metallicity effects. However, as was already shown, unless the burst strength f_b is as high as $> 15\%$ and the burst age $T_b \sim 0.5$ Gyr, the burst population colour change is similar to those resulting from other effects. These populations are short lived and are expected to be relatively rare. Therefore, omitting the recent star burst model should not greatly affect the quality of our global redshift estimation. We should note, however, this could be a problem if significant fraction of cluster members would be strongly affected by a recent burst, due to cluster-cluster merging for example (e.g. the E+A galaxies of Poggianti et al. 1999). In such a case, we would need to include the extra set of models of recent star burst to correctly estimate redshifts, although it would lead to greater estimation errors.

6.3.4 Error estimates

At this stage, the redshift and galaxy type estimates are in the form of the 'probability map' $P_{\rm Gal}(z, {\rm B/T})$. However, an estimate of a given galaxy's redshift and type is often required for e.g. comparison with real redshifts, or cluster member identification. Best estimates for redshift ($z^{\rm best}_{\rm estimated}$) and effective 1σ confidence intervals ($z^{\rm min}_{\rm estimated}$, $z^{\rm max}_{\rm estimated}$) are obtained by taking the $P_{\rm Cum}(z) = 0.5$ and the $P_{\rm Cum}(z) = [0.16, 0.84]$ intervals, respectively, of the cumulative distribution:

$$P_{\rm Cum}(z) = \int_0^z dz' \int_{\rm B/T=0}^{\rm B/T=1} d({\rm B/T})\, P_{\rm Gal}(z', {\rm B/T}). \tag{6.13}$$

These error estimates depend on the estimated photometric errors: through the use of the covariance matrix $\boldsymbol{C}$, the error estimates in the photometry are explicitly included in the determination of $P_2(z, {\rm B/T})$. Large uncertainty in the colours propagates through into larger uncertainties in the $(z, {\rm B/T})$ combinations capable of adequately reproducing the observed colours. It is important to know how much photometric accuracy we need to achieve the error in redshift within the expected bound, as it will certainly constrain the accuracy of any future applications of this method.

To produce redshift error estimates as a function of photometric accuracy, simulations using 100 galaxies with $K < 20$, chosen at random in the range of $0 <$B/T< 1 and $0.2 \leq z \leq 1.8$ were undertaken. The bulge metallicity $\langle$[M/H]$\rangle_{\rm bulge}$ was chosen randomly between 0.061 and -0.523. After allocating the model magnitude in each passband for each galaxy, Gaussian photometric errors were then applied. We used these magnitudes and photometric errors of the

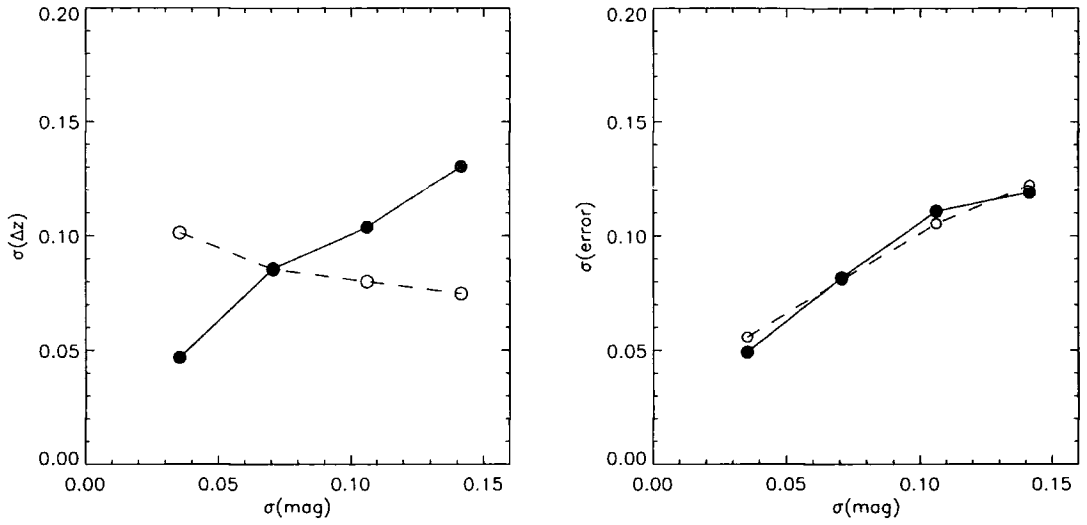

Figure 6.5: The effects of photometric error on the quality of redshift estimation. Simulations with 100 galaxies using the B, V, R, I and K passbands were used to assess the effects of changing photometric quality in magnitude in all bands (solid lines). The RMS difference between the best estimate and the real redshift $\sigma(\Delta z)$ is plotted against the Gaussian photometric error $\sigma(mag)$ in the left panel, while the RMS redshift error $\sigma(error)$ is plotted in the right panel. The effects of under- or over-estimation of the photometric error were also assessed by keeping the real photometric error fixed at 0.071 mag, and varying the estimated photometric errors going into the covariance matrix $\boldsymbol{C}$ (dashed lines).

simulated galaxies in the course of the redshift estimation. Here B, V, R, I and K passbands were used. The quantities $\sigma(\Delta z)$ and $\sigma(error)$, corresponding to the root mean square (RMS) of real and estimated redshift error respectively, were then plotted in Fig. 6.5 where:

$$\Delta z = z^{\text{best}}_{\text{estimated}} - z_{\text{real}}, \tag{6.14}$$

$$error = (z^{\text{max}}_{\text{estimated}} - z^{\text{min}}_{\text{estimated}})/2, \tag{6.15}$$

$$\sigma(\Delta z) = \sqrt{\overline{(\Delta z)^2}}, \tag{6.16}$$

$$\sigma(error) = \sqrt{\overline{error^2}}. \tag{6.17}$$

As seen from the solid lines, both $\sigma(\Delta z)$ and $\sigma(error)$ increase with photometric error. Importantly, even the photometric error is as poor as 0.15 magnitudes in all bands, the average redshift error $\sigma(\Delta z)$ is still kept smaller than 0.1. As for the estimated redshift error $\sigma(error)$, it is roughly comparable to the photometric error.

Next we consider the effect of mis-estimation of the photometric error on the redshift estimation error. It is possible that if the errors are under- or over-estimated, the redshift estimator will make

the distribution of likely $(z, \mathrm{B/T})$ too broad or multiply-peaked, reducing the accuracy of the redshift estimate. Therefore, it is important to test the effects that uncertainty in the determination of the errors can have on the redshift estimate accuracy. We realise this situation by fixing the real photometric error at 0.071 mag and varying the estimated photometric error going into the covariance matrix C. The result is shown by the dashed lines in Fig. 6.5. It is clear that the under- or over-estimation of the photometric errors has little, if any, effect on the quality of redshift estimation $\sigma(\Delta z)$. Errors in the determination of the photometric quality do, however, have a marked effect on the *estimated* quality of the redshift determination, given by $\sigma(error)$. It is clear, therefore, that it is important to be careful in the estimation of the photometric errors in order to estimate the quality of the redshift determination effectively.

Table 6.4. Passband choice for random galaxy simulations

	all		E/S0	
passbands	$\sigma(\Delta z)$	$\sigma(error)$	$\sigma(\Delta z)$	$\sigma(error)$
$BVRIK$	0.065	0.076	0.060	0.074
RIK	0.127	0.135	0.121	0.129
$BVRI$	0.178	0.199	0.176	0.210

The quality of the redshift estimation also sensitively depends on the passband choice. We investigated three sets of passbands for the randomly generated galaxies with 0.071 mag photometric errors, and the results are summarised in Table 6.4. With R, I and K passbands, the result is about a factor of two worse than the B, V, R, I and K case. This is because it gets harder to disentangle the colour degeneracies between lower redshift early-types and higher redshift late-types without using bluer passbands such as B or V. If, instead, we omit K band, the quality of the redshift considerably worsens, as high redshift galaxies with $z > 0.8 - 1.0$ no longer have a passband longwards of the 4000 Å break. It is, therefore, important to choose the passbands carefully for photometric redshift estimation according to redshift ranges under consideration and the depth of the photometric sample.

6.4 Testing

In this section, we focus on testing our method using photometry for galaxies with known spectroscopic redshifts. Because we wish to focus on the recovery of high redshift clusters at $z \gtrsim 1.0$,

it would be best to test with an extensive dataset for a real high redshift cluster. However, such data are not available to us at the moment, since we need both multi colour photometry covering the 4000 Å break (at least 3–4 bands) and spectroscopically determined redshifts for individual galaxies. Therefore, we have decided to test our method with two independent sets of data: a well-studied cluster Abell 370 at $z = 0.374$ and the northern Hubble Deep Field.

6.4.1 Abell 370

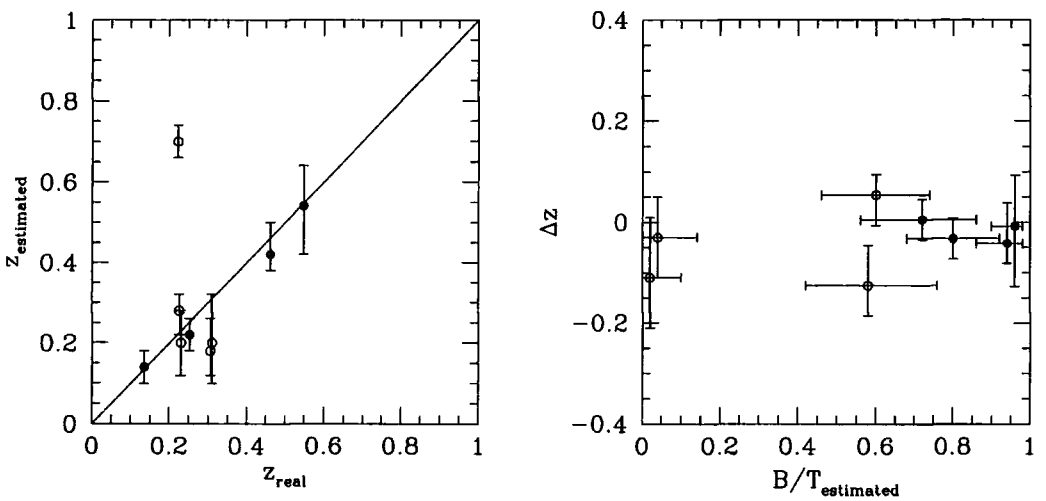

Figure 6.6: Field galaxies in the Abell 370 cluster field. Estimated redshift vs. spectroscopically determined redshift (left) and redshift error vs. estimated B/T ratio (right). Filled circles indicate E/S0 galaxies, while open circles indicate disc galaxies and those without morphological information.

The photometric data are taken from Pickles & van der Kruit (1991). We use their B, V, R and I photometry, using a 7 arcsec aperture. We selected 59 galaxies with spectroscopically determined redshifts. The redshifts are primarily taken from Pickles & van der Kruit (1991) and supplementarily from Stanford, Eisenhardt, & Dickinson (1995), although the latter gives only cluster memberships to which we assigned the cluster mean redshift $z = 0.374$. To separate the sample of E/S0 galaxies, we use galaxy morphology as given by HST images (Stanford et al. 1995). As Abell 370 has a redshift $z = 0.374$, the filter combination (B, V, R and I) is expected to do a good job of picking out cluster members, as these filters bracket the 4000 Å break (section 6.2.2), although U band would be useful to allow us to discriminate between galaxies with lower B/T ratios at the cluster redshift and galaxies with higher B/T ratio at lower redshifts.

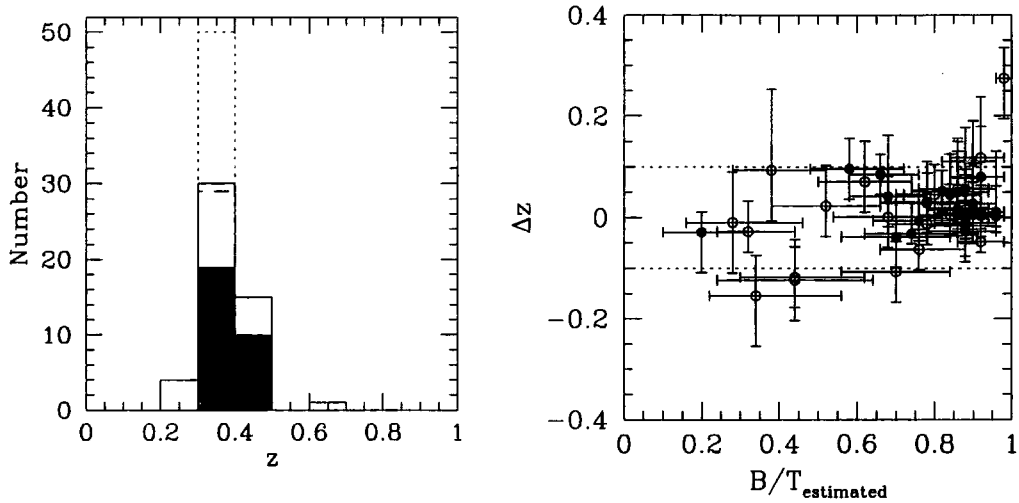

Figure 6.7: Cluster members of Abell 370. Distribution of the estimated redshifts (left) and redshift error vs. estimated B/T ratio (right). The filled histogram and filled circles indicate E/S0 galaxies, while the open histogram and open circles indicate disc galaxies and those without morphological information. The dotted and dashed histograms show the real redshifts of all types and E/S0's, respectively. The two dotted lines (right) show the region of $|\Delta z| < 0.1$ where galaxies are taken to be cluster members.

Unfortunately, the photometric accuracy is poor, especially in B and I bands (0.13–0.19 mag in B, 0.04–0.08 mag in V, 0.03–0.07 mag in R and 0.08–0.16 in I).

We estimated the photometric redshifts for our sample galaxies. The results for field galaxies and cluster members are shown separately in Figs. 6.6 and 6.7, respectively. The cluster members are defined as those which have spectroscopic redshifts $0.374 - 0.02 < z < 0.374 + 0.02$. For the E/S0 galaxies, we can estimate the redshifts within $|\Delta z| < 0.1$ both for field galaxies and cluster members. The situation for disc galaxies is less encouraging: some disc galaxies have significantly under or over-estimated redshifts. In Fig. 6.6, there is a galaxy with $\Delta z > 0.4$. That is because the galaxy's I band photometry is very poor (as indicated by Pickles & van der Kruit 1991), and in fact, if we use only B,V and R bands for this galaxy, the estimated redshift agrees with the real redshift at the 1.5 σ level. Two other field disc galaxies have slightly underestimated redshifts with $\Delta z \sim -0.1$. These galaxies have very blue colours in $B - V$ or $V - R$, and it is suggested that they are either disc dominated galaxies or the ones strongly influenced by a recent star burst. For the cluster members (Fig. 6.7) also, there are some galaxies whose redshifts are underestimated as much as $\Delta z \sim -0.15$. These galaxies tend to have low estimated B/T ratios and are again degenerate with galaxies at lower redshift. The discrimination between a blue cluster member and

a slightly redder galaxy at lower redshift can be difficult, especially when we lack a bluer passband corresponding to far-UV region (2500-3000 Å).

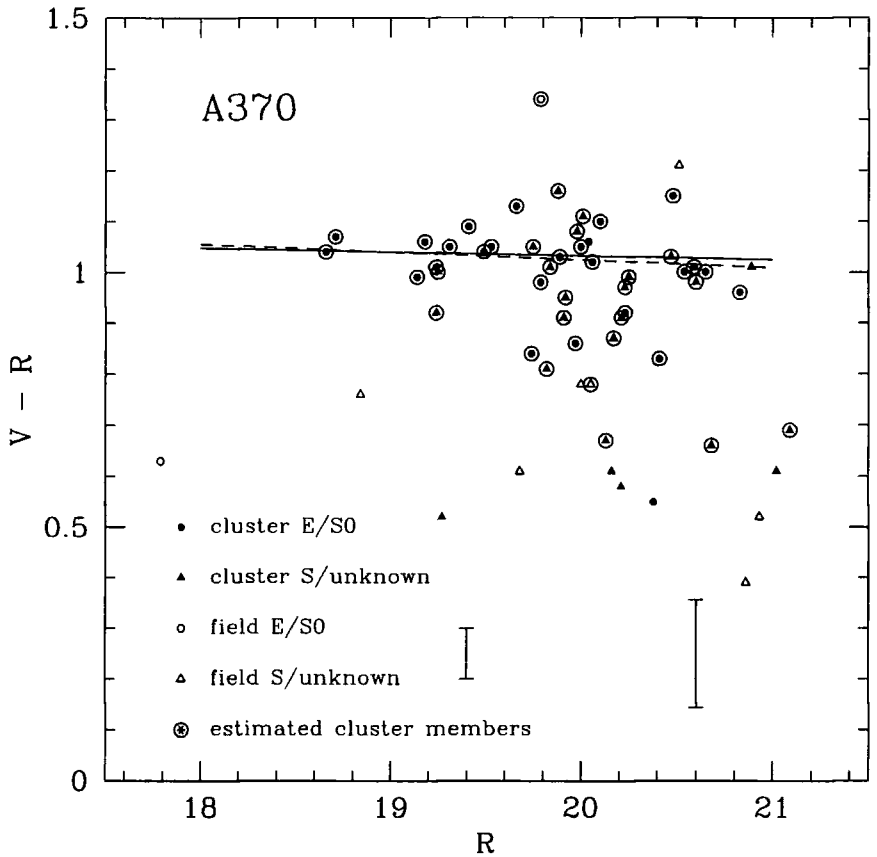

Figure 6.8: The colour-magnitude diagram for Abell 370. The filled symbols indicate cluster members, while the open symbols show field galaxies. The symbols surrounded by a large circle indicate the estimated cluster members selected using $|\Delta z| < 0.1$. Two error bars at the lower part of the figure indicate the typical one sigma observational errors. The solid and dashed lines indicate the CMR of the the real cluster E/S0's and that of the estimated cluster E/S0's, respectively, calculated using bi-weight fitting to the data.

Nevertheless, if we adopt the criteria of defining cluster members as $|\Delta z| < 0.1$, we can pick out most of the cluster members with little field contamination as shown in Figs. 6.8 and 6.9. This is especially true for early-type galaxies. As a result, the colour-magnitude relation (CMR) of the E/S0 galaxies is well recovered (Fig. 6.8). The solid line shows the real relation for the real cluster members, while the dashed line shows the estimated relation for the estimated cluster members. We used a bi-weight fitting method to calculate these CMRs (Beers, Flynn & Gebhardt 1990). Both relations are nearly identical.

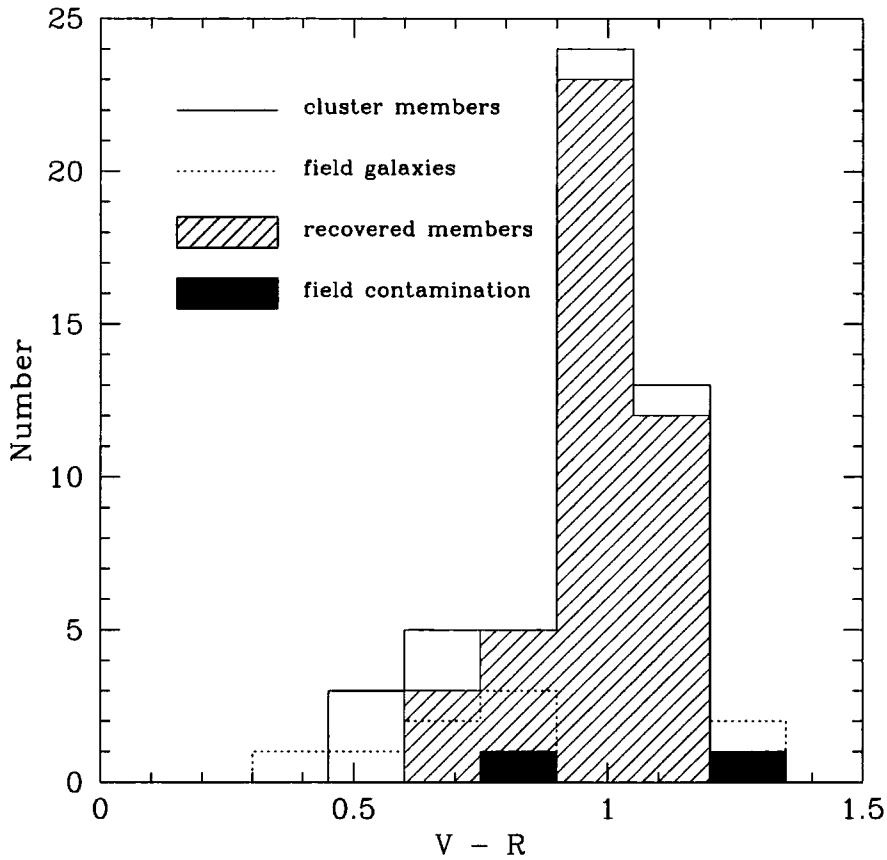

Figure 6.9: The colour histogram for Abell 370. The solid line shows the real cluster members, and the dotted line shows the real field galaxies. The slantwise hatched area indicates recovered cluster members, while the black shaded area indicates field contamination. It is shown that most of the cluster members are recovered, although a small number of the bluest galaxies are dropped out. This would be improved if the U band data were available. Field contamination is also negligibly small.

In summary, although the photometric accuracy is not ideal, we can still pick out most of the cluster members in Abell 370 using our method—especially the earlier types. The field contamination is negligible. The method has difficulty in recovering cluster members bluer than $V - R = 0.6$: this may, however, be improved with the inclusion of U band data.

6.4.2 Hubble Deep Field

To further test our method, we apply it to galaxies taken from the Hubble Deep Field. We use Cowie's K-selected galaxy sample (http://www.ifa.hawaii.edu/~cowie/k_table.html), all of which have spectroscopic redshifts, mainly from Cohen et al. (1996). Isophotal magnitudes in four HST WFPC2 filters (F300W[U300], F450W[B450], F606W[V606] and F814W[I814]) are taken from

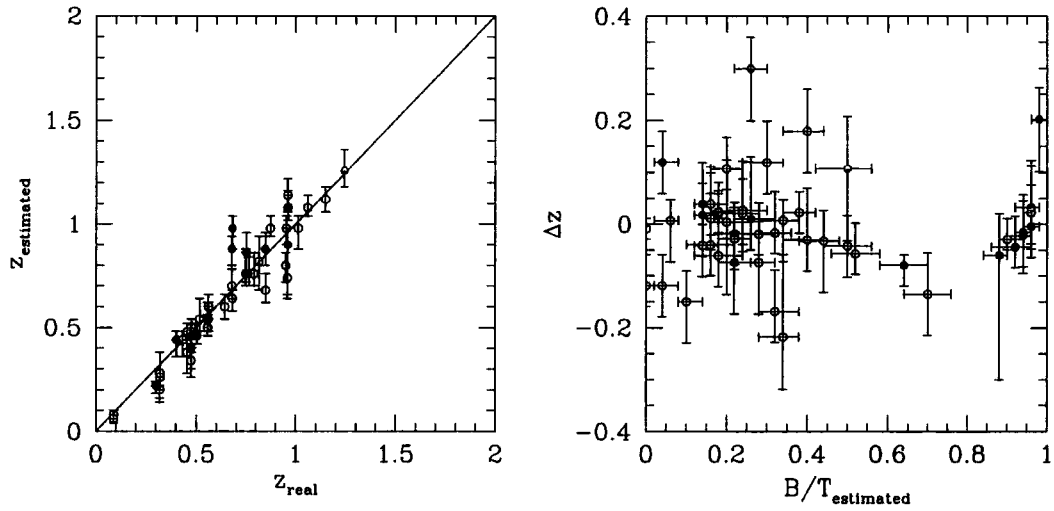

Figure 6.10: HDF galaxies. $U300$, $B450$, $V606$, $I814$, and J passbands are used. Filled symbols indicate morphologically classified E/S0 galaxies, while the rest show other type galaxies or unclassified galaxies.

Williams et al. (1996). We cross-identify galaxies between Cowie's catalogue and the photometry catalogue using RA and DEC. We choose only isolated galaxies to avoid mis-identification. Also we excluded galaxies with $z > 2$, as the current passbands no longer bracket the 4000 Å break. Photometric errors are calculated from S/N ratios, but, for those less than 0.05 magnitude, we assume a minimum error of 0.05 magnitude. We give larger minimum error of 0.2 magnitude to U_{300} for galaxies with $z^{\rm best}_{\rm estimated} > 0.2$ and to B_{450} for galaxies with $z^{\rm best}_{\rm estimated} > 0.8$, in order to avoid placing too much weight on uncertain model far-UV colours. This is an iterative approach but is unavoidable given the uncertainty of the model UV spectrum (see also Chapter 7). The infrared photometry data in J are acquired from Cowie's table. A photometric accuracy of 0.1 magnitude is assumed in J band as no errors were given.

Applying the model directly to this data set, we find a systematic offset of $\Delta z \sim -0.1$ between the real redshifts and the estimated redshifts. The most likely cause of this discrepancy is a zero-point mismatch of order 0.1 magnitude between the data and the model in such a way that the model is slightly redder in optical colours and a bit bluer in far-UV colours. It might be an intrinsic zero-point uncertainty in the model, since these offsets are comparable to the limiting accuracy of current population synthesis models (Charlot, Worthey & Bressan, 1996), although it is puzzling that a similar problem is not seen in Abell 370. To correct this situation, we shift the model zero-points for this case only: i.e. +0.1 magnitude is added onto the model $U300$, $I814$ and J magnitudes. With this zero-point shift, most of the HDF redshifts are correctly estimated as shown in Fig 6.10. In Chapter 7, we find that this offset is well reproduced (for early-type galaxies

only) by a metallicity offset (to lower metallicities); therefore, in Chapter 7 we adopt this (more physical) solution to the zero point problem. However, note that the zero point offset is present for both bulge- and disc-dominated galaxies, so here (where we are concerned with the whole range of galaxy types) we adopt the zero point shift outlined above to solve this problem. The RMS errors of the estimated redshift are smaller than 0.1; *i.e.*$\sigma(\Delta z) = 0.091$ and $\sigma(error) = 0.075$. Although the zero-point mismatch is a problem, it is encouraging that our method can estimate redshifts correctly over a wide range of redshifts. However, this exercise makes it clear that the model should be calibrated with real data rather than being applied blind to high redshift systems. This can be achieved using a handful of spectroscopically confirmed members of the target cluster without compromising the overall aim of examining the star formation histories of the galaxy populations.

6.5 Application to high redshift clusters

Table 6.5. Simulated galaxies in a $z = 1$ cluster field.

	type	n	$\langle$[M/H]$\rangle_{\rm bulge}$	z_f	B/T
cluster	E/S0	10	$0.06 \sim -0.52$	4.5	1.0
		10	$0.06 \sim -0.52$	$4.5 \sim 1.5$	1.0
		10	$0.06 \sim -0.52$	4.5	$1.0 \sim 0.5$
	Sp	20	$0.06 \sim -0.52$	4.5	$0.5 \sim 0.0$
field	E	6	$0.06 \sim -0.52$	4.5	$1.0 \sim 0.6$
	S0	26	$0.06 \sim -0.52$	4.5	$0.6 \sim 0.5$
	Sab	17	$0.06 \sim -0.52$	4.5	$0.5 \sim 0.15$
	Sc–Im	5	$0.06 \sim -0.52$	4.5	$0.15 \sim 0.05$

We are interested in applying this classifier to high redshift clusters around $z \gtrsim 1.0$, but, at present, a suitable data set is not available. To show the applicability of the classifier to targets at that redshift, we simulated a $z = 1$ cluster field using the model described in section 6.2. Although this is a self-consistency check (most importantly, it assumes that the photometric properties of real galaxies are accurately described by the stellar population synthesis code), it allows us to estimate the biases present in the recovered galaxy samples and to determine how

much photometric accuracy and which combination of passbands is required to pick out cluster members effectively.

We generated field galaxies using the type-dependent prior distribution outlined in section 6.3.2. We simulate a K-limited galaxy sample with $m_K < 20$ for a 1 arcmin^2 field of view (corresponding to 0.5 Mpc $\times$ 0.5 Mpc at $z = 1$) using the prior distribution, taking the type-dependent LF into account. The number of galaxies in each type is summarised in the lower half of Table 6.5.

To simulate the cluster members, we assume a mix of galaxy populations given in upper half of Table 6.5; i.e. 10 E/S0's from a metallicity sequence, 10 E/S0's from an age sequence, 10 E/S0's from a B/T sequence and 20 disc galaxies. Firstly, using the K band spiral and E/S0 luminosity functions of high redshift cluster galaxies (mean redshift 0.43; Barger et al. 1998), we assigned a K band absolute magnitude at $z = 0.43$ for a given galaxy. Secondly, a formation epoch (z_f) and a B/T ratio are randomly assigned in the respective range given in Table 6.5. Then we can assign its bulge metallicity using its $M_V^{\rm bulge}$ at $z = 0$ calculated from M_K at $z = 0.43$. If a galaxy has $m_K > 20$ at $z = 1$, it is rejected from our sample, and the process is repeated until we finally obtain 50 cluster galaxies in total. We assigned the model magnitudes in various bands for each galaxy both in the field and in the cluster. A Gaussian photometric error with $\sigma = 0.071$ is added on each colour of each galaxy. These colours are then used as input to the redshift estimator.

6.5.1 Biases in the recovered galaxy properties

The results for field galaxies and cluster members are shown separately in Figs. 6.11 and 6.12. We used V, R, I and K colours to estimate the redshifts. B band was not used, since at $z = 1$ it falls in the far-UV spectral region, well below 2500 Å. The overall agreement between the estimated and real redshifts is excellent. Most redshifts are well recovered to within $|\Delta z| = 0.1$, regardless of real redshift and irrespective of galaxy type. As a result, as shown in Fig 6.13, the recovery of cluster members is very encouraging. Here we considered a galaxy as a cluster member if $|\Delta z| < 0.1$, considering the photometric accuracy (see Fig. 6.5). This redshift cutoff also ensures that we do not pick up a large amount of field contamination. In this case, only one cluster spiral is not recovered. Field contamination is also negligible (only four galaxies). We have recovered not only old ellipticals, but also young or star forming ellipticals and spirals as well. To see the bias in the identification of cluster members as a function of galaxy colour, we show the colour histogram of the recovered cluster members and the field contamination in Fig. 6.14. As is clear from Fig. 6.14, there is little colour bias in either the cluster or the field. Consequently, we recover the CMR of E/S0 galaxies very accurately (identically in this case), as shown by the solid line in Fig. 6.14.

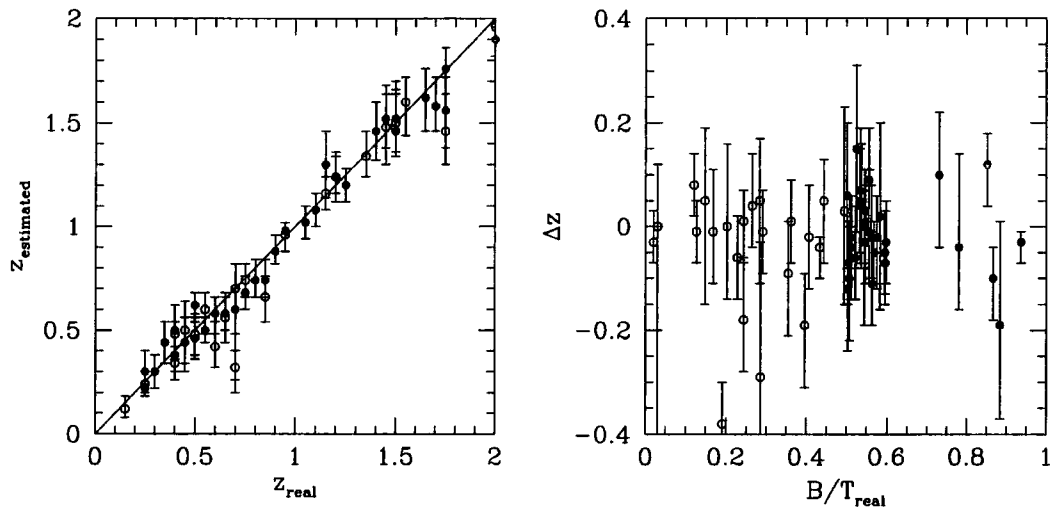

Figure 6.11: Field galaxies in the simulated cluster field at $z = 1$. Plotted are the estimated redshift vs. input real redshift (left), and redshift error vs. input real B/T ratio (right). Redshifts are estimated using V, R, I and K passbands with random Gaussian photometric errors of $\sigma = 0.071$ magnitude in all bands. Filled circles indicate E/S0 galaxies defined as B/T$\geq$ 0.5, while open circles indicate disc galaxies with B/T$<$ 0.5.

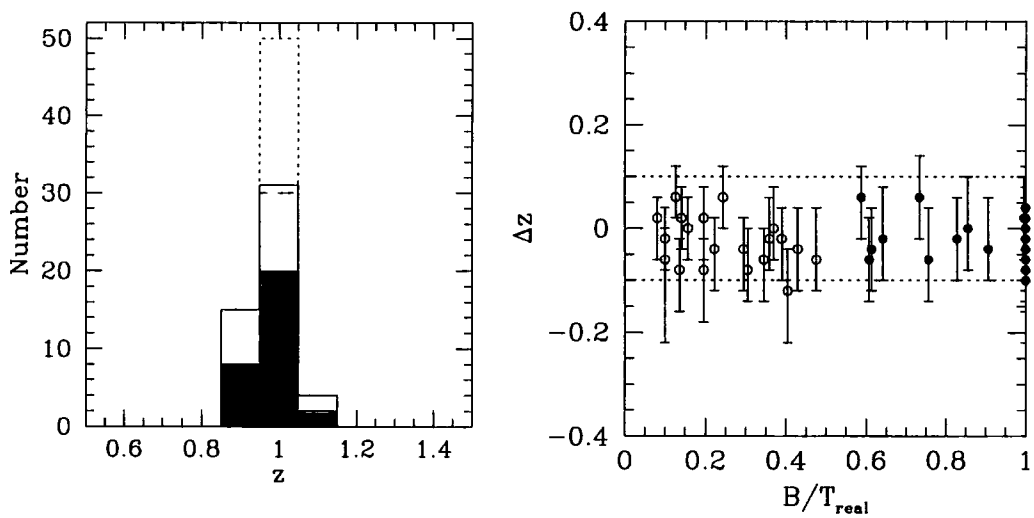

Figure 6.12: Cluster members in the simulated cluster field at $z = 1$. Distribution of the estimated redshifts (left) and redshift error vs. input real B/T ratio (right). The plot symbols are described in Fig. 6.7.

The slope and bi-weight scatters around the relation calculated and are given in Table 6.6. The corresponding figures for Abell 370 are also given in the same table. Both the scatters and slopes are accurately estimated irrespective of galaxy type.

All the above results are encouraging. If the models were perfect, we could assign redshift with 0.1 accuracy or better with <0.1 mag photometric errors in all bands. With this success, we will be

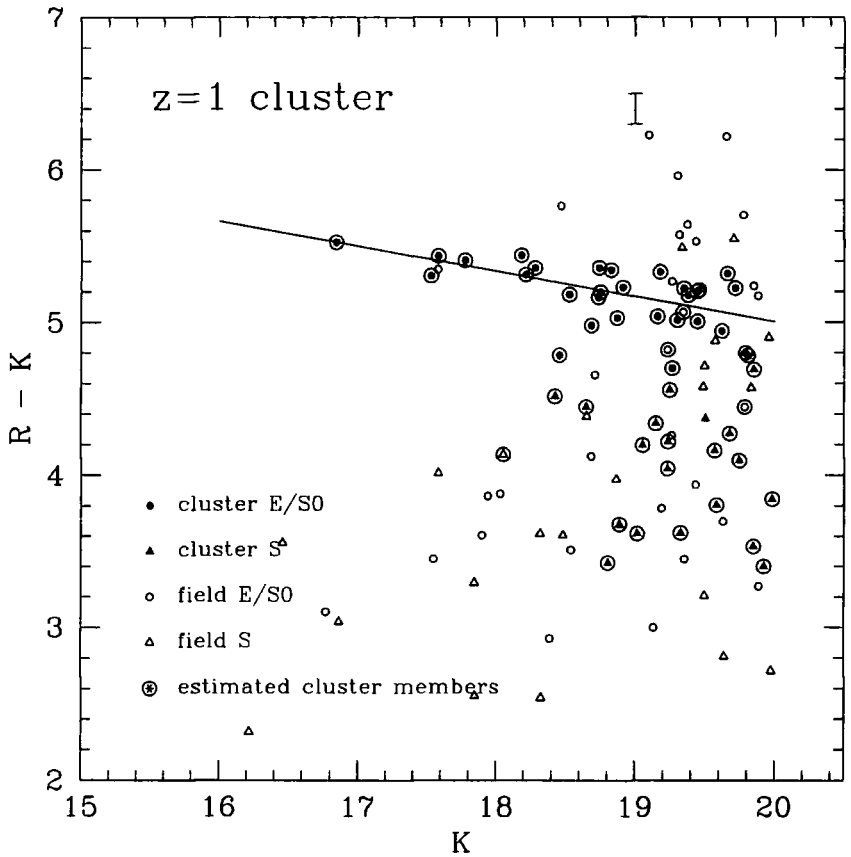

Figure 6.13: The colour-magnitude diagram for a simulated cluster field at $z = 1$. The plot symbols are the same as for Fig. 6.8. Note that the real CMR and the estimated one are identical (solid line).

Table 6.6. The bi-weight scatters and slopes of the CMR. the values for all types and E/S0 galaxies are shown separately. The scatters are measured with respect to the CMR of E/S0 galaxies only.

		Abell 370		$z = 1$ cluster	
		all	E/S0	all	E/S0
scatter	real	0.125	0.073	0.613	0.169
	estimated	0.112	0.072	0.603	0.189
slope	real	−0.018	−0.008	−0.423	−0.165
	estimated	−0.018	−0.016	−0.381	−0.165

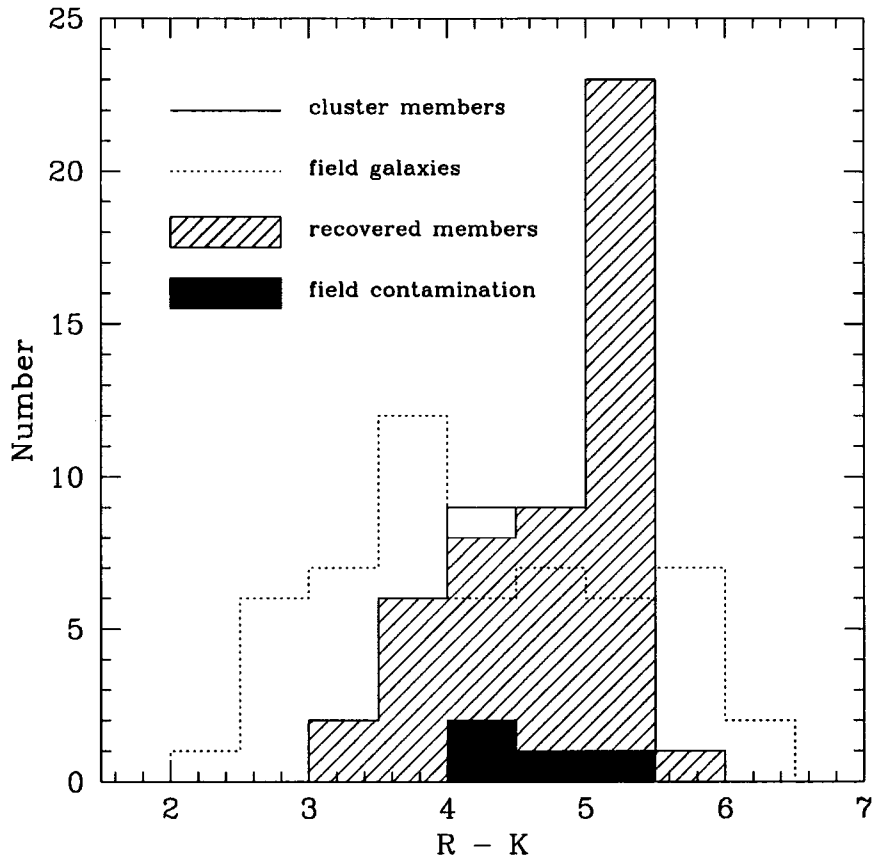

Figure 6.14: The colour histogram of a simulated cluster field at $z = 1$. The solid line shows the real cluster members, and the dotted line shows the real field galaxies. The slantwise hatched area indicates recovered cluster members, while the black shaded area indicates field contamination. There are few unrecovered clusters members and little field contamination: importantly there is no significant colour bias in the cluster recovery.

able to extend the CMR analysis (e.g. Kodama et al. 1998; Ellis et al. 1997; Stanford, Eisenhardt, & Dickinson 1998) to $z \gtrsim 1$ clusters without taking a large number of spectroscopic redshifts. Importantly, we can pick out cluster galaxies with diverse stellar populations; i.e. not only the passively evolving old galaxies but also the galaxies which have a significant contribution from younger stellar populations. This is encouraging, as it is important to select the cluster members with as little bias as possible. Our method will allow us to conduct a colour scatter analysis around the CMR reliably and to look into the age dispersion of field or cluster galaxies at high redshifts (c.f. Chapter 7).

Table 6.7. Passband choice for a simulated cluster field at $z = 1$. The number of unrecovered cluster members and the field contamination are also presented. The percentage of unrecovered members and field contamination is defined per real cluster members and per estimated cluster members, respectively.

	all		E/S0		unrecovered members		field contamination	
passbands	$\sigma(\Delta z)$	$\sigma(error)$	$\sigma(\Delta z)$	$\sigma(error)$	all	E/S0	all	E/S0
$BVRIK$	0.070	0.074	0.068	0.074	3 (6%)	3 (10%)	5 (10%)	4 (13%)
$VRIK$	0.079	0.099	0.064	0.095	1 (2)	0 (0)	4 (8)	3 (9)
VIK	0.141	0.129	0.069	0.112	7 (14)	1 (3)	4 (9)	3 (9)
VRK	0.114	0.131	0.087	0.129	4 (8)	2 (7)	3 (6)	3 (10)
VRI	0.231	0.232	0.243	0.216	9 (18)	3 (10)	10 (20)	7 (21)
RIK	0.155	0.133	0.074	0.118	16 (32)	3 (10)	3 (8)	3 (10)
RJK	0.211	0.212	0.159	0.216	38 (76)	21 (70)	7 (37)	4 (31)

6.5.2 Optimal passbands for cluster identification

In Table 6.7, we summarise the effect of passband choice on the estimated redshift error. Photometric errors of 0.071 mag are assumed in all passbands. Two cases in particular are found to be ideal: B, V, R, I and K, and V, R, I and K. The redshift errors are always well below 0.1 regardless of galaxy type, and hence the number of galaxies lost from the cluster sample and the field contamination are minimised. It is encouraging that we can do comparably well without B band, as it is better to minimise the use of passbands shortwards of rest frame 2500 Å where possible. It should be noted that V, I and K and V, R and K work comparably well, although $\sigma(error)$ is larger, especially for galaxies with ongoing star formation. This is because it becomes difficult to separate the effects of changes in stellar population and those of changing redshift. If both B and V band are missing (and we have R, I and K only), we tend to underestimate the redshift of bluer galaxies. This is analogous to lacking U band for Abell 370: it becomes difficult to disentangle galaxy type and redshift without the UV colours of star forming galaxies. For the early type galaxies, however, the redshift errors are reasonable, as we would expect from Fig. 6.2. In contrast, if K band is missing, the errors in the redshift estimation become much larger, irrespective of galaxy type, as there is no passband longwards of the rest-frame 4000 Å break. In this context, it is crucial for high redshift work to have both optical and near infrared passbands for accurate redshift estimation.

6.6 Conclusions

We present a new Bayesian photometric redshift estimator which is optimised for the identification and study of galaxy clusters at high redshifts. We use several broad passbands covering the 4000 Å break, and find in practice that it is possible to avoid the use of the uncertain colours shortwards of rest frame 2500 Å. In our models, we considered as wide a variety of stellar populations as is possible to minimise the selection bias in the recovered cluster members. However, most of the colour changes caused by changing stellar populations are highly degenerate. Accordingly, we chose to represent the wide range of parameters that affect the colours of galaxies using two main parameters, metallicity and local B band bulge-to-total luminosity ratio: these two parameters cover the full range of variations in colour caused by e.g. changes in dust content, cosmology or age. A potentially important limitation of our input spectra is the omission of galaxies with recent starburst spectra (with ages $\sim$ 0.5 Gyr; e.g. E+A galaxies), however the inclusion of these galaxies in the input spectra would increase the redshift error of non-starbursting galaxies, and so

these models were not included at this stage. With these input spectra, we find that it is possible to estimate redshifts with reasonable accuracy for a range of galaxy types, ranging from those with old, passively evolving stellar populations, through to those with younger stellar populations and on-going star formation. A particularly nice feature of this algorithm is that it is Bayesian: we can use our prior knowledge of galaxy properties to discriminate between reasonable and unreasonable redshift solutions based on the magnitude of the galaxy.

We successfully tested our method with data from Abell 370 and from the Hubble Deep Field, and applied the method to a simulated cluster at $z = 1$. We have shown that the estimation of redshifts with accuracies better than $|\Delta z| < 0.1$ can be achieved with multi-passband photometry of moderate quality ($\lesssim 0.1$ mag) in a small number of passbands, and the cluster members can be reliably identified. Therefore, the recovery of the CMR both in terms of the slope and scatter is expected to be accurate and almost free from any selection bias. We now have a means of analysing the photometric properties of high redshift field and cluster galaxies without thorough spectroscopic identification.

Chapter 7

The colour-magnitude relation of early-type galaxies in the Hubble Deep Field

7.1 Introduction

Early-type galaxies in clusters exhibit a strong correlation between their absolute magnitudes and colours: the colour-magnitude relation (CMR; e.g. Visvanathan & Sandage 1972; Bower, Lucey & Ellis 1992, BLE). The tightness of the CMR can be used to set important constraints on the star formation history of these galaxies, indicating an impressive degree of homogeneity in their formation processes. The CMR is most naturally accounted for as a metallicity sequence, with the scatter being driven primarily by differences in galaxy age. This paradigm correctly predicts the evolution of the zero-point and slope of the relation with redshift (Kodama et al. 1998; Stanford et al. 1998), and is supported by line index analysis of galaxies in the Fornax and Coma clusters (Kuntschner & Davies 1998; Terlevich et al. 1999). Bower, Kodama & Terlevich (1998; BKT hereafter) have recently reviewed the limits on formation history that can be derived from local clusters. They conclude that the small scatter of the CMR implies that the bulk of the stellar populations are old, with most of the stars having been formed before a look-back time of 9 Gyr ($z \sim 1$ with $H_0 = 50$ km/s/Mpc and $q_0 = 0.5$); although some residual star formation in a fraction of the galaxies is *required* to account for the increasing fraction of blue galaxies observed in the core of intermediate redshift clusters (e.g. Butcher & Oemler 1984).

A key question is to determine whether the same homogeneity that is seen in the clusters extends to galaxies in lower density environments. One of the most homogeneous studies is that of Larson,

Tinsley & Caldwell (1980). They found that scatter of field (i.e. galaxies selected along an average line of sight) ellipticals was greatly enhanced over equivalent cluster galaxies; however, the same trend was not seen in the S0 galaxy population. Because of photometric and galactic foreground reddening uncertainties, more recent studies have concentrated on spectroscopic indicators of stellar populations. For instance, Guzman et al. (1992) report a small offset in the normalisation of the Mg_2-σ correlation of early-type galaxies between the core and outskirts of the Coma cluster. However, the implied differences in mean stellar population ages are smaller than 10 per cent.

In this Chapter, we use the photometric redshift estimator developed in the last Chapter to address the homogeneity of the formation of early-type galaxies in low density environments using the colours of morphologically classified E and S0 galaxies in the northern Hubble Deep Field (HDF; Williams et al. 1996). The galaxies are typically at redshifts of order unity, allowing us to take advantage of the large look-back time. Despite the large distances to these objects, the narrow point spread function of the Hubble Space Telescope allows accurate morphological classification. Furthermore, because these galaxies cover only a small area of sky, uncertainties in the photometric zero-point and galactic extinction do not introduce spurious scatter into the relation as they might do in the local surveys.

The plan of the Chapter is as follows. In section 7.2, we describe the method used to create the rest-frame CMR. The star formation history is derived by comparing the colour distribution with models in section 7.3; this procedure is discussed in section 7.4. We then briefly summarise our results in section 7.5.

7.2 The field colour-magnitude relation at $z = 0.9$

7.2.1 Early-type galaxies in the Hubble Deep Field

For this study, we use a sample of 35 morphologically classified early-type galaxies from Franceschini et al. (1998; hereafter F98). We assume that this sample will be representative of the field early type galaxy population at the sample's median redshift of $z \sim 0.9$. Their initial selection is based on K band surface brightness profiles from the KPNO-IRIM images of Dickinson et al. (1997). Further checks are performed using HST V or I band data (Fasano et al. 1998). The sample galaxies are flux-limited with $K < 20.15$. F98 present photometry in 7 passbands from the UV to near-infrared (U_{300},B_{450},V_{606},I_{814},J,H,K) using a fixed $2.5''$ diameter aperture.

7.2.2 Rest-frame colours and magnitudes

Fifteen out of the 35 F98 galaxies have spectroscopic redshifts available from the literature (Cohen et al. 1996; Cowie 1998). For the remainder, redshifts must be estimated using photometric redshift techniques; we use the estimator developed in Chapter 6. At $z \sim 1$, the bluer optical colours primarily reflect the colours of the rest frame far UV, where model colours are highly uncertain: we therefore adopt an iterative redshift estimation scheme. We used all seven passbands from U_{300} to K for the first estimation. For the second estimation, we excluded the passbands which would fall below rest frame 2500 Å, assuming that the first galaxy redshift estimate was reasonably close to the final redshift estimate. We used the 15 galaxies with spectroscopic redshifts to assess the uncertainty of the technique. The agreement between our estimates and the spectroscopic ones are generally good, with redshift errors of $\overline{|\Delta z|} \sim 0.08$. This uncertainty is propagated through to the rest frame colours and luminosities as described below. As a final check, we confirmed that our estimates are also consistent with F98's, again with $\overline{|\Delta z|} \sim 0.1$. So-called *catastrophic* redshift errors can occur when the spectra of the model templates are a poor match to the observed colours (Yee 1998; Chapter 6), which happens predominantly with star forming late-type galaxy spectra. In this analysis, we expect that the redshift estimates of the redder, early-type galaxies will be robust to this type of error, but we bear in mind that the redshifts of the fainter, blue galaxies in our sample may be susceptible to this source of error. In addition to a redshift, our code also gives an estimate of the bulge-to-total light (B/T) ratio, which we use below to determine the K-correction for the galaxy.

K-corrections are applied to the data using evolutionary models for early-type galaxies (in which chemical evolution is taken into account) from Kodama et al. (1998) and Chapter 6. The model galaxy has an old bulge component with mean stellar metallicity $\langle \log Z/Z_{\odot} \rangle = -0.23$ and a disc component added in the right proportion to give the above B/T ratio. The star formation rate in the disc is regulated by a mass-dependent star formation law with a star formation timescale of 5 Gyr. The formation redshift of the galaxies is fixed at $z_{\rm form} = 4.4$. In practice, the galaxies lying near the red envelope of the CMR are unaffected by the details of star formation in the model galaxy since they are dominated by bulge light. Galaxies for which this correction process is potentially important lie far from the ridge-line of the main relation. Rest frame U-V colours are estimated by K-correcting the observed colours in passbands (M_1, M_2) chosen to bracket the rest frame 4000 Å break. We use $(M_1, M_2) = (U_{300}, V_{450})$ for $z < 0.2$, (B_{450}, I_{814}) for $0.2 \leq z < 0.6$, (V_{606}, J) for $0.6 \leq z < 1.3$, (I_{814}, J) for $1.3 < z < 1.6$, and (I_{814}, H) for $z \geq 1.6$.

Because the sample is at a range of different redshifts in the field, it is also important to apply evolution corrections (E-corrections), so that a single coeval CMR can be constructed. For the sake of simplicity we assume, to first order, that all the galaxies are formed in a single burst at $z = z_{\rm form}$. Using this model, we transform the colours of all the galaxies to the median redshift of the sample to minimise the uncertainty in the E-correction. However, it is clear from the range of galaxy colours that the evolution of individual galaxies will not be well described by this model. For instance, the amount of E-correction for the bluer galaxies at lower redshift ($z < 0.9$) will be underestimated, given that these galaxies are supposed to be younger. The colour should evolve more rapidly, be bluer and the colour deviation from the passively evolved Coma CMR at $z = 0.9$ should be larger, compared to the passive evolution of old stellar population. We, therefore, use the same passive evolution correction for all the galaxies as a first approximation, and then apply an additional (smaller) correction according to the colour deviation from the red sequence.

We adopt a B/T=1.0 model and $z_{\rm form} = 4.4$ for the primary passive evolution correction. The deviation of the galaxy from the Coma cluster CMR at $z = 0.9$ (see below) is then used to estimate the secondary correction by multiplying by a correction factor:

$$\Delta(U-V)_{\rm corrected} = \Delta(U-V) \times \frac{t_{z=z_g} - t_{z=4.4}}{t_{z=0.9} - t_{z=4.4}}, \tag{7.1}$$

where t_z indicates the time from the Big Bang at a given redshift. This correction is adequate since the integrated colour $U - V$ of a galaxy scales roughly logarithmically with age. For galaxies lying within $|\Delta(U-V)| < 0.5$ of the fiducial CMR, this correction amounts to only $\lesssim 0.1$. We apply this additional correction only to the colour. As the slope of the CMR is quite shallow, the corresponding magnitude correction has a negligible effect on the final results, and is, therefore, neglected for the sake of simplicity.

The key aim of this work is to examine the spread of field galaxies around the CMR defined by rich clusters. Therefore, relatively accurate knowledge of the photometric uncertainties is important. The limiting uncertainties for galaxies with both spectroscopic and photometric redshifts lie in the matching of the model and object spectra (leading to uncertainties in redshift, evolution and K-corrections): the quality of the optical and near-infrared photometry for the northern Hubble Deep Field is very high. For galaxies with photometric redshifts only, the dominant source of error is the redshift uncertainty due to mismatches between the object and model spectra. We, therefore, adopt the RMS difference between the spectroscopic and photometric redshifts (0.08) as the redshift uncertainty. For those galaxies with spectroscopic redshifts, the dominant source of rest-frame colour uncertainty is the error introduced by our use of a single bulge model for the K-

corrections. Differences between the assumed bulge metallicity and the object's bulge metallicity (and similarly with age, because of the age/metallicity degeneracy; Worthey 1994, Chapter 6) is an unavoidable source of error in the K-correction. To estimate these effects, we applied the K+E-corrections using other elliptical galaxy models with different metallicities in a range of $-0.52 \leq \langle \log Z/Z_{\odot} \rangle \leq 0.06$: the resultant colours and magnitudes differ by less than 0.1 mag. This shows that the corrections that we have made are relatively insensitive to the metallicity variations that drive the CMR.

Because of the evolutionary corrections, our results depend slightly on the adopted cosmological framework. For our fiducial model, we adopt an open universe with (H_0, q_0)=(64,0.1). We also consider a flat universe with (H_0, q_0)=(50,0.5). Both models give the same age of the universe at 13 Gyr. Hereafter, we use the parameter h to mean $H_0/100$.

7.2.3 The colour-magnitude relation

The final $z = 0.9$ rest-frame colours and magnitudes are shown for the fiducial model in Fig. 7.1. Galaxies with spectroscopically determined redshifts are shown as filled symbols, where the symbol shape indicates the observed galaxy redshift. Galaxies with photometric redshifts are shown as open symbols with error bars representing the estimated uncertainty in the rest-frame colour and absolute magnitude.

The ridge-line of the CMR is well defined even in field early-type galaxies at $z = 0.9$. This is a striking result, since the existence of a well defined old stellar population at high redshifts seems contradictory to the spirit — if not the details — of hierarchical galaxy formation models (e.g. White & Frenk 1991; Kauffmann, White & Guiderdoni 1993; Baugh et al. 1998; Kauffmann & Charlot 1998a; Cole et al. 1999). An important test is the comparison of field and rich cluster CMRs.

Firstly, we compare the HDF CMR with the Coma cluster. The $z = 0.023$ Coma cluster relation is redder than the observed envelope by ~ 0.3 mag at a fixed luminosity. To make the comparison fair, we need to apply a correction for passive evolution in order to determine the position of the ridge-line of the Coma relation at $z = 0.9$. This correction results in the reddest possible CMR at high redshift. To make the comparison, we use the $U - V$ data from BLE92. However, because of the existence of colour gradients internal to elliptical galaxies, we have been quite careful to match the apertures in which colours are measured for both the local and high redshift samples. To match the aperture adopted by F98, we use $25''$ apertures (8.4 h^{-1} kpc) for the $U - V$ colour and $32''$ (10.7 h^{-1} kpc) apertures for the M_V magnitude for the local Coma CMR. $25''$ is the

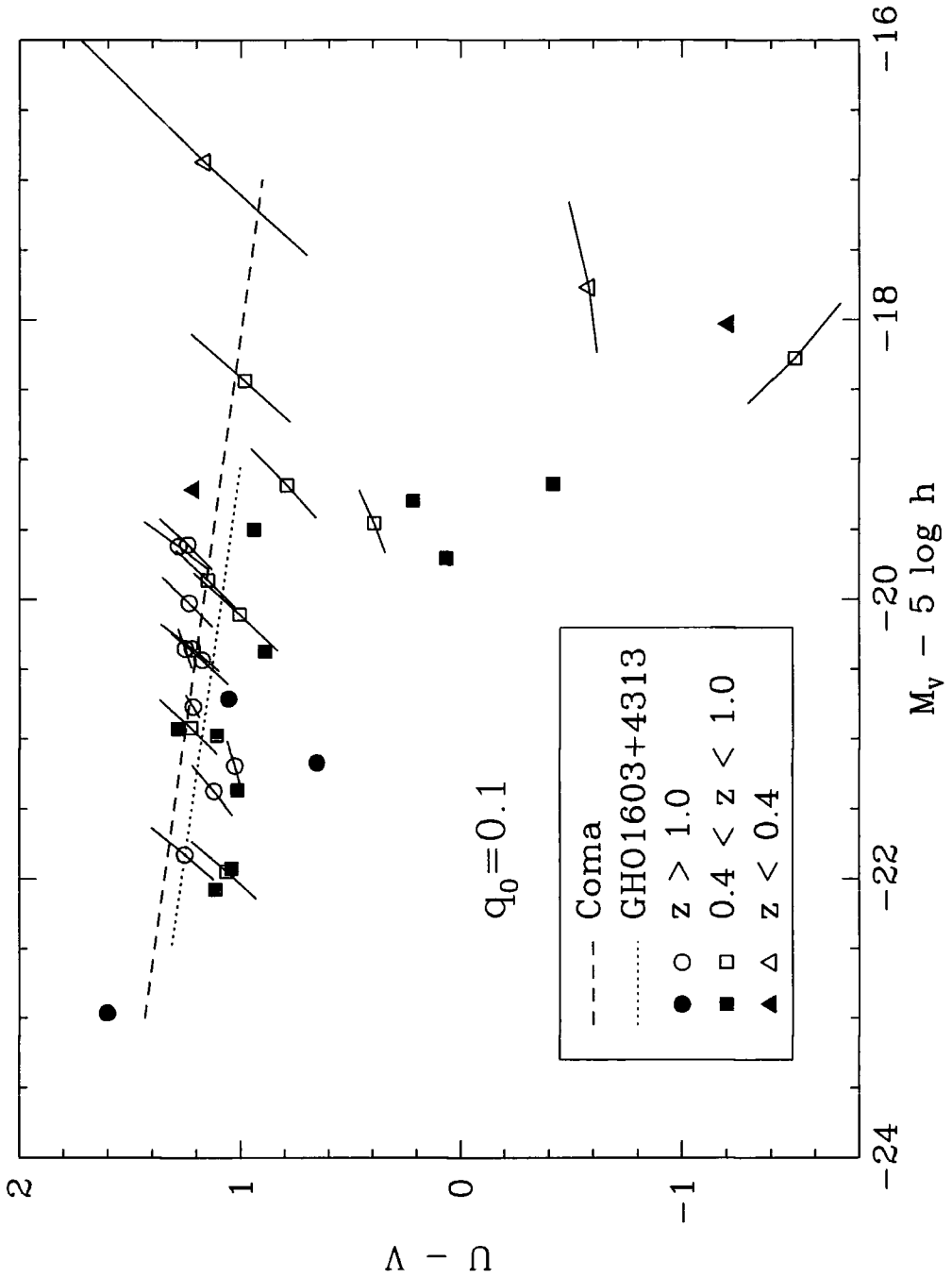

Figure 7.1: The colour-magnitude relation for early-type galaxies in the Hubble Deep Field observed at $z = 0.9$ with a $q_0 = 0.1$ cosmology. Filled symbols indicate galaxies with spectroscopic redshifts, open symbols refer to those with photometric redshifts only. The plot symbol indicates a galaxy's redshift. The dashed line shows the CMR of Coma transformed to $z = 0.9$ using a passive evolution correction. The dot-dashed line shows the CMR of a cluster GHO 1603+4313 at $z \sim 0.9$ from Stanford et al. (1998) after K-correction.

maximum aperture that allows us to reliably measure the $U - V$ colour. The large aperture Coma CMR is overplotted in Fig. 7.1. For the fiducial $q_0 = 0.1$ cosmology, the CMR just traces the reddest boundary of the HDF early-types. This suggests that at least some early-type galaxies in the HDF must be as old as those in rich clusters (provided, of course, that they obey the same mass-metallicity relation). We attempt to quantify this in section 7.3. For a flat cosmology $q_0 = 0.5$, the Coma relation lies blueward of many of the HDF galaxies. Taken at face value, this implies that many of the field galaxies formed their stars *before* the galaxies in rich clusters.

For further comparison, the CMR of the $z \sim 0.9$ cluster GHO 1603+4313 from Stanford et al. (1998) is also presented, applying a K-correction using $(M_1, M_2) = (R, J)$ as described in section 7.2.2. In this case, aperture and E-corrections are not required. The location of the relation is again consistent with the red early-types in the HDF, although there exists a slight systematic blue offset of order ~ 0.1 mag with respect to the Coma CMR. Although this offset could result from observational zero-point mismatches and/or slight model uncertainties, if we adopt this relation rather than the transformed Coma cluster relation, some HDF early-types appear older, or equivalently more metal rich, than their cluster counterparts. We note that this offset disappears in the $q_0 = 0.5$ cosmology.

Although the overall impression is of a well defined CMR, there are two important differences between this relation and the CMR in rich clusters. Firstly, the relation shows little evidence of a slope (although this may be masked by the large scatter). Any attempt to measure the slope is dominated by the very bright, red galaxy 4-752-1. Because the slope is so poorly determined, we adopt the slope of the Coma cluster CMR in what follows. Secondly, the relation appears to have larger scatter. This impression remains even if only the objects with spectroscopic redshifts are considered. A maximum likelihood analysis of all the galaxies with $U - V > 0.7$ suggests an intrinsic scatter of 0.12 ± 0.06 after allowing for uncertainties in the individual data points. This value, while uncertain, looks to be larger than the corresponding cluster value of ~ 0.07 mag in the rest frame $U - V$ at the same redshift $z \sim 0.9$ (Stanford et al. 1998). Therefore, the scatter in the field, which is almost certainly *no less* than the corresponding scatter for the $z \sim 0.9$ cluster, allows an epoch of star formation similar to, if not more extended than, the epoch of major star formation in cluster early-types. This is in qualitative agreement with hierarchical models.

7.3 Constraints on star formation history

In order to quantify the constraints that are placed on the star formation history of HDF early-type galaxies, we compare the distribution of colour deviation from the $z = 0.9$ Coma CMR with the

predictions of a number of simple models. As discussed in the introduction, we adopt a paradigm in which the colour magnitude relation in clusters is primarily driven by universal correspondence between mass and metal abundance (KA97; Kodama et al. 1998; BKT). Following BKT, we consider two types of star formation history: a single burst model and a constant star formation (SF) model, truncated at some epoch. We randomly assign a single burst age $t_{\rm burst}$ between $t_{\rm burst,min}$ and $t_{\rm burst,max}$, or a truncation time $t_{\rm stop}$ between $t_{\rm stop,min}$ and $t_{\rm start}$, respectively. Note that $t_{\rm burst,max}$ and $t_{\rm start}$ should be less than the age of the Universe at $z = 0.9$, which is 6.0 Gyr for (H_0,q_0)=(64, 0.1) and 5.0 Gyr for (50, 0.5), respectively. We fix the stellar metallicity at solar abundance, since we compare colour *residuals* from the $z = 0.9$ CMR with the models (therefore, automatically taking out, to first order, the metallicity dependence in this comparison).

Given the significant scatter of the dataset, the most appropriate method of comparing the observed colour distribution with the models is to create a cumulative histogram and to apply a Kolmogorov-Smirnov (K-S) test to the resulting distributions. This test requires that the models provide accurate *absolute* colours, but this should not present a problem, as our model has been demonstrated to give the correct absolute colours for distant clusters out to $z \sim 1.2$ (Kodama et al. 1998). In the comparison, we convolve a Gaussian error of $\sigma = 0.1$ mag with the model colour in order to allow for errors in the K-corrected colours caused by redshift estimation uncertainties for the red envelope galaxies.

We applied the K-S test to the observed and model histograms using various combinations of ($t_{\rm burst,min}$, $t_{\rm burst,max}$) or ($t_{\rm stop,min}$, $t_{\rm start}$), putting constraints on these model parameters. A number of example histograms are presented in Fig. 7.2. The basic results are as follows:

- *All galaxies*—solid histogram: The observed cumulative histogram of colour residuals has a clear continuous blue tail down to $\Delta(U-V) \sim -2$. This allows for the existence of a fraction of young galaxies, and models that continue to produce galaxies until $z = 0.9$ are acceptable. However, half of the galaxies are very red, with $|\Delta(U-V)| < 0.2$. In order to make these red galaxies, $t_{\rm burst,max}$ should be larger than $\sim$ 4.5 Gyr in the single burst model or $t_{\rm start}$ should be larger than $\sim$ 3.5 Gyr in the constant star formation model at the 3 σ level. The former case corresponds to forming more than 40 per cent of the galaxies beyond $z > 2$, while the latter case corresponds to forming more than 40 percent of stars therein at $z > 2$. Note that, in either case, we do find a substantial fraction of galaxies in which *all* the stars would have been formed at redshifts greater than 2. The best fitting model is (single-burst, $t_{\rm burst,min} = 0$ Gyr, $t_{\rm burst,max} = 6$ Gyr). In this case, $\sim$ 60 per cent of the galaxies are older than $z > 2$.

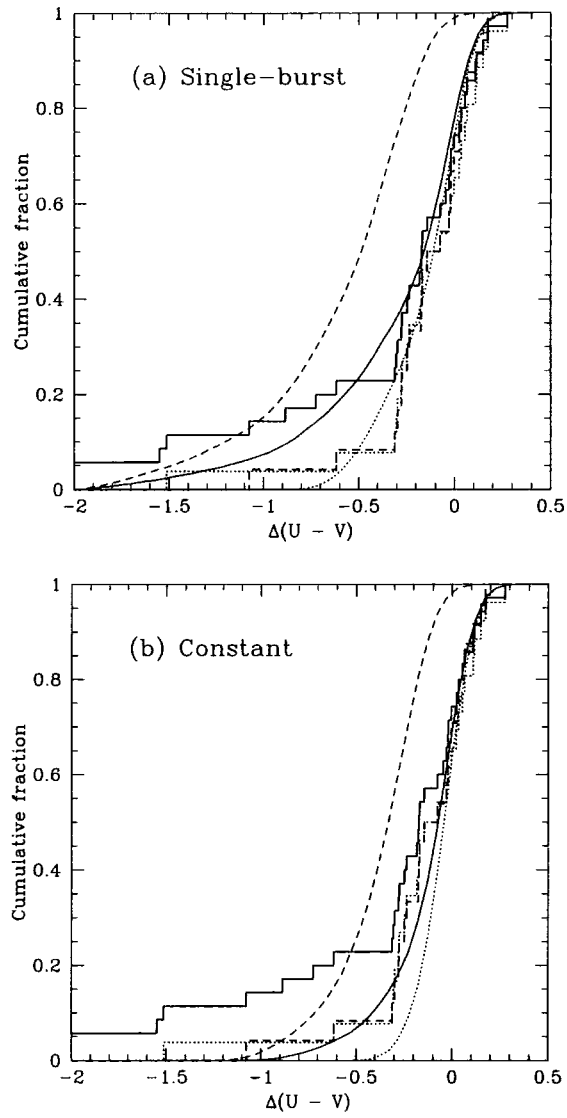

Figure 7.2: Cumulative histograms of the $U - V$ residuals from the K-corrected Coma CMR ($q_0 = 0.1$). Observed histograms are shown for all galaxies (solid histogram), the bright galaxies only (dashed histogram) and the galaxies without peculiars (dotted histogram). Single burst models and the constant SF models are superposed in the panel (a) and (b), respectively. The models shown have ($t_{\rm burst,min}$ or $t_{\rm stop,min}$, $t_{\rm burst,max}$ or $t_{\rm start}$)= (0, 6) [solid curve], (0, 3) [dashed curve] and (1, 6) [dotted curve].

- *Cosmology*: The $q_0 = 0.1$ cosmology is preferred because the position of the ridge line matches the reddest colours expected from passive evolution. If we use a $q_0 = 0.5$ cosmology, the evolutionary correction makes the Coma CMR too blue with respect to the HDF early-type galaxies. Note, however, that the colours of these galaxies are still consistent with the Coma CMR within $\sim 1\ \sigma$ K-correction and photometric redshift errors.

- *Bright galaxies*—dashed histogram: In this case, we use a faint cut-off of $M_V - \log h < -19.8$ ($q_0 = 0.1$), which roughly corresponds to 1 magnitude fainter than the local M_* (passively evolved out to $z = 0.9$). The blue tail is strongly suppressed since most of the younger galaxies are also faint. Therefore, the fraction of old galaxies ($z > 2$) is increased to more than 50 per cent. Their colour distribution is best fitted by (single-burst, $t_{\rm burst,min} = 1$-2 Gyr, $t_{\rm burst,max} =$ 6-5 Gyr) or (constant-SF, $t_{\rm stop,min} = 0$-1 Gyr, $t_{\rm start} = 6$-5 Gyr). In that case 70-80 per cent of galaxies or stars therein are older than $z > 2$. It is also worth pointing out that galaxies bluer than $U - V = 0.5$ will fade by at least one magnitude *more* than the old passively evolving galaxies before reaching the red envelope of the CMR. Thus, none of the blue early-type galaxies could be the progenitor of a red object brighter than $M_V - \log h \sim -18.5$.

- *No peculiar galaxies*—dotted histogram: F98's classification of the galaxies is mainly based on their (ground based) K band surface brightness profiles. We checked the HST frames in order to visually confirm these classifications. Several galaxies were found to have morphological peculiarities (Table 7.1). Most of these objects have bluer colours. With these objects excluded, the colour distribution looks quite similar to that of the bright galaxies, and the same arguments can be applied.

Table 7.1. Peculiar galaxies. Magnitudes and colours are given in the rest frame at $z = 0.9$ same as in Fig. 7.1 ($q_0 = 0.1$).

FOCAS ID	M_V $-5\log h$	$U-V$	Comments
4-727-0	−18.28	−1.51	Merger
4-565-0	−19.71	0.07	Unclassified by F98
1-86-0	−17.77	−0.58	Spiral structure
4-307-0	−20.77	1.22	Faint and peculiar
2-236-2	−18.44	0.98	Companion
3-143-0	−19.30	0.22	Chain galaxy
2-531-0	−19.46	0.39	Ring of HII regions
3-430-2	−20.71	1.06	Interaction
3-405-0	−18.03	−1.21	Spiral structure

In summary, the apparent tightness of the CMR can accommodate continuous formation of early-type galaxies down to the observed epoch. However, the redness of the galaxies is a considerable constraint; at least 40 per cent of field early-type galaxies at $z = 0.9$ or stars therein (not in the individual galaxies) should form beyond $z = 2$ in order to create enough objects that are sufficiently red.

7.4 Discussion

As we have described, the colour magnitude relation of early-types in the HDF suggests a wide range of formation times, where ongoing star formation is allowed in some galaxies right up to the epoch of observation. However, the well-defined red ridge-line of field early type galaxies in Fig. 7.1 indicates that a substantial fraction of galaxies must have been formed prior to $z > 2$.

Our conclusions are consistent with recent work on the HDF galaxies by Abraham et al. (1999), who concluded that 7 out of 11 I_{814}-band selected early-type galaxies are coeval and old, and 4 galaxies have had recent star formation. F98, from which we take our sample, claim that most of these galaxies have ages between 1.5 and 3.0 Gyr, corresponding to $z_{\rm form}$ between 1 and 3 ($q_0 = 0.15$) based on the rest-frame $B - J$ and $V - K$ colours. Although their upper limit on $z_{\rm form}$ is slightly lower, they do have a mixture of both young and old populations. They also find that lower-mass systems preferentially form at lower redshifts, the same tendency as we have found.

The substantial fraction of red galaxies raises two questions. Firstly, is the presence of such red galaxies compatible with theories of hierarchical galaxy formation? Although Governato et al. (1999) have shown that early star formation happens in a fraction of objects, these galaxies are likely to be subsequently bound into clusters. Field early-type galaxies should have systematically younger ages than their cluster counterparts (Kauffmann 1996). To definitively rule out a particular model, however, requires the selection process to be carefully taken into account. For instance, the star formation histories of early-type galaxies in the local field may differ substantially from early-type galaxies found in the field at $z = 0.9$. Furthermore, although our results suggest that nearly 60 per cent of early-type galaxies were formed prior to $z = 2$, the stars in these galaxies form only a small fraction of the present day early-type population and need not have been formed in a single monolithic unit. This is an extensive topic that we will investigate in the future.

It is interesting to try to understand these results in the context of the evolution of the K-band luminosity function (Songaila et al. 1994; Cowie et al. 1996) and the space densities of red galaxies in surveys such as the Canada-France Redshift Survey (Lilly et al. 1995). The decreasing space

density of red galaxies (relative to passively evolving models) have been shown to support the hierarchical picture, indicating a late formation epoch for the majority of field galaxies. Deep optical and near-infrared surveys find few objects red enough to be consistent with the colours of a $z > 1$ passively evolving stellar population, again supporting a late formation epoch for field galaxies (Zepf 1997, Barger et al. 1999). However, optical–near-infrared colours are very sensitive to even small amounts of star formation, making these constraints relatively weak. The evolution of the K-band luminosity function is a particularly strong constraint (Kauffmann & Charlot 1998b) since it is robust to small amounts of residual star formation; this has been found to be consistent with the expectations from hierarchical clustering models. In this context, our results, which indicate a substantial old early-type population at $z \sim 0.9$, seem to contradict these studies.

It is possible to reconcile these apparently contradictory observations in a number of ways. It is likely that the explicit selection of *morphologically* early-type galaxies preferentially excludes galaxies with ongoing star formation. We would, therefore, be in a situation where the field early-type galaxies at $z = 0.9$ are merely a subset of the present-day field early-type galaxies, which form from galaxies both with and without ongoing star formation at $z = 0.9$. Alternatively, F98 suggest that the disappearance of red early-type galaxies may be due to the onset of an epoch of extreme dust reddening at $z > 1.5$, but such a picture seems ad hoc. Another solution may be to allow a degree of merging between the early-type galaxies (e.g., Menanteau et al. 1999). This would not contradict our conclusions concerning the stellar populations, and, although the process would be expected to introduce additional scatter into the CMR, the observed relation is sufficiently broad that this constraint is unimportant. Merging tends to flatten the CMR (BKT), and in this respect it is intriguing that the HDF relation is so flat. We note that another resolution to this discrepancy could be the presence of a $z \sim 1$ cluster in the HDF itself. Our conclusions would then not be representative of the field (in the sense of representing an average line of sight). Indeed, this may well be the case: comparison of the northern and southern Hubble Deep Fields has shown that there are a factor of ~ 2 more galaxies in the redshift interval $0.4 < z < 1.2$ in the north than in the south (Gwyn 1999). Note that fluctuations in the redshift distribution at this level in Hubble Deep Field-sized patches are expected at roughly this level (Benson, private communication). What is clear is that further work is required to quantify this source of uncertainty: a first step in this direction would be to incorporate the southern Hubble Deep Field early-types in this analysis when we compare with the predictions from the semi-analytic models of Cole et al. (1999).

7.5 Conclusions

- Using the stellar population model and photometric redshift estimator of Kodama et al. (1998) and Chapter 6 respectively, we constructed a colour-magnitude relation for morphologically selected HDF early-type galaxies in the rest frame of the median redshift of the sample $z = 0.9$. The colour-magnitude diagram constructed in this way has intrinsic scatter no smaller than the $z = 0.9$ cluster GHO 1603+4313.

- Comparison of the residuals from the passively evolved Coma CMR with simple models indicates that a fraction of HDF early-types (primarily the low mass galaxies) can form continuously to the epoch of observation. However, around half of our sample must form at $z > 2$ (although not necessarily in a monolithic unit).

- Reconciling this (high) fraction of old field early-types at $z = 0.9$ with studies supporting late field galaxy formation (as in HGF models) may be possible by taking into account the morphological filtering of galaxies going into our CMR.

Chapter 8

Conclusions and prospects

In this thesis, we have explored aspects of the star formation histories of both late and early-type galaxies.

8.1 Part 1: The star formation histories of spiral galaxies

8.1.1 Conclusions

In Part 1, we presented an in-depth study of the star formation histories of spiral galaxies with a range of properties (such as magnitude, surface brightness or size). We used optical and near-infrared (near-IR) colours to constrain the ages and metallicities of our sample galaxies: our results should be robust in a relative (but not absolute) sense.

In Chapter 2, we present deep optical and near-infrared imaging for a diverse sample of 26 low surface brightness galaxies (LSBGs) and use this imaging to constrain their star formation histories. In Chapter 3, we extend the star formation history analysis to a much larger sample of 121 spiral galaxies with comparable quality optical–near-IR data. In Chapter 4, we explored how simple star formation laws and galaxy evolution prescriptions could describe the trends observed in Chapters 2 and 3. We have found the following.

- Optical–near-IR colour gradients are common in spiral galaxies of all types. These colour gradients indicate that the inner regions of galaxies are typically older and more metal rich than the outer regions of galaxies. The amplitude of age gradients (per K band disc scale length) increases from high surface brightness galaxies to low surface brightness galaxies. Two types of galaxies fail to conform with this trend: small lenticular galaxies in the Ursa Major Cluster tend to have younger, more metal rich cores, and some LSBGs lack significant colour gradients (Bergvall et al. 1999).

- The age of a spiral galaxy (or indeed a given region within a spiral galaxy) correlates strongly with the local K band surface brightness: the residuals from this trend only weakly correlate with K band absolute magnitude.

- The metallicity of a spiral galaxy (or a given region within a galaxy) correlates strongly with *both* the K band surface brightness and the K band absolute magnitude.

- We have constructed crude total (baryonic) galaxy mass and density estimators: the trends in star formation history and metallicity with surface brightness and magnitude reflect underlying trends in star formation history and metallicity with baryonic surface density and mass.

- Simple 'toy' models show that *the star formation history of a region within a galaxy depends primarily on the local surface density of gas*, with possible dependence on the dynamical timescale. Infall at late times is allowed for low mass galaxies, and would produce the observed weak correlation between mass and star formation history. *Metal-enriched outflow from low mass galaxies seems to be required by our data* to provide a sufficient mass dependence in the metallicity of spiral galaxies.

- There is significant intrinsic scatter in these correlations: this may be due to the influence of small bursts of star formation on the broad band colours. The existence of intrinsic scatter in the correlations means that mass, density and possibly the dynamical timescale *cannot* be the only parameters affecting the star formation history of spiral galaxies.

In Chapter 5 we investigate one of the implicit assumptions underlying Part 1: we implicitly assumed that galaxies come with a continuous range of surface brightnesses, magnitudes, etc. However, Tully and Verheijen (1997) challenged this view, claiming that the K' band distribution of disc central surface brightnesses in the Ursa Major Cluster was bimodal. We used the Kolmogorov-Smirnov statistic to investigate the significance of the bimodality in the Ursa Major Cluster. The isolated galaxy (with no significant projected neighbours within $80h_{85}$ kpc) surface brightness distribution is *not* bimodal: the sample of galaxies with well-determined inclination-corrected central surface brightnesses is too small to rule out a single-peaked distribution.

8.1.2 Future work

There are a great many interesting extensions to this work which can and should be undertaken. Below, we describe a few of the most promising ones.

- **Dark matter:** The dynamics of LSBGs are dominated by dark matter at all radii (de Blok et al. 1996). As such, they offer a unique chance to study the structure of dark matter haloes (e.g. Hernandez & Gilmore 1998; Navarro 1998). Because of the insensitivity of the K band stellar mass to light ratio to small amounts of recent star formation, the sample of LSBGs presented in Chapter 2 are an ideal dataset with which to study the dark haloes of LSBGs. In collaboration with Erwin de Blok, I have obtained HI interferometry of the southern sample of LSBGs with the Australia Telescope Compact Array: as the southern sample is relatively nearby, they offer a unique chance to study the rotation curves (and, therefore, dark matter distributions) of LSBGs with comparatively high spatial resolution (c.f. de Blok et al. 1996).

- **Star formation:** LSBGs, by virtue of their low gas surface densities, present a very different star formation environment to their higher surface brightness counterparts. In fact, most of a LSBG disk is below Kennicutt's (1989) proposed critical surface density for star formation, suggesting that star formation in LSBG discs should not happen at all (van der Hulst et al. 1993). Despite this, relatively shallow imaging of LSBGs has shown that star formation does occur in LSBGs, albeit at rates more than an order of magnitude lower than those observed in high surface brightness galaxies. We have obtained deep Hα imaging of a sample of 15 LSBGs: using these data, we intend to study e.g. the distribution of star formation in LSBGs, or by using these data in conjunction with the HI described above, we can test star formation laws at hitherto unexplored low gas surface densities.

- **Local colour trends in spiral galaxies:** In Chapters 2 and 3, we presented correlations between the star formation histories and metallicities derived using optical and near-IR colours and the local and global galaxy parameters. We argued that small bursts of star formation and e.g. the effects of dust were relatively minor; however, it would be preferable to truly understand and quantify these effects in influencing the colours of spiral galaxies. It would be interesting to carry out a relatively limited programme of very deep optical and near-IR imaging of a sample of spiral galaxies with a wide range of physical parameters, with the intention of constructing *local* colours. With data of this quality, it would be possible to e.g. compare arm and inter-arm colours in spirals and quantify the effects of dust on the global colours of spirals more directly.

In addition to these projects, a great many issues remain: for example, extending the type of analysis presented above to even lower surface brightness galaxies or to irregular galaxies (which do not appear to have established metallicity gradients, and, therefore, may lack age gradients

also). Another interesting extension would be to test the stellar population models more directly: by studying the optical–near-IR colours of young globular clusters in nearby merger remnants, we can constrain some of the more uncertain aspects of stellar population synthesis models, which are highly uncertain in the near-IR, and at young ages.

8.2 Part 2: The formation epoch of early-type galaxies

8.2.1 Conclusions

In Part 2, we presented a short exploration of the constraints that we can place on the formation epoch of early-type galaxies by studying their colours at high redshift.

In Chapter 6, we present a photometric redshift estimator optimised to recover populations of high redshift early-type galaxies with as little selection bias as possible. We use a Bayesian approach to take account of both colour and magnitude information in differentiating between reasonable and unreasonable redshift solutions. We explicitly account for both galaxy type (via B/T) and metallicity: colour changes due to dust, galaxy age, cosmology and small amounts of star formation are degenerate with changes of metallicity and B/T. Bursts involving $\sim$ 10 per cent of the galaxy mass with ages of $\sim$ 0.5 Gyr have a distinctive colour signature not accounted for in these models: however, galaxies with star formation bursts of this age should be relatively rare, and, if required, models describing this effect could be easily incorporated (at the expense of making redshifts of galaxies without bursts more uncertain). We tested the redshift estimator against galaxies in the field of Abell 370 and the northern Hubble Deep Field, finding that RMS accuracies of $\sim$ 0.1 in redshift are readily achievable with photometry accurate to $\sim$ 0.1 mag in 4 carefully chosen passbands.

In Chapter 7, we use this photometric redshift estimator to study the field colour-magnitude relation (CMR) of morphologically-selected early-type galaxies in the northern Hubble Deep Field. We find that the CMR at the median redshift of the sample $z = 0.9$ has a scatter no smaller than the $z = 0.9$ cluster GHO 1603+4313. Comparison of the residuals from the passively evolved Coma CMR with simple models indicates that a fraction of HDF early-types (primarily the low mass galaxies) can form continuously to the epoch of observation. However, around half of our sample must form at $z > 2$ (although not necessarily in a monolithic unit). Reconciling this (high) fraction of old field early-types at $z = 0.9$ with studies supporting late field galaxy formation (as in hierarchical galaxy formation models) may be possible by taking into account the morphological filtering of galaxies going into our CMR.

8.2.2 Future work

The existence of a well-defined CMR (especially in the field) at $z = 0.9$ may be difficult to accommodate in semi-analytic galaxy formation models: field galaxies are predicted to form much later than galaxies in denser cluster environments (Baugh et al. 1998; Kauffmann & Charlot 1998a). One important extension of this work is a detailed comparison of the CMR in the northern *and* southern Hubble Deep Fields with the predictions of semi-analytic models: preliminary comparisons indicate that the number densities, redshift distributions and observed colours of morphologically-selected early-types in the northern Hubble Deep Field are roughly consistent with the expectations of the semi-analytic galaxy formation model of Cole et al. (1999).

Other extensions of this work are planned: optical and near-IR imaging of known high redshift clusters, and surveys designed to detect high redshift clusters (e.g. the planned UKIRT Wide Field Survey) will allow probing of the CMR at ever-higher redshifts, placing interesting constraints on the formation epoch of early-type galaxies in clusters.

8.3 What have we learned from this thesis?

In the introduction, we outlined two of the significant problems in understanding the star formation histories of galaxies: 1) what are the most appropriate prescriptions for star formation and feedback over galactic scales and 2) how well do current nurture models explain the properties of the universe's early-type galaxies?

In this thesis, we have addressed these two questions:

1. In Part 1, we have used a novel approach to try to constrain and understand the star formation law and the importance of feedback on galactic scales. Instead of focussing on how stars form and interact with the ISM at the present day (e.g. Kennicutt 1989; Ferguson et al. 1998; Kennicutt 1998; Martin 1999), we have tried to use the optical and near-infrared colours of spiral galaxies to constrain *how stars must have formed and interacted with the ISM in the past.* The two approaches are complementary and are yielding consistent results: the star formation law depends on gas density, and most likely the dynamical timescale, and the importance of metal-enriched mass loss increases towards lower galaxy masses. Note that our star formation law is in direct variance with those used in most semi-analytic models (e.g. Kauffmann & Charlot 1998a; Somerville & Primack 1998; Cole et al. 1999) which typically explicitly depend on halo circular velocity and total cold gas mass (although sometimes with a dynamical time dependence). Further study of both the star formation histories and present-day star formation

will further test our star formation law, and allow us to zero in on acceptable star formation and stellar feedback laws, for use in simulations of galaxy formation and evolution.

2. In Part 2, we discussed the constraints that we can place on the formation epoch of early-type galaxies using their colours at high redshifts. A picture is emerging where we find substantial populations of old early-type galaxies in both the field and cluster environments at redshifts up to $z \sim 1$. This contradicts many of the naïve expectations of nurture models (e.g. Baugh et al. 1998; Kauffmann & Charlot 1998a). However, morphological selection effects may cause this discrepancy: a more detailed understanding of the predictions of the models is required before these observations can be used to test nurture models.

Appendix A

Low surface brightness galaxies: photometry results

A.1 Photometry results

We present the tables of the bulge/disc decomposition results from Chapter 2 in Table A.1 and the surface brightness, ellipticity and position angle profiles for the galaxies described in Chapter 2 in Figure A.1. For further description of the data, see Chapter 2, section 2.3.

Table A.1. Bulge/disc decompositions

		Disc Parameters		Bulge Parameters				
Galaxy	Passband	μ_0	h	μ_e	r_e	B/D	Type	m_T
UGC 128	U	23.96± 0.15	32± 6	25.16± 0.03	8± 2	0.04± 0.01	e	15.0± 0.2[b]
	B	23.55± 0.05	24.30± 0.6	24.66± 0.01	6.3± 0.3	0.05± 0.02	e	15.16± 0.05
	V	22.94± 0.02	24.7± 0.5	23.80± 0.01	7.0± 0.1	0.07± 0.01	e	14.50± 0.05
	R	22.50± 0.01	22.2± 0.1	23.27± 0.01	6.7± 0.1	0.08± 0.01	e	14.35± 0.05
	I	22.09± 0.04	21.1± 0.3	22.74± 0.01	6.7± 0.2	0.11± 0.01	e	14.06± 0.05
	K'	20.3± 0.2	21± 4	20.80± 0.03	7.3± 0.6	0.14± 0.01	e	12.1± 0.2[b]
ESO-LV 280140	B	23.15± 0.02	20.8± 0.2	—	—	—	—	14.94± 0.10
	R	21.93± 0.01	17.6± 0.1	—	—	—	—	13.95± 0.07
	K	20.24± 0.03	16± 1	—	—	—	—	12.5± 0.4[b]
UGC 334[f]	B	23.5± 0.1	25± 10	25.1± 0.1	5.5± 1.5	0.02± 0.02	e	15.4± 0.3[b,h]
	V	22.6± 0.2	23± 11	24.08± 0.2	5± 1.5	0.03± 0.03	e	14.7± 0.3[b,h]
	R	22.3± 0.2	21± 7	23.63± 0.05	5± 1	0.03± 0.03	e	14.4± 0.3[b,h]
	I	21.9± 0.1	17± 3	23.1± 0.1	5± 1	0.06± 0.04	e	14.4± 0.2[a,h]
	K'	20.0± 0.1	16± 3	21.2± 0.1	4.5± 0.5	0.05± 0.03	e	12.7± 0.2[b,h]

Table A.1. Continued.

		Disc Parameters		Bulge Parameters				
Galaxy	Passband	μ_0	h	μ_e	r_e	B/D	Type	m_T
0052-0119[e]	B	24.75± 0.02	36± 4	24.06±0.01	12.5± 0.1	0.8±0.2	r	14.7± 0.1[b]
	V	23.89± 0.05	30± 8	22.86± 0.01	11.4± 0.1	1.3± 0.7	r	13.9± 0.1[b]
	R	23.14± 0.03	24± 4	22.09± 0.01	9.9± 0.1	1.7± 0.7	r	13.5± 0.1[b]
	K'	21.53± 0.05	20.0[c]	19.6± 0.1	13.5± 1.5	10± 3	r	10.8± 0.5[b]
UGC 628	U	23.0± 0.1	17± 1	25.18± 0.05	5.8± 0.8	0.03± 0.02	e	15.5± 0.1
	B	23.1± 0.1	17± 2	24.66± 0.05	7± 1	0.07± 0.04	e	15.6± 0.1
	V	22.55± 0.05	16.5± 0.7	23.74± 0.04	7.6± 0.4	0.13± 0.03	e	15.1± 0.1
	R	22.14± 0.05	16.0± 0.3	23.24± 0.02	7.5± 0.2	0.15± 0.01	e	14.7± 0.1
	I	21.65± 0.02	15.2± 0.3	22.62± 0.02	8.3± 0.1	0.23± 0.01	e	14.20± 0.05
	K'	20.3± 0.3	16.4± 0.6	20.76± 0.05	8.2± 0.8	0.32± 0.05	e	12.6± 0.2[a]
0221+0001[j]	B	23.6± 0.1	7.7[c]	23.9± 0.4	2.10[c]	0.21± 0.04	r	17.20± 0.09
	V	22.4± 0.1	7.4± 0.5	22.1± 0.2	1.8± 0.3	0.27± 0.03	r	16.12± 0.09
	R	21.92± 0.05	7.0± 0.3	21.98± 0.04	2.5± 0.1	0.45± 0.03	r	15.63± 0.10
	K'	19.5± 0.1	6.2± 0.7	18.76± 0.05	2.7± 0.1	1.3± 0.4	r	12.82± 0.08
0237-0159[f]	B	23.89± 0.08	19± 3	22.33± 0.01	3.56± 0.05	0.29± 0.06	e	15.36± 0.10[a]
	V	23.10± 0.06	17.3± 1.4	21.25± 0.01	3.29± 0.03	0.38± 0.04	e	14.68± 0.10
	R	22.45± 0.15	13± 2	20.65± 0.01	3.13± 0.05	0.61± 0.07	e	14.52± 0.08
	K'	19.67± 0.05	14.60[c]	17.48± 0.01	2.45[c]	0.4± 0.2	e	11.6± 0.4[b]

Table A.1. Continued.

		Disc Parameters		Bulge Parameters				
Galaxy	Passband	μ_0	h	μ_e	r_e	B/D	Type	m_T
ESO-LV 2490360	B	24.0± 0.2	37± 8	—	—	—	—	15.0± 0.1
	R	22.9± 0.1	28± 3	—	—	—	—	14.3± 0.1
	K	20.96± 0.07	24± 3	—	—	—	—	12.45± 0.15[b]
F561-1[d,f]	U	23.2± 0.2	12.50[c]	—	—	—	—	16.0± 0.2 [b]
	B	23.14± 0.1	11± 1	—	—	—	—	16.18± 0.09
	V	22.51± 0.03	10.0± 0.6	—	—	—	—	15.66± 0.09
	R	22.15± 0.02	9.7± 0.1	—	—	—	—	15.43± 0.09
	I	21.63± 0.04	9± 1	—	—	—	—	15.0± 0.15 [a]
	K'	20.23± 0.04	9± 1	—	—	—	—	13.5± 0.1 [a]
C1-4	B	22.08± 0.02	8.1± 0.15	22.40± 0.01	2.17± 0.04	0.10± 0.01	e	16.16± 0.08
	V	21.1± 0.1	7.3± 0.5	21.7± 0.15	1.9± 0.4	0.07± 0.01	e	15.5± 0.1
	R	20.67± 0.01	8.03± 0.02	20.83± 0.01	2.04± 0.01	0.11± 0.01	e	14.75± 0.09
	I	20.10± 0.06	7.6± 0.3	20.99± 0.02	2.65± 0.15	0.10± 0.01	e	14.50± 0.09
	K'	18.20± 0.02	7.6± 0.1	17.76± 0.01	1.65± 0.01	0.13± 0.01	e	12.46± 0.08

Table A.1. Continued.

		Disc Parameters		Bulge Parameters				
Galaxy	Passband	μ_0	h	μ_e	r_e	B/D	Type	m_T
C3-2	U	21.90± 0.01	5.57± 0.06	—	—	—	—	16.80± 0.07
	B	21.74± 0.01	5.72± 0.04	—	—	—	—	16.52± 0.04
	R	20.08± 0.01	5.25± 0.03	—	—	—	—	15.06± 0.04
	I	19.43± 0.01	5.39± 0.08	—	—	—	—	14.35± 0.08
	K'	17.50± 0.01	4.72± 0.03	—	—	—	—	12.65± 0.05
F563-V2	B	22.16± 0.01	7.80[c]	—	—	—	—	16.25± 0.09
	V	21.64± 0.01	7.15± 0.05	—	—	—	—	15.81± 0.08
	R	21.24± 0.01	7.03± 0.02	—	—	—	—	15.45± 0.07
	K'	19.29± 0.04	6.4± 0.5	—	—	—	—	13.8± 0.1[a]
F568-3	U	22.5± 0.1	10± 1	—	—	—	—	16.0± 0.1
	B	22.33± 0.03	8.9± 0.2	—	—	—	—	16.12± 0.07
	V	21.64± 0.01	8.3± 0.1	—	—	—	—	15.55± 0.08
	R	21.22± 0.01	8.0± 0.1	—	—	—	—	15.22± 0.08
	I	20.71± 0.01	7.8± 0.1	—	—	—	—	14.83± 0.10
	K'	19.16± 0.02	8.0± 0.3	—	—	—	—	13.11± 0.08

Table A.1. Continued.

		Disc Parameters		Bulge Parameters				
Galaxy	Passband	μ_0	h	μ_e	r_e	B/D	Type	m_T
1034+0220	B	23.34± 0.08	10.1± 0.4	25.0± 0.1	8.8± 0.7	0.62± 0.08	r	16.11± 0.05
	V	22.42± 0.08	9.5± 0.4	23.08± 0.08	5.0± 0.3	0.55± 0.03	r	15.35± 0.05
	R	21.84± 0.05	7.6± 0.5	22.48± 0.05	5.2± 0.1	0.92± 0.02	r	15.16± 0.06
	K'	20.2± 1	8± 2	19.9± 0.2	8± 2	4.6± 1	r	12.20± 0.2[a]
N10-2[d]	U	22.8± 0.1	8± 1	—	—	—	—	17.0± 0.2[b]
	B	22.20± 0.02	6.9± 0.2	—	—	—	—	16.61± 0.08
	V	21.16± 0.02	6.0± 0.1	—	—	—	—	15.85± 0.09
	R	20.62± 0.01	5.50± 0.03	—	—	—	—	15.50± 0.08
	I	20.12± 0.02	5.5± 0.2	—	—	—	—	15.15± 0.1
	K'	17.84± 0.01	4.95± 0.05	—	—	—	—	13.00± 0.1
1226+0105	B	23.7± 0.3	10.5[c]	23.8± 0.7	4.6± 2	0.6± 0.3	r	16.30± 0.06
	V	22.60± 0.06	9.8± 0.1	22.16± 0.07	2.9± 0.1	0.48± 0.02	r	15.50± 0.09
	R	22.4± 0.2	9.8± 0.3	21.9± 0.1	3.8± 0.2	0.9± 0.2	r	15.02± 0.08
	K'	19.9± 0.5	11± 5	18.8± 0.3	3.5± 0.8	0.9± 0.2	r	12.13± 0.10

Table A.1. Continued.

		Disc Parameters		Bulge Parameters				
Galaxy	Passband	μ_0	h	μ_e	r_e	B/D	Type	m_T
F574-1	B	23.00± 0.04	11.5± 0.3	23.27± 0.06	2.0± 0.2	0.04± 0.01	e	16.67± 0.09
	V	22.40± 0.03	10.9± 0.15	22.64± 0.02	2.45± 0.05	0.08± 0.01	e	16.18± 0.09
	R	21.95± 0.06	10.3± 0.4	22.56± 0.03	2.7± 0.2	0.07± 0.01	e	15.9± 0.1
	K'	19.66± 0.03	8.3± 0.5	19.32± 0.01	2.19± 0.03	0.18± 0.01	e	13.8± 0.15 [a]
F579-V1	B	23.1± 0.1	10.3± 0.4	24.2± 0.1	1.5± 0.1	0.01± 0.01	e	16.29± 0.10
	V	22.4± 0.1	10.2± 0.4	23.5± 0.4	1.8± 0.4	0.02± 0.01	e	15.59± 0.09
	R	21.9± 0.1	9.8± 0.4	23.1± 0.4	1.6± 0.4	0.02± 0.01	e	15.16± 0.08
	K'	19.51± 0.06	9.5± 0.6	20.75± 0.06	2.3± 0.3	0.03± 0.01	e	12.68± 0.09
I1-2	B	22.9± 0.15	9.3± 0.8	24.09[c]	1.51[c]	0.02[c]	e	16.5± 0.1
	V	21.93± 0.01	7.36± 0.02	23.06± 0.01	1.09[c]	0.01± 0.01	e	15.75± 0.1
	R	21.48± 0.07	7.7± 0.4	22.1± 0.1	1.2± 0.2	0.02± 0.01	e	15.45± 0.08
	I	20.78± 0.07	7.3± 0.6	21.6± 0.1	1.09[c]	0.02± 0.01	e	14.7± 0.1
	K'	18.76± 0.03	6.1± 0.2	19.50± 0.07	1.09[c]	0.03± 0.01	e	13.1± 0.1

Table A.1. Continued.

		Disc Parameters		Bulge Parameters				
Galaxy	Passband	μ_0	h	μ_e	r_e	B/D	Type	m_T
F583-1	B	23.05± 0.04	12.40[c]	—	—	—	—	16.40± 0.08
	V	22.49± 0.09	11.4± 0.8	—	—	—	—	16.07± 0.08
	R	22.23± 0.03	11.40[c]	—	—	—	—	15.68± 0.07
	I	21.90± 0.08	11.00[c]	—	—	—	—	15.40± 0.09
	K'	19.8± 0.2	8± 2	—	—	—	—	13.5± 0.2[b]
ESO-LV 1040220	B	23.84± 0.05	40± 4	—	—	—	—	14.4± 0.1[a]
	R	22.9± 0.1	37± 5	—	—	—	—	13.6± 0.1[a]
	K	21.35± 0.01	39± 4	—	—	—	—	11.7± 0.15[a]
ESO-LV 1040440	B	23.4± 0.1	26± 2	—	—	—	—	14.72± 0.07
	R	22.47± 0.02	25.5± 0.7	—	—	—	—	13.64± 0.08
	K	20.9± 0.15	23± 4	—	—	—	—	12.0± 0.2[b]
ESO-LV 1870510	B	23.09± 0.05	26± 2	—	—	—	—	14.87± 0.07
	R	22.12± 0.08	26± 2	—	—	—	—	13.99± 0.09
	K	20.55± 0.05	23± 2	—	—	—	—	12.6± 0.2[b]
ESO-LV 1450250	B	23.08± 0.03	32± 1	—	—	—	—	14.11± 0.05
	R	22.05± 0.03	30± 1	—	—	—	—	13.31± 0.05
	K	20.42± 0.03	25± 1	—	—	—	—	11.95± 0.1[a]

Table A.1. Continued.

		Disc Parameters		Bulge Parameters				
Galaxy	Passband	μ_0	h	μ_e	r_e	B/D	Type	m_T
P1-7[g]	B	23.15± 0.01	15.9± 0.1	24.98± 0.03	3.2± 0.1	0.01± 0.01	e	15.36± 0.05
	V	22.35± 0.02	14.9± 0.4	23.86± 0.05	3.7± 0.3	0.03± 0.01	e	14.68± 0.09
	I	21.22± 0.02	13.9± 0.2	22.68± 0.02	4.0± 0.2	0.04± 0.01	e	13.70± 0.05
	K	19.4± 0.2	12± 2	20.7± 0.1	4± 2	0.07± 0.03	e	12.15± 0.1[a]
2327-0244	B	22.44± 0.03	18.0[c]	21.08± 0.01	3.17± 0.02	0.21± 0.01	e	14.50± 0.10
	V	21.29± 0.02	16.5± 0.4	20.29± 0.01	3.12± 0.01	0.17± 0.01	e	13.62± 0.10
	R	20.58± 0.01	16.5[c]	19.62± 0.01	2.90± 0.01	0.14± 0.01	e	13.00± 0.06
	K'	17.45± 0.03	12.6± 0.4	16.08± 0.01	2.23± 0.02	0.21± 0.01	e	10.32± 0.07

μ_0 is the bulge/disc decomposition extrapolated central surface brightness in mag arcsec^{-2}, and h is the disc scale length in arcsec. μ_e is the surface brightness at the half-light radius of the exponential (Type $= e$) or r$^{1/4}$ law (Type $= r$) bulge profile in mag arcsec^{-2}, and r_e is the half-light radius in arcsec. B/D is the ratio of bulge to disc luminosities, obtained by dividing the total luminosities of the fitted bulge by the fitted disc.

[a] Extrapolation > 0.15 mag [b] Extrapolation > 0.3 mag [c] Held constant [d] Disc only fit is chosen for simplicity

[e] Disc is a very weak component [f] The ellipticity and position angle have been constrained

[g] Fit is carried out using I band images

[h] The galaxy most likely continues out beyond $\sim 50''$. We state the extrapolated magnitude at $50''$, along with its uncertainty.

[j] The choice of bulge profile was essentially arbitrary.

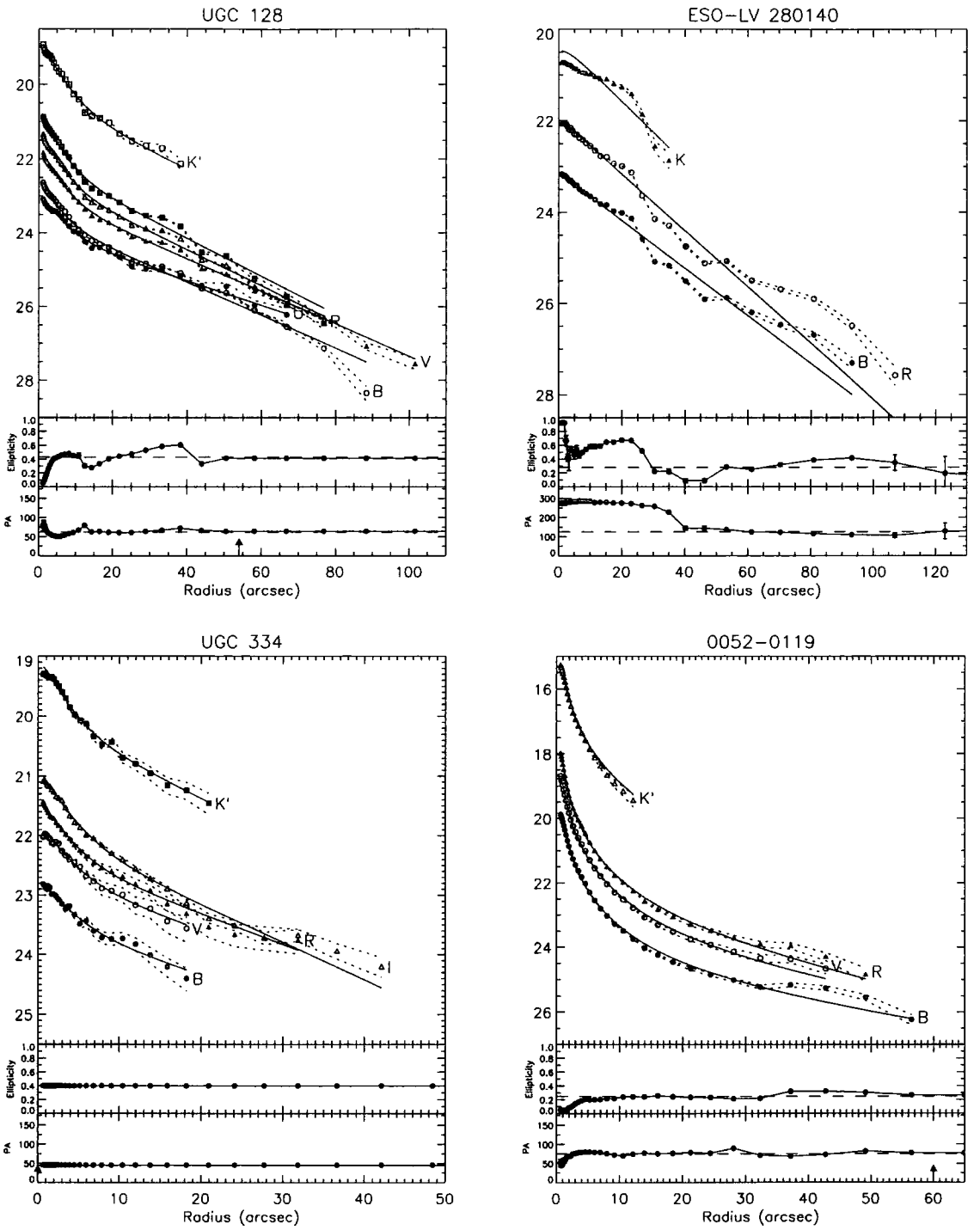

Figure A.1: Surface photometry in all available passbands, using the ellipse parameters determined from the R band image. The surface photometry (symbols) is plotted out to the radius where the sky subtraction error amounts to ± 0.2 mag or more. Also plotted are the bulge-disc fits to the surface photometry (solid lines) and the effects of the $\pm 1\sigma$ estimated error in the sky level (dotted lines). The fitted R band ellipticities and position angles are also plotted (with errors, which are sometimes smaller than the symbol size) as a function of radius for each galaxy (out to the maximum radius for which they were fit; arrow), along with the estimate for the global ellipticity and position angle (dashed lines). The position angle and ellipticity for UGC 334 have been fixed.

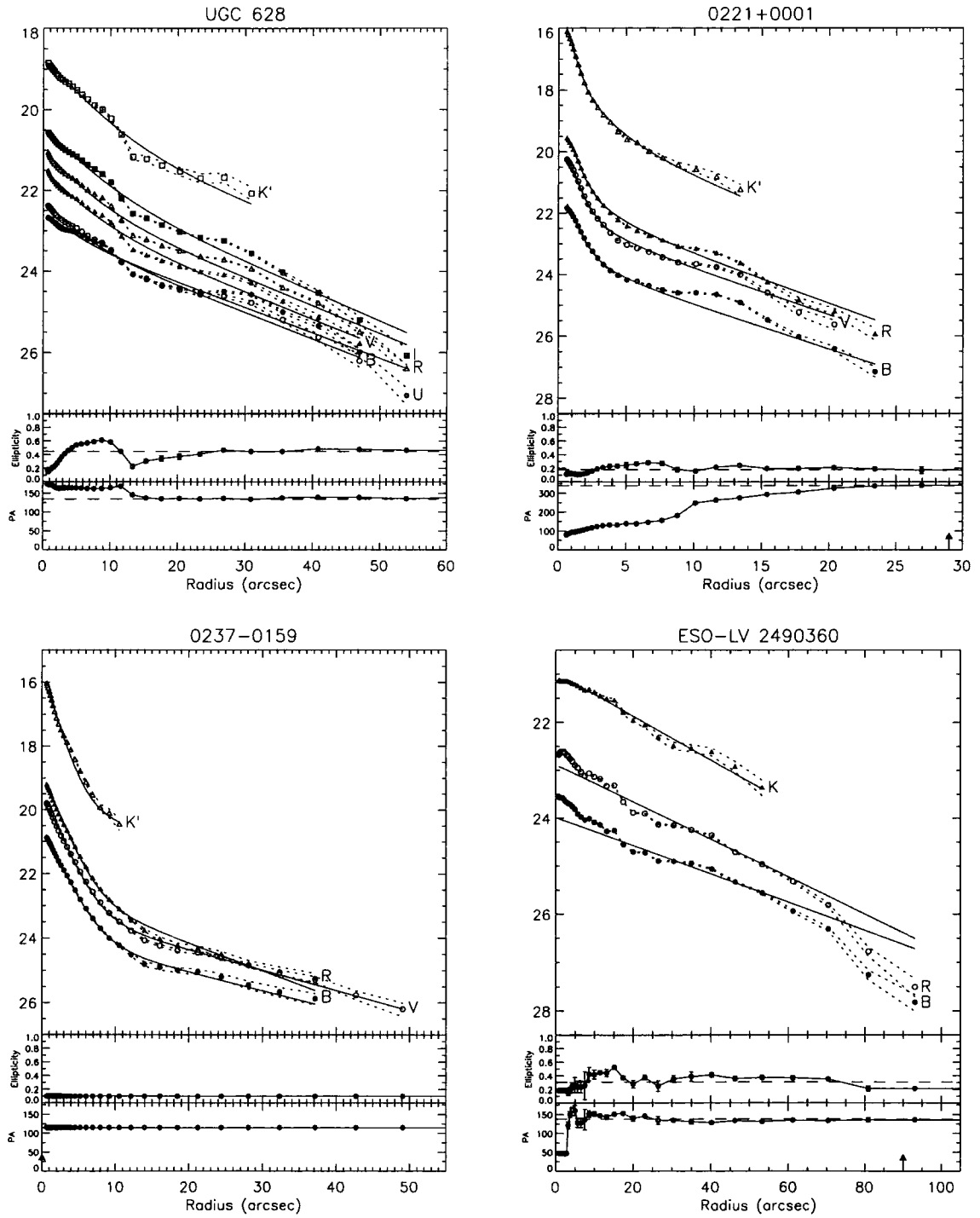

Figure A.1: Continued. The position angle and ellipticity of 0237-0159 has been fixed.

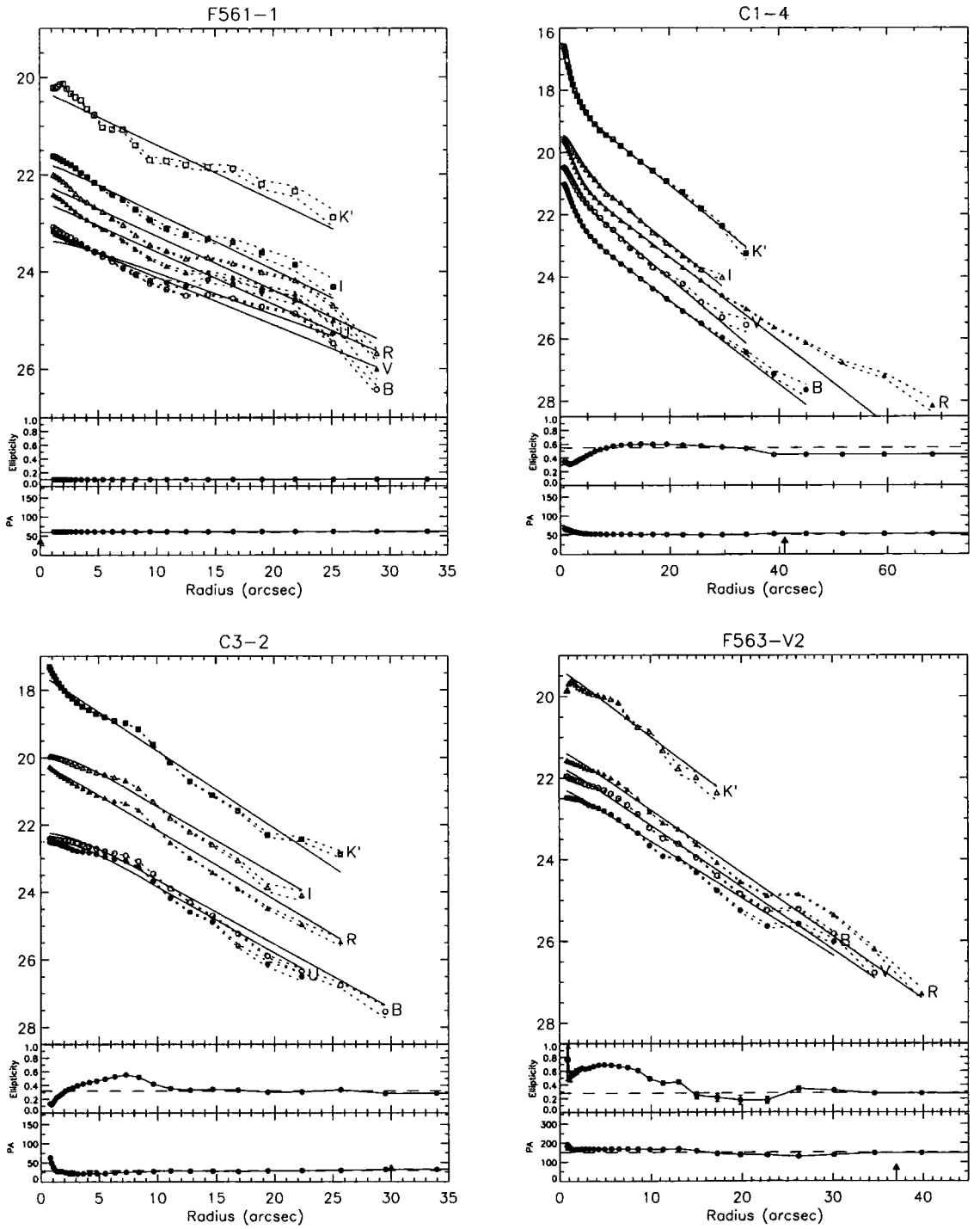

Figure A.1: Continued. The position angle and ellipticity of F561-1 have been fixed.

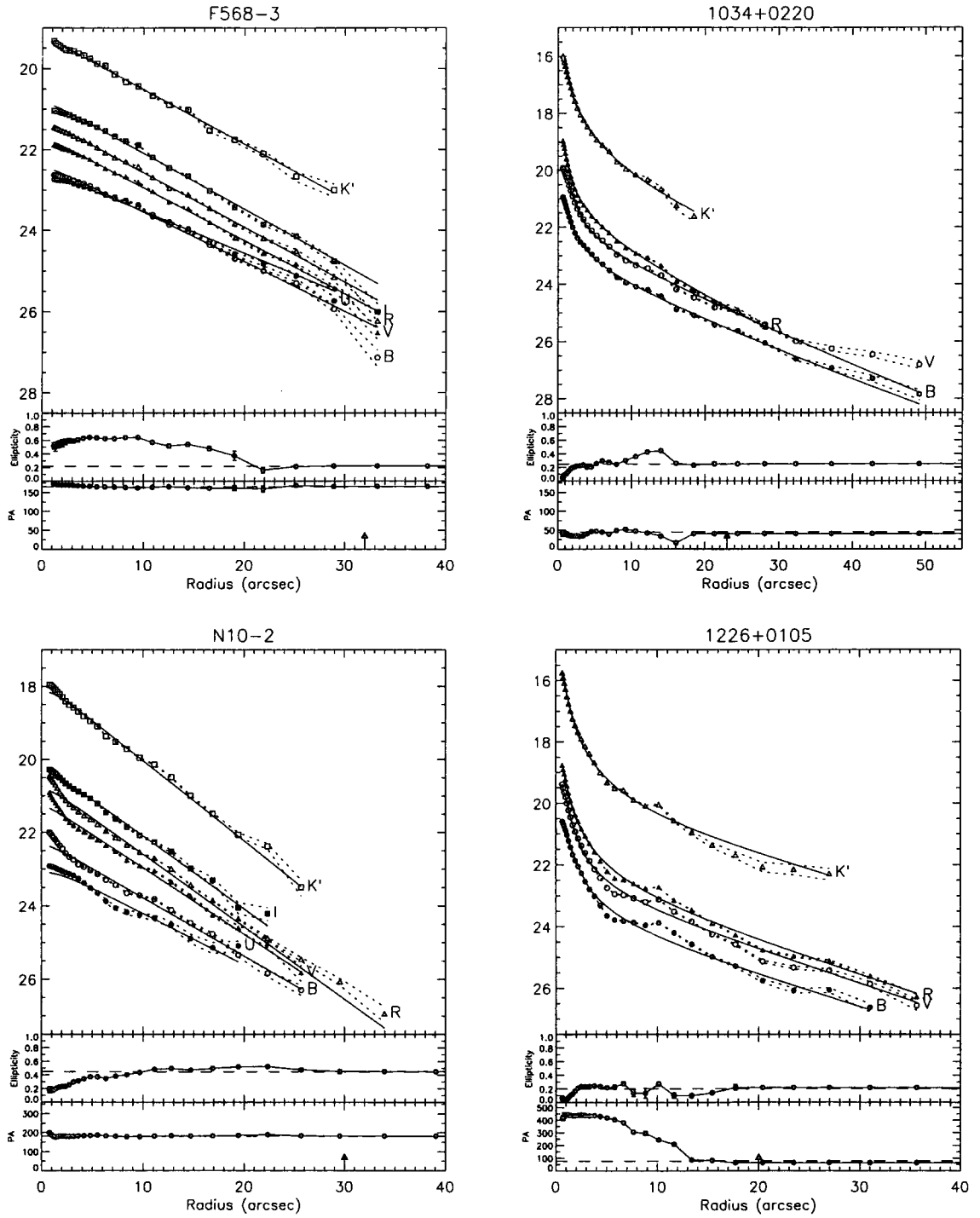

Figure A.1: Continued.

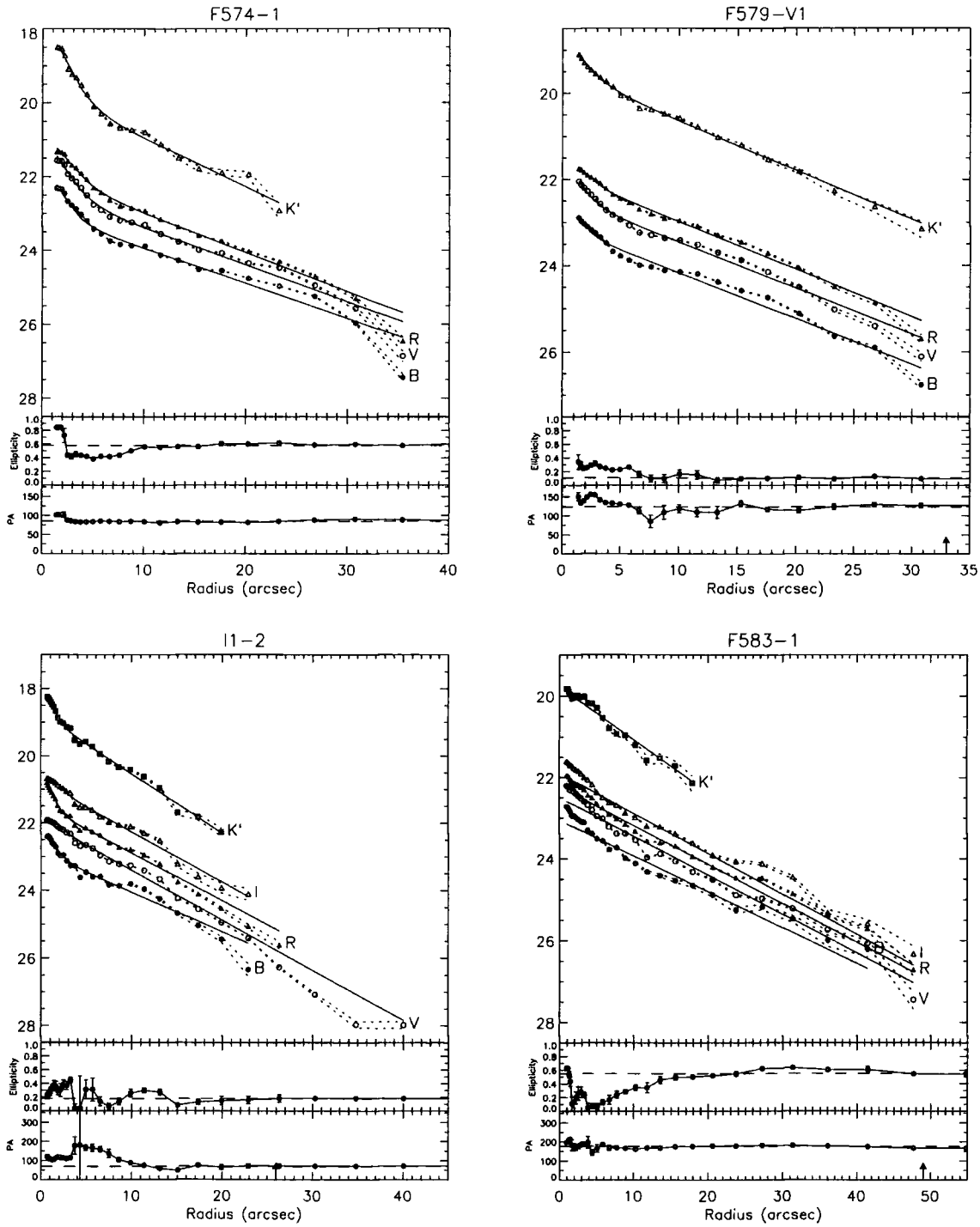

Figure A.1: Continued.

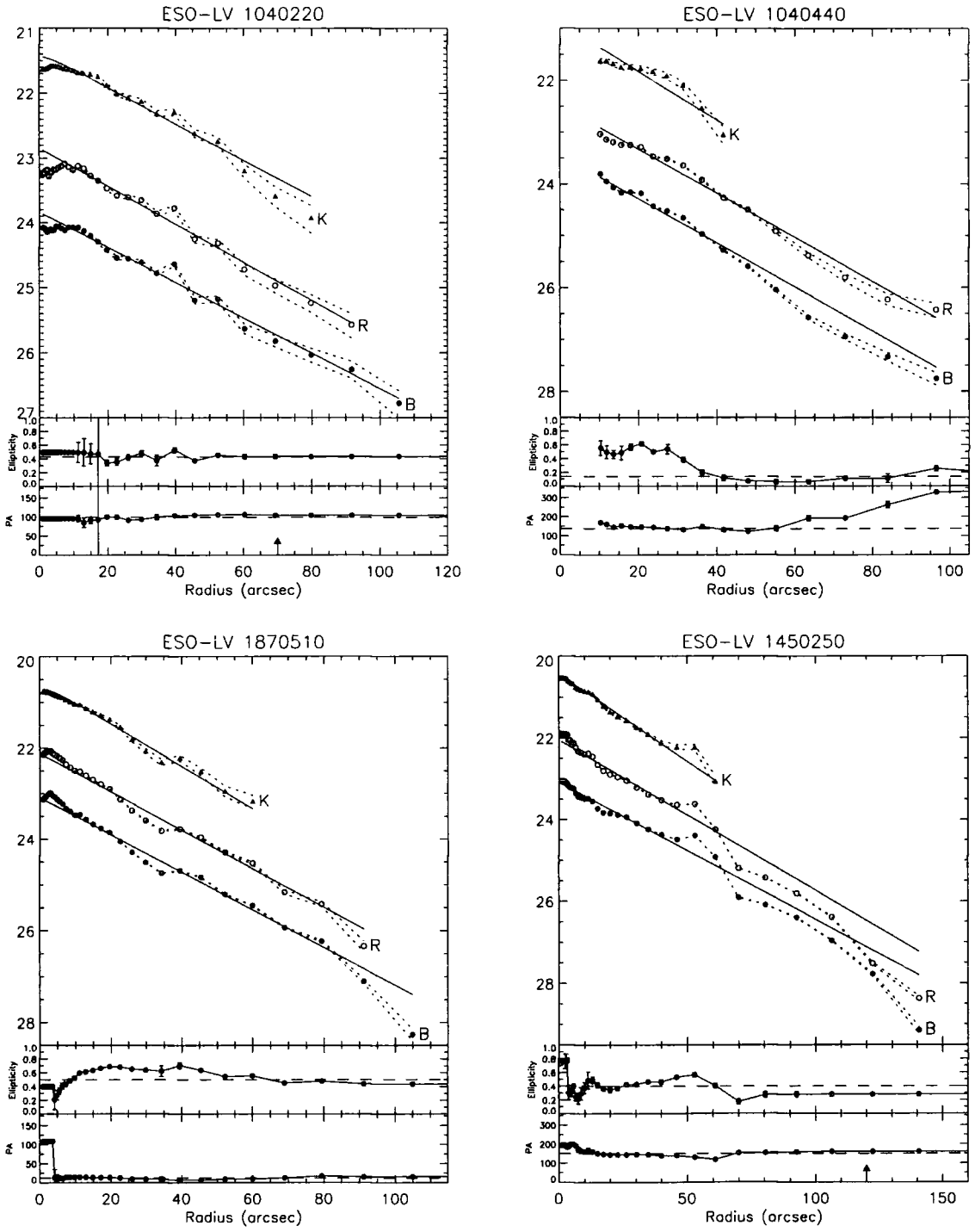

Figure A.1: Continued. All of the above galaxies have relatively low surface brightnesses and fairly irregular structures and therefore have relatively noisy position angles and/or ellipticities at both small and large radii.

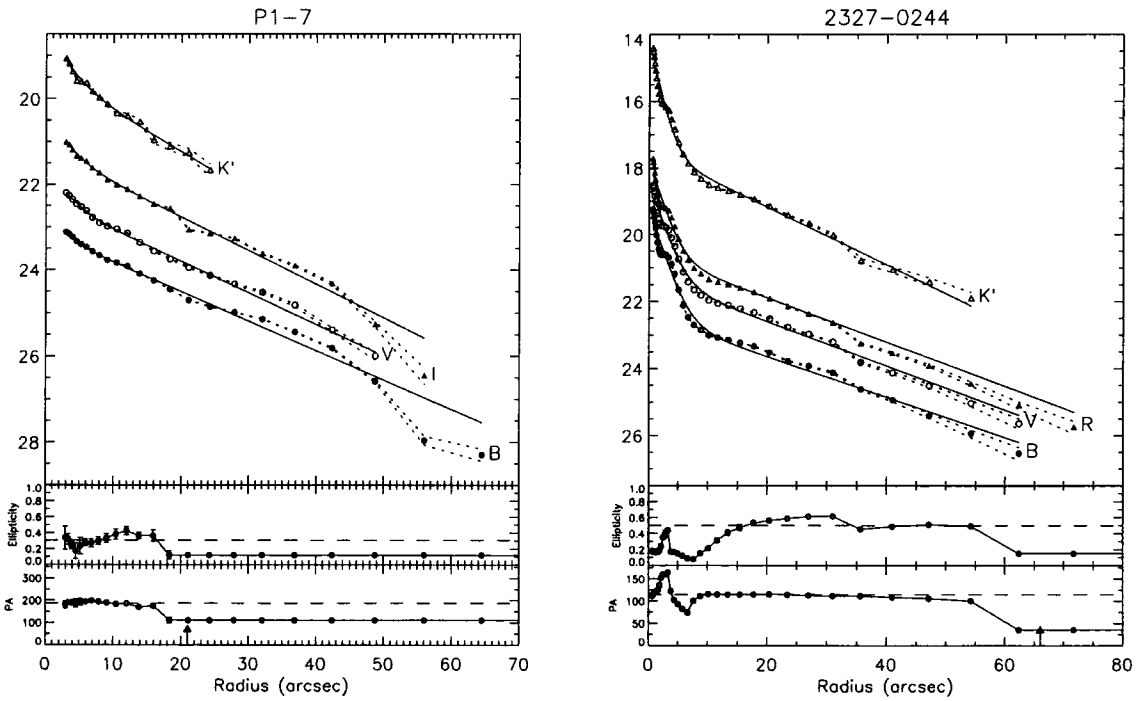

Figure A.1: Continued. Note that P1-7 has no R band data, so I band is used to determine the ellipse parameters.

Bibliography

References

Abadi M. G., Moore B., Bower R. G., 1999, MNRAS in press, astro-ph/9903436

Abraham R. G., Ellis R. S., Fabian A. C., Tanvir N. R., Glazebrook K., 1999, MNRAS, 303, 641

Allen C. W., 1973, "Astrophysical Quantities", University of London, The Athlone Press

Allington-Smith J., et al., 1994, PASP, 106, 983

Arimoto N., Yoshii Y., 1987, A&A, 173, 23

Balcells M., González A. C., 1998, ApJ, 505, 109L

Barger A. J., Aragón-Salamanca A., Smail I., Ellis R. S., Couch W. J., Dressler A., Oemler A., Poggianti B. M., Sharples R. M., 1998, ApJ, 501, 522

Barger A. J., Cowie L. L., Trentham N., Fulton E., Hu E. M., Songaila A., Hall D., 1999, AJ, 117, 102

Barnaby D. A., et al. 1999, in preparation

Barnes J. E., 1999, astro-ph/9903234

Barnes J. E., Hernquist L., 1992, ARA&A, 30, 705

Barnes J. E., Hernquist L., 1996, ApJ, 471, 115

Baugh C. M., Cole S., Frenk C. S., Lacey C. G, 1998, ApJ, 498, 504

Beers T. C., Flynn K., Gebhardt K., 1990, AJ, 100, 32

Bell E. F., Bower R. G., de Jong R. S., Hereld M., Rauscher B. J., 1999, MNRAS, 302, 55L

Bergvall N., Rönnback J., Masegosa J., Östlin G., 1999, A&A, 341, 697

Berlind A. A., Quillen A. C., Pogge R. W., Sellgren K., 1997, AJ, 114, 107

Bernardi M., Renzini A., da Costa L. N., Wegner G., Alonso M. V., Pellegrini P. S., Rité C., Willmer C. N. A., 1998, ApJ, 508, 143L

Bertelli G., Bressan A., Chiosi C., Fagatto F., Nasi E., 1994, A&AS, 106, 275

Bica E., 1988, A&A, 195, 76

Bingelli B., Sandage A., Tammann G. A., 1988, ARA&A, 26, 509

Block D. L., Ivânio P., 1999, A&A, 342, 627

Block D. L., Bertin G., Stockton A., Grosbøl P., Moorwood A. F. M., Peletier R. F., 1994, A&A, 288, 365

Bosma A., 1998, astro-ph/9812013

Bower R. G., Lucey J. R., Ellis R. S., 1992a, MNRAS, 254, 589

Bower R. G., Lucey J. R., Ellis R. S., 1992b, MNRAS, 254, 601 (BLE)

Bower R. G., Kodama T., Terlevich A., 1998, MNRAS, 299, 1193 (BKT)

Brainerd T. G., Blandford R. D., Smail I., 1996, ApJ, 466, 623

Branchini E. F., Teodoro L., Frenk C. S., Schmoldt I., Efstathiou G., White S. D. M., Saunders W., Rowan-Robinson M., Keeble O., Tadros H., Maddox S., Oliver S., Sutherland W., 1999, MNRAS, in press

Bromley B. C. , Press W. H., Lin H., Kirschner R. P., 1998, ApJ, 505, 25

Bruzual A. G., Charlot S., 1993, ApJ, 405, 538

Bruzual A. G., Charlot S., 1999, in preparation

Bruzual A. G., Magris G., Calvet N., 1988, ApJ, 333, 673

Burstein D., Bertola F., Buson L. M., Faber S. M., & Laner T., 1988, ApJ, 328, 440

Buta R., Mitra S., de Vaucouleurs G., Corwin, Jr. H. G., 1994, AJ, 107, 118

Buta R., Williams K. L., 1995, AJ, 109, 543

Butcher H. Oemler A., 1984, ApJ, 285, 426

Calzetti D., Kinney A. L., Storchi-Bergmann T., 1994, ApJ, 429, 582

Carignan C., Freeman K. C., 1988, ApJ, 332, 33L

Carlberg R. G., Yee H. K. C., Ellingson E., Abraham R., Gravel P., Morris S., Pritchet C. J., 1996, ApJ, 462, 32

Carroll S. M., Press W. H., Turner E. L., 1992, ARA&A, 30, 499

Casali M. M., Hawarden T. G., 1992, JCMT-UKIRT Newsletter, 3, 33

Cash W. C., 1979, ApJ, 228, 939

Charlot S., Worthey G., Bressan A., 1996, ApJ, 457, 625

Chiosi C., Bressan A., Portinari L., Tantalo R., 1998, A&A, 339, 355

Cohen J. G., Cowie L. L., Hogg D. W., Songaila A., Blandford R., Hu E. M., Shopbell P., 1996, ApJ, 471, 5

Cole S., Lacey C. G., Baugh C. M., Frenk C. S., 1999, in preparation

Coles P., Lucchin F., 1995, "Cosmology: The Origin and Evolution of Cosmic Structure" (Wiley, Chichester)

Colless M., Burstein D., Davies R. L., McMahan R. K., Saglia R. P., Wegner G., 1999, MNRAS, 303, 813

Connolly A. J., Csabai I., Szalay A. S., Koo D. C., Kron R. G., Munn J. A., 1995, AJ, 110, 2655

Courteau S., 1997, AJ, 114, 2402

Cowie L. L., 1998, unpublished catalogue of Hubble Deep Field redshifts, http://www.ifa.hawaii.edu/~cowie/tts/tts.html

Cowie L. L., Songaila A., Hu E. M., Cohen J. G., 1996, AJ, 112, 839

Dalcanton J. J., 1998, ApJ, 495, 251

Dalcanton J. J., Spergel D. N., Summers F. J., 1997, ApJ, 482, 659

Davies R. L., Efstathiou G., Fall S. M., Illingworth G., Schecter P. L., 1983, ApJ, 226, 41

de Blok W. J. G., van der Hulst J. M., 1998a, A&A, 335, 421

de Blok W. J. G., van der Hulst J. M., 1998b, A&A, 336, 49

de Blok W. J. G., van der Hulst J. M., Bothun G. D., 1995, MNRAS, 274, 235

de Blok W. J. G., McGaugh S. S., van der Hulst J. M., 1996, MNRAS, 283, 18

de Jong R. S., 1996a, A&AS, 118, 557 (dJII)

de Jong R. S., 1996b, A&A, 313, 45 (dJIII)

de Jong R. S., 1996c, A&A, 313, 377 (dJIV)

de Jong R. S., Davies R. L., 1997, MNRAS, 285, 1L

de Jong R. S, Lacey, C., 1998, in Proceedings of IAU 171: "The Low Surface Brightness Universe", eds. Davies J. I., Impey C. & Phillipps S. (astro-ph/9810511)

de Jong R. S., van der Kruit P. C., 1994, A&AS, 106, 451 (dJI)

de Jong R. S., Davies R. L., Minchin R. F., Lucey J. R., Steel J., 1998, in proceedings of IAU Symp. 184, ' 'The Central Regions of the Galaxy and Galaxies", ed: Y. Sofue, (Kluwer, Dordrecht), p.385

Dekel A., Silk J., 1986, ApJ, 303, 39

de Vaucouleurs G., de Vaucouleurs A., Corwin H. G., Buta R. J., Paturel G., Fouqué P., 1991, "Third Reference Catalog of Bright Galaxies" (Springer, Berlin) (RC3)

Dickinson M., et al., 1997, in preparation

Disney M. J., Davies J. I., Phillipps S., 1989, MNRAS, 239, 939 (DDP)

Dopita M. A., 1985, ApJ, 295, 5L

Dopita M. A., Ryder S. D., 1994, ApJ, 430, 163

Edmunds M. G., 1990, MNRAS, 246, 678

Edmunds M. G., Greenhow R. M., 1995, MNRAS, 272, 241

Edmunds M. G., Pagel B. E. J., 1984, MNRAS, 211, 507

Eggen O. J., Lynden-Bell D., Sandage A. R., 1962, ApJ, 136, 748

Elias J. H., Frogel J. A., Matthews K., Neugebauer G., 1982, AJ, 87, 1029

Ellis R. S., Smail I., Dressler A., Couch W. C., Oemler Jr., A. O., Butcher H., Sharples R. M., 1997, ApJ, 483, 582

Elmegreen B. G., 1999, in "The Evolution of Galaxies on Cosmological Timescales", eds. Beckman J. E. & Mahoney T. J., ASP Conference Series

Elmegreen B. G., Parravano A., 1994, ApJ, 435, 121L

Evans R., 1994, PhD Thesis, University of Cardiff

Fasano G., Christiani S., Arnouts S., Filippi M., 1998, AJ, 115, 1400

Ferguson A. M. N., Wyse R. F. G., Gallagher, III J. S., Hunter D. A., 1996, AJ, 111, 2265

Ferguson A. M. N., Wyse R. F. G., Gallagher, III J. S., Hunter D. A., 1998, ApJ, 506, 19L

Fort B., Mellier Y., 1994, Astron. Astrophys. Rev., 5, 239

Franceschini A., Silva L., Fasano G., Granato G. L., Bressan A., Arnouts S., Danese L., 1998, ApJ, 506, 600 (F98)

Freeman K. C., 1970, ApJ, 160, 811

Gallart C., Freedman W. L., Aparicio A., Bertelli G., Chiosi C., 1999, astro-ph/9906121

Garnett D. R., Shields G. A., Skillman E. D., Sagan S. P., Dufour R. J., 1997, ApJ, 489, 63

Gerritsen J. P. E., de Blok W. J. G., 1999, A&A, 342, 655

Glazebrook K., Ellis R. S., Colless M., Broadhurst T., Allington-Smith J. J., Tanvir N., 1995, MNRAS, 273, 157

González J. J., 1993, PhD Thesis, University of California, Santa Cruz

Gordon K. D., Calzetti D., Witt A. N., 1997, ApJ, 487, 625

Goudfrooij P., de Jong T., 1995, A&A, 298, 784

Goudfrooij P., Hansen L., Jorgensen H. E., Norgaard-Neilsen H. U., 1994, A&AS, 105, 341

Governato F., Gardner J. P., Stadel J., Quinn T., Lake G., 1999, submitted to AJ, astro-ph/9710140

Grebel E. K., 1998, astro-ph/9812443

Guzman R., Lucey J. R., Carter D., Terlevich R. J., 1992, MNRAS, 257, 187

Gwyn S. D. J., 1999, astro-ph/9907336

Gwyn S. D. J., Hartwick F. D. A., 1996, ApJ, 468, 77L

Halliday C., 1998, PhD Thesis, University of Durham

Hammer F., Flores H., Lilly S. J., Crampton D., Le Fèvre O., Rola C., Mallen-Ornelas G., Schade D., Tresse L., 1997, ApJ, 481, 49

Hau G. K. T., Thomson R. C., 1994, MNRAS, 270, 23L

Hau G. K. T., Carter D., Balcells M., 1999, MNRAS, 306, 437

Henry R. B. C., Worthey G., 1999, astro-ph/9904107

Hernandez X., Gilmore G., 1998, MNRAS, 294, 595

Holmberg E., 1958, Medd. Lunds Astron. Obs. Ser., 2, No. 136

Holtzman J. A., Gallagher, III J. S., Cole A. A., Mould J. R., Grillmair C. J., et al., 1999, astro-ph/9907259

Hubble E. P., 1936, "The Realm of the Nebulae", Yale University Press, New Haven

Huchtmeier W. K., Richter O.-G., 1989, "A General Catalog of HI Observations of Galaxies", New York, Springer-Verlag

Huizinga J. E., 1994, PhD Thesis, University of Groningen

Hunt L. K., Mannucci F., Testi L., Migliorini S., Stanga R. M., Baffa C., Lisi F., Vanzi L., 1998, AJ, 115, 2594

Hunter D. A., Thronson H. A., 1995, ApJ, 452, 238

Hurley-Keller D., Mateo M., Nemec J., 1998, AJ, 115, 1840

Isobe T., Feigelson E. D., Akritas M. G., Babu G. J., 1990, ApJ, 364, 104

Izotov Y. I., Lipovetsky V. A., Chaffee F. H., Foltz C. B., Guzeva N. G., Kniazev A. Y., 1997, ApJ, 476, 698

Jablonka P., Martin P., Arimoto N., 1996, AJ, 112, 1415

Jimenez R., Padoan P., Matteucci F., Heavens A. F., 1998, MNRAS, 299, 123

Jones H., Bland-Hawthorn J., 1997, PASA, 14, 8

Jørgensen I., 1999, MNRAS, 306, 607

Kauffmann G., 1996, MNRAS, 281, 487

Kauffmann G., Charlot S., 1998a, MNRAS, 294, 705

Kauffmann G., Charlot S., 1998b, MNRAS, 297, 23L

Kauffmann G., White S. D. M., Guiderdoni B., 1993, MNRAS, 264, 201

Kennicutt Jr., R. C., 1983, ApJ, 272, 54

Kennicutt Jr., R. C., 1989, ApJ, 344, 685

Kennicutt Jr., R. C., 1992, ApJS, 79, 255

Kennicutt Jr., R. C., 1998, ApJ, 498, 181 (Ke98)

King C. R., Ellis R. S., 1985, ApJ, 288, 456

Kobayashi C., Arimoto N., 1999, ApJ in press, astro-ph/9907091

Kodama T., 1997, PhD Thesis, University of Tokyo

Kodama T., Arimoto N., 1997, A&A, 320, 41 (KA97)

Kodama T., Arimoto N., Barger A. J., Aragón-Salamanca A., 1998, A&A, 334, 99

Köppen J., Arimoto N., 1990, A&AS, 240, 22

Kormendy J., Bender R., 1996, ApJ, 464, 119L

Kuchinski L. E., Terndrup D. M., Gordon K. D., Witt A. N., 1998, AJ, 115, 1438

Kuntschner H., 1998, PhD Thesis, University of Durham

Kuntschner H., Davies R. L., 1998, MNRAS, 295, 29L

Kurucz R. L., 1979, ApJS, 40, 1

Lacey C. G., Fall S. M., 1983, MNRAS, 204, 791

Lacey C. G., Fall S. M., 1985, ApJ, 290, 154

Landolt A. U., 1992, AJ, 104, 372

Lanzetta K. M., Yahil A., Fernández-Soto A., 1996, Nature, 381, 759

Larson R. B., 1972, Nature Phys. Sci., 236, 7

Larson R. B., 1975, MNRAS, 173, 671

Larson R. B., 1976, MNRAS, 176, 31

Larson R. B., Tinsley B. M., Caldwell C. N., 1980, ApJ, 237, 692

Lauberts A., Valentijn E. A., 1989, "The surface photometry catalogue of the ESO-Uppsula galaxies."

Lilly S. J., Tresse L., Hammer F., Grampton D., Le Fèvre O., 1995, ApJ, 455, 108

MacLow M.-M., Ferrera A., 1999, ApJ, 513, 142

Maraston C., 1998, MNRAS, 300, 872

Maraston C., Greggio L., Thomas D., 1999, astro-ph/9906088

Martin C. L., 1999, ApJ, 513, 156

Martin P., Roy J.-R., 1994, ApJ, 424, 599

Marzke R. O., Geller M. J., Huchra J. P., Corwin Jr., H. G., 1994, AJ, 108, 437

Marzke R. O., da Costa L. N., Pellegrini P. S., Willmer N. A., Geller M. J., 1998, ApJ, 503, 617

Mateo M., 1998, ARA&A, 36, 435

Mathis J. S., 1990, ARA&A, 28, 37

McCracken H. J., 1999, PhD Thesis, University of Durham

McGaugh S. S., 1994, ApJ, 426, 135

McGaugh S. S., 1996, MNRAS, 280, 337

McGaugh S. S., Bothun G. D., 1994, AJ, 107, 530

McGaugh S. S., de Blok W. J. G., 1997, ApJ, 481, 689

McGaugh S. S., Schombert J. M., Bothun G. D., 1995, AJ, 109, 2019

Menanteau F., Ellis R. S., Abraham R. G., Barger A. J., Cowie L. L., 1999, MNRAS, accepted (astro-ph/9811465)

Mihos J. C., Spaans M., McGaugh S. S., 1999, ApJ, 515, 89

Miller G. E., Scalo J. M., 1979, ApJS, 41, 513

Minniti D., Zijlstra A. A., Alonso M. V., 1999, AJ, 117, 881

Mo H. J., Mao S., White S. D. M., 1998, MNRAS, 295, 319

Mobasher B., Rowan-Robinson M., Georgakakis A., & Eaton N. 1996, MNRAS, 282, 7

Moshir M., Kopan G., Conrow T., McCallon H., Hacking P., Gregorich D., Rohrbach G., Melnyk M., Rice W., Fullmer L., et al., 1990, 'Infrared Astronomical Satellite Catalogs—The Faint Source Catalog', Version 2.0.

Navarro J. F., 1998, astro-ph/9807084

Nguyen H. T., Rauscher B. J., Severson S. A., Hereld M., et al. , 1996, PASP, 108, 718

Nilson P., 1973, Uppsula General Catalogue of Galaxies (Roy. Soc. Sci. Uppsula) (UGC)

Nomoto K., 1993, private communication

O'Neil K., Bothun G. D., Cornell M. E., 1997a, AJ, 113, 1212

O'Neil K., Bothun G. D., Schombert J. M., Cornell M. E., Impey C. D., 1997b, AJ, 114, 2448

O'Neil K., Bothun G. D., Schombert J. M., 1999, astro-ph/9909129

Origlia L., Goldader J. D., Leitherer C., Schaerer D., Oliva E., 1999, ApJ, 514, 96

Padoan P., Jimenez R., Antonuccio-Delogu V., 1997, ApJ, 481, 27L

Pagel B. E. J., 1998, "Nucleosynthesis and Chemical Evolution of Galaxies" (Cambridge University Press, Cambridge)

Pagel B. E. J., Patchett B. E., 1975, MNRAS, 172, 13

Peletier R. F., de Grijs R., 1998, MNRAS, 300, 3L

Peletier R. F., Willner S. P., 1992, AJ, 103, 1761

Peletier R. F., Valentijn E. A., Jameson R. F., 1990, A&A, 233, 62

Persic M., Salucci P., 1991, ApJ, 368, 60

Persson S. E., Murphy D. C., Krzeminski W., Roth M., Rieke M. J., 1998, AJ, 116, 2475

Phillipps S., Edmunds M. G., 1991, 251, 84

Phillipps S., Edmunds M. G., Davies J. I., 1990, 244, 168

Pickles A. J., van der Kruit P. C., 1991, A&AS, 91, 1

Poggianti B. M., Smail I., Dressler A., Couch W. J., Barger A. J., Butcher H., Ellis R. S., Oemler, Jr. A., 1999, ApJ, 518, 576

Prantzos N., Aubert O., 1995, A&A, 302, 69

Prantzos N., Silk J., 1998, ApJ, 507, 229

Press W. H., Flannery B. P., Teukolsky S. A., Vetterling W. T., 1986, Numerical Recipes—The Art of Scientific Computing (Cambridge University Press, Cambridge).

Quillen A. C., Pickering T. E., 1997, astro-ph/9705115

Rauscher B. J., Lloyd J. P., et al., 1998, ApJ, 506, 116

Rauscher B. J., Lloyd J. P., et al., 1999, Submitted to MNRAS

Richter O.-G., Tammann G. A., Huchtmeier W. K., 1987, A&A, 171, 33

Rönnback J., Bergvall N., 1995, A&A, 302, 353

Rubin V. C., Waterman A. H., Kenney J. D. P., 1999, astro-ph/9904050

Ryder S. D., Dopita M. A., 1994, ApJ, 430, 142

Salpeter E. E., 1955, ApJ, 121, 61

Sawicki M. J., Lin H., Yee H. K. C., 1997, AJ, 113, 1

Scalo J. M., 1986, Fundam. Cosmic Phys., 11, 1

Scalo J. M., 1998, in "The Stellar Initial Mass Function", eds. Gilmore G. & Howell D., ASP Conference Series, 142, 201

Schechter P. L., 1976, ApJ, 203, 297

Schlegel D. J., Finkbeiner D. P., Davis M., 1998, ApJ, 500, 525

Schmidt M., 1959, ApJ, 129, 243

Schneider S. E., Thuan T. X., Magnum J. G., Miller J., 1992, ApJS, 81, 5

Schombert J. M., Bothun G. D., Impey C. D., Mundy L. G., 1990, AJ, 100, 1523

Sekiguchi M., Fukugita M., 1999, astro-ph/9904299

Shimasaku K., Fukugita M., 1998, ApJ, 501, 578

Simard L., Koo D. C., Faber S. M., Sarajedini V. L., Vogt N. P., Phillips A. C., et al., 1999, ApJ, in press (astro-ph/9902147)

Simien F., de Vaucouleurs G., 1986, ApJ, 302, 564

Skillman E. D., Kennicutt Jr., R. C., Hodge P. W., 1989, ApJ, 347, 875

Somerville R. S., Primack J. R., 1998, astro-ph/9802268

Songaila A., Cowie L. L., Hu E. M., Gardiner J. P., 1994, ApJS, 94, 461

Sprayberry D., Impey C. D., Bothun G. D., Irwin M. J., 1995, AJ, 109, 558

Stanford S. A., Eisenhardt P. R. M., Dickinson M., 1995, ApJ, 450, 512

Stanford S. A., Eisenhardt P. R. M., Dickinson M., 1998, ApJ, 492, 461

Tamura K., Kobayashi C., Arimoto N., Ohta K., Kodama T., 1999, in preparation

Taylor K., 1995, A&AS, 186, 4406

Terlevich A. I., Kuntschner H., Bower R. G., Caldwell N., Sharples R. M., 1999, MNRAS in press, astro-ph/9907072

Terlevich R., Melnick J., Masegosa J., Moles M., Copetti M. V. F., 1991, A&AS, 91, 285

Theureau G., et al., 1998, A&AS, 130, 333

Thuan T. X., Izotov Y. I., Foltz C. B., 1999, astro-ph/9905345

Tinsley B. M., 1980, Fundamentals of Cosmic Physics, Vol.5, p.287

Tinsley B. M., Larson R. B., 1978, ApJ, 221, 554

Tolstoy E., 1999a, astro-ph/9901245

Tolstoy E., 1999b, astro-ph/9901252

Tolstoy E., Gallagher J. S., Cole A. A., Hoessel J. G., Saha A., Dohm-Palmer R. C., Skillman E. D., Mateo M., Hurley-Keller D., 1998, AJ, 116, 1244

Toomre A., 1964, ApJ, 139, 1217

Toth G., Ostriker J. P., 1992, ApJ, 389, 5

Traat P., 1998, astro-ph/9812425

Trager S. C., 1999, in "Photometric Redshifts and High Redshift Galaxies", eds. R. Weymann, L. Storrie-Lombardi, M. Sawicki & R. Brunner (astro-ph/9906396)

Tully R. B., Verheijen M. A. W., 1997, ApJ, 484, 145 (TV)

Tully R. B., Verheijen M. A. W., Pierce M. J., Huang J., Wainscoat R. J., 1996, AJ, 112, 2471 (TVPHW)

Tully R. B., Pierce M. J., Huang J., Saunders W., Verheijen M. A. W., Witchalls P. L., 1998, AJ, 115, 2264

Valageas P., Schaeffer R., 1999, A&A, 345, 329

van der Hulst J. M., Skillman E. D., Smith T. R., Bothun G. D., McGaugh S. S., de Blok W. J. G., 1993, AJ, 106, 548

van Dokkum P. G., Franx M., 1995, AJ, 110, 2027

van Zee L., Haynes M. P., Salzer J. J., 1997, AJ, 114, 2479

Vazdekis A., Arimoto N., 1999, astro-ph/9906140

Velazquez H., White S. D. M., 1999, MNRAS, 304, 254

Verheijen M. A. W., 1997, PhD Thesis, University of Groningen

Vila-Costas M. B., Edmunds M. G., 1992, MNRAS, 259, 121

Visvanathan N., Sandage A., 1972, ApJ, 216, 214

Vogt N. P., Forbes D. A., Phillips A. C., Gronwall C., Faber S. M., Illingworth G. D., Koo D. C., 1996, ApJ, 465, 15L

Wainscoat R. J., Cowie L. L., 1992, AJ, 103, 332

Wang J., Heckman T. M., Lehnert M. D., 1999, ApJ, 515, 97

Wegner G., Haynes M. P., Giovanelli R., 1993, AJ, 105, 1251

White III, R. E., Keel W. C., Conselice C. J., 1996, astro-ph/9608113

White S. D. M., Frenk C. S., 1991, ApJ., 379, 52

Williams R. E., et al., 1996, AJ, 112, 1335

Worthey G., 1994, ApJS, 95, 107

Wyse R. F. G., Silk J., 1989, ApJ, 339, 700

Yee H. K. C., 1998, Proceedings of "Xth Recontres de Blois: Birth of Galaxies", astro-ph/9809347

Yi S., Demarque P., Oemler Jr., A., 1997, ApJ, 486, 201

Young J. S., Knezek P. M., 1989, ApJ, 347, 55L

Zaritsky D., White S. D. M., 1994, ApJ, 435, 599

Zaritsky D., Kennicutt Jr., R. C., Huchra J. P., 1994, ApJ, 420, 87

Zepf S. E., 1997, Nature, 390, 377